The structure and stellar population of the Nuclear Bulge of the Milky Way

UNIVERSIDAD
DE GRANADA

Francisco Nogueras Lara

Supervisor: Dr. Rainer Schödel
Dr. Antonio María Alberdi Odriozola
Radioastronomy and galactic structure department
Instituto de Astrofísica de Andalucía

Programa de doctorado en Física y Ciencias del Espacio

This dissertation is submitted for the degree of
Doctor of Philosophy
September 2019

Editor: Universidad de Granada. Tesis Doctorales
Autor: Francisco Nogueras Lara
ISBN: 978-84-1117-162-5
URI: http://hdl.handle.net/10481/71853

Francisco Nogueras Lara, for the Doctor of Philosophy degree in Physics, presented on 23rd September 2019, at the Instituto de Astrofísica de Andalucía.

TITLE: ***"The stellar structure and population of the Nuclear Bulge of the Milky Way"***

SUPERVISORS: Dr. Rainer Schödel
Dr. Antonio María Alberdi Odriozola

EXAMINATION PANEL:

PRESIDENT:	Dr. José Manuel Vílchez Medina
SECRETARY:	Dr. Almudena Zurita Muñoz
BOARD MEMBERS:	Dr. Koraljka Muzic
	Dr. Miriam García García
	Dr. Mathias Schultheis
SUBSTITUTES:	Dr. João Alves
	Dr. Banafsheh Shahzamanian
EXTERNAL REFEREES:	Dr. Anja Feldmeier-Krause
	Dr. Andreas Eckart

The following publications summarise the main results obtained during doctoral study:

GALACTICNUCLEUS: A high angular resolution JHK$_s$ imaging survey of the Galactic centre. I. Methodology, performance, and near-infrared extinction towards the Galactic centre by F. Nogueras-Lara, A. T. Gallego-Calvente, H. Dong, E. Gallego-Cano, J. H. V. Girard et al. Published in Astronomy & Astrophysics, Volume 610, id.A83. Year: 2018. DOI: 10.1051/0004-6361/201732002.

Star formation history and metallicity in the Galactic inner bulge revealed by the red giant branch bump by F. Nogueras-Lara, R. Schödel, H. Dong, F. Najarro, A. T. Gallego-Calvente et al. Published in Astronomy & Astrophysics, Volume 620, id.A83. Year: 2018. DOI: 10.1051/0004-6361/201833518.

GALACTICNUCLEUS: A high-angular-resolution JHKs imaging survey of the Galactic centre II. First data release of the catalogue and the most detailed CMDs of the GC by F. Nogueras-Lara, R. Schödel, A. T. Gallego-Calvente, H. Dong, E. Gallego-cano, et al. Accepted for publication in Astronomy & Astrophysics. Year: 2019. arXiv:1908.10366.

Variability of the near-infrared extinction curve towards the Galactic centre by F. Nogueras-Lara, R. Schödel, F. Najarro, A. T. Gallego-Calvente, E. Gallego-cano, et al. Accepted for publication in Astronomy & Astrophysics. Year: 2019.

The nuclear disc of the Milky Way: Early formation, long quiescence, and starburst activity one billion years ago by F. Nogueras-Lara, R. Schödel, A. T. Gallego-Calvente, E. Gallego-cano, B. Shahzamanian et al. Submitted to Nature Astronomy. Year: 2019.

I would like to dedicate this thesis to my parents. Ellos son los que la han hecho posible.

Acknowledgements

Llegó el momento. Después de un largo camino se cierra una etapa de aprendizaje y desarrollo profesional y personal. ¡Esta es la última sección que escribo de la tesis! Todo lo que pueda escribir aquí se queda corto para expresar la alegría y la emoción de ver casi alcanzada una meta, un sueño que persigo y deseo prácticamente desde que empecé a estudiar. La astronomía hizo que empezara la carrera de Física hace ya algunos años y es la que me ha traído hasta este punto. Esta tesis es el resultado del esfuerzo y la pasión de años de trabajo arropado por todos aquellos que me han ayudado y me han permitido llegar hasta aquí. En primer lugar, le dedico esta tesis a mis padres. Ellos han sido los verdaderos artífices de que yo haya llegado a cumplir mi sueño. Me han apoyado en todo y me han brindado las mejores oportunidades para poder desarrollarme de la mejor manera educativa y sobretodo personalmente. ¡Muchas gracias a los dos! Mi mayor pesar es que mi madre no podrá acompañarme el día de la defensa ya que falleció hace algunos años. Sin embargo, estoy seguro de que la disfrutará desde el cielo estrellado. Muchas gracias por tu ejemplo y por tu amor incondicional. Pensar en ti siempre me da fuerzas. A ti papá, gracias por tu apoyo y por tu ejemplo. Es un orgullo ser tu hijo. Gracias a vosotros he aprendido que la constancia te permite llegar a donde te propongas. Muchas gracias también a mi hermana que siempre me ha ayudado y ha estado siempre a mi lado y para cualquier cosa, desde leerse un TFM a una tesis doctoral... No me puedo olvidar tampoco de mis abuelas Aurelia (DEP) y Concha que me han dado su cariño desde que nací y me han animado y apoyado siempre. También le doy las gracias a mi tío Manolo con el que, junto con mi padre, he recorrido un buen número de las mejores salas de ópera del mundo y nos hemos bebido una parte de Alemania (3 o 4 cervezas... no me acuerdo bien). ¡Qué bien nos lo hemos pasado los tres! Por supuesto a mi tía

Nieves y a mi tío Pascual, que siempre han estado a mi lado. Muchas gracias también a mis suegros Paco y Mari. ¡Muchas gracias a mi familia que es estupenda!

En mayor o menor medida estos años me ha tenido que aguantar mucha gente. Mi familia más cercana lo sabe bien, y es que, hacer una tesis no es siempre un camino de rosas... y hay días buenos y días malos. Muchas gracias a Sandra, mi pareja, que es la que ha tenido que aguantarme todos los días. ¡Eso sí que se merece un título! ;) Muchas gracias por darme ánimos siempre que los he necesitado y por saber hacerme ver el lado bueno de las cosas. Eres increíble, ¡Te quiero!

Durante estos años he conocido a gente excepcional en el trabajo que me han ayudado durante el proceso y que se merecen todo mi cariño y reconocimiento. Voy a intentar no olvidarme de nadie mientras oigo "Eye of the Tiger", la canción que me ha dado moral siempre que me ha tocado dar una charla o hacer un examen. En primer lugar, muchísimas gracias a mis directores Rainer Schödel y Antxón Alberdi. Muchas gracias, Rainer, por darme la oportunidad de unirme a tu grupo y por ofrecerme tantas posibilidades para poder aprender y desarrollar mi carrera investigadora. ¡Ha sido un placer trabajar contigo! Muchas gracias también a Antxón y a Emilio Alfaro por su ayuda fundamental y sus consejos siempre que los he necesitado. Muchas gracias a todos los miembros del Grupo del Centro Galáctico del IAA por vuestra ayuda. Nunca olvidaré las largas y divertidas noches de observación en el VLT con Laly o las salidas A "Chicote" con Teresa en Madrid. Muchas gracias también a Ban y Hui por su ayuda durante mi tesis y por sus comentarios sobre las versiones preliminares. ¡Me habéis ayudado un montón! Muchas gracias a Angela. También ha sido un privilegio haber podido conocer y colaborar con grandes científicos y mejores personas: muchas gracias Michael (y familia) por haberme ayudado tanto durante mi estancia en la ESO. ¡Aprendí un montón! Muchas gracias a Tim de Zeeuw, Nadine Neumayer, Paco Najarro, Anja Feldmeier-Krause, Julien Girard, Shogo Nishiyama y Santi Cassisi. He aprendido mucho colaborando con vosotros y me habéis ayudado cuando lo he necesitado. También me gustaría agradecer a los miembros del tribunal de mi defensa el tiempo que se han tomado para poder evaluar mi trabajo.

¡Además mis compañeros dentro y fuera del IAA me han ayudado a no perder la cabeza durante el doctorado! Gracias a Antonio Lorenzo por haber compartido despacho conmigo casi desde que empecé y por los desayunos y ratos de pádel. Gracias también a Marta por los ratos de "parrishita" y las tardes de juegos. Gracias

a Salva, Antonio Fuentes y Laura por nuestros desayunos y cafés de media tarde (glu glu?). Gracias a mis amigos del rayo Javi y Alejandro, y también a Estefanía y Feli. Con todos ellos he compartido despacho y han hecho que el trabajo diario sea muy agradable.

Muchas gracias a mis amigos de siempre: Fran, Silvia, Víctor, Cal, Cala, Dani Camino, Javi Bolivar, Migue Calles, Emilio, Antonio (el abogado) Antonio (el abuelo), Rafa Navajas, Luis Samos y todos los del tenis y a tantos otros que seguro que se me olvidan. Muchas gracias también a todos mis amigos de la ESO.

¡Un enorme gracias a toda la gente del IAA que tanto me ha ayudado! Espero volver pronto.

Paco

This work has made use of BaSTI web tools. The research leading to these results has received funding from the European Research Council under the European Union's Seventh Framework Programme (FP7/2007-2013) / ERC grant agreement n° [614922]. This work is based on observations made with ESO Telescopes at the La Silla Paranal Observatory under programmes IDs 195.B-0283 and 091.B-0418. We thank the staff of ESO for their great efforts and helpfulness. F N-L acknowledges

financial support from a MECD pre-doctoral contract, code FPU14/01700. We acknowledge support from the State Agency for Research of the Spanish MCIU through the Centre of Excellence Severo Ochoa Award of the Instituto de Astrofísica de Andalucía (CSIC) (SEV-2017-0709).

Abstract

The centre of the Milky Way is a fundamental astrophysical target since it is the closest galaxy nucleus ($\sim$ 8 kpc from Earth) and the only one where we can study individual stars with high angular resolution. It is an extreme environment characterised by extreme conditions such as: very high stellar densities ($\sim 10^{5-7}$ pc^{-3}, Launhardt et al., 2002; Schödel et al., 2007, 2018), a tidal field so intense that even massive, young clusters dissolve into the background in less than 10 Myr (Portegies Zwart et al., 2002), high turbulence and temperature of the interstellar medium (Morris & Serabyn, 1996), a strong magnetic field (Crocker, 2012), and intense UV radiation (Launhardt et al., 2002). Despite, or possibly because of these extreme properties, the Galactic centre (GC) is the Galaxy's most prolific massive star forming environment (Mauerhan et al., 2010b; Schödel et al., 2007; Yusef-Zadeh et al., 2009). Moreover, it possesses a supermassive black hole, SgrA*, in its centre. Therefore, it is a unique laboratory to improve our understanding about the inner regions of the galaxies. Nevertheless, in spite of its importance only ~ 1 % of its total area has been studied with the sufficient wavelength coverage and high angular resolution to analyse its stellar structure and population. In addition, the high extinction (and its strong variation on arc second scales) and the extreme source crowding of the central regions of the Milky Way pose great difficulties to the study of the GC. In this way, all the existing surveys that contain the GC (2MASS, UKIDSS, VVV, SIRIUS) fail at covering adequately the GC area.

This thesis aims at improving the state of the art in order to enable us to perform a detailed study of the stellar population of the GC. For this, we carried out the GALACTICNUCLEUS survey during this PhD thesis. This is a high angular near infrared (NIR) survey (JHK_s bands) with the HAWK-I instrument located at the VLT UT4 (ESO, Paranal-Chile). In this dissertation, I explain the whole process

to perform the survey from the observing strategy to the first data release of the catalogue. The development of the data reduction (highly non standard) pipeline and the analysis of the data to obtain accurate photometry and astrometry, lie at the heart of this thesis. To achieve the necessary high angular resolution to analyse the stellar population of the GC, we use the speckle holographic technique described in Schödel et al. (2013), which has been optimised for crowded fields. To assess the data quality, we compare GALACTICNUCLEUS with the up-to-now best surveys for the GC: VVV, SIRIUS and NICMOS (HST) data.

The catalogue covers a total region of $\sim 0.3^\circ$ (~ 6000 pc^2) located at the nuclear bulge, the inner bulge and the transition region between them. We obtained accurate JHK_s photometry of $\sim 3.3 \times 10^6$ stars in the GC detecting around 20 % in J, 65 % in H and 90 % in K_s. The GALACTICNUCLEUS survey reaches 5 σ detection limits for $J \sim 22$ mag, $H \sim 21$ mag and $K_s \sim 21$ mag. The uncertainties are below 0.05 mag at $J \sim 21$ mag, $H \sim 19$ mag and $K_s \sim 18$ mag. The zero point systematic uncertainty is $\lesssim 0.04$ mag in all three bands.

As a main result of the GALACTICNUCLEUS survey, I show and explain the colour-magnitude diagrams (CMDs) obtained for the different regions analysed by the catalogue. We clearly distinguish the foreground population, the AGBB (asymptotic giant branch bump), the post main sequence, the ascending giant branch, the RC (stars in their He core burning sequence, Girardi, 2016) and the RGBB (red giant branch bump, see, e.g., Cassisi & Salaris, 1997; Nataf et al., 2014; Nogueras-Lara et al., 2018b; Salaris et al., 2002). The CMDs also show clearly the effect of the strong and highly variable interstellar extinction toward the GC.

Using the exquisite data set from GALACTICNUCLEUS, we study the extinction curve towards the GC in the NIR regime. The extinction curve is generally accepted to follow a power law in the NIR. I explain our findings using the central pointing of the survey where we analysed the extinction index using several independent methods based on red clump stars and spectroscopically identified stars. We determined an extinction index $\alpha = 2.30 \pm 0.08$. Moreover, we created and published an extinction map to correct for differential extinction in the studied region (Nogueras-Lara et al., 2018a). In a second step, we use the central region of the nuclear bulge (combining 14 pointings of the GALACTICNUCLEUS survey) to analyse in detail the dependence of the extinction index on the line of sight and its dependence on the extinction

and the wavelength. We do not find any significant dependence of the interstellar extinction toward the GC on the line of sight. We do, however, find a dependence of the extinction index on wavelength. The extinction indices α_{JH} and α_{HK_s} differs by $\Delta\alpha = 0.19 \pm 0.05$. Therefore, the single power-law approximation used up to now may be an over-simplification. This might explain the different values obtained in the literature for the extinction index in the NIR. We also obtain the values for the extinction indices, $\alpha_{JH} = 2.43 \pm 0.03$ and $\alpha_{HK_s} = 2.23 \pm 0.03$. Small differences of α ($\sim 10-15\%$) can lead to a change of absolute extinction by ~ 0.3 mag, which results in a wrong estimation of the distances because, for a GC distance of 8 kpc, an uncertainty of 0.3 mag on the distance modulus corresponds to an uncertainty in the physical distance of ~ 1 kpc (Matsunaga et al., 2016). Thus, this work might contribute to a change in the picture of the inner region of the Milky Way.

Once the extinction curve is characterised, I study the stellar structure and population of the nuclear bulge of the Milky Way. Firstly, I present the analysis of the stellar population of the innermost region of the nuclear bulge using the central pointing of the GALACTICNUCLEUS survey. We estimate that the majority of the stars have solar or super-solar metallicity by comparing our extinction-corrected colour-magnitude diagrams with isochrones with different metallicities and a synthetic stellar model with a constant star formation. We extend our analysis studying the star formation history of the nuclear bulge using the K_s photometry to build a de-reddened K_s luminosity function. We fit the luminosity function with theoretical models (BaSTI and MIST) and obtain that the star formation history is not continuous for the nuclear bulge as it was previously accepted. Our results contradict the previously accepted paradigm and point towards a mainly old stellar population ($\sim 90\,\%$ of the stars are >8 Gyr). After this initial star formation, there was a quiescent period that was ended abruptly by a star formation event $\lesssim 1$ Gyr ago. This star formation event accounts for $\sim 5\,\%$ of the total mass of the nuclear bulge and may arguably have been one of the most energetic events in the whole history of the Milky Way. The star formation continued on a lower level, creating a few percent of the mass in the past ~ 500 Myr, with an increase around 30 Myr ago according to previous work (Matsunaga et al., 2011).

Finally, I compare the star formation history in the nuclear bulge with that in the inner regions of the Milky Way bulge covered by the GALACTICNUCLEUS survey.

Analysing the star K_s luminosity function, we identify the red giant branch bump. Fitting the luminosity function with theoretical models, we conclude that the stellar population is old ($\sim$ 12 Gyr) and metal rich (around twice solar metallicity). We also analyse the NIR extinction curve towards the inner bulge regions and find that the extinction index is compatible with what we found for the nuclear bulge. Finally, we also analyse the metallicity gradient in the bulge and conclude that there is a flattening of the metallicity increase for the inner regions of the bulge, in agreement with the previous work by Rich et al. (2007).

Resumen

El centro de la Vía Láctea constituye un objetivo fundamental para la astrofísica, puesto que es el núcleo galáctico más cercano ($\sim$ 8 kpc desde la Tierra) y el único donde es posible estudiar las estrellas individuales con alta resolución angular. Es un entorno extremo caracterizado por condiciones límite como: densidades estelares muy elevadas ($\sim 10^{5-7}$ pc^{-3}, Launhardt et al., 2002; Schödel et al., 2007, 2018), un campo de marea tan intenso que incluso los cúmulos jóvenes y masivos se disuelven en menos de 10 Myr entre la población estelar circundante (Portegies Zwart et al., 2002), alta turbulencia y temperatura del medio interestelar, un fuerte campo magnético (Crocker, 2012), y una intensa radiación ultravioleta (Launhardt et al., 2002). A pesar de estas condiciones, o precisamente debido a ellas, el centro Galáctico (CG) es el entorno estelar más prolífico en nuestra galaxia para la formación de estrellas masivas (Mauerhan et al., 2010b; Schödel et al., 2007; Yusef-Zadeh et al., 2009). Además, su centro está ocupado por un agujero negro supermasivo, SgrA*. Por lo tanto, es un laboratorio único para mejorar nuestro conocimiento sobre las regiones internas de las galaxias. Sin embargo, a pesar de su extraordinaria importancia, solo $\sim$ 1 % de su área total ha sido estudiada con la suficiente resolución angular y cobertura en diferentes longitudes de onda para analizar su estructura y población estelar. Además, la alta extinción (y su fuerte variación en escalas de segundos de arco) y la extrema densidad de fuentes de las regiones centrales de la Vía Láctea, constituyen serios obstáculos para su estudio. De esta forma, todos los catálogos existentes que contienen el CG (2MASS, UKIDSS, VVV, SIRIUS) fracasan al cubrir este área en detalle.

El objetivo fundamental de esta tesis es contribuir a la mejora del estado del arte, para permitir un estudio detallado de la población estelar del bulbo nuclear de la Vía Láctea. Para ello, hemos desarrollado un nuevo catálogo, GALACTICNUCLEUS,

durante esta tesis doctoral. Este catálogo se caracteriza por estar diseñado especialmente para la observación del CG en el infrarrojo cercano (bandas JHK_s) con alta resolución angular. Los datos fueron tomados con el instrumento HAWK-I situado en el UT4 del VLT (ESO, Paranal-Chile). En esta disertación, se trata detalladamente el proceso completo desde la elaboración de la estrategia de observación hasta la primera publicación de los datos del catálogo. El desarrollo de un procedimiento para la reducción de los datos (altamente no estándar) y el análisis de los mismos para obtener fotometría y astrometría precisas constituyen una parte fundamental de la tesis. Para conseguir la resolución angular necesaria para analizar la población estelar del CG, utilizamos la técnica de holografía descrita en Schödel et al. (2013), que ha sido optimizada para campos con altas densidades estelares. Para comprobar la calidad de los datos, llevamos a cabo una comparación de GALACTICNUCLEUS con los mejores catálogos existentes hasta la fecha para el CG: VVV, SIRIUS y NICMOS (HST).

Nuestro catálogo cubre una región total de $\sim 0.3^\circ$ (~ 6000 pc^2) localizados en el bulbo nuclear, el bulbo interno galáctico y la región de transición entre ellos. Se obtiene fotometría precisa, JHK_s, para $\sim 3.3 \times 10^6$ de estrellas de las cuales se detecta un 20 % en J, un 65 % en H y un 90 % en K_s. GALACTICNUCLEUS alcanza detecciones de 5 σ para $J \sim 22$ mag, $H \sim 21$ mag y $K_s \sim 21$ mag. Las incertidumbres son menores de 0.05 mag para $J \sim 21$ mag, $H \sim 19$ mag y $K_s \sim 18$ mag. Las incertidumbres del punto cero son $\lesssim 0.04$ mag para las tres bandas.

Como resultado principal del catálogo, se muestran y explican los diagramas color-magnitud obtenidos para las diferentes regiones analizadas. En ellos se distingue claramente la población estelar que pertenece al camino desde la Tierra al CG (principalmente tres brazos espirales que se atraviesan en la línea de visión), la acumulación de la rama asintótica gigante (AGBB, por sus siglas en inglés), la post-secuencia principal, la rama ascendente gigante, el llamado "red clump" y la acumulación de estrellas de la rama gigante roja (RGBB, ver, e.g., Cassisi & Salaris, 1997; Nataf et al., 2014; Nogueras-Lara et al., 2018b; Salaris et al., 2002). También se observa claramente el efecto de la fuerte y altamente variable extinción hacia el CG.

Utilizando los datos de alta resolución de GALACTICNUCLEUS, estudiamos la curva de extinción hacia el CG en el rango infrarrojo cercano. Generalmente

se acepta que la extinción se comporta como una ley potencial en el infrarrojo cercano. En la disertación se discuten nuestros resultados obtenidos a partir del campo central del catálogo, donde analizamos el índice de extinción utilizando varios métodos independientes basados en estrellas "red clump" y en estrellas cuyo tipo ha sido identificado previamente. Obtenemos un índice de extinción $\alpha = 2.30 \pm 0.08$. Además, creamos y publicamos mapas de extinción para corregir la extinción diferencial en las regiones estudiadas (Nogueras-Lara et al., 2018a). A continuación, utilizamos la región central del bulbo nuclear (combinando los 14 campos centrales de GALACTICNUCLEUS) para analizar en detalle la variación del índice de extinción con la línea de visión y su dependencia con la extinción y la longitud de onda. No encontramos ninguna variabilidad significativa con la línea de visión o la extinción dentro de las incertidumbres experimentales. Sin embargo, obtenemos una variación del índice de extinción en función de la longitud de onda considerada. Esta variación es de $\Delta\alpha = 0.20 \pm 0.05$ entre los índices de extinción α_{JH} y α_{HK_s}. Por lo tanto, la aproximación de ley de potencias individual podría ser constituir una sobre simplificación. Esta dependencia del índice de extinción con la longitude de onda en el infrarrojo cercano puede explicar los valores discrepantes obtenidos en la bibliografía reciente. También se obtienen los valores concretos $\alpha_{JH} = 2.43 \pm 0.03$ y $\alpha_{HK_s} = 2.23 \pm 0.03$. Es importante notar que pequeñas diferencias en el valor α ($\sim 10 - 15\%$) pueden originar errores en la extinción absoluta de ~ 0.3 mag, lo que puede ocasionar estimaciones incorrectas de las distancias basadas en el módulo de las distancias (~ 1 kpc (Matsunaga et al., 2016) a la distancia del CG). Por lo tanto, nuestros resultados podrían cambiar la visión que se tiene actualmente de la región más interna de la Vía Láctea.

Una vez caracterizada la curva de extinción, procedemos a estudiar la estructura y la población estelar del bulbo nuclear galáctico. En primer lugar, se presenta el análisis de la población estelar de la región más interna utilizando el campo central de GALACTICNUCLEUS. Estimamos que la mayoría de estrellas presentan metalicidades de solar a super-solar comparando diagramas color-magnitud corregidos de extinción con isocronas de diferentes metalicidades y un modelo sintético con formación estelar constante. Posteriormente, extendemos nuestro análisis estudiando la historia de formación estelar del bulbo nuclear utilizando la fotometría en banda K_s para construir una función de luminosidad desenrojecida. Ajustándola con modelos

teóricos (BaSTI y MIST) se obtiene que la formación estelar no es continua en esta región, tal y como se creía con anterioridad a nuestro estudio. Nuestros resultados contradicen el paradigma previamente aceptado y apuntan hacia una población estelar principalmente vieja ($\sim 90\,\%$ de las estrellas son >8 Gyr). Tras este periodo inicial de formación estelar, no se formaron apenas estrellas hasta un fuerte evento de formación estelar que tuvo lugar hace $\lesssim 1$ Gyr. En este evento se formó un $\sim 5\,\%$ de la masa total de las estrellas del bulbo nuclear, en el que puede haber sido uno de los eventos más energéticos de la historia de la Vía Láctea. La formación estelar continuó a un nivel inferior, creándose $\sim 1-2\,\%$ de su masa total en los pasados ~ 500 Myr, con un incremento significativo hace aproximadamente 30 Myr de acuerdo con trabajos anteriores (Matsunaga et al., 2011).

Finalmente, comparamos la historia de formación estelar en el bulbo nuclear con la de las regiones más internas del bulbo galáctico (observadas por GALACTICNUCLEUS). Analizando la función de luminosidad en la banda K_s, identificamos el RGBB. Ajustando los datos experimentales con modelos teóricos, concluimos que la población estelar es vieja (~ 12 Gyr) y rica en metales (alrededor del doble de la metalicidad solar). Por otra parte, también analizamos la curva de extinción en el infrarrojo cercano en las regiones internas del bulbo, encontrando que el índice de extinción es compatible con los resultados obtenidos previamente para el bulbo nuclear. Por último, también analizamos el gradiente de metalicidad en el bulbo y concluimos que hay una interrupción (o menor tendencia) del crecimiento de la metalicidad hacia el CG, de acuerdo con el trabajo realizado por Rich et al. (2007).

Table of contents

List of figures

List of tables

Glossary

Acronyms / Abbreviations

2MASS Two Micron All-Sky Survey

AGBB Asymptotic Giant Branch Bump

AIC Akaike Information Criterion (Akaike, 1974)

ALMA Atacama Large Millimeter/submillimeter Array

AO Adaptive optics

AT Auxiliary telescope

BaSTI Bag of Stellar Tracks and Isochrones (Pietrinferni et al., 2014)

BIC Bayesian Information Criterion (Schwarz, 1978)

CCD Colour-Colour diagram

CMD Colour-magnitude diagram

CMZ Central molecular zone

CONICA Near-Infrared Imager and Spectrograph

DIMM Differential Image Moption Monitor

DIT Detector integration time

ELT Extremely Large Telescope

ESO European Southern Observatory

FoV Field of view

FWHM Full width at half maximum

GC Galactic Centre

GLAO Ground-Layer Adaptive Optics

GMM GaussianMixture (SCIKIT-LEARN python function)

GRAAL GRound layer Adaptive optics Assisted by Lasers

HAWK-I High Acuity Wide-field K-band Imager

HST Hubble Space Telescope

IDL Interactive Data Language

IDW Inverse-Distance Weight

IFU Integral-Field unit

IRSF InfraRed Survey Facility

ISM Interstellar Medium

JWST James Webb Space Telescope

KLF K_s Luminosity Function

KMOS K-band Muti Object Spectrograph

LF Luminosity Function

mas milli-arcsecond

MC MonteCarlo

MIST MESA Isochrones & Stellar Tracks(e.g., Dotter, 2016)

MW Milky Way

NACO NAOS-CONICA

NAOS Nasmyth Adaptive Optics System

NB Nuclear bulge

NDIT Number of exposures per pointing

NIR Near infrared

NSC Nuclear star cluster

NSD Nuclear stellar disc

PARSEC Stellar models with the PAdova and TRieste Stellar Evolution Code (e.g., Bressan et al., 2012a)

PSF Point spread function

RC Red Clump

RGBB Red Giant Branch Bump

SAAO South African Astronomical Observatory

SFH Star formation history

Sgr A* Sagittarius A*

Sgr B2 Sagittarius B2

SIRIUS Simultaneous Infrared Imager for Unbiased Survey

SKA Square Kilometre Array

SMBH Super Massive Black Hole

TMT Thirty Meter Telescope

UKIDSS UKIRT Infrared Deep Sky Survey

UT Unit telescope

VISTA Visible and Infrared Survey Telescope for Astronomy

VLT Very Large Telescope

VST VLT Survey Telescope

VVV VISTA Variables in the Vía Láctea

ZP Zero point

Symbols

α Extinction index

χ^2	Chi square
$\lambda_{\mathbf{eff}}$	Effective wavelength
λ	Wavelength
μ	Distance modulus
σ	Sigma
$\mathbf{A_{band}}$	Extinction for a given band
b	Galactic latitude
dec	Declination
l	Galactic longitude
$\mathbf{M_{\odot}}$	Solar mass
$\mathbf{M_{band}}$	Absolute magnitude for a given band
$\mathbf{R_{\odot}}$	Solar radius
$\mathbf{r_h}$	Half-light radius
ra	Right Ascension
$\mathbf{z^t_{component}}$	Scales height
Z	Metallicity

"Me llamo Máximo Décimo Meridio, comandante de los ejércitos del norte. General de las Legiones Phoenix. Leal servidor del verdadero emperador Marco Aurelio. Padre de un hijo asesinado, marido de una mujer asesinada... y alcanzaré mi venganza en esta vida o en la otra."

Gladiator

1 Introduction

"At a distance of only 8 kpc (26,000 light years) the Galactic Centre is the closest nucleus of a galaxy, 100 to 1000 times closer than the nearest extragalactic systems. It is thus a unique laboratory in which physical processes that are relevant in general for the nuclei of all similar galaxies can be studied with the highest resolution possible". -The black hole at the centre of the Milky Way. A. Eckart, R. Schödel and C. Straubmeier.

1.1 Galactic nuclei

Galactic nuclei have been a leitmotif of astrophysical research since many decades. They are extreme environments characterised by high stellar densities whose centre normally hosts a super massive black hole (SMBH). In particular, the vast majority of spiral and elliptical galaxies have a SMBH in their cores.

High-angular resolution (sub-arcsecond) studies in the past three decades, mainly carried out with the Hubble Space Telescope (HST), but also with adaptive optics (AO) assisted ground-based instruments, have shown the high complexity and activity of the central region of galaxies. In this way, observations with angular resolution $\sim 0.1'' - 0.2''$ have resolved the radii of influence of SMBHs and have allowed to estimate their masses excluding other alternative scenarios showing that only SMBHs can explain the high observed mass densities.

Most SMBHs are embedded in compact, dense stellar systems that are distinct from the large-scale bulges (e.g., Graham & Spitler, 2009; Neumayer & Walcher, 2012; Seth et al., 2008). These stellar nuclei appear mainly in the form of nuclear star clusters (NSCs). NSCs are the most massive and densest star clusters in the present-day Universe (Neumayer, 2017; Seth et al., 2019). They have a rather well defined half light radius of ~ 3 pc (e.g. Figure 2 in Neumayer, 2017) and often show complex star formation histories, including very young (a few Myr) populations, particularly when they are located in spiral galaxies, (Rossa et al., 2006; Seth et al., 2006; Walcher et al., 2006). Some NSCs are in the centre of larger stellar discs or star forming rings of few tens to few hundred of parsecs that are known as nuclear stellar discs (NSD, Balcells et al., 2007; Launhardt et al., 2002).

The formation scenario of stellar nuclei is not clear yet. Nevertheless, their morphology, kinematics, and complex stellar populations suggest that they form, at least partially, through repeated or quasi-continuous accretion of gas, followed by star formation. The inner regions of the galaxies are linked with the whole galaxy and constitute a source of information about its growth and evolution (and vice versa). In this way, understanding galactic nuclei is a fundamental goal for astrophysics, since it can teach us about galaxy evolution and star formation in the most extreme environments. The main obstacle for studying galactic nuclei is their huge distance. We are limited to the study of their integrated light, averaged over scales of a few parsecs to several tens of parsecs and dominated by the brightest stars. Even with the next generation of 30-40 m class telescopes this situation will remain fundamentally unchanged. Thus, the only option to know more about these far-away, unresolved targets, the best option is to rely on nearby analogues that can be observed at higher spatial resolution.

1.2 The centre of the Milky Way

Just looking at the sky with the naked eye in a dark night offers us the possibility of observing our galaxy, the Milky Way (MW). Since we are inside it, the MW gives us a fantastic chance of analysing in detail a galactic nucleus. The Galactic centre (GC) is located at only 8 kpc from Earth, and it is therefore the closest galactic nucleus. Recently the studies by Gravity Collaboration et al. (2018) and Do et al. (2019a) have used very accurate measurements of the orbit of the closest star to Sagittarius A* (Sgr A*), S0-2, to obtain the distance to the SMBH with an unprecedented detail: 8.122 ± 0.031 kpc and 7.971 ± 0.059, respectively. This means that the GC is located about a hundred times closer than the Andromeda galaxy, and a thousand times closer than the next active galactic nucleus. In particular, the angular size of the GC is $\sim 100'$, whereas for the centre of Andromeda this number is $\sim 1'$, both quantities corresponding to ~ 200 pc. In this way, the GC is the only galactic nucleus where we can resolve individual stars down to mili-parsec scales (Genzel et al., 2010; Gravity Collaboration et al., 2018; Schödel et al., 2014). Therefore, it constitutes a unique laboratory to study stellar nuclei and their role in the context of galaxy evolution. It is a prime target for the major ground-based and space-borne observatories and will be so for future facilities, such as ALMA, SKA, the JWST, the TMT, or the ELT.

1.2.1 The GC in the sky

The precise position of the GC is marked by the massive black hole Sgr A*: $17^h45^m40^s.0409$, $29°00'28''.118$ (J2000.0 positions according to Reid & Brunthaler, 2004, caption to Table 1).

For those of us who like to study the sky by eye at night, there are two clues to locate the GC: (1) The Sagittarius constellation. Its central part, known as Teapot, points towards the GC. (2) The Scorpius constellation. The GC lies above the stinger of the scorpion. Figure 1.1 shows the location of the GC in the sky from Granada (Spain) at the beginning of September.

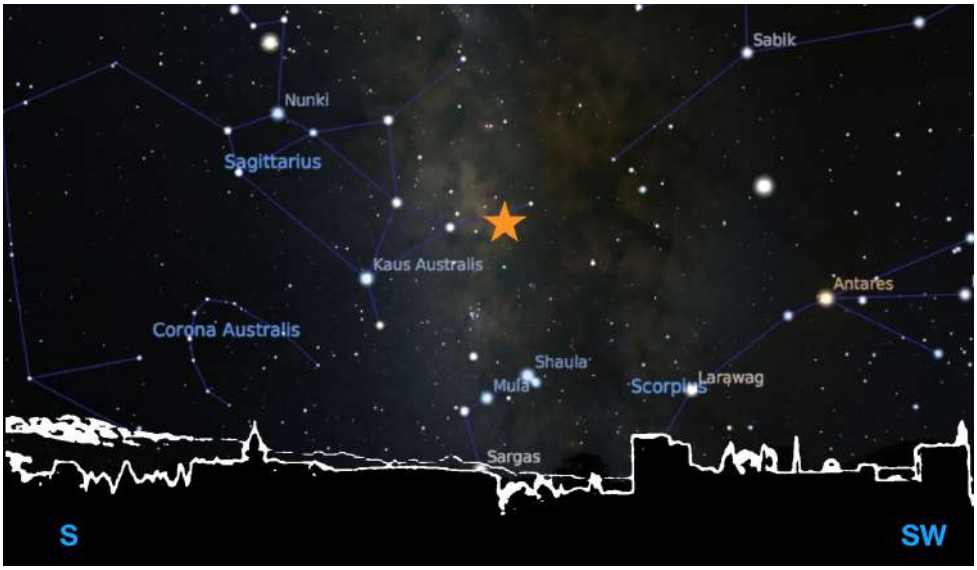

Fig. 1.1 Sky view toward the GC from Granada in September. The orange star marks the position of the GC. The name of the constellations and the main stars are indicated in the figure. The Cardinal points are also marked. This figure has been produced using *Stellarium (https://stellarium-web.org)*.

1.2.2 Main features of the GC

The GC is roughly delimited by the nuclear bulge (NB, Launhardt et al., 2002). The NB is a distinct stellar structure that stands clearly out from the kiloparsec-scale Galactic Bulge/Bar and constitutes a flattened, possibly disk-like structure (NSD) with a radius of ~ 230 pc and a scale height of ~ 45 pc. Figure 1.2 outlines a schematic view of the MW indicating the location of the NB. The NB partially overlaps with the so called central molecular zone (CMZ). The CMZ is a region formed by gas, that is channeled toward the GC by the Galactic Bar and finally settles in closed orbits (Morris & Serabyn, 1996). Several star forming regions are located within the CMZ, including one of the most massive star forming regions of the MW, Sgr B2 (e.g., Kruijssen et al., 2014; Longmore et al., 2013; Zhao & Wright, 2011). Fig. 1.3 shows a scheme of the shape of the CMZ and the main features of the GC.

The NB is characterised by high stellar densities, strong tidal fields, high magnetic fields, and high turbulence and temperature of the interstellar medium (e.g. Böker,

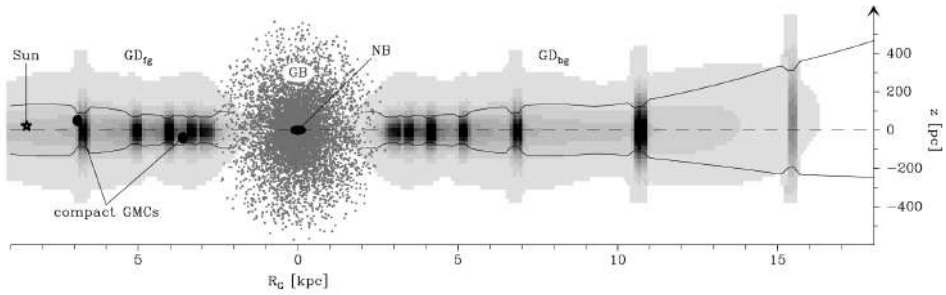

Fig. 1.2 Scheme of the main galactic features of the MW. The grey-scale used for the image indicates the average hydrogen density in the Galactic Disk (from 0.1 to 1 cm^{-3}. Credits: Fig.1 from Launhardt et al. (2002).

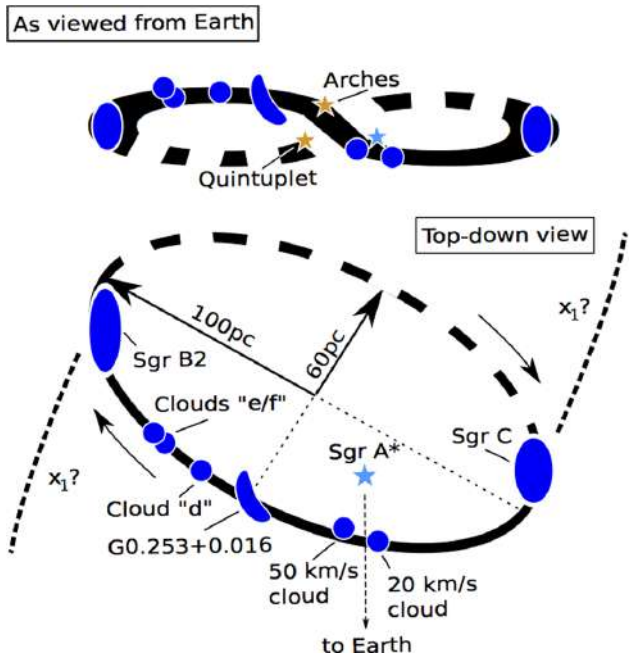

Fig. 1.3 Representation of the CMZ as it is seen from the Earth (top panel) and from above (bottom panel). The main features of the GC are indicated in the Figure. The black lines sketch a possible orbital geometry of the gas in the CMZ. x1 indicates the regular periodic orbit elongated along the galactic bar major axis (Contopoulos & Grosbol, 1989). Credits: Fig.5 from Kruijssen et al. (2014).

2010; Launhardt et al., 2002; Morris & Serabyn, 1996; Nishiyama et al., 2008). In spite of - or possibly because of - these harsh conditions, the NB is the Galaxy's most prolific massive star forming environment. It may be similar to the star forming rings found at the centres of other disk galaxies (e.g., Ledo et al., 2010; Pizzella et al., 2002).

The presence of HII regions, massive young stars, massive young clusters (a few 10^4 $M_\odot$, like the Arches, Quintuplet and the NSC), as well as an overabundance of luminous giants, provide evidence for recent star formation throughout the NB (Genzel et al., 2010; Matsunaga et al., 2011; Portegies Zwart et al., 2010). In this way, the NB emits more than 10 % of the total galactic Lyman continuum flux in spite of occupying less than 1 % of the total galaxy volume. Moreover, the recent discovery of classical cepheids within 40 pc of the SMBH Sgr A* (Matsunaga et al., 2011), leads to the estimation that on the order of 10^6 $M_\odot$ of stars may have formed in the NB in the past 30 Myr. Nevertheless, the known young clusters at the GC only make up less than a tenth of this mass. This discrepancy is so stark that the conclusion appears inevitable that an important number of young stars/clusters have so far escaped their detection. Identifying them is extremely difficult due to the high interstellar extinction toward the GC ($A_v \sim 30$ mag), that dominates stellar colours through reddening, and by the high stellar density. The isolated Wolf-Rayet-like stars that have been found throughout the NB (Dong et al., 2011; Mauerhan et al., 2010a) may be the remnants of such dissolved clusters, or may have been ejected from the known clusters. Even clusters as massive as the Arches cluster will dissolve in the strong tidal field of the GC within about 10 Myr below the mean density of the surrounding NB (Portegies Zwart et al., 2002). Therefore, the standard method of detecting high density regions to identify young clusters is not valid in the GC but for very young clusters as the Arches and Quintuplet.

The NSC is located in the centre of the NB. It has a half-light radius around 5 pc ($\sim 2'$) following the work by Schödel et al. (2014) ($r_h = 4.2 \pm 0.4$ pc) and Fritz et al. (2016) ($r_h = 7 \pm 2$ pc). Its shape is point-symmetric in projection with respect to Sgr A* and it is flattened with a ratio between its minor and major axis of $q = 0.71 \pm 0.02$ (e.g., Fritz et al., 2014; Graham & Spitler, 2009; Schödel, 2011; Schödel et al., 2014). Its total mass is around $\sim (3.0 \pm 1.5) \times 10^7$ $M_\odot$ (Boehle et al., 2016; Gravity Collaboration et al., 2018; Launhardt et al., 2002; Schödel et al., 2014)

and its luminosity is $M_{K_s} = -16.0 \pm 0.5$. The NSC has been found to rotate slowly approximately parallel to overall Galactic rotation (Schödel et al., 2009; Trippe et al., 2008). It shows a very complex stellar population that has been formed through a quasi-constant star formation history with repeated bursts of star formation (Pfuhl et al., 2011, Schödel et al., submitted). The last episode occurred $\sim 3-6$ Myr ago and originated a mass of newly formed stars of approximately 1.5×10^4 $M_\odot$, among them about 200 OB stars (Genzel et al., 2010).

The formation of the NSC is still under debate. There are two main scenarios that are being discussed: (1) Star formation in situ. (2) Accretion of smaller clusters formed in their enviroments. Both processes may also contribute to the formation of the NSC (e.g. Böker, 2010; Neumayer, 2017, and references therein). Figure 1.4 shows a Near infrared (NIR) image of the NSC created using the GALACTICNUCLEUS survey (Nogueras-Lara et al., 2018a).

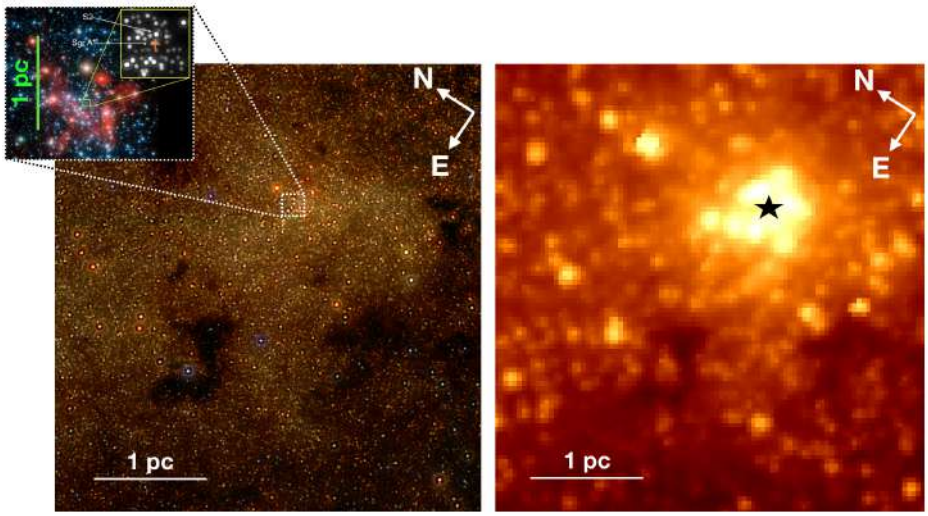

Fig. 1.4 Left panel: RGB image of the NSC created using the JHK_s bands of the GALACTICNUCLEUS survey (0.2" FWHM angular resolution). The inset shows the inner parsec. Right panel: IRAC/Spitzer 4.5 μm image of the NSC (2" FWHM angular resolution). The black star indicates the position of Sgr A*.

The NSC hosts the SMBH Sgr A* in its heart. This is a very compact and variable radio source with a variable X-ray and infrared counterpart coincident with the mass

centroid < 1 mas (e.g., Do et al., 2019b; Doeleman et al., 2009; Falcke et al., 2000; Plewa et al., 2015). The recent study by Do et al. (2019a) and the independent work by Gravity Collaboration et al. (2018) have determined the mass of the SMBH with very high precision using the orbital information of its closest orbiting star, S0-2. The obtained masses were $3.984 \pm 0.058 \pm 0.026 \times 10^6$ $M_\odot$ and $4.100 \pm 0.034 \times 10^6$ $M_\odot$, respectively.

The point cannot be overstressed that the centre of the Milky Way is the only galaxy nucleus in which we can actually resolve the NSC and the NB observationally and examine its properties and dynamics. Nevertheless, only around 1% of the projected area of the GC has been explored with the sufficient angular resolution and wavelength coverage to allow an in-depth study of its stellar population. Moreover, the well-explored regions, as the central parsec or the Arches and Quintuplet clusters, are extraordinary and we do not know whether they can be considered representative for the entire GC. Accurate data are key to understanding the evolution of the GC and to infer which physical processes shape our Galaxy.

1.2.3 Observational challenges

The observation of the GC is hampered by the high stellar crowding and the extreme interstellar extinction ($A_V \gtrsim 30$, $A_{K_s} \gtrsim 2.5$, e.g. Fritz et al., 2011; Nishiyama et al., 2008; Nogueras-Lara et al., 2018a; Schödel et al., 2010; Scoville et al., 2003). Therefore, the stellar population is mainly studied in the NIR regime since it is less prone to extinction. Figure 1.5 shows both issues, extinction and crowding, in a region close to the NSC. In principle, the stellar density that can be seen in some regions of the image is expected to be almost constant across the observed field. Nevertheless, there are large patterns with almost no stars. These large regions that appear dark are infrared dark/dense clouds in front of the GC, where extinction is so extreme that even infrared radiation cannot penetrate them.

Crowding

The observations of the GC are limited by the very high stellar densities of this region. The extreme crowding can produce source confusion and is an important source of photometric uncertainty if the angular resolution is not high enough. For

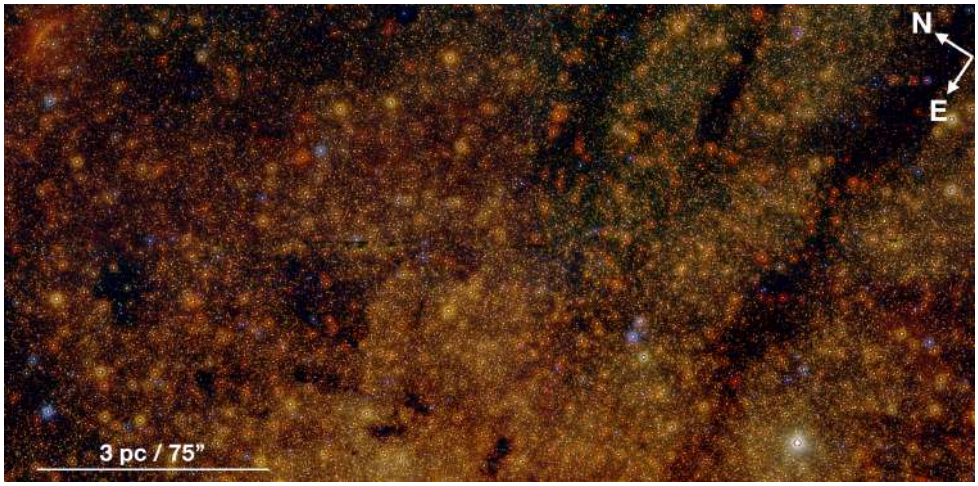

Fig. 1.5 Extinction and crowding in the GC. RGB image obtained using the JHK_s images of F2 of GALACTICNUCLEUS (see Sec. 3).

instance, the 50 % completeness limit at diffraction-limited resolution with an 8 m telescope in the K-band ($\theta \approx 0.06''$) is $K \approx 18$ for the central arc-seconds around Sgr A* (Schödel et al., 2007). This corresponds to a star of ~ 2 $M_\odot$ and constitutes an observing constrain. The stellar surface density of such stars is several tens per square arcsecond in the central parsec, but drops rapidly with projected distance from Sgr A* to a few stars per square arcsecond at distances $\gtrsim 1$ pc from Sgr A*. Thus, the situation is better for the NB and an angular resolution of $\sim 0.2''$ allows a detailed analysis of the giant stars. To get down to the main sequence it is necessary to wait until the next generation of 30 m telescopes.

Extinction

The extinction, and its variation on arc-seconds scales in particular, towards the GC make the characterisation of the stellar population and structure of the inner regions of the Galaxy extremely difficult. Figure 1.6 shows how the extinction affects the observations at different wavelengths. There are several open windows to study the GC. From each of them it is possible to obtain information about different properties of the GC. For instance, stars only can be observed in the near- and mid-

infrared regime, whereas observations at larger wavelengths give us information on the properties of the gas distributed along the NB. In spite of having spectral ranges to observe the GC, they all suffer from extinction in a more or less dramatic way. Since one of the main goals of the thesis is the study of the stellar population of the NB, we are going to be focused on NIR observations. For this, the first step is to know how the extinction affects this wavelength to apply a proper correction that allows us to obtain a reliable photometry.

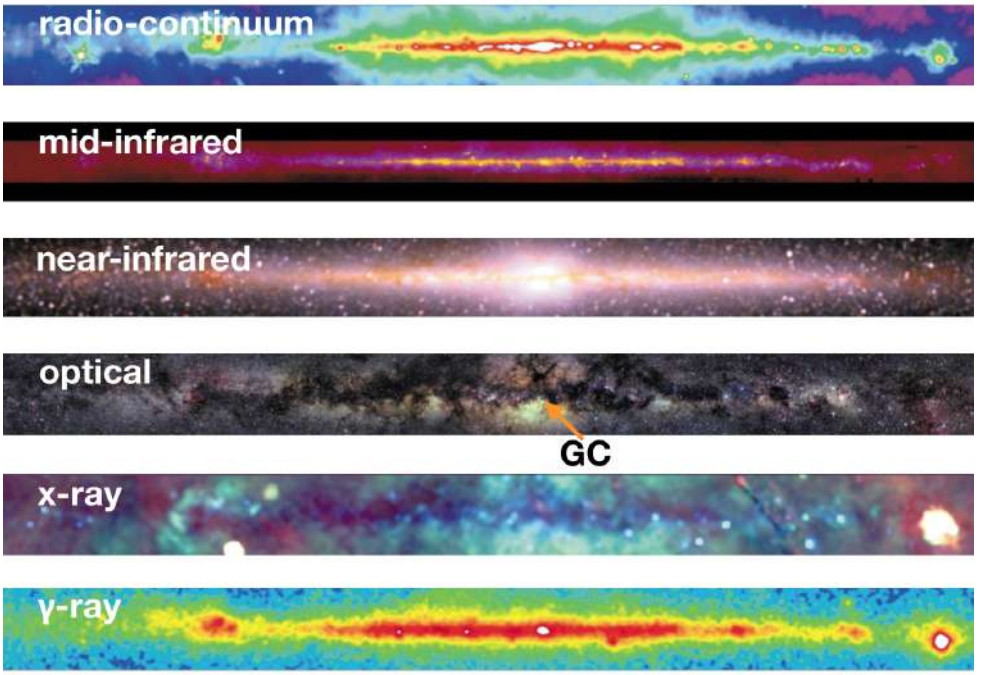

Fig. 1.6 The multi-wavelength view of the MW. The wavelengths and the position of the GC are indicated in the figure. Credits: image adapted from NASA, http://adc.gsfc.nasa.gov/mw.

The characterisation of the extinction curve towards the NIR is a main goal of the GC astronomy. It is generally accepted that the extinction curve in the NIR can be approximated by a power law (e.g. Fritz et al., 2011; Nishiyama et al., 2008) of the form

$$A_\lambda \propto \lambda^{-\alpha} \quad , \tag{1.1}$$

where A_λ is the extinction at a given wavelength (λ) and α is the power-law index. While early work found values of $\alpha \approx 1.7$ (e.g. Draine, 1989; Rieke & Lebofsky, 1985), recently a larger number of studies has appeared, with particular focus on the GC, where interstellar extinction reaches very high values ($A_{K_s} \gtrsim 2.5$) that suggest steeper values of $\alpha > 2.0$ (e.g. Fritz et al., 2011; Gosling et al., 2009; Nishiyama et al., 2006a; Schödel et al., 2010; Stead & Hoare, 2009).

1.3 Open questions

There are still many open questions that need to be addressed to improve our knowledge on the GC. In this section I only focus on some of them that are treated and discussed in this dissertation.

- Firstly, it is necessary to characterise the NIR extinction curve towards the GC using high angular resolution data and several bands in the NIR regime. Up to now, the majority of existing studies have been based on data at galactic latitudes $b \gtrsim 1^\circ$ that may not adequately reflect the properties of extinction toward the actual GC (e.g., Gosling et al., 2009; Nishiyama et al., 2006a; Stead & Hoare, 2009). Moreover, the extinction is not as large in those regions as the one in the GC. On the other hand, a high angular resolution multi-wavelength catalogue of large areas in the NB is necessary to obtain significant results on the line-of-sight variability of the extinction index. These kind of data would allow to also study the possible dependance of the extinction index on the wavelength.

- The characterisation of the extinction variation on arc-second scales is also fundamental for improving our understanding on the stellar population and structure of the inner regions of the galaxy. Thus, the development of extinction maps that allow to correct for differential extinction is important.

- The star formation history (SFH) of the NB is not well known yet. There are only few studies on this and they used very small regions with low extinction that might not be representative of the whole NB (Figer et al., 2004). On the other hand, only the central parsec of the NSC has been studied in detail

combining photometric and spectroscopic techniques (e.g., Pfuhl et al., 2011). Extrapolating our knowledge from the central parsec to the entire cluster may therefore be an approach that is prone to bias. The situation is even more complicated when analysing the whole area of the NB.

- The metallicity of the stellar population of the GC is not clear yet. The studies that have been carried out are based on spectroscopic measurements of few stars and need to be developed for larger areas. Recent studies indicate that the stellar population has a solar to super-solar metallicity (e.g., Alves-Brito et al., 2010; Do et al., 2015; Najarro et al., 2009; Nandakumar et al., 2018; Rich et al., 2017; Schultheis et al., 2019). In addition, the behaviour of the metallicity gradient in the innermost parts of the Galaxy is still largely unknown (e.g., Gonzalez et al., 2013; Ness et al., 2013; Zoccali et al., 2008).

- The relation between the NSC and the NB has not been properly analysed yet. A detailed analysis is necessary to study the characteristics of the stellar populations of both components to better understand their relation. In this way, it might be possible to find a gradient in age or metallicity toward the NSC or the SMBH.

- Only $\lesssim 10\,\%$ of the expected mass of young clusters has been identified so far. To improve the situation it is necessary to develop new techniques to identify early type stars that can be tracers of recent star formation.

- It is necessary to study the transition region between the inner bulge and the NB. Their stellar populations are different, but their main stellar properties are not properly characterised yet (e.g., Nogueras-Lara et al., 2018b). The transition region might help us to understand the differences between both components.

1.4 State of the art

The characterisation of the stellar population via spectroscopic observations is not an option to investigate the stellar population at the GC on large scales because it would be prohibitively expensive considering the necessary high angular resolution

and large number of sources ($> 10^5$) that have to be targeted. This kind of analysis is limited to small regions of great interest, whose considerably smaller number of stars makes them suitable for spectroscopic follow-up. Therefore, to be able to study the stars in a general way in this extremely crowded environment, it is necessary to rely on photometric catalogues. Several large imaging surveys include the GC region (e.g., 2MASS, UKIDSS, VVV, SIRIUS/IRSF), but they are limited in angular resolution to $> 0.6''$ by atmospheric seeing. Hence, their photometry is inaccurate and their completeness limit is as shallow as $K \sim 14$ mag. Additionally, stars brighter than $K \approx 9-10$ mag are usually heavily saturated in these surveys. Moreover, the well-explored regions, the central parsec around the SMBH and the Arches and the Quintuplet clusters, are extraordinary and we do not know whether they can be considered as representative for the entire GC. Accurate data are key to understanding the evolution of the GC and to infer which physical processes shape our Galaxy.

1.5 Goals of this thesis

The aim of obtaining a far more global view of the stellar population, structure, and history of the GC, and the methods to achieve this lie at the heart of this thesis. In this thesis we present the GALACTICNUCLEUS survey. This is a high angular resolution ($0.2''$) NIR JHK_s imaging survey of the NB. This survey is based on a 160h Large Programme with the ESO VLT (ID 195.B-0283, PI R. Schödel) with the NIR camera HAWK-I (Kissler-Patig et al., 2008) located at UT4 of the Very Large Telescope (ESO/Paranal observatory). We have designed the observing strategy, have prepared a semi-automatic pipeline to reduce the data and have obtained the PSF (point spread function) photometry of the more than three million stellar sources that make up this new catalogue of the GC. The GALACTICNUCLEUS survey improves the state of the art superseding all existing surveys and constitutes the first one offering 10 mag dynamic range in JHK_s. As the final product of the thesis, we have published the final catalogue (Nogueras-Lara et al., 2019).

In this thesis, we have tried to solve some of the open questions outlined previously by means of our new survey. We have also tested the capabilities of the GALACTICNUCLEUS survey showing its incredible potential and obtaining high

quality results that have been only possible thanks to the high angular resolution of the new catalogue.

"The cosmos is within us. We are made of star-stuff. We are a way for the universe to know itself."

Carl Sagan

2

Telescopes and Instruments

In this chapter I describe the main instruments that have been used in this thesis.

2.1 ESO Very Large Telescope

The Paranal observatory constitutes one of the world's most advanced visible-light astronomical observatories. It is the largest optical-infrared observatory considering the total light-collecting area (followed by the Maunakea Observatory in Hawaii). Operated by the European Southern Observatory (ESO), it is placed on Cerro Paranal, Atacama Desert (Chile), in one of the driest places on Earth, at approximately 2600 m altitude. The location combines excellent atmospheric conditions and the necessary isolation (the closest big city, Antofagasta, is located at $\sim$ 120 km) to allow unique observing conditions. In particular, the median seeing measured by the Differential Image Moption Monitor (DIMM) was $0.69''$ from Apr-2016 to Apr-2018.

The Very Large Telescope (VLT) constitutes the largest telescope on the Paranal observatory and consists of four different unit telescopes (UTs) of 8.2 m (primary mirror size). It was designed to either allow interferometric observations combining the telescopes under different configurations (VLTI-Very Large Telescope Interferometer), or the individual use of the UTs. For the interferometric mode there are four auxiliary telescopes (ATs) of 1.8 m. The observatory also hosts two survey telescopes designed specially to observe wide regions of the sky to carry out new catalogues. They are the VST (VLT Survey Telescope) and the VISTA (Visible and Infrared Survey Telescope for Astronomy) telescopes. Their primary mirrors are 2.61 m and 4.1 m in size. Figure 2.1 shows a scheme of the telescopes at the Paranal Observatory.

Cerro Paranal constitutes an excellent place to observe the GC since it reaches the zenith during the summer season and, therefore, observations with very low air mass are possible. Moreover, the very low amount of water vapour (the relative humidity is $\lesssim 5$ %) makes the VLT very suitable to observe in the NIR where it is possible to characterise the stellar structure and population of the innermost region of the Milky Way.

2.1.1 HAWK-I

An important part of the data used in this thesis were acquired using the NIR camera HAWK-I (High Acuity Wide field K-band Imager, Kissler-Patig et al. 2008) located at the ESO VLT UT4. HAWK-I is a cryogenic wide field camera situated at the Nasmyth A focus. It has a field of view (FoV) of $7'.5 \times 7'.5$ with a cross-shaped gap of $15''$ between its four Hawaii-2RG detectors. The pixel scale is $0.106''$ per pixel. The instrument comprises ten filters (4 broad band and 6 narrow band) of which we used the broad-band filters J, H, and K_s to carry out the GALACTICNUCLEUS survey.

2.1.2 NACO

The NACO (NAOS-CONICA) instrument (Lenzen et al., 2003; Rousset et al., 2003) was located at the UT4 from 2001-2013, and is now placed at UT1. It is composed of NAOS (Nasmyth Adaptive Optics System) and CONICA (Near-Infrared Imager

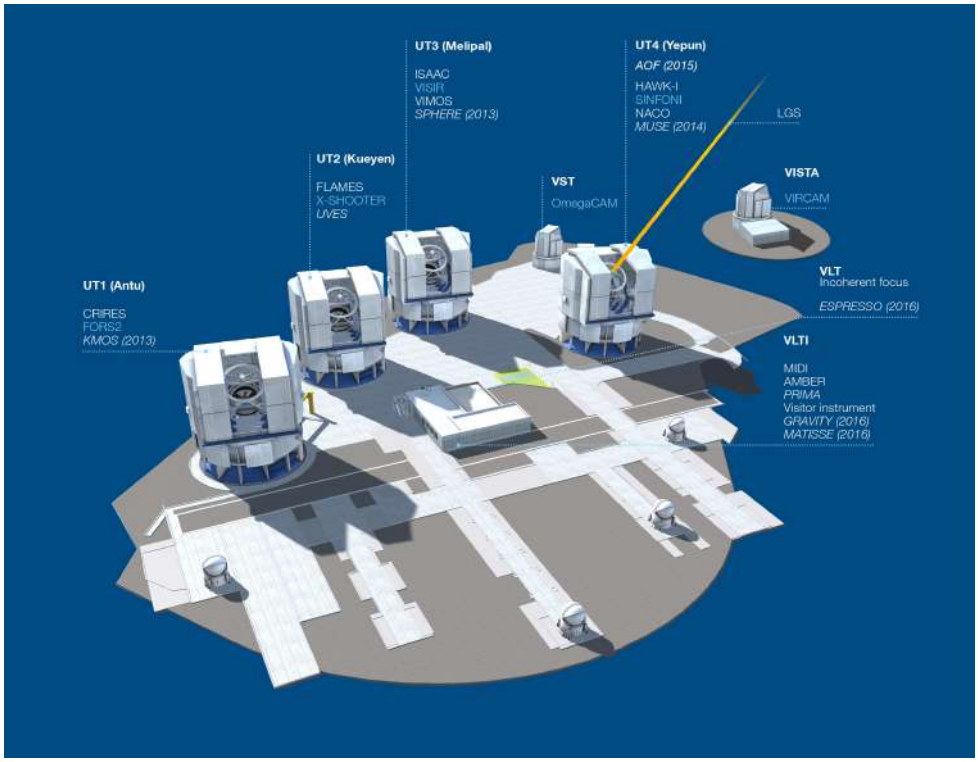

Fig. 2.1 Scheme of the telescopes that constitute the Paranal Observatory. Credits: ESO.

and Spectrograph). NAOS is an adaptive optics system combined with a NIR camera and spectrograph (CONICA). It allows to obtain high angular resolution images ($0.027''$/pixel) using its NIR filters. In particular, we have used GC deep data obtained in K_s band (Gallego-Cano et al., 2018) to compare with the GALACTICNUCLEUS survey and assess the completeness limits that we obtain for our catalogue.

2.1.3 KMOS

KMOS (K-band Muti Object Spectrograph) is a multi object spectrograph (Sharples et al., 2013) located at UT1 that allows to observe up to 24 objects simultaneously. It has a FoV of 7.2 arcmin in diameter to place each of its 24 IFUs (Integral-Field units) and a pixel scale of 0.2 arcsec. The IFUs have a FoV of 2.8' $\times$ 2.8' and are distributed

in three independent modules (8 IFUs per module) that correspond to two independent detectors (12 IFUs per detector). KMOS allows observations in five different NIR bands. We have used data from Feldmeier-Krause et al. (2017) acquired with KMOS to identify late- and early-type stars in a sample of the GALACTICNUCLEUS survey in the central pointing.

2.2 VISTA telescope

The VISTA telescope is located at the Paranal Observatory (see Fig. 2.1). It is a wide-field telescope specialised in producing surveys at the NIR wavelengths. It posses a primary mirror of 4.1 m across and a wide field of view that allows to cover rapidly large portions of the sky with a pixel scale of 0.34 arcsec.

VIRCAM (Vista InfraRed CAMera, Dalton et al., 2006; Emerson et al., 2006) is the only instrument placed at the VISTA telescope. It is a near infrared camera with a FoV of 1.65°. It includes five broad-band filters and three additional narrow band ones at specific wavelengths. In particular, in this thesis we have used data from the VVV (Vista Variables in the Via Lactea) survey, to asses the data quality of the GALACTICNUCLEUS catalogue.

2.3 IRSF telescope

The IRSF (InfraRed Survey Facility) is a telescope situated at the SAAO (South African Astronomical Observatory) observatory in Sutherland. This is a survey facility to map the sky in the NIR. The telescope has a primary mirror of 1.4 m with a photometric camera that poses three broad-band filters (JHK_s). The pixel scale is 0.45 ”/pixel and the FoV is 7.7’ $\times$ 7.7’. The SIRIUS (Simultaneous Infrared Imager for Unbiased Survey) IRSF survey carried out by this telescope has been key to calibrate the GALACTICNUCLEUS catalogue. This survey was specifically designed to observe the GC and uses PSF photometry, which makes it very suitable for comparison with our survey.

"Caminante, son tus huellas el camino y nada más; Caminante, no hay camino, se hace camino al andar. Al andar se hace el camino, y al volver la vista atrás se ve la senda que nunca se ha de volver a pisar. Caminante no hay camino sino estelas en la mar."

Antonio Machado

3

Observations and Data

One of the main goals of the thesis is to carry out the GALACTICNUCLEUS catalogue. This is a JHK_s high angular resolution survey to characterise the stellar structure and population of the nuclear bulge of the Milky Way. In this chapter, I explain in detail the observing strategy and the obtained data.

The imaging data were obtained with the NIR camera HAWK-I (High Acuity Wide field K-band Imager, Kissler-Patig et al. 2008) located at the ESO VLT (Very Large Telescope) UT4, using the broadband filters J, H, and K_s (Fig. 3.1). We applied the speckle holography algorithm (see e.g. Petr et al., 1998; Primot et al., 1990) optimised for crowded fields (Schödel et al., 2013) to increase the angular resolution of the instrument up to $0.2''$ FWHM (full width at half maximum). This is an image reconstruction technique that combines a high number of short exposure frames (speckle frames) using an averaged division of quantities in Fourier space (eq. 1, Schödel et al., 2013):

$$O = \frac{\langle I_m P{*}_m \rangle}{\langle |P_m^2| \rangle} \ , \tag{3.1}$$

where O is the Fourier transform of the object; I_m, P_m and $P{*}_m$ are the Fourier transform of the $m-th$ speckle frame, the Fourier transform of its PSF and the conjugate complex of P_m, respectively. The brackets indicate the mean over the total number of frames. Considering a large number of frames allow to suppress the noise in the final holographic product.

The final product is convolved with a Gaussian of FWHM (full width at half maximum) of $0.2''$. This determines the final angular resolution of the catalogue. The necessary short readout times constrained the observing strategy and required windowing of the detector.

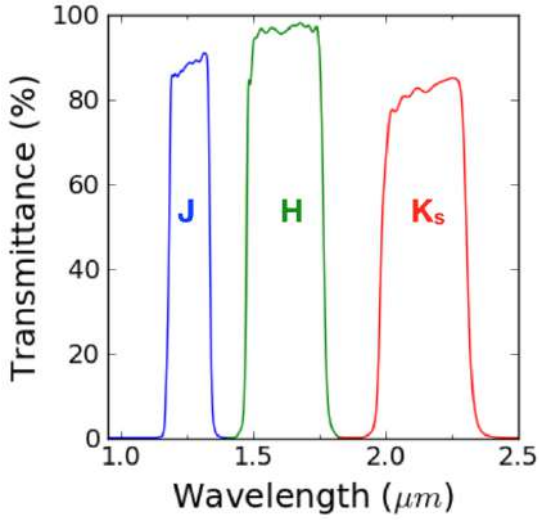

Fig. 3.1 Photometric filters used for the GALACTICNUCLEUS survey.

3.1 Pilot study

To check the feasibility of the survey and the data quality, we used a pilot study to observe the central region of the GC. It was centred on Sgr A* ($17^h\ 45^m\ 40.05^s$, -29° $00'\ 27.9''$) with a size of $8.2' \times 2.8'$. This field was observed in JHK_s. The DIT

Table 3.1 Details of the imaging observations of the pilot study

Date	HAWK-I band	Seeing[a] (arcsec)	N[b]	NDIT[c]	DIT[d] (s)
07 June 2013	J	0.46	16	32	0.85
07 June 2013	H	0.42	16	32	0.85
07 June 2013	K_s	0.41	16	32	0.85

Notes. [a]In-band seeing estimated from the PSF FWHM measured in long exposure images. [b]Number of pointings. [c]Number of exposures per pointing. [d]Integration time for each exposure. The total integration time of each observation is given by N×NDIT×DIT.

(detector integration time) was set to 0.851 s, which restricted us to the use of the upper quarter of the lower two detectors and the lower quarters of the upper detectors. The FoV of each of the four detectors was thus 2048×512 pixels. A four offset pointing pattern was used to cover the gap between the detectors. Each pointing has a series of 480 exposures each. Table 3.1 summarises the relevant information of the observations.

After very good results, we presented a Large Programme proposal (ESO 195.B-0283, PI R. Schödel) that was approved with 80 hours in service mode plus 11 nights in visitor mode.

3.2 Observing strategy

The GALACTICNUCLEUS survey consists of 49 pointings toward the GC and the inner Bulge (Fig 3.2). We used the fast photometry mode and increased the DIT up to 1.26 s after the pilot study, to use a larger fraction of the detector. The FoV resulted in 2048×768 pixels for each of the four HAWK-I chips.

To cover the gap between the detectors and to achieve some overlap between the pointings, we applied random jittering with a jitter box varying from $30''$ (2015 data) to $1'$ (2016-2018 data) width. The jitter box was increased after the first epoch to optimise the data coverage in the cross-shaped gap. For each pointing we took ~ 49

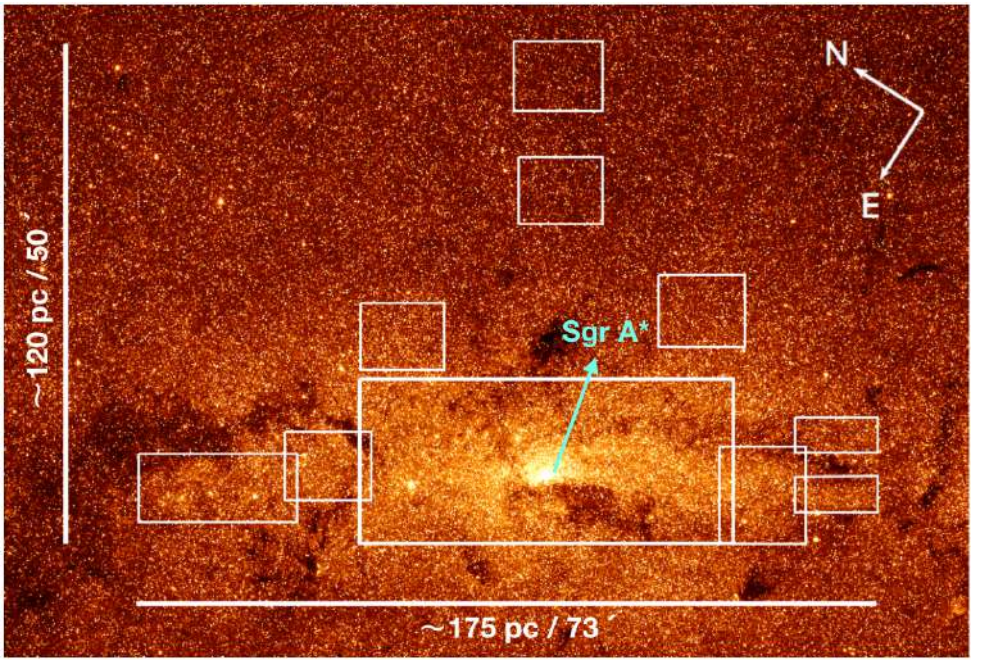

Fig. 3.2 Scheme of the target fields for the GALACTICNUCLEUS survey over-plotted on a Spitzer/IRAC image at 3.6 μm. The position of Sagittarius A* is highlighted in cyan.

dithered observations with ~ 21 frames each one to end up with ~ 1000 frames in total.

HAWK-I was rotated to align the rectangular FoV with the Galactic Plane (assuming an angle of 31.40° east of north in J2000.0 coordinates, Reid & Brunthaler, 2004). Each science observation was preceded or followed by randomly dithered observations, with the same filter, of a field centred on a dark cloud in the GC, located approximately at $17^h\ 48^m\ 01.55^s$, -28° 59′ 20″, where the stellar density is very low. These observations were used to determine the sky background. The FoV was rotated by 70° east of north to align it with the extension of the dark cloud. Figures 3.3 and 3.4 show the finding charts corresponding to the first pointing of the survey and the region used to estimate the sky. The red rectangle depicts the used window in comparison with the full size of the detector (black square).

The observing strategy also included calibration frames such as dark frames and flat fields. The dark frames were taken in Y band and were observed the same day

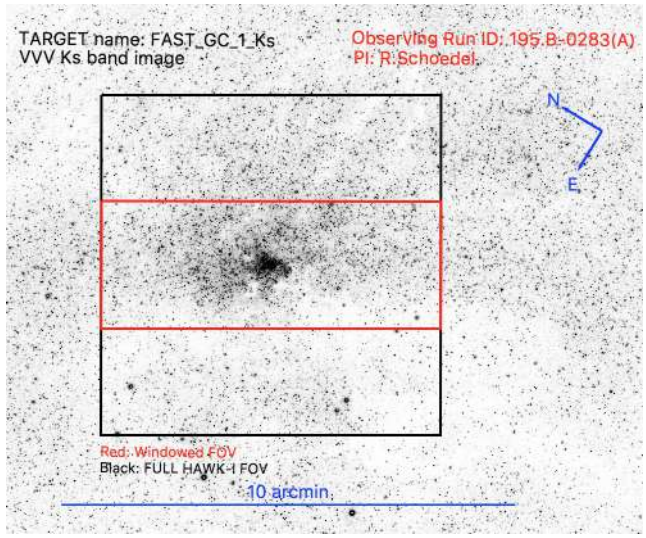

Fig. 3.3 Example of a finding chart used for the science frames observations. This one corresponds to the central field in K_s band. All the details are specified in the figure.

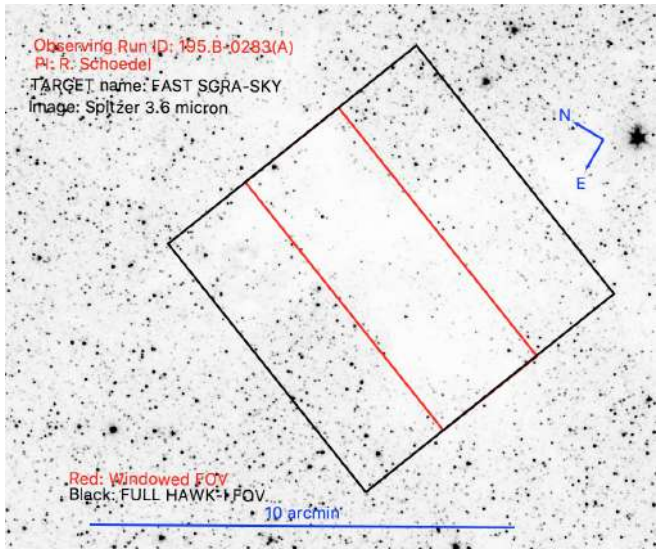

Fig. 3.4 Example of a finding chart used for the sky observations. This one corresponds to the K_s band. All the details are specified in the figure.

as the science data under the same windowing configuration. The flat fields have been taken in all three bands in a maximum range of two weeks from the science data acquisition. During the observations in visitor mode we compared the flat fields obtained with and without windowing. We concluded that there is no significant difference for the reduction process. We therefore observed the flat fields without windowing to avoid asking for a special set-up.

The 49 pointings cover the Galactic Centre in four distinct groups: (1) A continuous, rectangular area of about $36' \times 16'$ centred on Sgr A* (30 pointings), (2) nine pointings toward the east and west of the central field to cover low-extinction areas in the central part of the nuclear stellar disk, (3) four pointings in the transition zone between the GC and the inner bulge, and (4) four pointings toward comparison fields in the inner bulge just north of the nuclear disc. The entire survey area is outlined in Fig. 3.2, while Fig. 3.5 allows an identification of each pointing. All pointings overlap with at least one adjacent pointing. In this way, we were able to compare the common stars to assess the data quality.

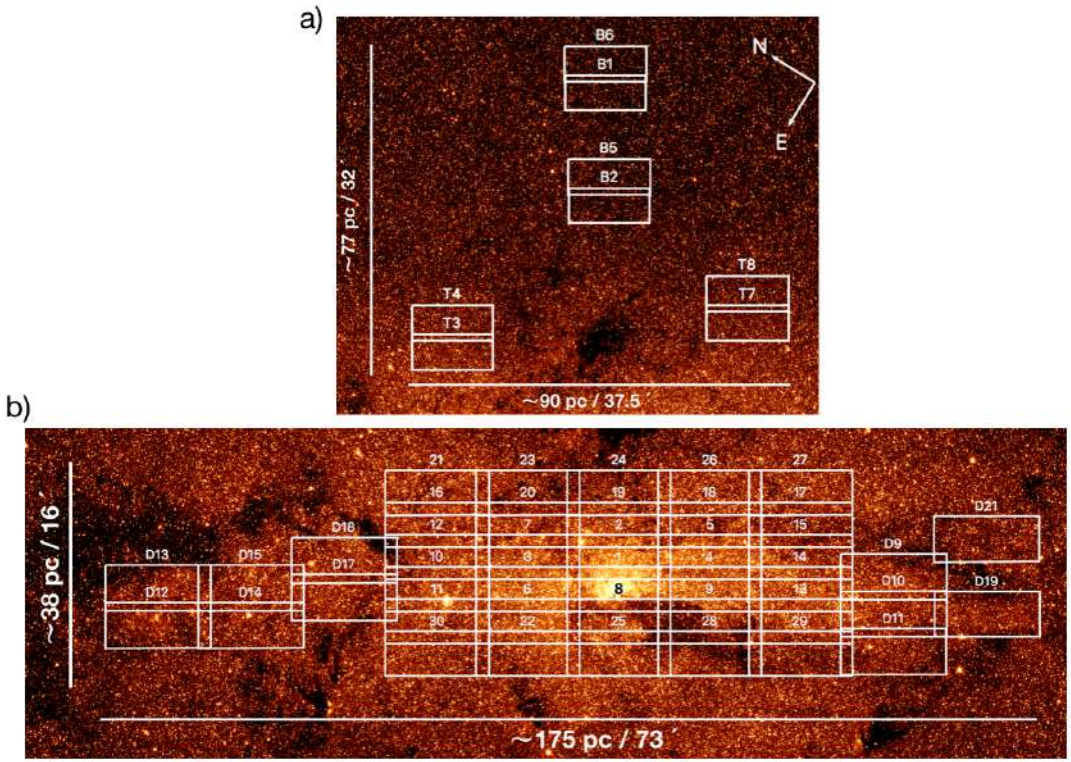

Fig. 3.5 Detailed scheme of all the fields observed in the GALACTICNUCLEUS survey. Each white square represent a field of the survey. Labels are included in white to identify the fields. Fields in the NSD, inner Galactic bulge, and transition zone between the bulge and the centre are identified by the letters 'D', 'B' and 'T'. Fields in the central region are identified by numbers from 1 to 30.

3.3 Data quality

The observations took three years to complete (2015-2018). Tables 3.2, 3.3, and 3.4 summarise the observing conditions for each pointing.

Table 3.2 Observing details for the fields used for the central catalogue.

HAWK-I filter	Field	Date (d/m/year)	Seeing[a] (arcsec)	N[b]	Field	Date (d/m/year)	Seeing[a] (arcsec)	N[b]
J		08/06/2015	0.37	49		06/06/2015	0.58	49
H	F1	06/06/2015	0.52	49	F2	06/06/2015	0.70	48
K_s		06/06/2015	0.57	49		07/06/2015	0.60	49
J		08/06/2015	0.40	49		06/06/2015	0.76	49
H	F3	06/06/2015	0.73	49	F4	06/06/2015	0.74	49
K_s		06/06/2015	0.60	49		06/06/2015	0.86	49
J		06/06/2015	0.58	49		07/06/2015	0.57	49
H	F5	06/06/2015	0.60	49	F6	07/06/2015	0.63	49
K_s		07/06/2015	0.55	49		07/06/2015	0.53	49
J		-	-	-		07/06/2015	0.57	49
H	F7	07/06/2015	0.47	50	F8	07/06/2015	0.56	49
K_s		10/06/2018	0.62	49		08/06/2015	0.60	48
J		08/06/2015	0.40	49		08/06/2015	0.35	49
H	F9	08/06/2015	0.40	49	F10	08/06/2015	0.46	49
K_s		08/06/2015	0.54	49		08/06/2015	0.45	49
J		08/06/2015	0.36	49		08/06/2015	0.36	49
H	F11	09/06/2015	0.47	49	F12	09/06/2015	0.43	49
K_s		09/06/2015	0.62	49		09/06/2015	0.62	49
J		09/06/2015	0.46	49		09/06/2015	0.40	49
H	F13	09/06/2015	0.45	48	F14	09/06/2015	0.53	48
K_s		09/06/2015	0.48	49		09/06/2015	0.66	49
J		10/06/2015	0.53	49		10/06/2015	0.48	49
H	F15	10/06/2015	0.62	49	F16	10/06/2015	0.46	47
K_s		10/06/2015	0.64	49		10/06/2015	0.55	49
J		10/06/2015	0.52	49		27/06/2015	0.47	48
H	F17	10/06/2015	0.60	48	F18	27/06/2015	0.32	49
K_s		10/06/2015	0.57	48		04/07/2015	0.66	49

Table 3.2 Observing details for the fields used for the central catalogue.

HAWK-I filter	Field	Date (d/m/year)	Seeing[a] (arcsec)	N[b]	Field	Date (d/m/year)	Seeing[a] (arcsec)	N[b]
J		27/06/2015	0.34	49		27/06/2015	0.33	49
H	F19	27/06/2015	0.38	49	F20	21/07/2015	0.47	49
K_s		02/07/2015	0.45	49		05/07/2015	0.76	48
J		27/06/2015	0.39	48		12/07/2015	0.42	49
H	F21	21/07/2015	0.62	49	F22	21/07/2015	0.73	47
K_s		12/07/2015	0.53	49		13/07/2015	0.56	49
J		12/07/2015	0.41	49		19/07/2015	0.38	49
H	F23	24/07/2015	0.41	48	F24	25/07/2015	0.60	49
K_s		13/07/2015	0.51	49		13/07/2015	0.68	48
J		19/07/2015	0.41	49		21/07/2015	0.64	49
H	F25	24/07/2015	0.62	46	F26	25/07/2015	0.88	48
K_s		25/07/2015	0.67	49		25/07/2015	0.72	51
J		21/07/2015	0.59	41		20/07/2015	0.46	49
H	F27	03/10/2015	0.51	49	F28	04/10/2015	0.50	49
K_s		18/09/2015	0.49	49		27/03/2016	0.60	30
J		23/07/2015	0.45	49		24/07/2015	0.43	49
H	F29	27/03/2016	0.59	50	F30	20/05/2016	0.56	48
K_s		12/05/2016	0.67	47		07/10/2015	0.74	48

Notes. (a) In-band seeing estimated from the PSF FWHM measured in long exposure images. (b) Number of pointings. The data corresponding to F7 (J band) were obtained under bad conditions and have not been included in the final data release of the survey.

Table 3.3 Observing details for the fields used for the inner bulge and the transition zone.

Filter	Field	Date (d/m/year)	Seeing (arcsec)	N	Field	Date (d/m/year)	Seeing (arcsec)	N
J		24/07/2015	0.43	49		24/07/2015	0.43	49
H	B1	20/05/2016	0.56	49	B2	26/05/2016	0.33	49
K_s		28/06/2015	0.54	49		14/05/2016	0.58	49
J		24/07/2015	0.39	51		27/06/2016	0.46	49
H	B3	21/05/2016	0.51	50	B4	12/06/2016	0.79	49
K_s		14/05/2016	0.47	50		12/06/2016	0.56	50
J		27/06/2016	0.48	49		27/06/2016	0.51	49
H	B5	12/06/2016	0.83	49	B6	13/06/2016	0.46	33
K_s		12/06/2016	0.95	30		05/04/2017	0.46	44
J		27/06/2016	0.55	49		27/06/2016	0.56	49
H	B7	24/04/2017	0.42	38	B8	27/06/2016	0.54	59
K_s		26/06/2016	0.73	49		02/05/2017	0.64	43

Notes. (a) In-band seeing estimated from the PSF FWHM measured in long exposure images. (b) Number of pointings. The data corresponding to B6 (H band) were obtained under bad conditions and have not been included in the final data release of the survey.

Table 3.4 Observing details for the fields used for the NSD.

Filter	Field	Date (d/m/year)	Seeing (arcsec)	N	Field	Date (d/m/year)	Seeing (arcsec)	N
J		27/06/2016	0.49	49		27/06/2016	0.81	49
H	D9	27/06/2016	1.13	49	D10	28/06/2016	0.91	49
K_s		03/05/2017	0.77	50		27/06/2016	0.81	48
J		28/06/2016	0.87	48		20/07/2017	0.51	44
H	D11	28/06/2016	0.89	49	D12	03/06/2017	0.33	44
K_s		28/06/2016	0.90	49		03/06/2017	0.35	39
J		23/09/2017	0.54	44		30/09/2017	0.49	44
H	D13	24/06/2017	0.70	44	D14	23/07/2017	0.66	44
K_s		24/06/2017	0.61	48		11/08/2017	0.65	44
J		01/10/2017	0.85	44		27/03/2018	0.41	44
H	D15	21/09/2017	0.75	44	D17	22/03/2018	0.34	43
K_s		11/08/2017	0.85	44		27/03/2018	0.37	43
J		21/05/2018	0.38	44		25/05/2018	0.49	44
H	D18	28/03/2018	0.82	47	D19	21/05/2018	0.41	44
K_s		28/03/2018	0.79	44		16/04/2018	0.54	44
J		10/06/2018	0.88	44				
H	D21	25/05/2018	0.59	44				
K_s		106/06/2018	0.51	44				

Notes. (a) In-band seeing estimated from the PSF FWHM measured in long exposure images. (b) Number of pointings.

"Do, or do not. There is no try." The Empire Strikes Back.

Master Yoda

4

Data reduction and methodology

Since the observations and the obtained data are completely non-standard, we developed a full package for data reduction and analysis. In this chapter, I explain the main steps of the methodology used for the data treatment. To illustrate the process, we used the pointing F1, as it is the most challenging pointing due to the high crowding and variable extinction towards this region.

4.1 Data reduction

As HAWK-I has four independent detectors, all data reduction steps were applied independently to each of them. We followed a standard procedure (bad-pixel correction, flat fielding, and sky subtraction), paying special attention to the sky subtraction. Due to the extremely high stellar density in the GC, it was impossible to estimate the sky background from dithered observations of the target themselves. The dark cloud

that we observed provided us with good estimates of the sky, but at intervals of about once per hour, which is far longer than the typical variability of the NIR sky (on the order of a few minutes). To optimise sky subtraction, we therefore scaled the sky image from the dark cloud to the level of the sky background of each exposure. The latter was estimated from the median value of the 10% of pixels with the lowest value in each exposure. A dark exposure was subtracted from both the sky image and from each reduced science frame before determining this scaling factor. A comparison of noise maps obtained with this strategy, or not, showed that this approach reduced the noise by a factor of about 10.

4.2 Image alignment

We corrected the dithering in a two-step procedure (it was not necessary for the pilot study because the four offset pattern that we designed let us reduce every pointing independently). Firstly, we used the image headers to obtain the telescope offsets with respect to the initial pointing and shifted the images accordingly. Subsequently, we fine-aligned the frames by using a cross-correlation procedure on the long-exposures (merged image of all the corrected dithered frames) for each pointing.

4.3 Distortion solution

Geometric distortion is significant in HAWK-I. When comparing the long-exposure image with the VVV (VISTA Variables in the Via Lactea) corresponding images, the position of a given star can deviate by as much as $1''$ or about ten HAWK-I pixels between them. To correct that effect we used the VVV survey (Minniti et al., 2010; Saito et al., 2012) as astrometric reference. We cross-identified stars in both the VVV and a long exposure image for a given HAWK-I pointing (using as criterion a maximum distance of $0.1''$). We iteratively matched the stellar positions by first using a polynomial of degree one and, subsequently, of degree two. Due to serious saturation problem in the VVV images at the H and K_s bands, as well as the lower stellar density in the VVV J images, we used the J-band image of tile b333 to perform the distortion solution in all three bands. We found that the common stars

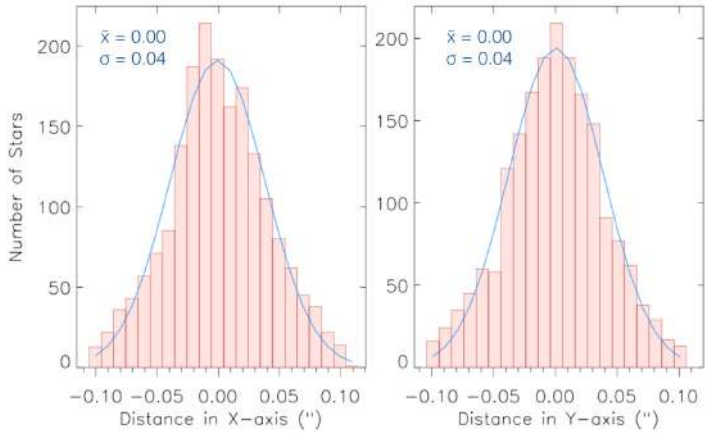

Fig. 4.1 Goodness of the distortion solution (detector #2 H-band F1 data). Differences in arcseconds between the relative positions of stars in the corrected HAWK-I frames and in the VVV reference image. Left panel X-axis and right panel Y-axis. The blue lines are Gaussian fits to the histograms. For both histograms, the centre of the fit lies at 0.0 arcseconds, with $\sigma = 0.04$ arcseconds.

were homogeneously distributed over the detectors, so that no region had an excessive influence over the derived distortion solution.

To check the quality of the distortion solution, we compared the relative positions of the stars found in the corrected HAWK-I long exposure image with their positions in the VVV reference image. As can be seen in Fig. 4.1, the correction is quite satisfactory ($\sigma < 0.05''$). Besides, we checked whether the application of the distortion solution had any systematic effect on the photometry. Figure 4.2 shows a comparison between photometric measurements of stars on chip #3 with and without distortion correction. As it can be seen, applying the distortion solution has no significant effect on the photometry. The distortion solution was computed for each band and chip independently and then applied to each individual frame with a cubic interpolation method.

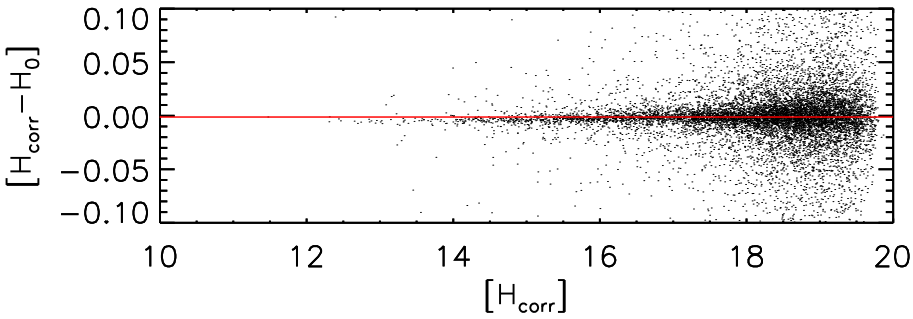

Fig. 4.2 Difference in H-band photometry before and after applying the distortion solution. The results of the photometry computed before and after the application of the distortion solution are indicated by H_0 and H_{corr}, respectively. This plot corresponds to detector #3 of F1 data. The units are magnitudes, with the zero point being the one specified in the HAWK-I user manual.

4.4 Speckle holography

To produce high angular resolution images from the short exposure images, we used the speckle holography algorithm (see e.g. Petr et al., 1998; Primot et al., 1990). This requires the knowledge of the point spread function (PSF) for each short exposure. For the latter purpose, we applied the methodology described by Schödel et al. (2013), which works very well in crowded fields such as the GC. In brief, this methodology consists in the superposition of multiple reference stars and iterative improvement to determine the PSF (see Sec. 3 for further details). The image resulting from the speckle holography algorithm was convolved with a Gaussian beam of 0.2″ FWHM in order to suppress noise at high spatial frequencies. In this way we overcome the image blurring imposed by seeing. As the PSF not only varies with time but is also a function of position, mainly due to anisoplanatic effects, we divided the aligned frames into regions of 1 arcmin × 1 arcmin (from now on referred to as *sub-regions*). Figure 4.3 shows the grid of the sub-regions drawn on a long exposure image. Overlap between the sub-regions corresponds to one half of their width. Speckle holography was applied to every single sub-region independently.

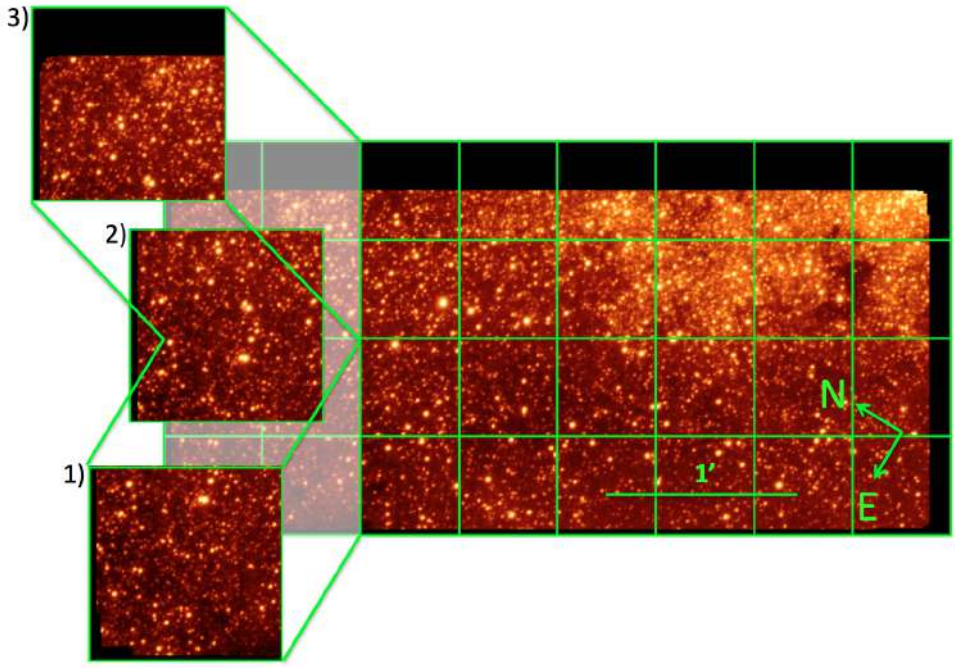

Fig. 4.3 Long exposure image (*H*-band chip1, F1 data) divided to obtain the sub-regions used in the holographic procedure. Region 2) corresponds to an overlapping region between 1) and 3) showing the overlapping strategy described in the text. The green lines show the division of the rest of the detector.

The PSF for each sub-region and exposure was extracted in an automatic way. First, we generated long exposures and corresponding noise maps from all the frames corresponding to a given pointing and filter. Then, we used the *StarFinder* software package (Diolaiti et al., 2000) for PSF fitting astrometry and photometry. From the list of detected stars we selected reference stars for PSF extraction in each exposure according to the following criteria:

- Reference stars had to be fainter than $J \approx 12$; $H \approx 12$, $K_s \approx 11$ to avoid saturated stars. To compute these limits we performed PSF fitting photometry on the long exposure images and computed a preliminar ZP (zero point) using the SIRIUS/IRTF (Infrared Survey Facility telescope) GC survey (e.g. Nagayama et al., 2003; Nishiyama et al., 2006a). We obtained a systematic

deviation for the brightest stars when we compared the ZP versus the magnitude in the SIRIUS/IRTF GC survey. Thus, the starting point of the deviation gave us the limit for the saturation.

- Reference stars had to be brighter than $J = 18$; $H = 14$, $K_s = 13$.
- For a given exposure, the full PSF of a reference star needed to be visible, meaning stars close to the image edges were excluded.
- Reference stars had to be isolated. Any neighbouring star within a distance corresponding to two times the FWHM of the seeing PSF had to be at least 2.5 magnitudes fainter. No star brighter than the reference one was allowed within a distance corresponding approximately to the full radial extent of the PSF.

After having determined the PSF for each frame, we applied the speckle holography algorithm. Once the process was finished for each sub-region, we created the final image by combining the holographically reduced sub-regions. To do that, we performed PSF fitting astrometry and photometry (with *StarFinder*) for each sub-region in each band and used the positions of the detected stars to align all three bands with each other, taking as reference the H-band image. This step was important to correct small relative shifts between the sub-regions that may arise from the holography algorithm. We also produced an exposure map that informs us about the number of frames contributing to each pixel in the final image (see Fig. 4.4), and a noise map computed using for each pixel the error of the mean (the standard deviation of the mean divided by $\sqrt{N-1}$, where N is the number of the measurements) of the frames that contribute to it. We produced a deep image from all the data and three so-called *sub-images* from three disjunct sub-sets of the data, with each one containing $1/3$ of the frames, as well as the corresponding noise maps. The sub-images were used to determine photometric and astrometric uncertainties of the detected stars as described in the next chapter.

4.5 Rebinning

Since we aim to obtain final images with $0.2''$ angular resolution, the sampling ($0.106''$ per pixel) is barely sufficient. The quality of the reconstructed images can be

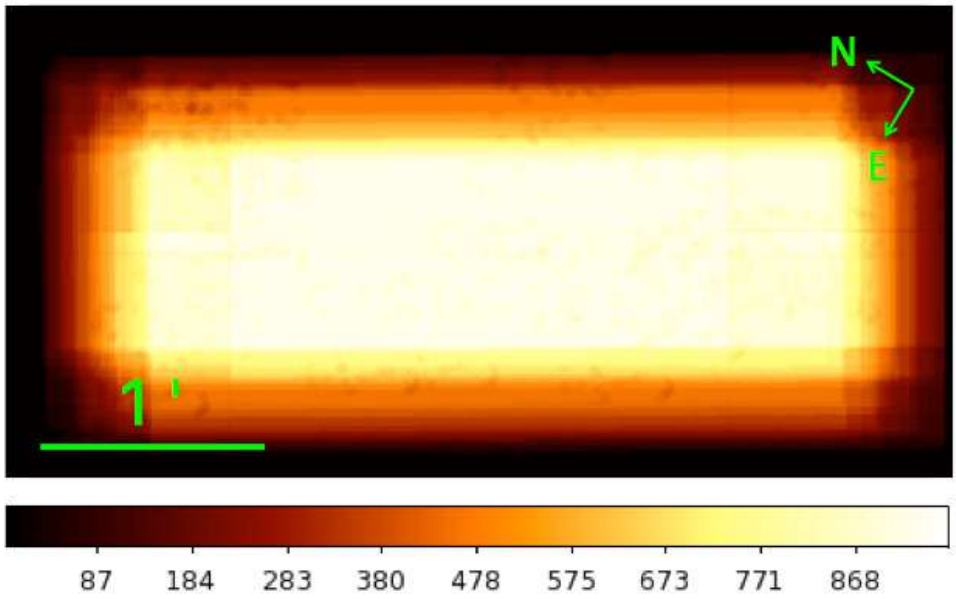

Fig. 4.4 Example of an exposure map for a final holographic product (detector #1 H-band, F1 data). The scale depicts the number of valid frames for each pixel.

improved by rebinning each input frame by a factor > 1 (using cubic interpolation). The PSF fitting algorithm then can fit and disentangle the stars in this crowded field with higher accuracy. To test the optimum value of this factor and its usefulness, we simulated several hundreds of images and then applied exactly the same procedure that we followed when we reduced and analysed our science images. To do so, we selected the most difficult region that we studied in our data, namely, a square of $27''$ centred on SgrA*, where the source density is the highest in the entire Galactic Centre. We used a list of stars extracted from diffraction-limited K_s-band observations of the GC with NACO (NAOS-CONICA) instrument installed at the ESO VLT (S27, camera, date 9 Sept 2012), consisting of 9840 stars with magnitudes of $9 \lesssim Ks \lesssim 19$. This allowed us to test also the reliability of our procedure under the worst crowding conditions possible.

To generate the images, we used cubes of real PSFs from HAWK-I and we added readout and photon noise for stars and sky. Speckle holography was applied in

Table 4.1 Results of simulations with different rebinning factors.

Rebinning factor	Detections[a]	Spurious[b]	Success[c] (%)
1	1571	3	76.4
2	2041	11	81.6
3	1918	10	77.4

Notes. [a]Detections that have a counterpart in the data used to simulate the images once we have removed detections with uncertainties above 10 %. [b]Stars without a counterpart after removal of detections with photometric uncertainties > 0.1 mag. [c]Rate of valid identifications with $K_s \leq 15$.

those images using rebinning factors of 1, 2, and 3. Then, we applied the procedure described in Chapter 5 to obtain the photometry and the uncertainties of the stars. The obtained results are shown in Table 4.1.

As we can see, without rebinning the number of real detected sources was the lowest value obtained, whereas rebinning increased the number of detected sources significantly. To compare with the input data we discarded the outliers, removing all the stars with a photometric uncertainty > 0.1 mag. A rebinning factor of 2 turned out to be a reasonable choice. Higher rebinning factors do not improve the final product significantly and may lead to additional uncertainties from interpolation. Also, computing time increases quadratically with the image size. The completeness until magnitude 15 for a rebinning factor of 2 is above 81%. We note that the completeness of our actual data will be almost 100% at $K_s \approx 15$ in less crowded regions outside the central parsec.

With respect to the photometric accuracy obtained, we compared the stellar fluxes measured in our simulations with their known input fluxes. Then, we defined a mean flux, f_{tot} , and its associated uncertainty, df_{tot}:

$$f_{tot} = \frac{f_{HAWK-I} + f_{input}}{2},$$
$$df_{tot} = \frac{f_{HAWK-I} - f_{input}}{2}, \tag{4.1}$$

where f_{HAWK-I} corresponds to the flux measured in the simulated image and f_{input} refers to the one in the input list. Once we computed those fluxes, we expressed them in magnitudes, obtaining Fig. 4.5. As can be seen, the photometry is slightly more accurate in the rebinned image, in particular at faint magnitudes.

4.6 Scripts

We designed a reduction pipeline to carry out the data reduction using IDL (Interactive Data Language). We divided the scripts into several blocks according to the steps of the reduction:

4.6.1 Calibration frames

- **tmp_check.pro**

  This code allows us to check all the images that are used in the data reduction (darks, flats, sky and science images). In this way, we are able to delete a frame if we detect potential problems on it.

- **Dark.pro**

  This code generates a master dark using the raw dark frames.

- **Gasgano recipe flat hawki_cal_flat**

  We use a routine from the ESO standard pipeline to produce the master flat.

- **joinflats.pro**

  This code changes the format of the master flat to reduce the data.

- **Sky.pro**

  This routine computes the sky for each chip from the sky observations.

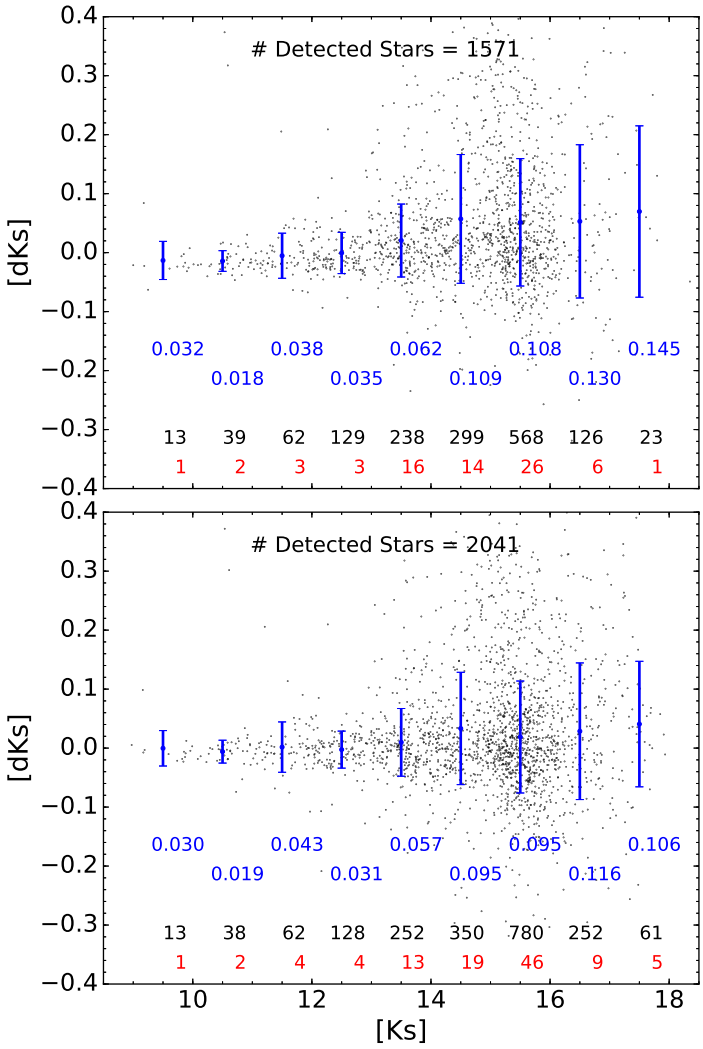

Fig. 4.5 Photometric precision for simulated data with different rebinning factors. The upper and lower panels show results for rebinning factors of 1 and 2 respectively. Blue error bars depict the standard deviation of the points in bins of one magnitude. The first rows of numbers are the standard deviation in those bins. The second and third rows are the number of points used to compute the standard deviation and the number of rejected outliers.

- **Fullbpm.pro**

  It generates a bad pixel map using the dark frames, the sky and the master flat.

- **Makemask.pro**

  Using the bad pixel map, it produces the final mask to be used for the reduction.

4.6.2 Standard reduction

- **Reduce.pro**

  Using the bad pixel map, it produces the final mask to be used for the reduction.

- **Cleancubes.pro**

  This code cleans the frames and remove bad pixels and cosmic rays.

- **makecubes.pro**

  This script joins the individual chips into cubes to be treated independently.

- **jittering.pro**

  It aligns the all the frames corresponding to each chip correcting the dithering (see Sec. 4.2).

- **lng_jitering.pro**

  This code combines all the aligned frames to create a "long exposure" image for each chip.

- **findstars.pro**

  This code uses the *StarFinder* package (Diolaiti et al., 2000) to perform PSF photometry on the "long exposure" images.

- **alignquadrants.pro**

  We computed a solution to correct the geometric distortion aligning the stars in each chip with a reference VVV image (see Sec. 4.3)

- **mosaic.pro**

  This code combines the distortion corrected images for all four chips to create a mosaic that allow us to visually check the product of the reduction.

- **alignframes.pro**

  It applies the distortion solution computed for the "long exposure" images to all the frames for each chip.

4.6.3 Speckle holography algorithm

- **subcubes.pro**

  To apply the speckle holography algorithm, we divided each chip into smaller regions (1'×1') to avoid PSF variations (see Sec. 4.4).

- **findstars_holo.pro**

  It computes the PSF photometry on the distortion corrected images using *StarFinder* (Diolaiti et al., 2000), to look for reference stars to apply the speckle holography algorithm.

- **holoall.pro**

  We apply the speckle holography algorithm as it is indicates in Sec. 4.4. This code also applies the rebinning to increase the sampling per pixel (see Sec. 4.5).

- **reconstruct.pro**

  This code allows us to reconstruct each chip by means of the small subregions used to compute the holography.

"Don't only practice your art, but force your way into its secrets, for it and knowledge can raise men to the divine."

Ludwig van Beethoven

5 Photometry and astrometry

In this chapter, I explain in detail the obtention of the photometry and its uncertainty estimation. As in the previous chapter, we used F1 as a reference to compute the photometry.

5.1 Stellar fluxes

Stellar fluxes in the final images were measured by means of PSF fitting photometry with *StarFinder*. We used the noise map produced previously for the deep image, which facilitates the detection of stars and suppresses the detection of spurious sources. Since the formal uncertainties given by the *StarFinder* package tend to under-estimate the real uncertainties significantly (Emiliano Diolaiti, private communication), we determined the error computing the photometry on the three independent sub-images.

We developed an automatic routine for PSF extraction that chooses the reference stars taking into account isolation, saturation, brightness limits (depending on the band), and weight of the stars (the number of frames contributing to the final image at a star's position). We also excluded stars near the image edges. We used the following *StarFinder* parameters: A minimum correlation value of $min\_corr = 0.8$, no diffuse background estimation, that is $ESTIM\_BG = 0$, and a detection threshold of $5\,\sigma$ with two iterations.

5.2 Photometric uncertainties

We took into account two different effects for the uncertainty: statistical uncertainties and the PSF variation across the detectors.

5.2.1 Statistical uncertainties

A star was accepted only if it was detected in all three sub-images and in the deep image, using as a criterion a maximum distance of one pixel between its relative positions (corresponding to about $0.05''$ because of the rebinning factor used, or about one quarter of the angular resolution). This is a conservative strategy as the deep image has a higher signal to noise ratio than the sub-images. In this way we can be certain that hardly any spurious detections will be contained in the final lists. We used the flux of a star as measured on the deep image and estimated the corresponding uncertainty, Δf, from the measurements on the three sub-images according to the formula

$$\Delta f = \frac{f_{max} - f_{min}}{2\sqrt{N}}, \tag{5.1}$$

where f_{max} and f_{min} correspond to the maximum and minimum flux obtained for each star in the measurements on the sub-images and N is equal to 3, the number of measurements.

We compared the formal errors provided by *StarFinder* on the deep image with the ones obtained with the procedure described above. We confirm that *StarFinder* generally under-estimates the uncertainties systematically. However, for some stars

(mainly faint ones), the uncertainty given by *StarFinder* can be larger than the one obtained by the previous procedure. In those cases, we took the larger value, to be conservative.

The position uncertainties of the individual stars are also computed using the sub-images and the eq. 5.1.

5.2.2 PSF uncertainties

The PSF can potentially vary across the field. To quantify this effect, we divided the deep image horizontally into three equal regions as shown in Fig. 5.1. Subsequently, we obtained a PSF for each region as described above. From a comparison between the PSFs (essentially fitting the PSF from one sub-region with that from another), we estimated the corresponding photometric uncertainty and added it quadratically to the statistical uncertainties. The effect of PSF variability is only of the order of $\lesssim 2\%$ and depends on the observing conditions.

This small effect of PSF variability highlights the excellent performance of the speckle holography algorithm. It also justifies our choice of relatively large sub-regions ($1' \times 1'$ for the speckle holographic reconstruction). The regions are considerably larger than the size of the isoplanatic angle in the near-infrared, which is, depending on the filter used, of the order of $10'' - 20''$. A possible explanation why we can use such large regions is that we do not reconstruct images at the diffraction limit of the telescope, but rather at a less stringent $0.2''$ FWHM. We suspect that we are therefore working in a "seeing-enhancer" regime, similar to ground-layer adaptive optics (GLAO) systems. GLAO corrects image degradation by turbulence in a layer close to the ground and leads therefore to moderate corrections, but over large fields (see e.g. the description of HAWK-I's future GLAO system GRAAL (GRound layer Adaptive optics Assisted by Lasers) in Arsenault et al., 2014; Paufique et al., 2010, and references therein). We obtained the uncertainty for each individual star by adding quadratically the statistical and the PSF uncertainties. A plot of the final, combined statistical and PSF uncertainties for chip #1 is shown in Fig. 5.2.

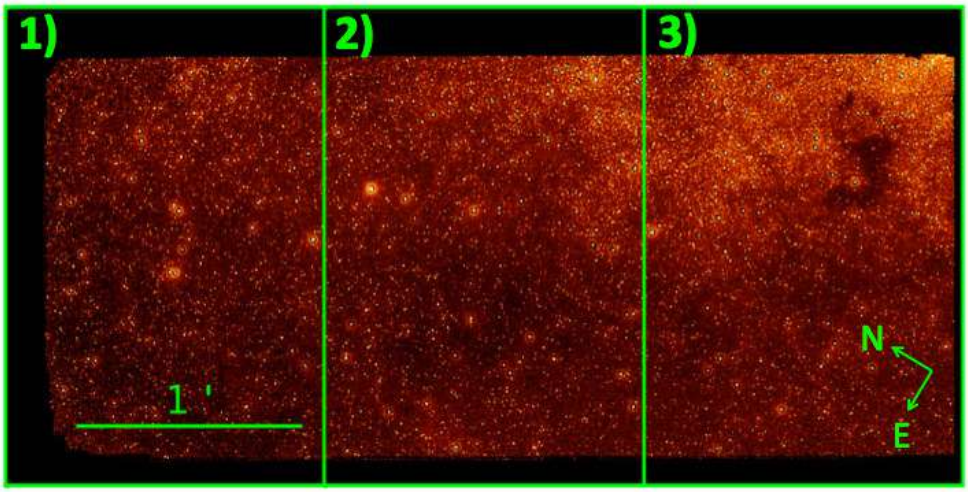

Fig. 5.1 Image division of chip #1 H-band (F1) to obtain three PSFs to quantify the PSF variation across the image. Each of the numbers indicates the region considered to extract the three PSFs.

5.3 Astrometric calibration

We calibrated the astrometry by using VVV catalogue stars as reference that we cross-identified with the stars detected in the images. The astrometric solution was computed with the IDL (Interactive Data Language) routine SOLVE_ASTRO (see IDL Astronomy User's Library, Landsman, 1993).

To estimate the uncertainty of the astrometric solution, we compared all stars common to our image and to the VVV survey. Figure 5.3 shows the histograms of the differences in right ascension and declination. For all bands and chips the standard deviation of this distribution is $\lesssim 0.05$ arcseconds.

5.4 Zero point calibration

Since the VVV catalogue uses aperture photometry, which will lead to large uncertainties in the extremely crowded GC field, the zero point calibration was carried out relying on the near infrared JHK_s SIRIUS/IRSF survey (e.g., Nagayama et al.,

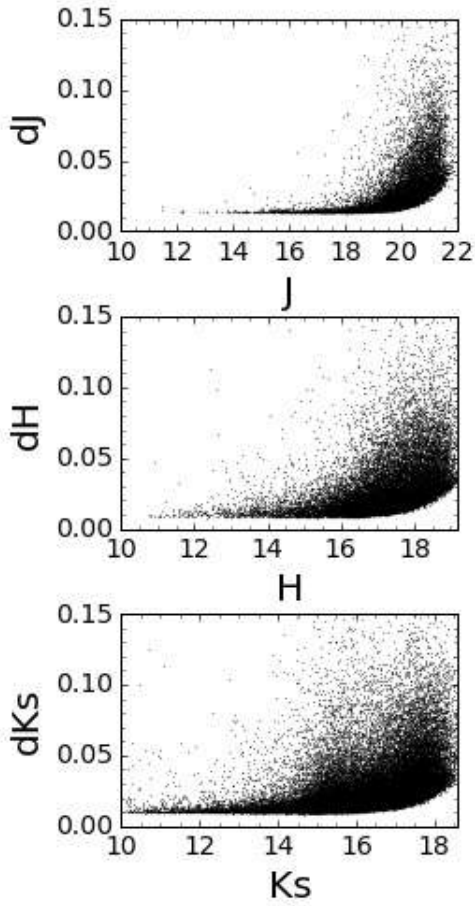

Fig. 5.2 Combined statistical and PSF photometric uncertainties versus magnitude for J (top), H (middle), and K_s (bottom) for chip #1 (F1 data).

2003; Nishiyama et al., 2006a). In this catalogue, the zero point was computed with an uncertainty of 0.03 mag. It was specially designed to study the GC and it uses PSF photometry, which allows to improve the photometry in crowded fields. Thus, its characteristics make this survey a very appropriate reference. Moreover, we compared both photometric systems to check whether there is some significant difference between the filters:

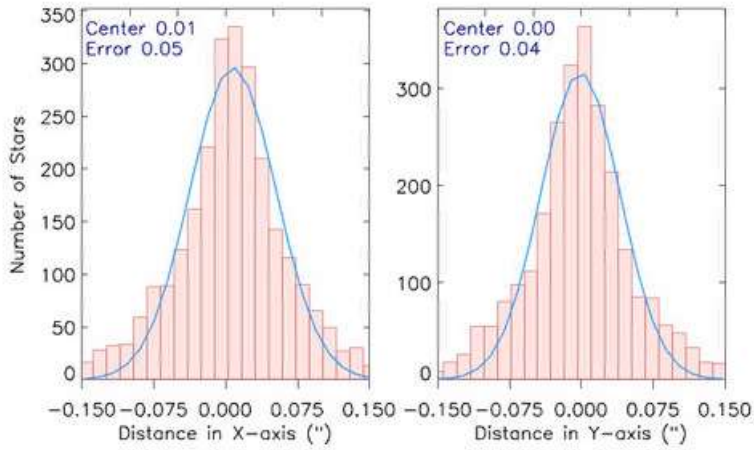

Fig. 5.3 Position accuracy. Differences in arcseconds between the positions of stars in the final HAWK-I chip #4 (F1 H-band) and in the VVV reference image. Left panel X-axis and right panel Y-axis. The mean and standard deviation are $0.01 \pm 0.05''$ in X and $0.00 \pm 0.04''$ in Y.

- Firstly, we computed the effective wavelength obtained for a RC (red clump, e.g., Girardi, 2016) star located at the GC distance with an extinction of $A_{K_s} \sim 1.9$ mag, corresponding to the extinction expected at the GC (Nogueras-Lara et al., 2018a). We obtained that the effective wavelength for the same bands differs by $\lesssim 0.5\%$.

- We also calculated the photometry in both photometric systems for a RC star and a early type star (T = 45,000 K) located at the GC distance and assuming a extinction of $A_{K_s} \sim 1.9$ mag. We obtained that the difference is $\lesssim 0.8\%$ in all three bands.

Therefore, we concluded that the differences between both photometric systems are negligible.

5.4.1 Reference stars

To select the reference stars, we took into account several criteria:

- Only stars with an uncertainty $< 5\,\%$ in both the SIRIUS catalogue and our final list were accepted.
- To avoid saturation or faint stars, we imposed brightness limits for all three magnitudes.
- The reference stars should be as isolated as possible. For that reason, we excluded all the stars which have a neighbour within a radius of $0.5''$ in our final list.
- We did not use stars near the edges of the FoV or in regions with a low number of exposures (see, e.g. Fig. 4.4).
- Finally, we applied a two-sigma clipping algorithm to remove outliers.

Figure 5.4 shows the zero points computed for common stars between the SIRIUS catalogue and our data in each band and chip. In all cases the reference stars were well distributed across each detector. There were also sufficient reference stars for a robust calibration: ~ 50 in J band, ~ 300 in H band, and ~ 175 in K_s band on each chip in the case of the 2015 data (about 30% less because of the smaller FoV in the case of the pilot study).

We also checked for spatial variability of the zero point across the chips assuming a variable ZP and computing it with a slanting plane (i.e. a one-degree polynomial). However, we did not find any significant difference with the assumption of a constant ZP within the uncertainties. This agrees with the findings of Massari et al. (2016), who also concluded that constant zero points could be used to calibrate their HAWK-I imaging data.

5.4.2 Pistoning correction

Once the photometry obtained for every chip and band was calibrated, we corrected the possible residual zero point offset that could have remained between different

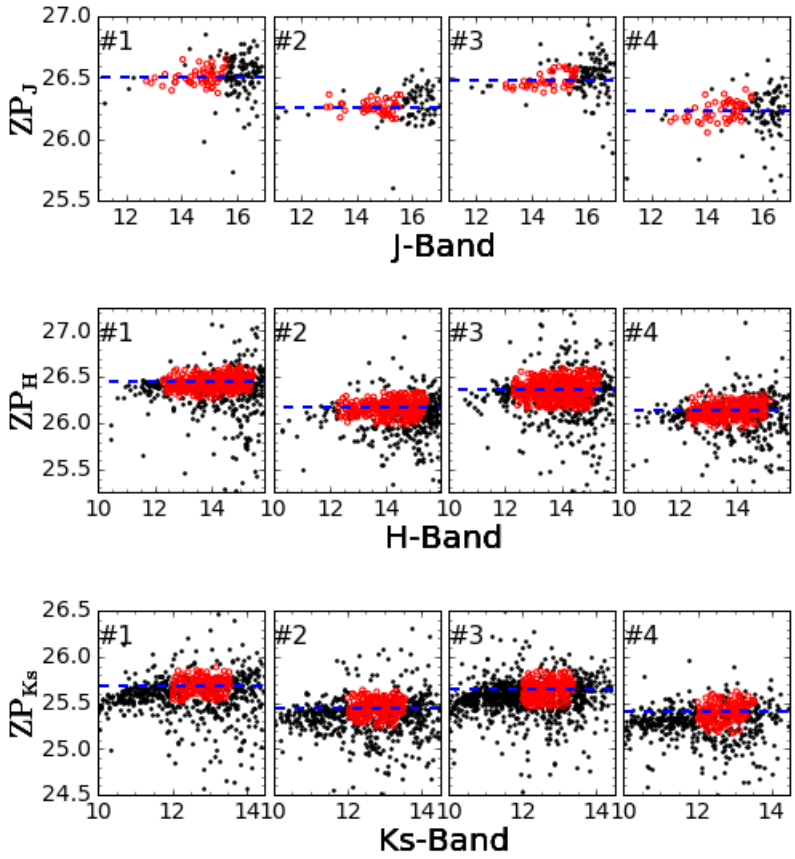

Fig. 5.4 Zero point calibration for each chip and band in F1 data. Black points represent stars common to the SIRIUS catalogue and our final list. Red points mark the stars used to compute the zero points. The mean zero points are indicated by the blue lines. The systematic deviations for the brightest stars are due to saturation.

chips (and pointings in the case of the 2013 data), known as "pistoning". To do that we used the technique described in Dong et al. (2011), which consists in minimising a global χ^2 that takes into account all the common stars for all chips simultaneously. For that, we only used stars with less than 0.05 mag of uncertainty. As expected, the variation in zero point between the chips was quite low (less than 0.1 magnitude even in the worst cases for all three bands and in both epochs). Calibrating the photometry for every chip independently with the SIRIUS catalogue before applying the pistoning

correction let us compare the overlapping region of the different calibrated chips and estimate the relative offset as described in Sect. 5.7.

5.4.3 Combined star lists

To produce the final catalogue we merged all the photometric and astrometric measurements. For the overlap regions between the chips, the value for stars detected more than once was taken as the mean of the individual measurements. In those cases, the uncertainty was computed as the result of quadratically adding the individual uncertainties of each measurement detection. The pistoning corrections can result in minor zero point shifts of the combined star lists. To avoid them, we re-calibrated the zero point of the final, merged catalogue. This procedure was completely analogous to the one described above. Figure 5.5 shows the final calibration. The deviations at magnitudes $Ks \lesssim 11$ are due to saturation.

5.4.4 Zero point uncertainty

The final ZP uncertainty was estimated by comparing the common stars of the pilot study (see Sec. 3.1) and F1 combined lists (Fig. 5.6). As they were calibrated independently, the photometric offset that appears between them is a measurement of the error associated with the calibration procedure. To compare the photometry, we used Eq. 4.1, where the fluxes are calculated from the magnitudes in both epochs. This gives us an upper limit for the uncertainties that is shown in Fig. 5.6. We obtained a rounded upper limit of 0.02 mag for the ZP offset between the epochs. This value takes into account possible variations of the ZP across the detector, as every star was located in a different position of the detector (or even different detectors) in both epochs. It also takes into account one of the main sources of uncertainty, namely that roughly 10% of the stars in the GC are variable (Dong et al., 2017b). Therefore, the absolute uncertainty of our catalogue results from quadratically adding this uncertainty to that of the SIRIUS catalogue. We thus obtain an absolute ZP uncertainty of 0.036 mag for each band.

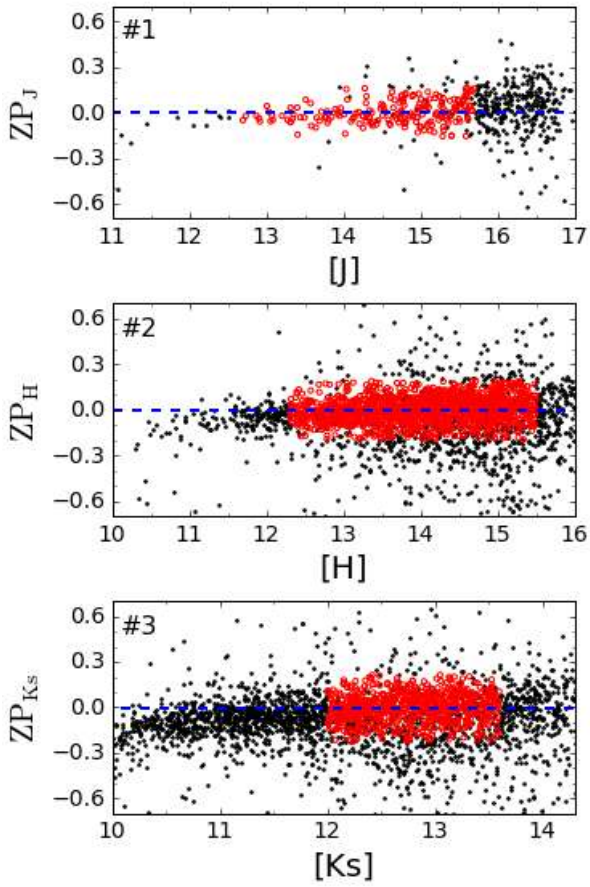

Fig. 5.5 Zero points calculated in all three bands after merging the list for every chip and pointing (F1). Black points represent all the common stars between the SIRIUS catalogue and our data. Red points depict the stars used to compute the zero point and the blue line is its average. Systematic deviations for the brightest stars are due to saturation.

5.5 Scripts

To compute the photometry and astrometry, we have developed a pipeline using the *StarFinder* package (Diolaiti et al., 2000):

- **block_psf.pro**

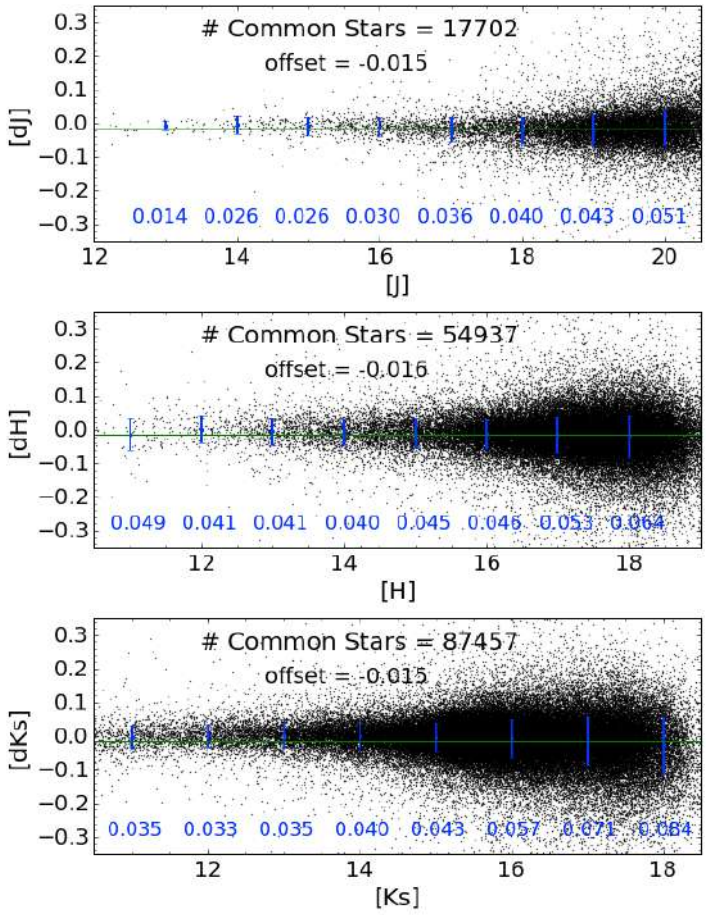

Fig. 5.6 Photometric comparison of the common stars between the final lists of the pilot study and F1 data obtained using Eq. 4.1. The green line depicts the mean of the difference between the points (we applied a two-sigma clipping algorithm to compute it). Blue lines and the number below them depict the standard deviation of the points in bins of one magnitude width.

This block runs in parallel the obtention of the PSF of each of the sub-images for each chip and band.

- **block deepastro.pro**

This block computes in parallel the photometry for each sub-image using the PSF obtained in the previous step.

- **deepastro_psf_comparison.pro**

  We estimate the uncertainty associated to the variability of the PSF as indicated in Sec. 5.2.

- **final_photometry_list.pro**

  This code combines the photometry obtained for each sub-image and the one for the deep image. It also estimates the uncertainty for the photometry and removes spurious sources that have not been detected in all three sub-images, as it is explained in Sec. 5.2.1.

- **astronomy_cal_def.pro**

  This script computes the astrometric solution and the ZP calibration for the final photometry list for each chip and band (see Secs. 5.3 and 5.4).

- **match_list.pro**, **ZPcalib.pro** and **applying_the_offsets.pro**

  These codes compute the pistoning correction and apply the offset to the ZP as indicated in Sec. 5.4.2.

- **combined_list_each_band.pro**

  This script creates the final photometric list joining the lists for the individual chips.

- **calib_second.pro**

  We recomputed the photometric calibration to avoid small photometric offset during the process of correcting the pistonning (see 5.4.3).

- **combined_list.pro**

  This code creates the final photometric list for each field combining all three bands.

For the ESO phase 3 data release, we produced final lists for each chip instead of combining all four chips into a single catalogue.

5.6 Summary of the analysis

Figure 5.7 summarises the whole analysis explained in this chapter and in chapter 4 from the raw data to the final photometry list obtained for each chip.

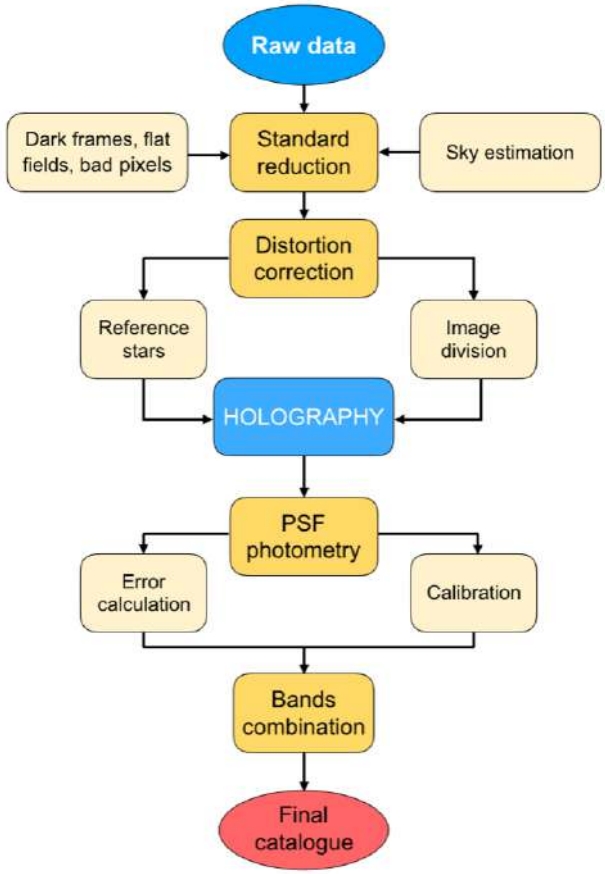

Fig. 5.7 Scheme of the obtention of the final catalogue for each chip.

5.7 Quality assessment

To check the accuracy of the photometry, we performed several tests:

(1) We compared the overlapping regions of all four chips in F1 data, using Eq. 4.1. We excluded the borders and compared the inner regions of the overlap, where at least 100 frames contribute to each pixel (see, e.g., the weight map in Fig. 4.4). Figure 5.8 shows the results for the overlap between chips #1 and #4. As can be seen, the photometric accuracy is satisfactory. The uncertainties are at most a few 0.01 mag. These independent estimates of the photometric uncertainties agree well with the combined statistical and systematic uncertainties of our final list.

(2) We compared the photometry from two different epochs, the pilot study and F1. In this case, we compared the common stars from each epoch. The overlap region is much larger than the one that we had in the previous test, so we found far more common stars, letting us improve on the quality of the analysis and extend it to the central regions of the chips. We computed uncertainty upper limits using Eq. 4.1 and plotted the standard deviations in bins of one magnitude in Fig. 5.6. The result demonstrates that the estimates of the photometric uncertainties of our final lists are accurate.

(3) We took HAWK-I observations of several reference stars from the 2MASS (Two Micron All-Sky Survey) calibration Tile 92397 (ra(J2000) 170.45775 dec(J2000) -13.22047), in all three bands, as a crosscheck to test the variability of the zero point. The calibration field was observed in a way that for each chip a reference star was positioned at nine different locations. We applied a standard reduction process to those images taking into account the special sky subtraction that we described above. Then, we performed aperture photometry for all nine positions taking four different aperture radii to test the uncertainties. All nine measurements for all the chips agree within the uncertainties with the assumption of a constant ZP across the chips.

(4) All the previous tests estimate the uncertainties supposing that only the detected sources are in the field. To complement the quality assessment, we used the simulations described in Sec. 4.5 and their corresponding uncertainties. They show the influence of extreme crowding in the photometry, as they simulated the inner parsec, which supposes the most crowed field. The photometric uncertainties that we obtained are lower because only the central region, the inner arcminute, suffers from

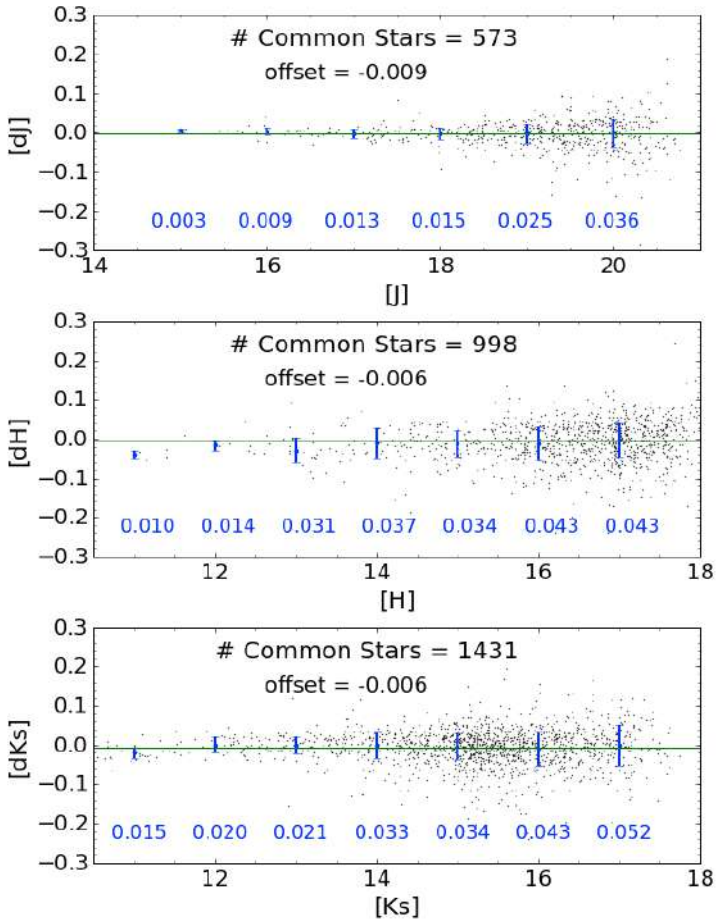

Fig. 5.8 Photometric accuracy in the overlap regions between chips #1 and #4 (F1 data). Blue lines and the number below them depict the standard deviation of the points in bins of one magnitude width.

extreme crowding. Therefore, the obtained results are consistent with this analysis.

(5) We qualitatively compared the K_s luminosity functions obtained with our HAWK-I data and the VVV survey. For that, we performed PSF fitting photometry with *StarFinder* on a final VVV mosaic centred on SgrA* observed in 2008. We produced luminosity functions for both VVV and HAWK-I data in a region of ap-

proximately $8' \times 2.5'$. Figure 5.9 shows the results.The HAWK-I data are roughly three magnitudes deeper than the VVV data. The brightest part of the luminosity function is slightly different as a consequence of the important saturation of the K_s band in the central parsec in VVV.

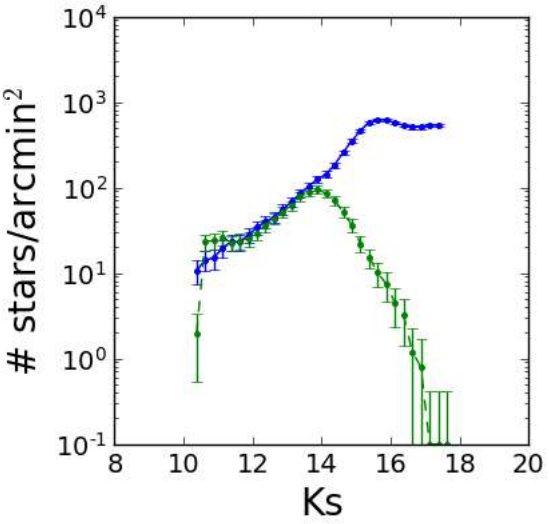

Fig. 5.9 Luminosity functions in K_s obtained with HAWK-I (blue line) and VVV (green dashed line).

"Querido Daniel, cuanto antes usted se dé cuenta de esto, mejor: Nada en esta cochina vida vale dos duros si no tienes alguien con quien compartirlo."

La sombra del Viento. Carlos Ruiz Zafón

6

GALACTICNUCLEUS: The catalogue

In this chapter, I explain the creation of the GALACTICNUCLEUS catalogue combining the photometry computed for each pointing and band as previously described. The data quality assessment and the comparison with previous surveys are also discussed.

6.1 Preparation of the catalogues

Since the GALACTICNULEUS survey covers different regions in the GC (Fig. 3.2), we prepared several catalogues: 1) Four catalogues for the regions (consisting of two pointings each) shown in Fig. 3.5a). They correspond to the inner bulge and the transition region between the inner bulge and the NB. 2) Three catalogues for the central region shown in Fig. 3.5b): GC West (pointings D12 to D18), GC Central (pointings 1 to 30), and GC East (pointings D9 to D11, D19 and D21).

Table 6.1 Fields included in each catalogue.

Catalogue	Fields included
Central	1-30
NSD East	D12-D18
NSD West	D9-D11, D19, D21
Transition East	T3-T4
Transition West	T7-T8
Inner Bulge North	B1,B6
Inner Bulge South	B2,B5

Notes. The name of each field stars by a capital letter that indicates its position in the survey: 'D' -> Nuclear stellar disk, 'B' -> Inner bulge, 'T'-> transition zone inner bulge-nuclear stellar disk and ' ' for the fields in the central part of the survey.

6.1.1 Astrometry

For each band, we identified common stars in the overlapping regions and computed their positions through averaging the multiple detections. The final catalogue was created by combining all three bands. The maximum offset allowed for a star present in different bands was set to $\sim 0.1''$, half the angular resolution of the images. The final positions of the stars detected in more than one band were computed as the mean positions of the individual detections. The absolute astrometric uncertainty derives from the alignment with the VVV stars that were used to compute the astrometric solution. We estimated an upper limit of the absolute astrometric uncertainty of 0.05" with respect to VVV. As concerns the relative astrometric uncertainty of the stars, we examined the following sources of uncertainty: 1) Uncertainties derived from the measurements in the the three independent sub-images for each band and pointing (see Sec. 5.2.1). 2) Uncertainties measured from the common stars in the overlapping area between the four chips for each pointing. 3) Uncertainties estimated from common stars when combining the different pointings to produce the final list for each band. 4) Uncertainties estimated from the combination of the positions

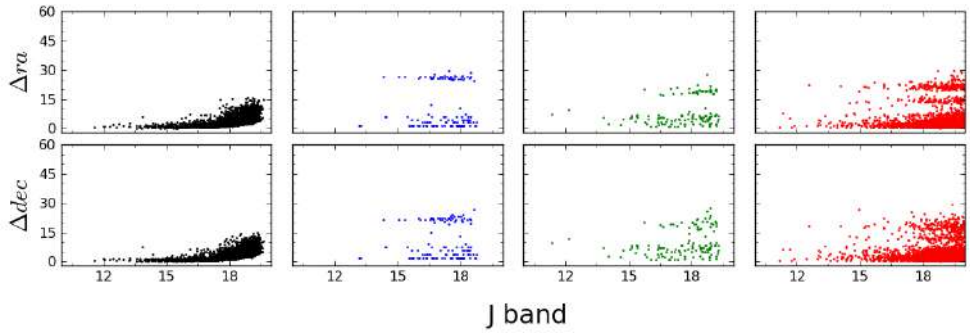

Fig. 6.1 Analysis of the astrometric uncertainties for the *J*-band. The y-axes have units of milli-arcseconds. Each column depicts the uncertainties associated to: 1) Relative astrometry measured on a single chip and pointing (F6, chip1 is shown as an example). 2) Combination of chips for a given pointing (F6 shown as an example). 3) Combination of all fields for the central region. 4) Combination of the three different bands for the central region. The plots in columns 2, 3 and 4 show steps in the distributions which are caused by systematic offsets between different chips, pointings, and filters.

of the stars from the three different bands. Figure 6.1 shows the corresponding uncertainties for chips, pointings, and the central catalogue for the case of the *J*-band. We concluded that the relative astrometric uncertainty is dominated by the combination of the different pointings and bands (points 3 and 4 above).

The final catalogues include the uncertainty due to 3) and 4) for the case of stars detected in more than one field and/or detected in more than one band. For the remaining stars we estimated an upper limit of $\sim$30 mili-arcsec that is the maximum value obtained in the analysis presented in Fig. 6.1.

6.1.2 Photometry

For stars detected in more than one pointing we computed the mean flux as the average value of the individual detections and estimated the photometric uncertainty by means of the quadratic propagation of the individual uncertainties of each detection. We compared the uncertainties derived from multiple detections with the one determined from the measurements in the three sub-images (Eq. 5.1). We used a two sigma clipping algorithm to calculate the mean of the uncertainties obtained with both

methods and concluded that both values are similar for all three bands (~ 0.03 mag). Figure 6.2 shows the uncertainties obtained using both methods.

For the combination of the pointings, we recomputed the ZP (zero point) using the SIRIUS catalogue when adding new pointings to the final catalogue. In this way, we avoided small photometric shifts that can appear when computing the average values for common stars.

We ended up with an uncertainty $\lesssim 0.05$ mag for all three bands at $J \lesssim 21$, $H \lesssim 19$ and $K_s \lesssim 18$, which is slightly better than for the case of the F1 alone (the central most field that suffers the worst crowding) that was analysed in the previous chapter and in Nogueras-Lara et al. (2018a).

Zero point

Once produced the final lists for each band, we recomputed the ZP using again the SIRIUS/IRSF GC survey. This calibration was done in the same way as explained in Sec. 5.4 (for further details see Nogueras-Lara et al., 2018a). We identified non-saturated common stars (coincident in position within a radius of $\sim 0.1''$). Moreover, in order to use only isolated stars, we excluded all sources with a secondary star within $\sim 0.5''$ in the GALACTICNUCLEUS catalogue (SIRIUS is a seeing-limited survey with an angular resolution $\sim$1"). We excluded all stars with an uncertainty > 0.05 mag in the GALACTICNUCLEUS catalogue or > 0.1 mag in the SIRIUS catalogue. The calculation of the ZP was done using a 2-sigma clipping algorithm to remove outliers. Figure 6.3 shows all the common stars and those selected for calibration.

Zero point uncertainties

To estimate the uncertainties of the ZPs, we took several effects into account: 1) The ZP uncertainty associated to the SIRIUS catalogue, 0.03 mag in all three bands (Nishiyama et al., 2006b, 2008). 2) The process to combine the chips and pointings until obtaining the final catalogue is complex and may lead to additional systematic uncertainties of the ZP. Figure 6.4 shows the comparison between the common stars in all three bands. The uncertainties were computed using eq. 5.1. From this comparison we estimated an upper limit for the differential ZP uncertainty of ~ 0.03

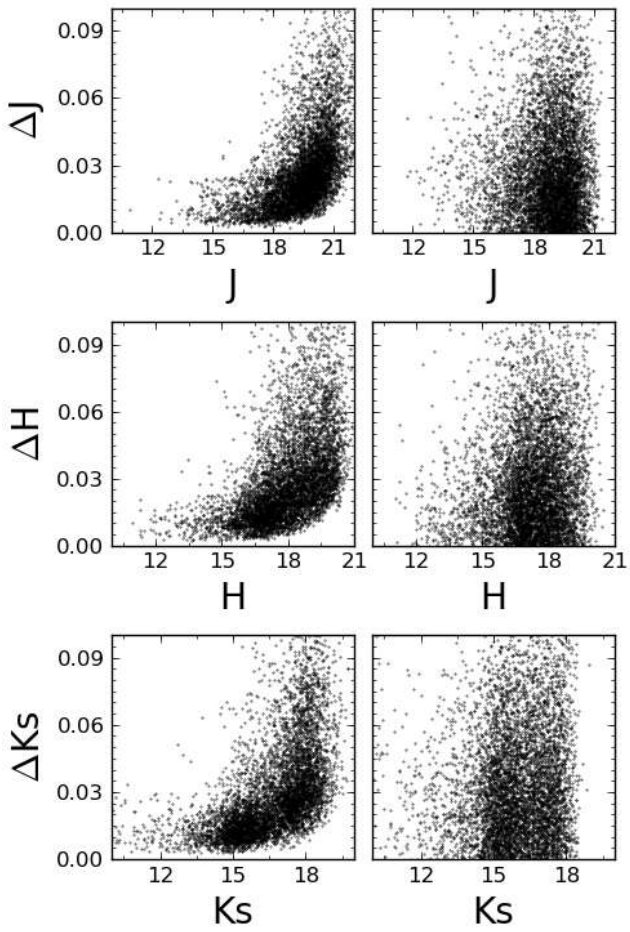

Fig. 6.2 Left panels: photometric uncertainties due to the quadratic propagation of the errors for each star. Right panels: uncertainties computed for stars detected in the overlapping regions between fields using eq. 5.1. The uncertainties shown in the right panels reach less deep magnitudes since those stars need to be detected in more than one field, and the slightly different atmospheric conditions between pointings complicate the detection of the faintest stars. Only a random fraction of the stars has been plotted for clarity.

mag in all three bands using a two sigma clipping algorithm. This is consistent with the uncertainty obtained in Nogueras-Lara et al. (2018a) for the central field

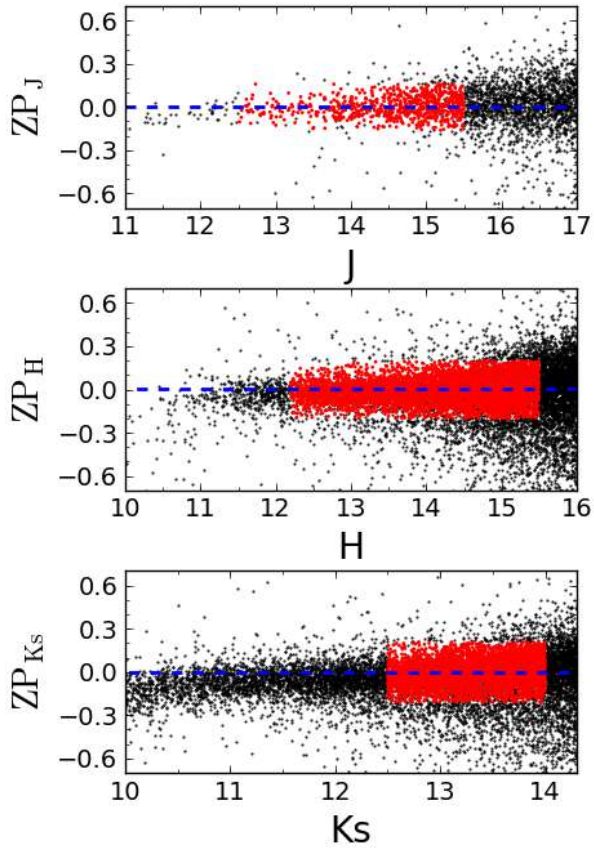

Fig. 6.3 Comparison of the photometry of GALACTICNUCLEUS and SIRIUS stars after obtaining the final lists for each band in the central catalogue. All common stars between SIRIUS and GALACTICNUCLEUS are plotted in black. Red points indicate those used for calibration. The deviation for bright stars is caused by saturation.

comparing observations taken at different epochs with HAWK-I and processed using the speckle holography technique. 3) Statistical uncertainty of the ZPs: The high number of stars used for the ZP calibration at each band results in a negligible statistical uncertainty.

Combining quadratically the uncertainties due to 1) and 2) we ended up with an uncertainty of the ZP of 0.04 mag in all three bands, which is in agreement with the value of 0.036 mag that was obtained for the central field F1 in the previous chapter.

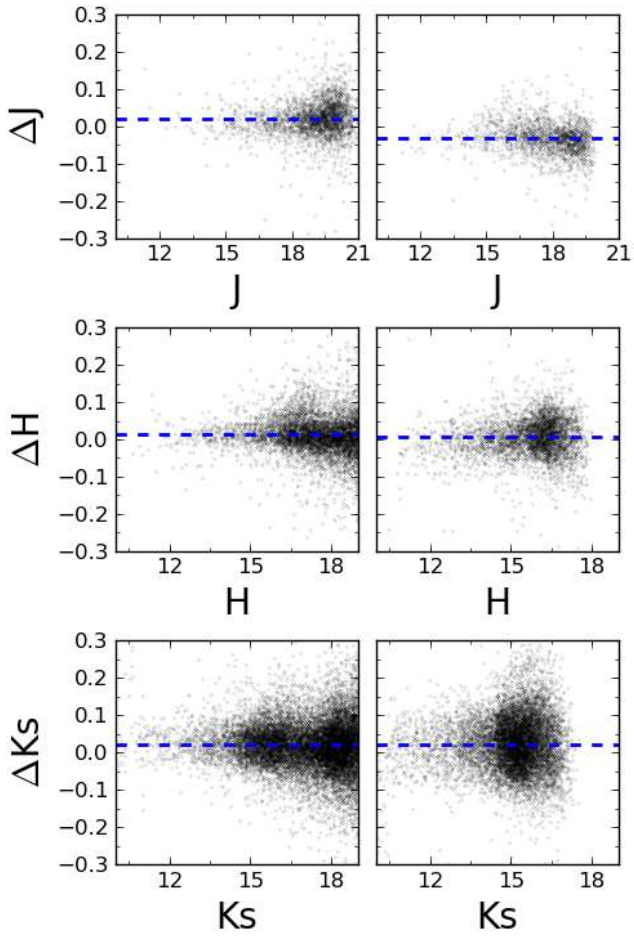

Fig. 6.4 Left panels: photometric comparison of the common stars between the central and the NSD East catalogues. Right panels: photometric comparison Central-NSD West catalogues. The uncertainties have been calculated using eq. 5.1. The blue dashed line indicates the mean offset existing between the considered regions.

6.1.3 Completeness

Given the high number of sources detected, using the standard approach of inserting artificial stars would increase enormously the computational time needed to analyse the regions covered. Instead of this, we have used an alternative approach based on the determination of the critical distance from a bright star at which we are able to detect a star of any given magnitude (Eisenhauer et al., 1998; Harayama et al., 2008). This information is later translated to completeness maps for each magnitude bin considered. This technique assumes that the detection probability of a single star is constant across the analysed field. Since our final catalogues are produced combining independent pointings that were obtained under non-uniform observing conditions and since the stellar density varies as a function of position in the GC, we analysed the completeness due to crowding on smaller subregions of $2' \times 1.4'$. For a rough assessment of overall completeness, we subsequently averaged over all the subregions. We applied this technique only to the central pointings (1-15) as they are the most challenging ones in terms of crowding. Crowding is the factor that dominates completeness in the sensitive K_s- and H-band images. We estimated a completeness of ~ 80 % at $K_s \sim 16$ mag and $H \sim 18$ mag. Crowding is hardly an issue in the J-band images because the much higher interstellar extinction (note that the reddening induced colours $J - K_s \approx 5$ at the GC) at short NIR wavelengths reduces the number of detected stars considerably. We run artificial stars tests in the central pointing of the central catalogue (F1), the most crowded one, and obtained a completeness of ~ 80 % at $J \sim 20$ mag. This is a conservative limit for completeness due to crowding because most other fields will be less crowded.

We also run the same simulations for H and K_s bands and confirmed the limits previously obtained. Moreover, a comparison with the deeper photometry obtained for the nuclear star cluster in H and K_s ($\sim 0.06''$ angular resolution) with NACO/VLT (Gallego-Cano et al., 2018), agrees with the completeness limits that we estimated here.

6.1.4 Final catalogues

We obtained accurate photometry in the NIR bands J, H and K_s of $\sim 3.3 \cdot 10^6$ stars. Approximately 20% of them where detected in J, 65% in H and 90% in K_s. The

catalogue covers a total area of ~ 0.3 square degrees, which corresponds to ~ 6000 pc^2. This supposes an average stellar density of ~ 600 stars/pc^2.

The final catalogues are made publicly available at the CDS via anonymous ftp to cdsarc.u-strasbg.fr or via http://cdsarc.u-strasbg.fr/, with the publication of Nogueras-Lara et al. (in press). Moreover, we are now preparing the individual catalogues for each chip and band for the ESO phase three data release of our ESO Large Programme that underlies this catalogue. The data will be available from the ESO Science Archive. The lists include 25 columns that contain information about:

- **Position and uncertainties between bands**: right ascension and declination expressed in degrees (columns 1 and 3) and their corresponding uncertainties expressed in arcseconds (columns 2 and 4). For stars detected in more than one band these coordinates have been calculated averaging the positions of the detections. The uncertainties refer to the deviation of the measurements (see column 4 in Fig. 6.1). For stars detected in a single band, we indicated the corresponding coordinates and the uncertainty associated to the detection (see column 3 in Fig. 6.1).

- **Relative position and uncertainties for each band**: We included the positions and the associated uncertainties estimated from multiple detections of the same star in different pointings within the same band (column 3 in Fig. 6.1). The positions are expressed in degrees and the uncertainties in units of arcseconds (columns 5-8 for J, 9-12 for H, 13-16 for K_s). A value of zero means that a stars was not detected in a given band or that it was not detected multiple times in overlapping pointings. In those cases we refer to the upper limit of 30 mili-arcsec derived previously (Sec. 6.1.1).

- **Photometry and uncertainty for each band**: For each star we included the photometry in J, H, and K_s and the associated uncertainties expressed in mag (columns 17-22). A value of 99 indicates a non-detection.

- **Number of multiple detections**: This value indicates the number of multiple detections in overlapping pointings for each band (columns 23, 24, 25).

Table 6.2 outlines the first rows of the central catalogue specifying the columns described previously.

Figure 6.5 shows an RGB image corresponding to the GC Central catalogue produced from a mosaic of pointings 1 to 30. More RGB images of the catalogue including examples of the different regions covered by GALACTICNUCLEUS are presented in Appendix C.

6.2 Quality assessment

We carried out several tests to check the photometric quality of our catalogues:

6.2.1 Comparison with SIRIUS catalogue

We compared the photometry obtained for all three bands with the SIRIUS/IRSF survey catalogue. To check that the ZP does not change significantly across the final region covered by the catalogues when combining the different fields. For this purpose we used the GC Central catalogue, which we expect to make a good test case because it contains the most complex region and combines 30 different pointings observed under different seeing conditions at different epochs (see table 3.2). We cross-matched both catalogues and identified common stars in all three bands. We divided the GC central region into four independent vertical columns, from east to west along the Galactic Plane, and analysed them independently. We used eq. 5.1 for comparing the photometry. Figure 6.6 shows the results. We calculated the offset using a two sigma clipping algorithm to remove outliers and avoided saturated and too faint stars. We kept stars of $J = 12.5 - 15.5$ mag, $H = 12.3 - 15.5$ mag, and $K_s = 12.5 - 14$ mag (see also Fig. 6.3). We then computed the difference between the maximum and the minimum offsets for each band between the 4 different columns. This difference is < 0.01 mag in all three bands. We conclude that there is no significant variability of the ZP across the GC Central field.

Table 6.2 First rows of the central catalogue.

ra	Δra	dec	Δdec	ra$_J$	Δra$_J$	dec$_J$	Δdec$_J$	ra$_H$	Δra$_H$	dec$_H$	Δdec$_H$	ra$_H$	Δra$_{Ks}$	dec$_{Ks}$	Δdec$_{Ks}$	J	dJ	H	dH	K_s	dK_s	i_J	i_H	i_{Ks}
°	”	°	”	°	”	°		°	”	°	”	°	”	°	”	mag	mag	mag	mag	mag	mag			
266.47	0.003	-28.97	0.003	266.47	0.007	-28.97	0.010	266.47	0.003	-28.97	0.004	266.48	0.004	-28.97	0.006	11.355	0.008	10.666	0.008	10.409	0.006	4	3	3
266.47	0.002	-28.97	0.002	266.47	0.010	-28.97	0.012	266.47	0.007	-28.97	0.010	266.48	0.005	-28.97	0.006	12.148	0.009	11.721	0.007	11.556	0.007	4	4	4
266.47	0.001	-28.98	0.001	266.47	0.006	-28.98	0.007	266.47	0.005	-28.98	0.006	266.47	0.007	-28.98	0.008	13.813	0.008	12.697	0.007	12.340	0.011	4	4	4
266.48	0.006	-28.96	0.007	266.48	0.002	-28.96	0.003	266.48	0.006	-28.96	0.007	266.48	0.003	-28.96	0.004	14.063	0.006	13.524	0.015	13.411	0.008	3	4	3
266.47	0.003	-28.97	0.004	266.47	0.002	-28.97	0.002	266.47	0.008	-28.97	0.010	266.47	0.007	-28.97	0.008	14.612	0.011	13.848	0.014	13.621	0.006	4	4	4
266.48	0.001	-28.97	0.002	266.48	0.005	-28.97	0.006	266.48	0.000	-28.97	0.000	266.48	0.007	-28.97	0.008	14.753	0.009	12.861	0.006	12.051	0.008	4	4	4
266.48	0.001	-28.97	0.001	266.48	0.005	-28.97	0.006	266.48	0.007	-28.97	0.009	266.48	0.003	-28.97	0.004	15.037	0.008	12.949	0.007	11.968	0.005	4	4	4
266.48	0.007	-28.97	0.009	266.48	0.006	-28.97	0.007	266.48	0.008	-28.97	0.010	266.48	0.027	-28.97	0.028	15.146	0.009	14.287	0.011	13.961	0.032	4	4	4
266.47	0.008	-28.97	0.007	266.47	0.007	-28.97	0.008	266.47	0.001	-28.98	0.002	266.47	0.024	-28.97	0.023	15.139	0.024	11.580	0.010	10.167	0.015	3	2	2
266.47	0.007	-28.96	0.008	266.47	0.004	-28.96	0.004	266.47	0.003	-28.96	0.003	266.47	0.024	-28.96	0.025	15.328	0.012	11.605	0.010	10.029	0.021	3	3	2
266.48	0.003	-28.97	0.003	266.48	0.007	-28.97	0.008	266.48	0.003	-28.97	0.004	266.48	0.006	-28.97	0.007	15.389	0.008	14.787	0.008	14.575	0.011	4	4	4
266.48	0.002	-28.97	0.002	266.48	0.006	-28.97	0.007	266.48	0.006	-28.97	0.007	266.48	0.002	-28.97	0.002	15.405	0.007	13.721	0.007	12.859	0.006	4	4	4
266.47	0.001	-28.97	0.001	266.47	0.007	-28.97	0.009	266.47	0.006	-28.97	0.007	266.47	0.003	-28.97	0.004	15.424	0.008	14.649	0.007	14.400	0.005	4	4	4
266.47	0.007	-28.96	0.007	266.47	0.020	-28.96	0.020	266.47	0.020	-28.96	0.015	266.47	0.005	-28.96	0.006	15.735	0.010	12.232	0.008	10.437	0.014	4	4	4
266.48	0.001	-28.96	0.002	266.48	0.003	-28.96	0.004	266.48	0.006	-28.96	0.007	266.48	0.002	-28.96	0.002	15.762	0.011	14.748	0.007	14.362	0.024	4	4	4
266.48	0.007	-28.97	0.007	266.48	0.002	-28.97	0.002	266.48	0.017	-28.98	0.019	266.48	0.017	-28.97	0.019	15.851	0.008	14.989	0.007	14.701	0.010	4	4	4
266.48	0.001	-28.97	0.002	266.48	0.007	-28.97	0.008	266.48	0.009	-28.97	0.011	266.48	0.006	-28.97	0.007	15.946	0.008	15.030	0.007	14.695	0.005	4	4	4
266.48	0.001	-28.97	0.002	266.48	0.005	-28.97	0.006	266.48	0.003	-28.97	0.004	266.48	0.004	-28.97	0.005	15.960	0.008	13.629	0.007	12.568	0.009	4	4	4
266.48	0.003	-28.97	0.003	266.48	0.001	-28.97	0.001	266.48	0.007	-28.97	0.008	266.48	0.008	-28.97	0.010	16.069	0.009	15.204	0.011	14.895	0.009	4	3	3
266.48	0.008	-28.97	0.011	266.48	0.003	-28.97	0.004	266.48	0.024	-28.97	0.027	266.48	0.027	-28.97	0.017	16.538	0.038	15.649	0.058	15.854	0.038	3	2	3
...	...	...	...	...	...	...	...	...	...	...	...	...	...	...	...	...	...	...	...	...	...	...	...	...

Notes. First rows of the central catalogue. ra, Δra and dec, Δdec are the right ascension and the declination of the sources (and their corresponding uncertainties) obtained combining the detections in several bands. ra$_i$, Δra$_i$ and dec$_i$, Δdec$_i$ correspond to the coordinates and uncertainties for any single band, i. The coordinates were rounded to two decimals in this table. J, dJ, H, dH, K_s and dK_s are the photometry and the associated uncertainties. A 99 indicates that there is no detection for a given source. i_J, i_H and i_{K_s} indicate the number of fields where a star were detected to obtain its final photometry.

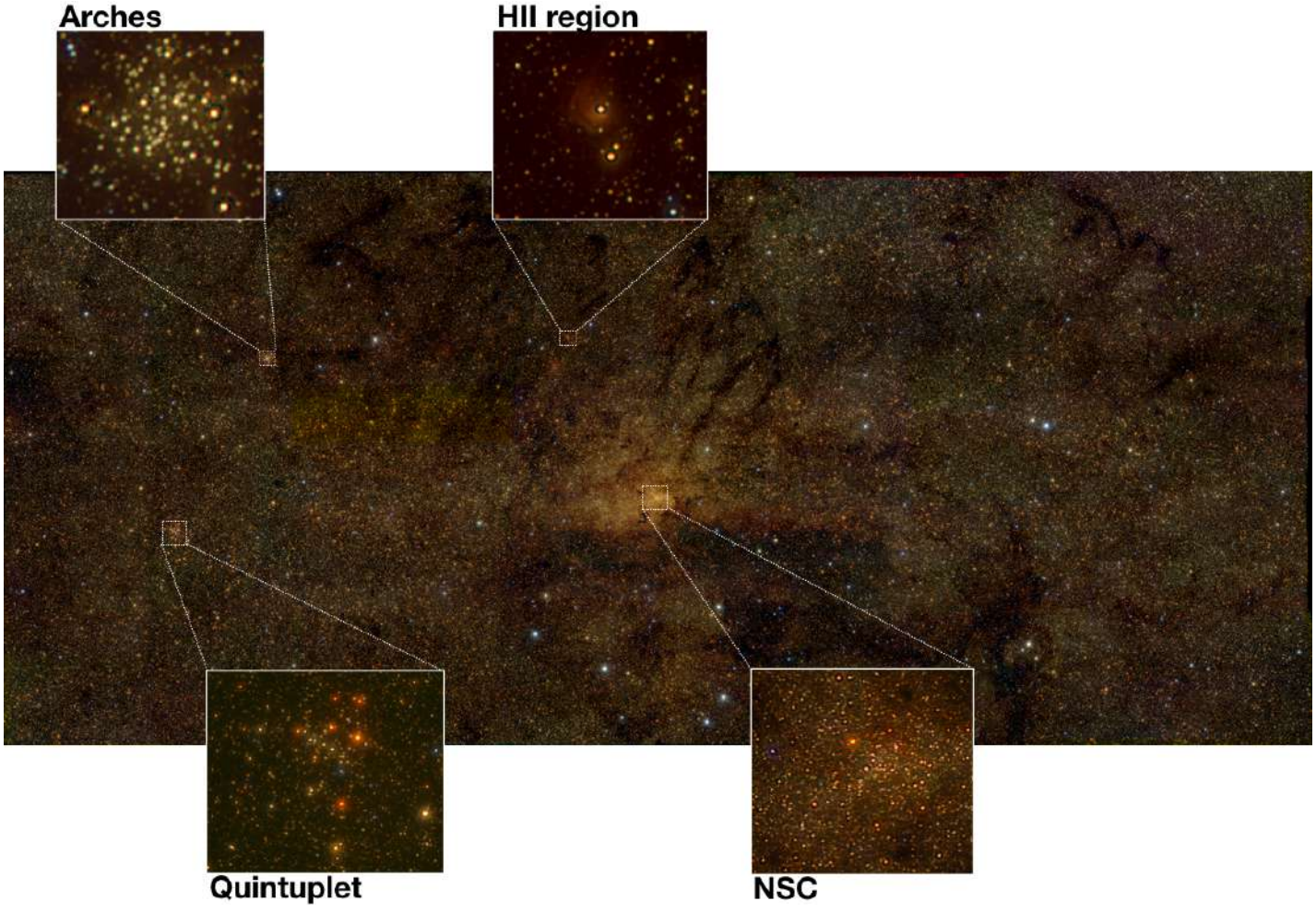

Fig. 6.5 RGB image (red = K_s band, green = H band and blue = J band) of the central catalogue corresponding to fields from 1 to 30. Field 7 is not included in J band since the observing conditions were not acceptable to include it in the survey.

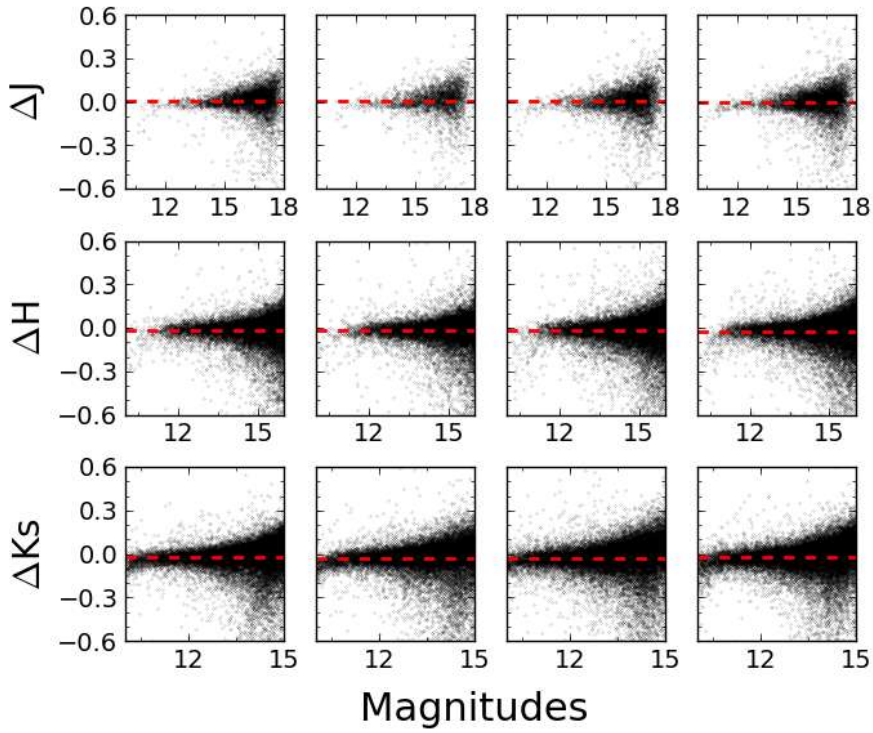

Fig. 6.6 Photometric comparison between GALACTICNUCLEUS and the SIRIUS IRSF survey across the central catalogue. We divided the central catalogue into 4 equal regions from east to west along the Galactic Plane, that are shown in each of the columns for all three bands. The red dashed line indicates the photometric offset.

6.2.2 Comparison with a previously used sub-catalogue

We compared the final GC Central catalogue with a previous version that included only 14 of 30 fields and that was used in previous work (Nogueras-Lara et al., submitted; Gallego-Cano et al., submitted). The main difference introduced by the final version is the photometry of the common stars detected in pointings that were not included in the former version. Also, the ZPs computed at intermediate steps could have varied (see Sec 6.1.2) because less fields were present in the previous version of the GC Central catalogue. Figure 6.7 shows the comparison between the preliminary and the final catalogues following eq. 5.1. Both catalogues agree very

well as expected.

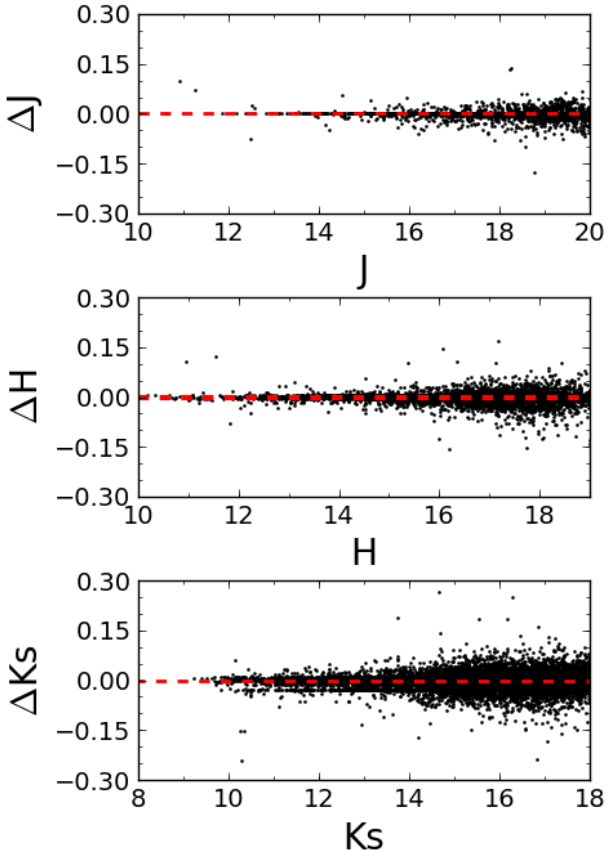

Fig. 6.7 Photometric comparison between the final version of the central catalogue of GALACTICNUCLEUS and a preliminary version obtained using the fields from 1-15 (except field 7). The red dashed line indicates the offset between the photometric ZPs.

6.2.3 Comparison with VVV

Up to now, the most complete multi-band catalogue with high angular resolution to study the GC was the VVV survey (Minniti et al., 2010; Saito et al., 2012). This survey covers an area of 520 deg^2 in the Galactic Bulge and a section of

the mid-plane with high star formation activity. It uses aperture photometry to characterise $\sim 10^9$ sources in the NIR. Since the JHK_s filters are very close to the GALACTICNUCLEUS ones, we have compared the photometry of common stars to analyse the systematics of the ZP and the data quality of our survey. We have used the VVV aperture photometry computed in a radius of $1''$. To calculate the ZP offset, we have removed all the stars with an uncertainty > 0.05 mag in both catalogues and in all three bands. Due to the extreme source crowding in the K_s band, we excluded all the stars with a fainter counterpart detected in GALACTICNUCLEUS within a radius of $1''$. We used a two sigma clipping algorithm to remove outliers and avoided saturated and too faint stars as indicated by the red dots in Fig. 6.8. We obtained that the small shifts agree with the systematic uncertainties estimated for the ZP. Moreover, we checked that a comparison between SIRIUS and VVV gives a similar result.

On the other hand, we compared the J, H and K_s luminosity functions from VVV, SIRIUS and GALACTICNUCLEUS obtained for the central catalogue (Fig. 6.9). GALACTICNUCLEUS reaches $\gtrsim 1$ mag deeper in J and $\gtrsim 2$ mag in H and K_s. The GALACTICNUCLEUS survey therefore improves significantly the number of stars detected at the faint end of the LFs. The GALACTICNUCLEUS LFs are also more complete at the bright end, where the VVV survey suffers from far stronger saturation (green bumps at the bright end in Fig. 6.9) because of the larger pixel scale of VIRCAM and the longer exposure time used in VVV. In particular, the GALACTICNUCLEUS catalogue covers completely the red clump (RC) bump in K_s. RC stars are important standard candles and tracers of Galactic structure. Multiple RC bumps can give information on recent star formation events or on different overlapping structures along the line-of-sight (e.g., Girardi, 2016). It can be also seen that the SIRIUS survey appears as a better reference for photometric calibration in comparison to the VVV catalogue since it is far less saturated and covers a larger magnitude range in H and K_s bands.

Finally, we compared a region in the central catalogue (centred on 17^h 45^m 47.524^s, -28° 55' 11.847" and covering and area of $\sim 20' \times 17'$) with the recent update of the VVV survey using PSF photometry (Alonso-García et al., 2018). We obtained that the VVV photometry is quite incomplete in the bright part and does not improve the faint end of the LFs obtained using the aperture photometry.

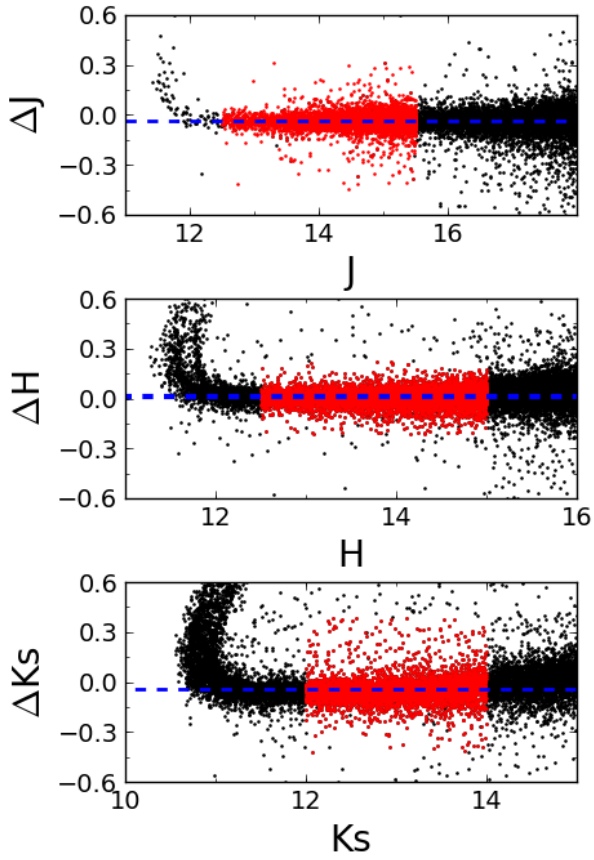

Fig. 6.8 Photometric comparison between the final version of the central catalogue of GALACTICNUCLEUS and a the VVV catalogue with aperture photometry. The red dots indicate the stars used to compute the offset. The blue dashed line corresponds to the photometric offset between both catalogues. The bright tails are due to the strong saturation in the VVV catalogue.

This is mainly because the new release of the catalogue only accepts a star if it is detected in at least three bands (out of Z,Y,J,H,K_s). Moreover, this survey has not been specially designed for the GC. For the same region we also compared the photometric uncertainties given by the VVV survey with PSF photometry and GALACTICNUCLEUS. We analysed both catalogues in the same magnitude range

to avoid a bias due to the different completeness limits. Therefore, we considered only stars with $J < 19$ mag, $H < 16$ mag and $K_s < 14$ mag. We obtained a mean uncertainty of $\Delta_J = 0.06$ mag, $\Delta_H = 0.02$ mag and $\Delta_{Ks} = 0.02$ mag for VVV and $\Delta_J = 0.02$ mag, $\Delta_H = 0.01$ and $\Delta_{Ks} = 0.01$ mag for GALACTICNUCLEUS. This supposes an improvement of factors two to three.

6.2.4 Comparison with NICMOS HST

We compared our data with the NICMOS HST survey carried out by Dong et al. (2011) using the narrow band filters F187 and F190. We selected a common region between both catalogues of $\sim 20' \times 10'$ centred on Sgr A*. We detected around three times more sources in the GALACTICNUCLEUS survey. We also compared the uncertainties and obtained that the relative uncertainty of the NICMOS HST survey is $\sim 6\%$ for F187 and $\sim 5\%$ for F190, whereas we reached a relative median uncertainty of $\sim 2\%$ in all three bands for GALACTICNUCLEUS. Moreover, we are able to achieve the same angular resolution, $\sim 0.2''$ using a ground based telescope. Figure 6.10 shows the comparison between the NSC as it is seen by NICMOS and by GALACTICNUCLEUS.

6.2.5 Detailed analysis of pointing F1

Additional tests were carried out for the most crowded field (pointing F1) in Sec 5.7. We checked the photometry and the photometric uncertainties comparing the field with previous data from a pilot study (2013), we used calibration stars to check the variation of the ZP across each detector, and we estimated the uncertainties using simulations to test the influence of the extreme crowding on the photometric errors. In general all the conclusions obtained for pointing F1 can be used as upper limits for the rest of the fields under the same observing conditions.

6.3 Limitations of the survey

As it was shown previously, the GALACTICNUCLEUS catalogue supposes a great improvement in the state of art to get to know the stellar structure and population of

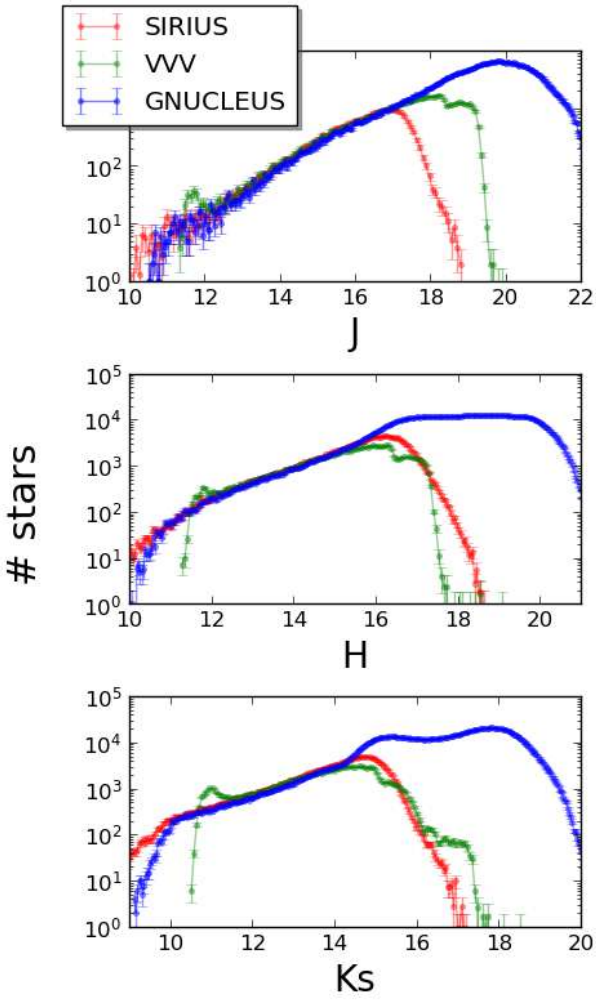

Fig. 6.9 Luminosity functions obtained with the SIRIUS survey (in red), the VVV survey (in green) and the GALACTICNUCLEUS survey (in blue). The uncertainties are Poisson errors (square root of the number of stars in each bin).

the nuclear bulge of the Milky Way. Nevertheless, there are two main limitations that need to be taken into account.

- **Photometric saturation**: in spite of the short exposure times used for the observations, the very good seeing conditions (see tables 3.2, 3.3 and 3.4)

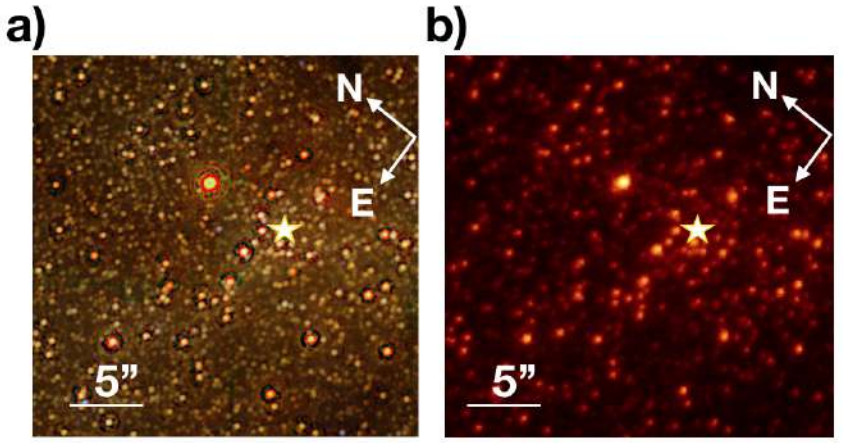

Fig. 6.10 Comparison of the NSC between (a) GALACTICNUCLEUS (JHK_s RGB image) and NICMOS HST F190 (b). The white star indicates the position of Sgr A*.

provoke a significant saturation of the bright sources in K_s band. To study this effect, we have created K_s LFs using GALACTICNUCLEUS and SIRIUS data. Because of the smaller size of the telescope used for SIRIUS (1.4 m), the effect of saturation is less important in comparison to GALACTICNUCLEUS. This comparison shows that for $K_s \sim 11.5$ mag the GALACTICNUCLEUS photometry is not reliable (see Fig. 6.3). Saturation is less important at H and almost negligible at J.

- **Restrictive criterion for accepting stars**: in order to estimate the uncertainties for individual stars and to avoid spurious detections, we have imposed that only stars detected in all three sub-images (see section 4.4) are accepted (see also Nogueras-Lara et al., 2018a). This can produce an estimated loss of $\sim 30-40$ % of the total number of stars present in the final holographic products. We are working on a bootstrapping algorithm to estimate the uncertainties and to obtain a deeper photometry improving the threshold for the detection of faint stars.

6.4 Colour-magnitude diagrams

The GALACTICNUCLEUS survey covers regions in the inner bulge, the NB and the transition region between them. The different stellar populations in these regions combined with the highly variable interstellar extinction result in significant differences between the corresponding color-magnitude diagrams (CMDs). Figure 8.2 shows the CMDs obtained for the GC Central, the Transition East and the Inner Bulge South catalogues (columns one, two and three, respectively). Typical types of stars found in the CMD are specified in the central panel: The foreground population ($J-H \lesssim 2$ mag, $J-K_s \lesssim 3$ mag and $H-K_s \lesssim 1$ mag) corresponds to stars along the line-of-sight from Earth to the GC probably tracing three spiral arms (Nogueras-Lara et al., 2018a). The stellar population located at $J-H \sim 2-3$ mag, $J-K_s \sim 3-5$ mag, $H-K_s \sim 1-2$ mag and $H \sim 15$ mag and $K_s \sim 13$ mag is composed of stars in the asymptotic giant branch (AGB) bump. The prominent feature located at $J-H \sim 2-3$ mag, $J-K_s \sim 3-5$ mag, $H-K_s \sim 1-2$ mag and $H \sim 16$ mag and $K_s \sim 15$ mag corresponds to the RC (giant stars in their Helium core burning sequence Girardi, 2016) and the red giant branch bump (RGBB, see, e.g., Cassisi & Salaris, 1997; Nataf et al., 2014; Salaris et al., 2002). The RC and the RGBB are of great interest since their relative properties can allow us to constrain the metallicity and age of the stellar population in the sample (e.g., Nogueras-Lara et al., 2018b). Finally, stars located at $K_s \gtrsim 17$ mag and below the RC and the RGBB belong to the ascending giant branch and post-main sequence.

6.5 Conclusions

We present the first public data release of the GALACTICNUCLEUS survey, a high angular resolution ($0.2''$) a JHK_s NIR imaging survey specially designed to study the GC. We describe in detail the reduction and analysis process from the raw images to the final photometric catalogue. We obtained accurate photometry for more than 3 million stars superseding previous surveys for the GC and reaching $J \sim 1$ mag and $H, K_s \gtrsim 2$ mag deeper than the so far best catalogues for the same region. We reached $5\,\sigma$ detection limits of $J \sim 22$ mag, $H \sim 21$ mag and $K_s \sim 21$ mag. The uncertainty of the photometric ZP is $\lesssim 0.04$ mag in all bands. Relative photometric

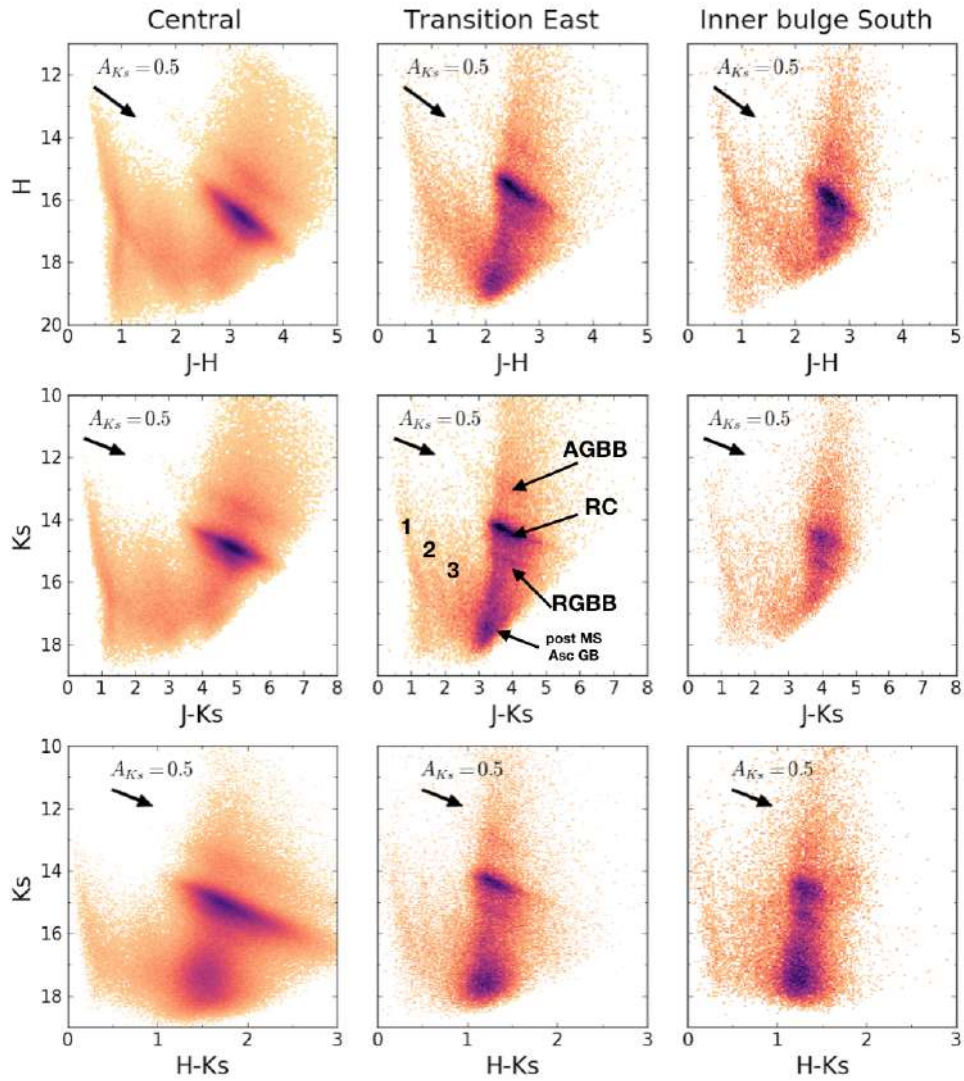

Fig. 6.11 Colour-magnitude diagrams for different regions of the GALACTICNUCLEUS survey. The colour code corresponds to stellar densities. First, second and third columns correspond to the central, the transition East and the inner bulge South catalogues. The black arrow indicates the reddening vector and an extinction of 0.5 mag in the K_s band. The labels in the central panel correspond to the different stellar types present in the CMDs: AGBB (asymptotic giant branch bump), RC (red clump), RGBB (red giant branch bump), post MS (post main sequence stars), Asc GC (ascending giant branch) and the numbers from 1 to 3 indicate the foreground population corresponding to three spiral arms.

uncertainties are $\lesssim 0.05$ mag at $J \lesssim 21$ mag, $H \lesssim 19$ mag and $K_s \lesssim 18$ mag. The absolute astrometric uncertainty is $\sim 0.05''$. All relative astrometric positions in the final catalogue are $< 0.05''$. We note that the relative astrometric positions between stars on individual chips for any given pointing are more than an order of magnitude smaller, typically only $\sim$1 milli-arcsecond for moderately bright stars. However, the uncertainties increase when combining the chips and pointings to the final catalogue.

We present what are probably the most complete CMDs of the GC so far, covering a large area and different regions in the nuclear stellar disc and inner bulge. The CMDs show clear differences caused by differential extinction and distinct stellar populations. We identified the foreground population, the AGBB, the post main sequence, the ascending giant branch and cover the RC and the RGBB.

Sharing our catalogue with the community, we expect to widen its usage and make it useful to solve a variety of problems and unknown questions related to the stellar population and structure of the innermost part of the Milky Way.

Dilegua, o notte!... Tramontate, stelle! Tramontate, stelle!... All'alba vincerò! vincerò! vincerò!

Turandot. Calaf. Giacomo Puccini

7

Extinction towards the central pointing

In this chapter, I use the central field of the GALACTICNUCLEUS survey (F1) to determine and characterise the extinction index in the near infrared towards the GC.

7.1 Introduction

Studying the extinction curve in the NIR is one of our goals. It is generally accepted that it can be approximated by a power law (e.g., Fritz et al., 2011; Nishiyama et al., 2008) of the form

$$A_\lambda \propto \lambda^{-\alpha} \quad , \tag{7.1}$$

where A_λ is the extinction at a given wavelength (λ) and α is the power-law index. While early work found values of $\alpha \approx 1.7$ (e.g., Draine, 1989; Rieke & Lebofsky, 1985), recently a larger number of studies has appeared, with particular focus on the GC, where interstellar extinction reaches very high values ($A_{K_s} \gtrsim 2.5$) that suggest

steeper values of $\alpha > 2.0$ (e.g., Fritz et al., 2011; Gosling et al., 2009; Nishiyama et al., 2006a; Schödel et al., 2010; Stead & Hoare, 2009). For a more complete discussion of the NIR extinction curve and corresponding references, we refer the interested reader to the recent work by Fritz et al. (2011). One of the limits of previous work on the GC was that it was limited either to small fields (e.g., Fritz et al., 2011; Schödel et al., 2010) or, because of crowding and saturation issues, to bright stars or to fields at large offsets from Sgr A* (e.g., Gosling et al., 2009; Nishiyama et al., 2006a). The high angular resolution of the GALACTICNUCLEUS survey allows us to study the extinction curve with accurate photometry in the J, H, and K_s bands with large numbers of stars and, in particular, with stars with well-defined intrinsic properties (red clump stars, e.g., Girardi, 2016). An accurate determination of the NIR extinction curve is indispensable for any effort to classify stars at the GC through multi-band photometry and to properly analysed the SFH of the GC.

7.2 Colour-magnitude diagrams

Figure 7.1 depicts the colour-magnitude diagrams (CMD) of the F1 data. We can easily distinguish several features. The three black arrows point to foreground stellar populations that probably trace spiral arms. The highly extinguished stars lie close to or in the GC. The red ellipse indicates stars that belong to the asymptotic giant branch (AGB) bump, the red square contains ascending giant branch and post-main sequence stars, and the area marked with red dashed lines corresponds to red clump (RC) stars. They are low-mass stars burning helium in their core (Girardi, 2016). Their intrinsic colours and magnitudes depend weakly on age and metallicity, so that these stars are a good tracer population to study the extinction and determine distances.

The GC field studied here contains large dark clouds that affect significant parts of the area. In order to study the stellar population towards the GC, it therefore appears reasonable to separate areas with strong foreground extinction from those where we can look deep into the GC. Since the effect of extinction is a strong function of wavelength, dark clouds can be easily identified via the low J-band surface density of stars associated to them. This method works better than using stellar colours because those are biased towards the blue in front of dark clouds (dominated by

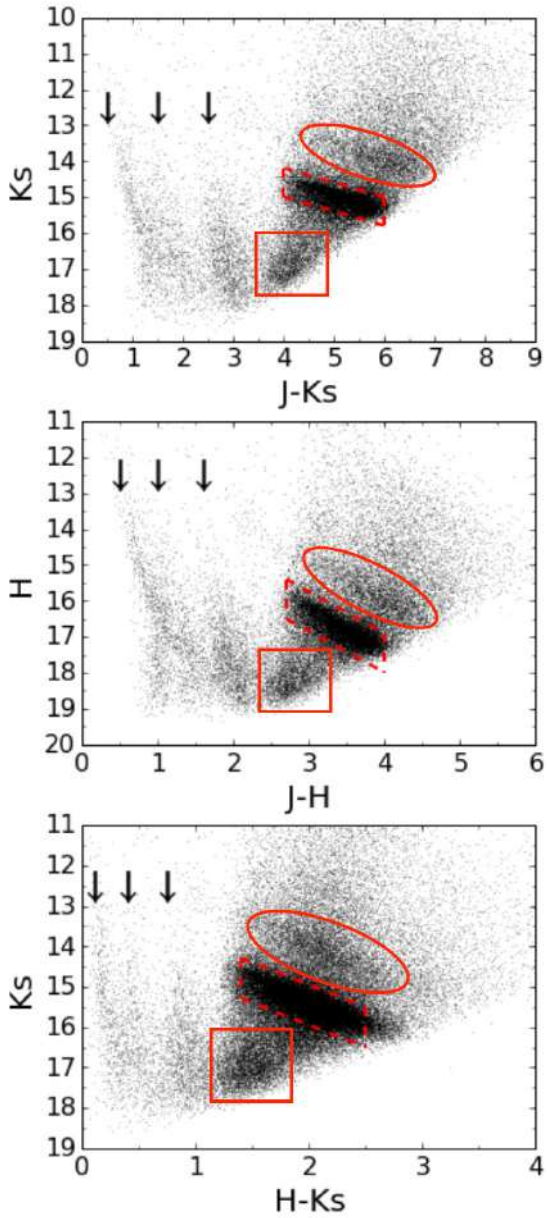

Fig. 7.1 Colour-magnitude diagrams for K_s versus $J-K_s$, H versus $J-H$, and K_s versus $H-K_s$ (F1 data). The red dashed parallelograms indicate the red clump, the red ellipse marks stars that belong to the asymptotic giant branch bump and the red square contains ascending giant branch and post-main sequence stars. The three black arrows indicate foreground stellar population probably tracing spiral arms.

foreground sources). The upper panel in Fig. 7.2 depicts the J-band surface stellar density.

To detect foreground stars and to avoid them in the subsequent analysis, we made CMDs (K_s versus $J-K_s$) for regions dominated by dark clouds in the foreground of the GC, using as criterion a stellar density below 40% of the maximum density in Fig 7.2, and for the more transparent regions a stellar density $>75\%$ of the maximum density. We normalised the resulting CMDs to the same area to compare them. For the transparent regions, the RC stellar population located at the GC forms a very clear clump on the right of the red dashed line in the left panel of Fig. 7.2. The density of foreground sources is much higher in the areas dominated by large dark clouds, as can be seen in the right panel of Fig. 7.2, where one of the potential spiral arms (at $J-K_s \approx 3$) stands out clearly in the CMD.

The separation between the groups of stars in the foreground of dark clouds and in the deep, more transparent regions, is not unambiguous, however. Two important reasons for the overlap of the two CMDs are (1) the clumpiness of the dark clouds and (2) the large area dominated by the dark clouds. The angular size of the clumps is smaller than the smoothing length used in the stellar surface density map shown in Fig. 7.2. Also, we can see that the area with stellar density larger than 75% of the maximum star density is roughly only one third of the area with 40% of the maximum star density.

To confirm the existence of two groups of stars in the field, with one group highly extinguished and the other group at lower extinction, we used data from HST WFC3 (Wide Field Camera 3) centred on Sgr A* with an approximate size of 2.7' $\times$ 2.6', to produce a CMD F153M versus F105W-F153M (Dong et al. 2017a, MNRAS; Dong et al. in preparation). Figure 7.3 shows that, when using these bands, there appears a clear gap between the two parts of the RC that we previously detected. If we select only stars that are bluer than $F105W-F153M=5.5$ in the HST CMD and identify those stars in our HAWK-I list, then we obtain the CMD shown in the upper right panel of Fig. 7.3. On the other hand, the stars on the red side of this colour produce the CMD in the lower right panel of Fig. 7.3. Unfortunately, the HST data cover only a fraction of the HAWK-I FOV. However, as shown in the right panels of Fig. 7.3, using a colour cut at $J-K_s=5.2$ we can separate fairly reliably the two giant populations with different mean extinctions.

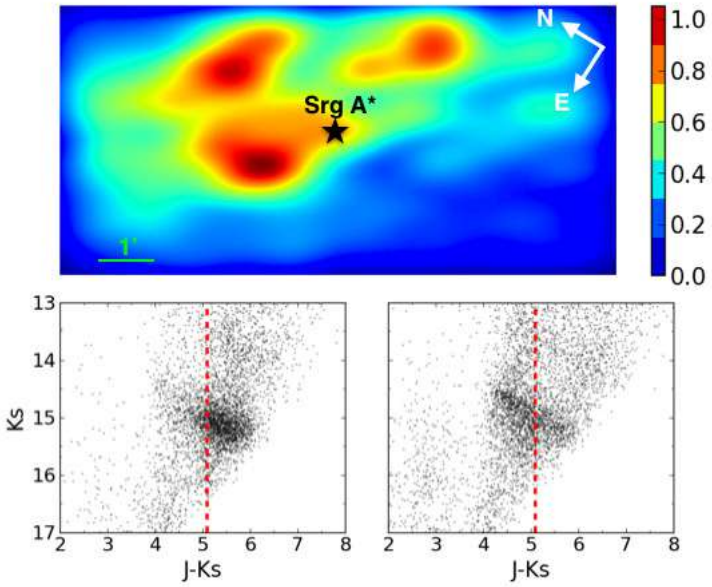

Fig. 7.2 Upper panel: Plot of the J-band stellar density. Lower left panel: CMD for stars located in areas with high stellar density normalised to the same area and maximum density. Lower right panel: CMD of stars in regions dominated by dark clouds. The red dashed line approximately separates the foreground population from stars located at the Galactic Centre.

7.3 Determination of the extinction curve

As outlined in the introduction, here we assume that the NIR extinction curve toward the GC can be described well by a power law of the form $A_\lambda \propto \lambda^{-\alpha}$, where λ is the wavelength, A_λ the extinction in magnitudes at a given λ , and α is the extinction index. We use our data set to investigate whether α has the same value across the JHK_s filters, whether it can be considered independent of the exact line of sight toward the GC, and whether it depends on the absolute value of extinction. If α can be considered a constant with respect to position, extinction, and wavelength, then we can determine its mean value. We apply several different methods to compute α and perform tests of its variability.

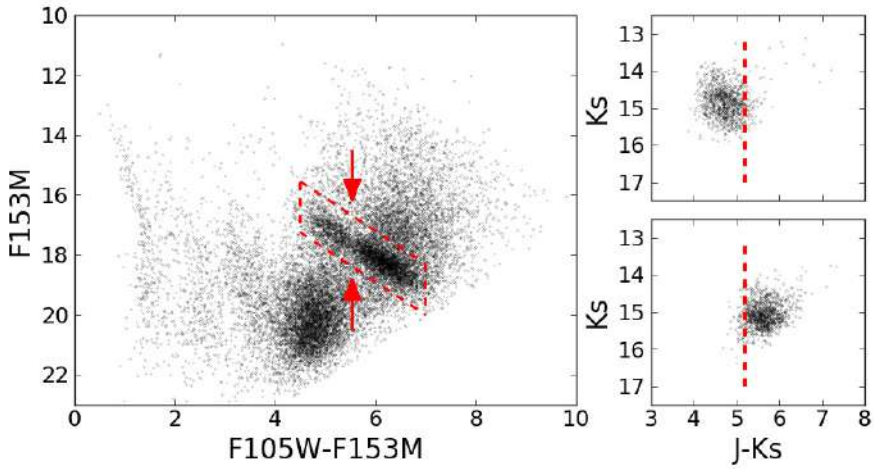

Fig. 7.3 Left panel shows the colour-magnitude diagram F153M versus F105W-F153M. The red dashed parallelogram traces the RC and the red arrows mark an obvious gap in the distribution of the RC stars, which follows the reddening vector. The upper right panel depicts stars from our HAWK-I catalogue in J and K_s with counterpart in the HST data in the first detected bump. Analogously, the lower panel represents stars located in the second bump.

7.3.1 Stellar atmosphere models plus extinction grids

We selected RC stars and assumed a Kurucz stellar atmosphere model (Kurucz, 1993) with an effective temperature of 4,750 K, solar metallicity, and $\log g = +2.5$ (Bovy et al., 2014). We set the distance of the GC to 8.0 ± 0.25 kpc (Malkin, 2013) and assumed a radius of $10.0 \pm 0.5 R_{\odot}$ for the RC stars (see Chaplin & Miglio, 2013; Girardi, 2016, with the uncertainty given in the former reference). Then, we computed the model fluxes for the J, H, and K_s bands assuming a grid of different values of α and the extinction at a fixed wavelength of $\lambda = 1.61\,\mu$m, $A_{1.61}$. The grid steps were 0.016 for both $A_{1.61}$ and α. To convert the fluxes into magnitudes, we used a reference Vega model from Kurucz. We refer to this method as the *grid method* in the following text. We produced histograms to represent the distribution of the obtained parameters and fitted them with a Gaussian model. We tested different ways of computing the bin widths of the histograms. Namely, we used the Freedman-Diaconis rule (Freedman & Diaconis, 1981), the Scott rule (Scott, 1979), the Sturges

rule (Sturges, 1926), or the Doane rule (Doane, 1976), among others. We did not observe any significant difference in the result of the fits. We generally adopted the Sturges rule for the histograms presented in this paper, as this rule is appropriate when the distributions to be represented are Gaussian-like. Besides, it smooths the histograms, which is convenient to overcome the segregation that can appear due to the grid step. This bin width selection criterion is applied for all the histograms presented in the paper.

We applied this method to compute α between the J and K_s bands, the H and K_s bands, the J and H bands, and across all three bands together. We defined for each star a $\chi^2 = \sum((band_{measured} - band_{model})/\sigma_{band})^2$ and searched for the parameters that minimised it.

RC stars in the high-extinction group

We applied the method to the RC stars with observed colours between $J - K_s > 5.2$ and $J - K_s < 6$. The histograms of the optimal values of α and $A_{1.61}$, along with Gaussian fits, are shown in Figs. 7.4 and 7.5, respectively. The statistical uncertainty is given by the error of the mean of the approximately Gaussian distributions and is negligibly small. We considered the systematic uncertainties due to the uncertainties in the temperature of the assumed model, its metallicity, the atmospheric humidity, the distance to the GC, the radius of the RC stars, and the systematics of the photometry. We re-computed the values of $A_{1.61}$ and $\alpha_{wavelength\_range}$ varying individually the values of each of these factors:

- For the model temperature we took two models with 4,500 K and 5,000 K. That range takes into account the possible temperature variation for the RC (Bovy et al., 2014).
- For the metallicity we took five values in steps of 0.5 from -1 to +1 dex.
- For the humidity we varied the amount of precipitable water vapour between 1.0, 1.6, and 3.0 mm.
- For the distance to the GC, we used 7.75, 8.0 and 8.25 kpc.
- We varied the stellar radius between 9.5, 10 and 10.5.

- We took three different values for the $\log g$ used in the Kurucz model: 2.0, 2.5, and 3.0.
- Finally, we tested the effect of the variation of the systematics of the photometry for every band independently, subtracting and adding the systematic uncertainty to all the measured values.

The largest errors arise from the uncertainty in the radius of the RC stars and the temperature of the models. The final systematic uncertainty was computed by summing quadratically all the individual uncertainties. Table 7.1 lists the values of α and $A_{1.61}$ we obtained along with their uncertainties. We can see that α_{JH}, α_{HK_s}, α_{JK_s} , and α_{JHK_s} are consistent within their uncertainties. On the other hand, we obtained very similar values for $A_{1.61\_JH}$, $A_{1.61\_HK_s}$, $A_{1.61\_JK_s}$, and $A_{1.61\_JHK_s}$ to what we expected because we used the same stars to compute them.

Table 7.1 Values of α and $A_{1.61}$ obtained with the grid method.

	Bands	α	$A_{1.61}$
High extinction	JH	2.45 ± 0.09	3.91 ± 0.16
	HK_s	2.23 ± 0.14	3.91 ± 0.15
	JK_s	2.34 ± 0.09	4.02 ± 0.20
	JHK_s	2.32 ± 0.09	3.98 ± 0.18
Low extinction	JH	2.41 ± 0.11	3.30 ± 0.16
	HK_s	2.19 ± 0.16	3.30 ± 0.15
	JK_s	2.28 ± 0.11	3.40 ± 0.19
	JHK_s	2.33 ± 0.10	3.36 ± 0.17
All RC stars	JH	2.44 ± 0.10	3.62 ± 0.16
	HK_s	2.21 ± 0.14	3.61 ± 0.16
	JK_s	2.31 ± 0.10	3.72 ± 0.20
	JHK_s	2.34 ± 0.09	3.67 ± 0.17

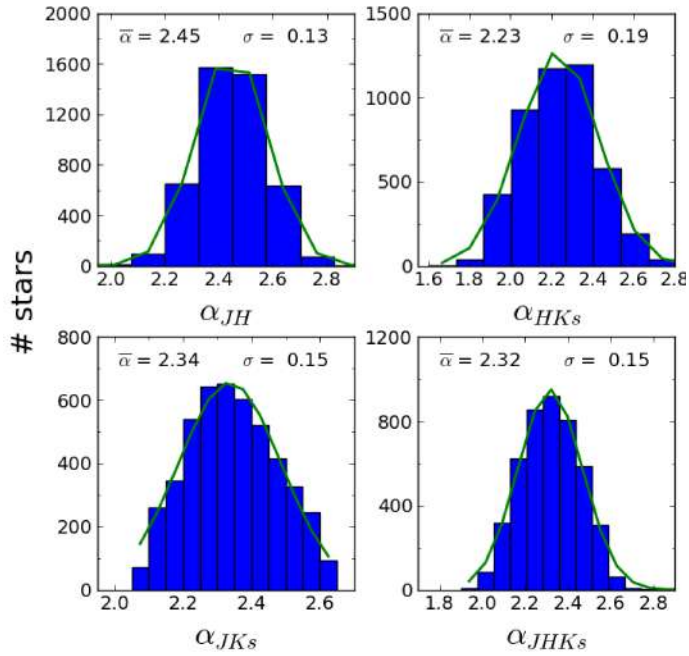

Fig. 7.4 Histograms of α computed with the grid method for the RC stars in the high-extinction group. Gaussian fits are overplotted as green lines, with the mean and standard deviations annotated in the plots.

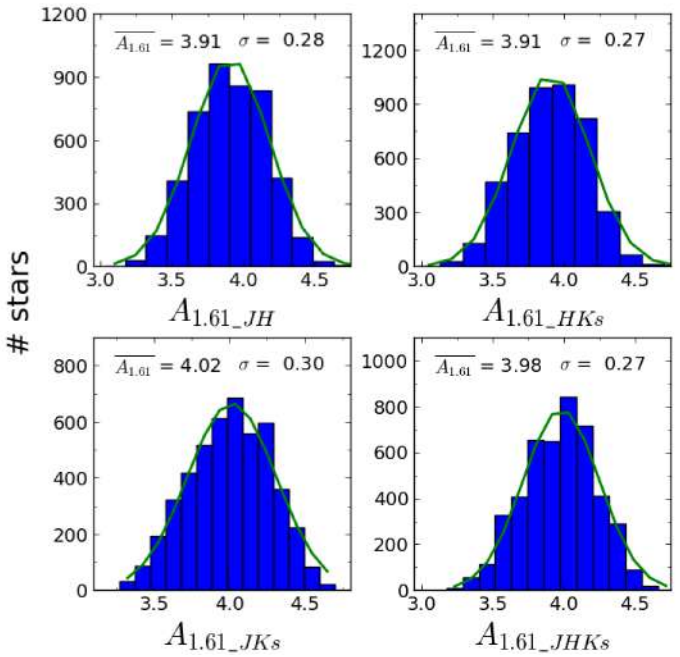

Fig. 7.5 Histograms of $A_{1.61}$ computed with the grid method for the RC stars in the high-extinction group. Gaussian fits are overplotted as green lines, with the mean and standard deviations annotated in the plots.

RC stars in the low-extinction group

We also applied this method to the RC stars located in front of the dark clouds, $J-K_s > 4.0$ and $J-K_s < 5.2$. Analogously, the main source of error is the systematic uncertainty, and statistical uncertainties given by the error of the mean are negligible. The Gaussian fits for the extinction index and $A_{1.61}$ for JH, HK_s, JK_s, and JHK_s are presented in Figs. 7.6 and 7.7. Table 7.1 shows the results for the fits and the corresponding uncertainties.

All RC stars, JHK$_s$

We also applied the previously described method to all the RC stars ($J-K_s > 4$ and $J-K_s < 6$), using JHK_s measurements. We thus obtain the extinction index simultaneously for low-extinction regions and for regions dominated by dark clouds. The results are shown in Figs. 7.8, 7.9 and 7.10. The mean values of the Gaussian fit and their uncertainties (dominated by systematics) are presented in Table 7.1. It can be seen that the mean and standard deviation of the histogram of the extinction indices agree very well with the values obtained for the two RC populations analysed before (Table 7.1). In the case of α_{JHK_s} and $A_{1.61\_JHK_s}$, a Gaussian fit for both gives a mean value of $\alpha_{JHK_s} = 2.34 \pm 0.09$ and $A_{1.61\_JHK_s} = 3.67 \pm 0.17$.

On the other hand, the extinction shows a broader distribution that extends to values $A_{1.61} < 3.4$. We fitted a combination of two Gaussians and compared it with the single Gaussian fit. For that, we used the SCIKIT-LEARN python object GaussianMixture, which implements the expectation-maximisation algorithm to fit a mixture of Gaussian models (Pedregosa et al., 2011). Computing the Bayesian Information Criterion (Schwarz, 1978) and the Akaike Information Criterion (Akaike, 1974), we checked that a combination of two Gaussians provides a significantly better fit than using a single Gaussian. In the case of $A_{1.61\_JHK_s}$, the mean values of the two Gaussians are $A_1 = 3.32 \pm 0.20$ and $A_2 = 3.88 \pm 0.20$, with a standard deviation of $\sigma_1 = 0.37$ and $\sigma_2 = 0.29$, respectively. Again, the uncertainties are dominated by the systematics. It is remarkable that the systematic uncertainties do not change the relative position of the two mean extinctions detected, since they affect both in the same direction. The mean extinctions A_1 and A_2 correspond to the low and highly reddened population. The results agree with their previously determined values based

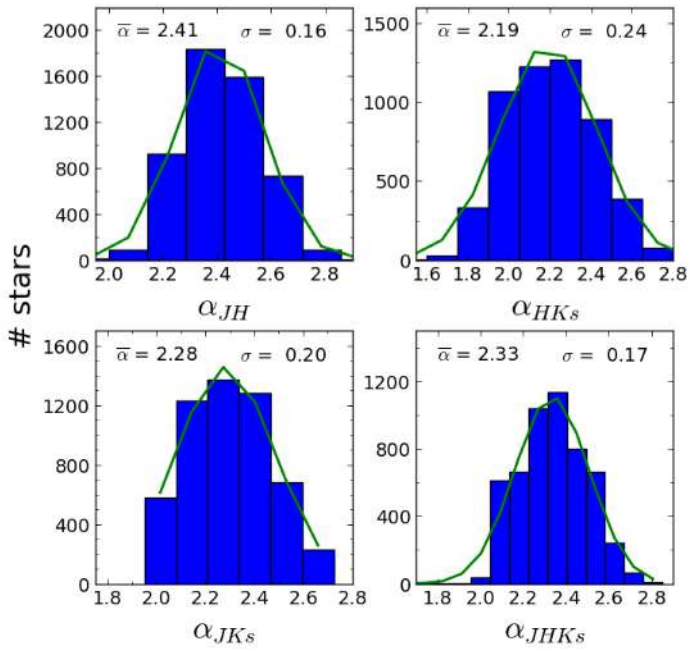

Fig. 7.6 Histograms of α computed with the grid method for the low-extinction group of RC stars. Gaussian fits are overplotted as green lines, with the mean and standard deviations annotated in the plots.

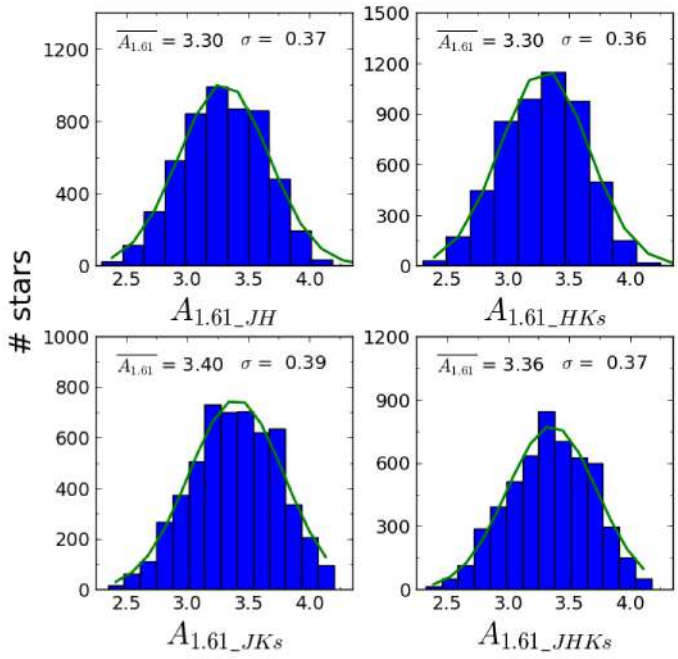

Fig. 7.7 Histograms of $A_{1.61}$ computed with the grid method for the low-extinction group of RC stars. Gaussian fits are overplotted as green lines, with the mean and standard deviations annotated in the plots.

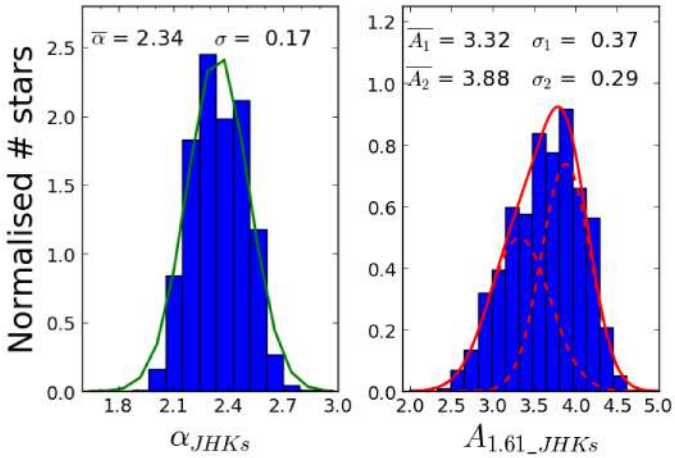

Fig. 7.8 Normalised histograms of α_{JHK_s} and $A_{1.61}$ computed with all the RC stars using the grid method. The green line shows a Gaussian fit for the extinction index. The red continuous line depicts a two Gaussian fit (with the individual Gaussians marked by the red dashed lines).

exclusively on each population independently. This indicates that the method is able to estimate α_{bands} and $A_{1.61\_bands}$ independently of the selected range of colour or extinction, distinguishing stars with different extinction. We repeated the procedure described above for JH, HK_s , and JK_s and found that the extinctions are compatible with a two-Gaussian model and the extinction index value is in agreement with one single α_{JHK_s} within the uncertainties of our study (Figs. 7.9 and 7.10).

The values of the extinction indices and extinctions agree within their uncertainties. However, it is noticeable that we have found a slightly steeper value for α_{JH} than for α_{HK_s}. Although the difference between those values is covered by the given uncertainties, the relative uncertainty between them is slightly lower. Namely, the variations in the temperature of the model, $\log g$, the radius of the RC stars, their metallicity, and the distance to the GC produce a systematic uncertainty in the same direction for all the values computed. Therefore, we found a small difference between the extinction index depending on the wavelength in the studied ranges. This difference will be studied in detail in the next sections.

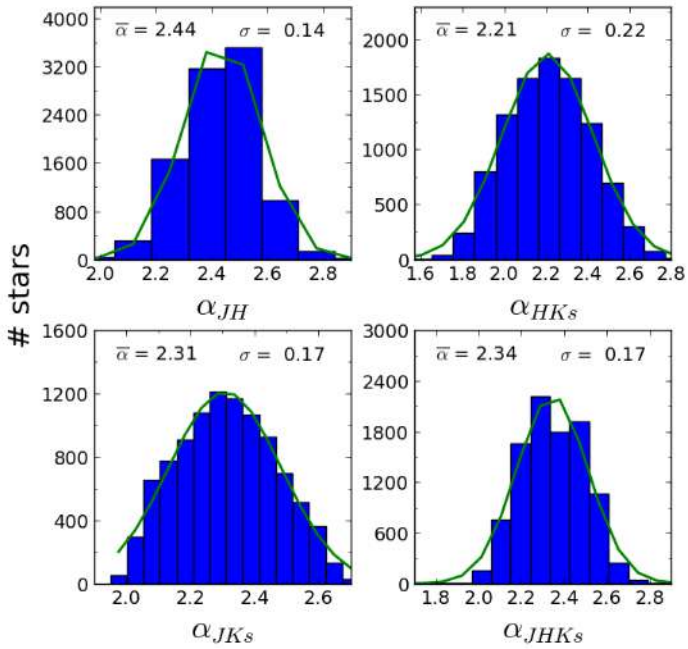

Fig. 7.9 Histograms of α computed with the grid method for all the RC stars. Gaussian fits are overplotted as green lines, with the mean and standard deviations annotated in the plots.

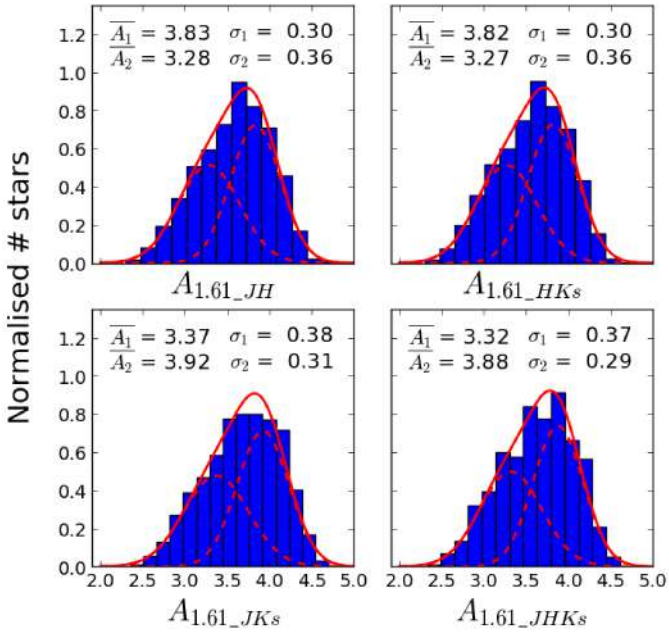

Fig. 7.10 Normalised histograms of $A_{1.61}$ computed with the grid method for all the RC stars. The red continuous line shows two-Gaussian fits and the red dashed lines show the individual Gaussians of the fit. The mean and standard deviations of the fits are annotated in the plots.

Spatial distribution of α

We studied the spatial variability of the extinction index, using the individual values obtained for all the RC stars in the previous section. To do that, we produced a map calculating for every pixel the corresponding value of α_{JHK_s}. To save computational time, we defined a pixel size of 100 real pixels ($\sim 5''$). The value for every pixel was obtained averaging (with a two-sigma criterion) the extinction indices obtained for all the stars located within a radius of $1'$ from its centre. The obtained map presents very small variations depending on the region, varying between $\alpha_{JHK_s} = 2.30$ and 2.38. Fitting with a Gaussian, we obtained a mean value of $\alpha_{JHK_s} = 2.35$ for all the pixels with a standard deviation of 0.03. We concluded that if there exists variation across the studied field, it is negligible. Therefore, we can assume that the extinction index does not vary with the position.

7.3.2 Fixed extinction

As a first estimation, a constant α from λ_J to λ_{K_s} can be assumed. Here, we use RC stars identified in all three bands to compute for each of them their corresponding α. To do that, we use the following expression:

$$\frac{\left(\frac{\lambda_H}{\lambda_J}\right)^{\alpha} - 1}{1 - \left(\frac{\lambda_H}{\lambda_{K_s}}\right)^{\alpha}} = \frac{J - H - (J-H)_0}{H - K_s - (H-K_s)_0}, \tag{7.2}$$

where λ_i refers to the effective wavelengths in each band, α is the extinction index, J, H, and K_s are the observed magnitudes in the corresponding bands, and the sub-index 0 indicates intrinsic colours (see Appendix B).

To compute the effective wavelength, λ_{eff}, and the intrinsic colours, we used as starting values the α and the $A_{1.61}$ calculated in Section 7.3.1 (as explained in Appendix A). We kept $A_{1.61}$ constant, but updated iteratively the values of λ_i and, subsequently, of α. After several iterations, the results converged. The systematic uncertainties were estimated via MonteCarlo (MC) simulations taking into account the uncertainties of the intrinsic colours, the zero points, and the effective wavelengths.

RC stars in the high-extinction group

We used the RC stars identified in the high-extinction group with $J - K_s > 5.2$ to compute the extinction index. The resulting histogram of α for all the stars is shown in Fig. 7.11. We obtained a value of $\alpha_{JHK_s} = 2.33 \pm 0.17$, where the systematic error is the main source of uncertainty and the statistical uncertainty is negligible.

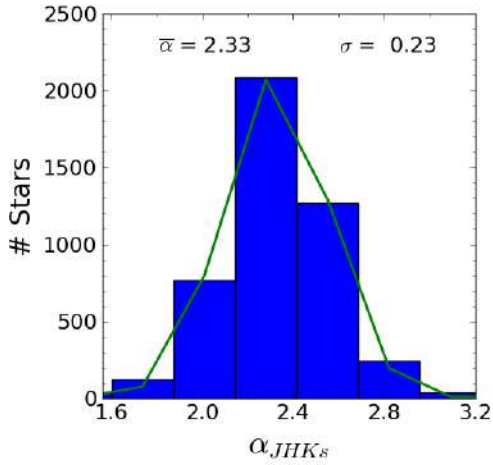

Fig. 7.11 Distribution of the extinction index for the RC stars in the high-extinction group ($5.2 < J - K_s < 6$) computed using Eq. 7.2. The green line shows a Gaussian fit, with the mean and standard deviation indicated in the legend.

Spatial distribution of α

As the RC stars that we employed were well distributed across the field, we used this method to test again the constancy of the extinction index for different positions. We selected several thousands of random regions of $1.5'$ radius to cover the entire field. We computed the mean α for every region and then studied the resulting distribution of values. This distribution can be described by a quasi-Gaussian distribution with a mean value of 2.35 and a small standard deviation of 0.03. This supports the notion that α can be considered independent from the position in the field.

Extinction towards dark clouds

Since this method computes the extinction index based on individual stars, it is appropriate to study the stars that appear in front of dark clouds. To do that, we used the RC stars with $J-K_s < 5.2$ (the ones on the left part of the red line in Fig. 7.2) and assumed the extinction derived for this group in Section 7.3.1. We obtained a value of $\alpha = 2.43 \pm 0.22$, where the statistical uncertainty given by the error of the mean is negligible and the systematics uncertainties are the main source of error. Figure 7.12 shows the corresponding distribution. The slightly higher extinction index for the low-extinction stellar group can be explained by the assumption of a constant $A_{1.61}$ that suffers from systematic uncertainties. That was taken into account for the error estimation and both values agree within their uncertainties.

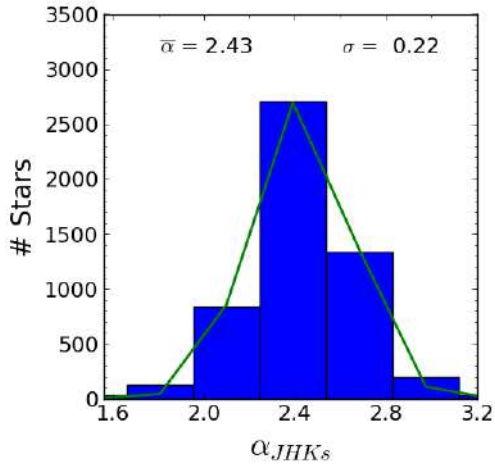

Fig. 7.12 Distribution of the extinction index for the RC stars in the low-extinction group ($4.0 < J-K_s < 5.2$) computed using Eq. 7.2. The green line shows a Gaussian fit, with the mean and standard deviation indicated in the legend.

7.3.3 Colour-colour diagram

Studying the extinction index using a colour-colour diagram (CCD) removes the distance effects and arranges the RC stars in a line that follows the reddening vector. For this method, we assume that the extinction curve does not depend on extinction,

which is supported by the tests in the preceding sections. By using RC stars across a broad range of extinction, a wider colour range can be used that reduces the uncertainty of the fit. Therefore, we selected RC stars with $H-K_s \in [1.4, 2.0]$ and $J-H \in [2.8, 4.0]$. To compute the extinction index, we used the slope of the RC stars's distribution in a $J-H$ versus $H-K_s$ CCD. We divided the cloud of points in the CCD into bins of 0.03 mag width on the x-axis. In every bin, we used a Gaussian fit to estimate the corresponding density peak on the y-axis. The slope of the RC line and its uncertainty were subsequently computed using a Jackknife resampling method. Finally, we applied Eq. 7.2 to calculate the value of α_{JHK_s}. To compute the effective wavelengths, which depend on the absolute value of extinction, we assumed the value obtained with the Gaussian fit in Fig. 7.8.

The final result was obtained after reaching convergence through several iterations that updated the values of λ_i and α_{JHK_s}. We obtained $\alpha_{JHK_s} = 2.23 \pm 0.09$, where the uncertainty takes into account the formal uncertainty of the fit and the error due to the effective uncertainty of the wavelength. If we omitted the bluest points, where the number of stars was lower, and repeated the fit, then we obtained a value of $\alpha_{JHK_s} = 2.29 \pm 0.09$ as shown in Fig. 7.13. In both cases, the agreement with the other methods is good.

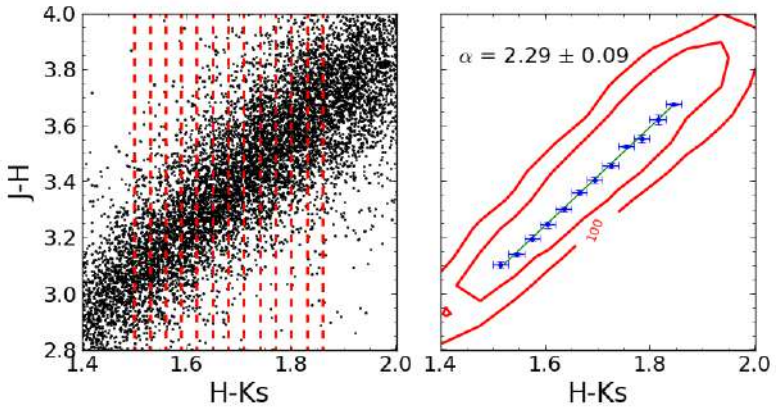

Fig. 7.13 Calculation of α_{JHK_s} using the distribution of the RC stars in the CCD. Left panel shows the cloud of points and the bins used to computed the slope. Right panel depicts the obtained points using the bins. The green line is the best fit and red contours depict the density distribution of the cloud of points.

7.3.4 Obtaining α using known late-type stars

We computed the extinction index using late-type stars whose near-infrared K-band spectra, metallicities, and temperatures are known (Feldmeier-Krause et al., 2017). Those stars are distributed in the central 4 pc^2 of the Milky Way nuclear star cluster, corresponding to the central region of our catalogue. We cross-identified those stars with our catalogue and excluded stars with a photometric uncertainty < 0.05 in any single band. We also excluded variable stars. For the latter purpose, we compared our F1 HAWK-I K_s -band photometry with the photometry from the pilot study (Sec. 3.1). In that way we excluded several tens of stars that are possible variable candidates. Finally, we found 367 stars for the subsequent analysis.

Variable extinction

Stars whose stellar type is known let us study in detail the dependance of the extinction index on the wavelength. We used a slightly modified version of the grid method described in Section 7.3.1 to overcome the unknown radius of each used star. In this case, we defined a new $\chi^2 = \sum(colour_{measured} - colour_{model})^2/\sigma^2_{colour}$. With this approach, we do not need to know either the distance to the star or its radius.

For each star we assumed the appropriate stellar atmosphere model. We used Kurucz models because of their wide range of metallicities and temperatures, which was necessary to analyse properly the data. We varied the metallicity in steps of 0.5 dex from -1 to 1 dex. The temperature of the models was 3,500 K, 4,000 K, and 4,500 K, consistent with the uncertainty in temperature for each star (~ 200 K in average). Because the lower limit for the model temperatures was 3,500 K, we deleted ten stars that were not covered by any model.

Because this method has only one known variable, the colour, we cannot compute simultaneously the extinction and the extinction index. Thus, we computed the individual extinction of each star using the measured colour $J - K_s$. We minimised the difference between the data and the theoretical colour obtained using the appropriate Kurucz model (taking into account the metallicity and the temperature) and a grid of extinctions, $A_{1.61}$, with a step of 0.01 mag. For that, we used the extinction index derived in Sect. 7.3.1. We obtained a quasi-Gaussian distribution for the extinction that is shown in the left panel of Fig. 7.14. The systematic uncertainty

dominates the errors whereas the statistical uncertainty is negligible. We computed the systematics taking into account the variation of the extinction index (using the uncertainties computed in Sect. 7.3.1), the systematic uncertainty of the ZP, and different amounts of precipitable water vapour (1.0, 1.6 and 3.0 mm). We ended up with a mean extinction of $A_{1.61} = 4.28 \pm 0.18$. We used $J - K_s$ because to convert colour into extinction, we need to assume a value of α to compute the grid of individual extinctions and, for that wavelength range, the value is similar to the one obtained assuming a constant extinction index for all the three bands (see Sect. 7.3.1) and we do not need to assume different values for the ranges $J - H$ and $H - K_s$. In this way, we computed the extinction for each star and fixed it to compute the extinction index. Figure 7.15 and Table 7.2 summarise the obtained results. The statistical uncertainties, given by the error of the mean, are negligible, and the systematic uncertainties are the main source of error. To compute them, we took into account the systematics introduced by the zero points, the initial α used to translate the colour $J - K_s$ into extinction, and the humidity of the atmosphere.

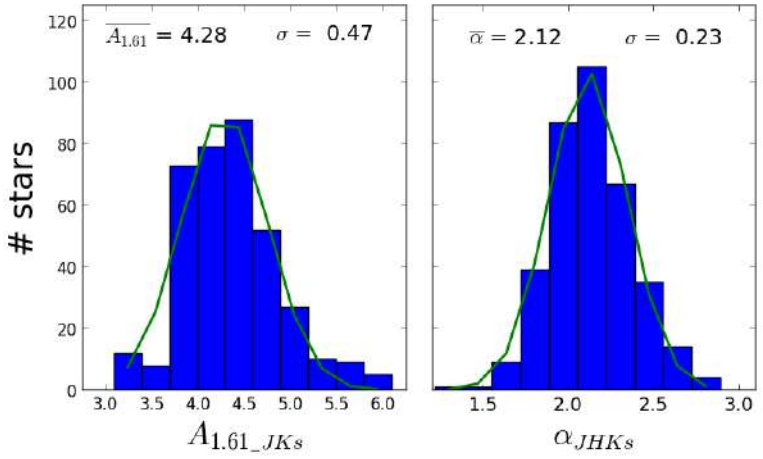

Fig. 7.14 Left panel: $A_{1.61}$ distribution computed individually for each spectroscopically studied late-type star. Right panel: α estimated using the fixed extinction method for the same stars. The green line shows a Gaussian fit, with the mean and standard deviation indicated in the legend.

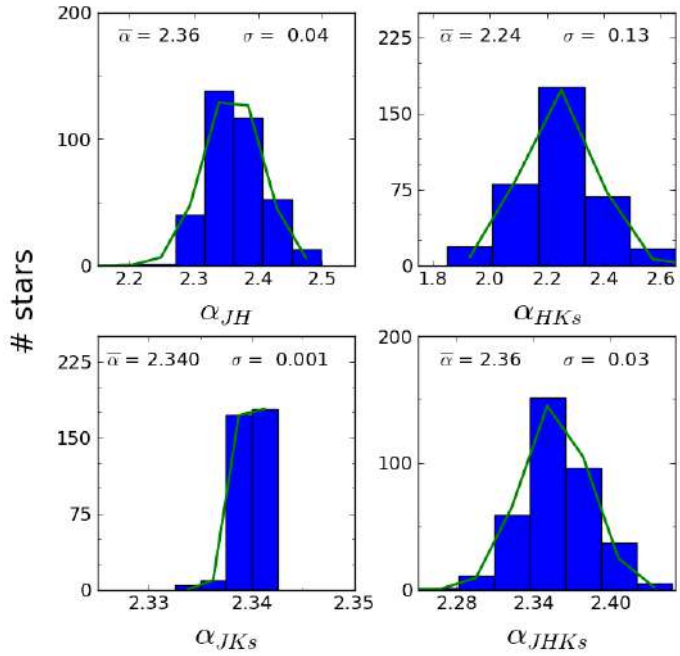

Fig. 7.15 Histograms of α computed with the modified grid method for known late-type stars. Gaussian fits are overplotted as green lines, with the mean and standard deviations annotated in the plots.

Fixed extinction

We employed the same approach described above (Sect. 7.3.2). In this case, we used the fixed extinction given by the Gaussian fit shown in Fig 7.14 (left panel). To obtain the final α_{JHK_s}, we used an iterative approach updating the value of the extinction index obtained in every step until reaching convergence. To start the iterations we used the extinction index derived in Sect. 7.3.1. The resulting distribution of α_{JHK_s} is shown in Fig. 7.14 (right panel). The estimation of the systematic uncertainty was carried out considering the systematics of the ZP, the possible variation of the fixed extinction, and different amounts of precipitable water vapour (1.0, 1.6 and 3.0 mm). The final result was $\alpha_{JHK_s} = 2.12 \pm 0.14$, which is in agreement with all the previous estimates. The slightly lower extinction index obtained can be explained

Table 7.2 Values of α obtained with the modified grid method for known late-type stars.

	Bands	α
	JH	2.36 ± 0.08
Known	HK_s	2.24 ± 0.16
late-type	JK_s	2.34 ± 0.09
	JHK_s	2.35 ± 0.08
	JH	2.36 ± 0.08
Known	HK_s	2.24 ± 0.13
early-type	JK_s	2.34 ± 0.09
	JHK_s	2.36 ± 0.08

by the assumption of a constant $A_{1.61}$, which suffers from systematic uncertainties. That was taken into account in the uncertainty estimation.

7.3.5 Computing the extinction index using early-type stars

We used again the same methods described in Sect. 7.3.4 to compute the extinction index towards known hot, massive stars near Sgr A* (Do et al., 2009). We used the data from the pilot study, which cover the central region far better than the F1 data. We excluded known Wolf-Rayet stars (Do et al., 2009; Feldmeier-Krause et al., 2015; Paumard et al., 2006) because they are frequently dusty and therefore intrinsically reddened. To avoid spurious identifications because of the high crowding of the region, we only used stars with $11.2 \leq K_s \leq 13$. We used the published NACO K_s magnitudes (approximately equivalent to the HAWK-I K_s band) and compared them with our HAWK-I data applying a $3-\sigma$ exclusion criterion to delete any possible variable stars. Finally, we excluded stars with photometric uncertainties larger than 0.05 mag in any single band. We ended up with 23 accepted stars for the analysis.

Variable extinction

As described in Sect. 7.3.4, we applied the modified grid method and computed the individual extinction to each star to analyse the variation of the extinction index with the wavelength. We used a 30,000 K model, a solar metallicity, a $\log g = 4.0$, and a humidity of 1.6 mm of precipitable water vapour. The uncertainties were estimated using the error of the mean of the quasi-Gaussian distribution and varying the parameters previously described to obtain the systematics. The final mean value is $A_{1.61\_JK_s} = 4.61 \pm 0.20$, where 0.13 and 0.16 correspond to the statistical and systematic uncertainties. Figure 7.16 (left panel) shows the obtained results. Figure 7.17 and Table 7.2 present the obtained results for the modified grid method.

We found again the variation in the extinction index that we already noticed in Sect. 7.3.1. This supports the evidence of having a steeper extinction index between J and H than between H and K_s. However, the difference between the extinction indices and the uncertainties that we found is not enough to clearly distinguish two different values. Therefore, we estimate that, in spite of being different, their close values make necessary a deeper analysis with better spectral resolution or wide wavelength coverage, to clearly distinguish them. Within the limits of the current study, we assume that a constant extinction index is enough to describe the extinction curve between the analysed bands.

Fixed extinction

A Kurucz model with a temperature of 30,000 K and solar metallicity was taken to compute α_{JHK_s}. We used the mean value obtained above and presented in Fig. 7.16 (left panel). The result is shown in Fig. 7.16 (right panel). The systematic uncertainty dominates the error and was computed using MC simulations considering the uncertainties in the ZP calibration of all three bands, the effective wavelength, and the intrinsic colour of $J-H$ and $H-K_s$. The final value was $\alpha_{JHK_s} = 2.19 \pm 0.13$, which is consistent with the values determined by the other methods.

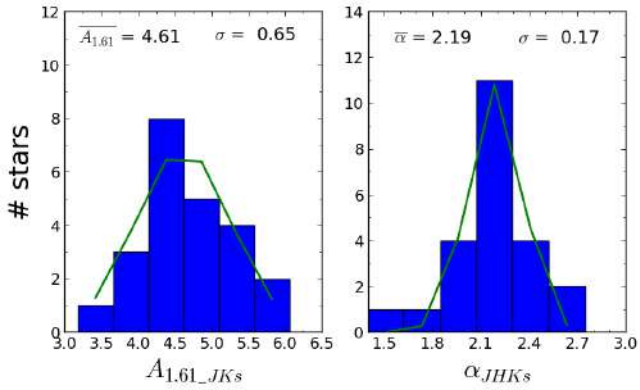

Fig. 7.16 Left panel: $A_{1.61}$ distribution computed individually for each spectroscopically studied early-type star. Right panel: α estimated using the fixed extinction method for the same stars. The green line shows a Gaussian fit, with the mean and standard deviation indicated in the legend.

7.3.6 Final extinction index value and discussion

Given our results from all the different methods to estimate the extinction index on our data, we can conclude that all the derived values of α agree within their uncertainties and that there is no evidence - within the limits of our study - for any variation of α with position, or absolute value of interstellar extinction. On the other hand, we observed a small dependence with the wavelength when we considered different values for α_{JH} and α_{HK_s}. However, a constant extinction index, α_{JHK_s} , seems to be sufficient to describe the extinction curve. We average all the values obtained with the different methods explained above and obtain a final value $\alpha_{JHK_s} = 2.30 \pm 0.08$, where the uncertainty is given by the standard deviation of the measurements, which takes into account the dispersion of the values obtained using the different methods.

To check the reliability of the obtained value for the extinction index, we used all the RC stars identified in Fig. 7.1 and computed their radii using the individual extinction for each star and the derived extinction index. We used the colour $J - K_s$ to calculate the individual extinctions employing the grid approach described in Sect. 7.3.4. Then, we computed the corresponding radius for each star assuming the final

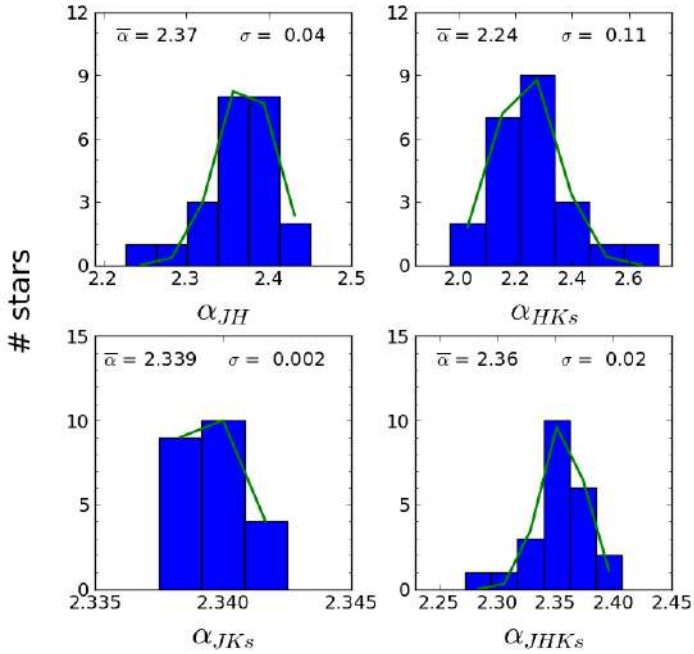

Fig. 7.17 Histograms of α computed with the modified grid method for known early-type stars. Gaussian fits are overplotted as green lines, with the mean and standard deviations annotated in the plots.

extinction index, the GC distance (8.0 kpc, (Malkin, 2013)) and a Kurucz model for Vega to convert the fluxes into magnitudes. We obtained the radius by comparing the obtained value with the measured K_s of each star. Figure 7.18 depicts the obtained individual extinctions (left panel) and the derived radius (right panel). We obtained a value of $A_{1.61} = 3.78 \pm 0.15$ and $r = 10.03 \pm 0.57\ R_{\odot}$, where the error is dominated by the systematic uncertainty. The comparison between the obtained extinction and the one computed in Sect. 7.3.1, and shown in Fig. 7.8, is consistent. Moreover, we have obtained a mean radius for the RC stars that agrees perfectly with the standard value of 10.0 ± 0.5 R$_{\odot}$ (Chaplin & Miglio, 2013; Girardi, 2016). Therefore, we conclude that the computed values for the extinction and the extinction index are consistent and let us calculate the radius of the RC stars obtaining an accurate value.

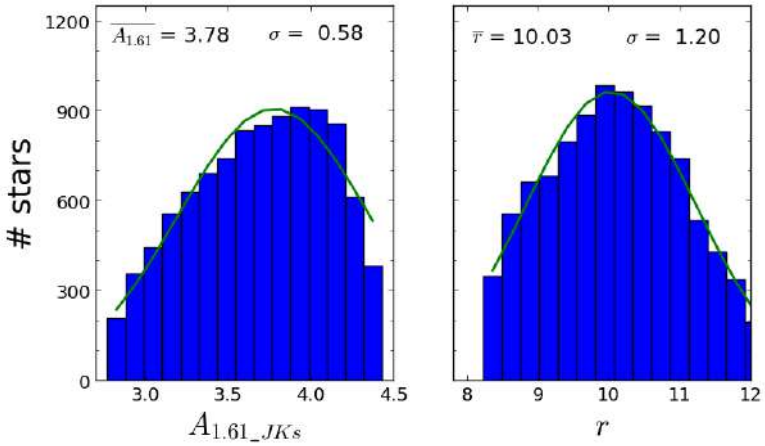

Fig. 7.18 Left panel: $A_{1.61\_JK_s}$ distribution computed for all the RC stars. Right panel: radii distribution of the RC stars (in solar radii). The green line shows a Gaussian fit, with mean and standard deviation indicated in the legend.

7.4 A high angular resolution extinction map

To produce an A_{K_s} extinction map, we removed all the foreground population and kept only the RC stars indicated by the parallelogram in Fig. 7.1 and detected in H and K_s bands. The observed colours were converted into extinction using the colour $H-K_s$ (as we have far more stars detected in H and K_s than in J) and the following equation:

$$ext = \frac{H-K_s-(H-K_s)_0}{\left(\frac{\lambda_H}{\lambda_{K_s}}\right)^{-\alpha}-1} \quad , \tag{7.3}$$

where the subindex 0 refers to the intrinsic colour and λ_i are the effective wavelengths.

To save computational time, we defined a pixel scale of 0.5”/pixel for the extinction map. For every pixel, we computed the extinction using the colour of the ten closest stars, limiting the maximum distance to 12” from its centre. If less than ten stars were found for a pixel, we did not assign any extinction value to avoid obtaining strongly biased values due to too distant stars. To take into account the different distances of the stars to every pixel, we computed the colour using an inverse distance

weight (IDW) method. Namely, we weighted every star based on the distance to the corresponding pixel following the expression:

$$v = \frac{\sum_{i=1}^{n} \frac{1}{d_i^p} v_i}{\sum_{i=1}^{n} \frac{1}{d_i^p}} \quad , \tag{7.4}$$

where v is the magnitude to be computed in the target pixel, d is the distance to that pixel, v_i are the known values, and p is the weight factor. We explored different values for p and ended up with $p = 0.25$ as the best estimate to avoid giving too much weight to the star closest to the pixel centre.

The uncertainty of the extinction map was computed estimating the colour uncertainty of every pixel, using a Jackknife algorithm in the calculation of the IDW. The resulting extinction map and its corresponding uncertainty map are shown in Fig. 7.19. The mean uncertainty is $\sim 5\%$. Besides, we estimate a systematic error of $\sim 5\%$, which takes into account the uncertainties of the effective wavelengths and the extinction index.

Due to the fact that the extinction can vary on scales of arc seconds, we tried to improve the extinction map using not only the RC stars, but all stars with K_s between 12 and 17, and $H - K_s$ between 1.4 and 3.0. In this way, we almost duplicate the number of selected stars, improving significantly the angular resolution of the map. To compute the intrinsic colour of every star, we assumed that the majority of the used stars can be considered as giants. We calculated the K_s reddened magnitude of several Kurucz models of giants (assuming an average extinction of 3.67 magnitudes at 1.61 μm, see Sect. 7.3.1) and their intrinsic colour. We interpolated the points to build a smooth function that gives the intrinsic colour based on the measured K_s magnitude (see Fig. 7.20). The resulting extinction map and its corresponding uncertainty map are shown in Fig. 7.21. It can be seen that it is very similar to Fig. 7.19, but with a higher angular resolution. The statistical and systematic uncertainties are similar as well.

With this approach, we generated, in addition, two more extinction maps taking into account the two groups of stars that we identified in Sect. 7.2. Namely, we produced the first map using stars with $1.4 < H - K_s < 1.7$ (Fig. 7.22, upper panel) and the second one with stars between $1.7 < H - K_s < 3.0$ (Fig. 7.22, lower panel).

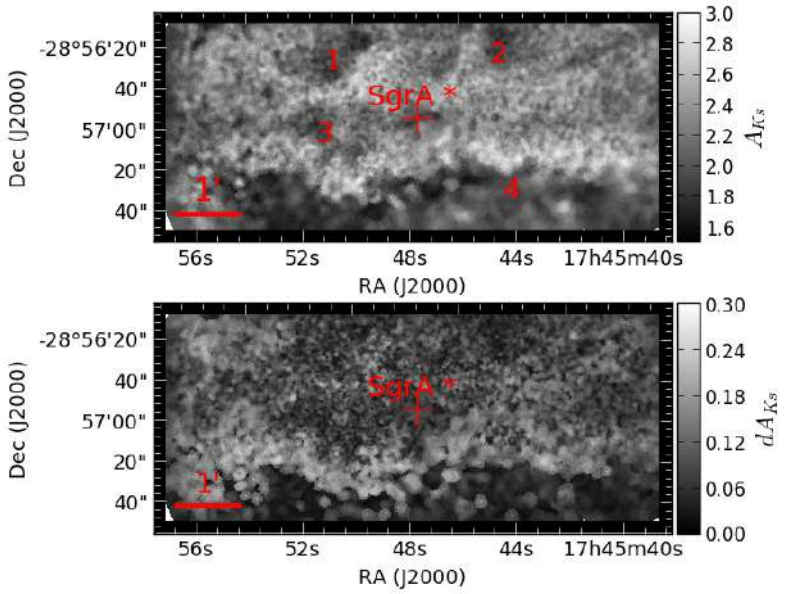

Fig. 7.19 Upper panel: Extinction map A_{K_s} obtained using all the RC stars shown in Fig. 7.1. Lower panel: Corresponding uncertainty map. The numbers in red indicate regions to be compared between the different extinction maps (see main text).

In this way, the first map represents the extinction screen toward the foreground population (excluding stars in the spiral arms), whereas the second one includes the interstellar extinction all the way toward GC stars. Although the first map does show some correlation with the second map (e.g. in regions 1, 2, 3) because it is impossible to separate the two stellar populations without any overlap, it shows a rather constant extinction, with a mean of 1.72 and a standard deviation of 0.06. This demonstrates that this foreground screen can be considered to vary on very large scales. The statistical and systematic uncertainties for this first extinction map are ~ 2 % and ~ 6 % respectively. In this case the uncertainty is lower because we consider a narrower range in $H - K_s$ and all the stars are closer without mixing stars with different extinctions. On the other hand, the second map contains fine structure on scales of just a few arcseconds, which is consistent with the extinction being caused by a clumpy medium close to the GC. The statistical and systematic uncertainties of the map are ~ 4% and ~ 5 % respectively.

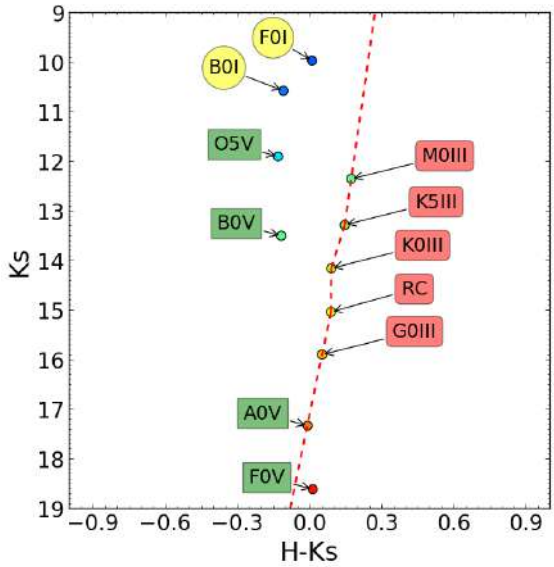

Fig. 7.20 Reddened observed magnitude (assuming a distance modulus of 14.51 and a mean extinction $A_{1.61} = 3.67$) versus intrinsic colour for several types of stars computed using Kurucz models. The red dashed line indicates the intrinsic colours used for the stars selected to compute the extinction map.

When comparing the extinction map in the lower panel of Fig. 7.22 with the J-band density plot (Fig. 7.2), we can see that the high density regions, marked with numbers 1, 2, and 3, correspond to low extinction as we expected. However, while region 4 can be identified as a high-extinction region in the density plot, it appears as a low-extinction one in the lower panel of 7.22, but as a relatively high-extinction region in the upper panel. We interpret this as evidence for a large dark cloud with very high density that blocks most of the light from the stars behind it. This is also rather evident from inspecting a JHK_s colour image of our field (Fig. 7.23). We conclude that our method cannot produce reliable extinction maps for regions marked by the presence of highly opaque foreground clouds.

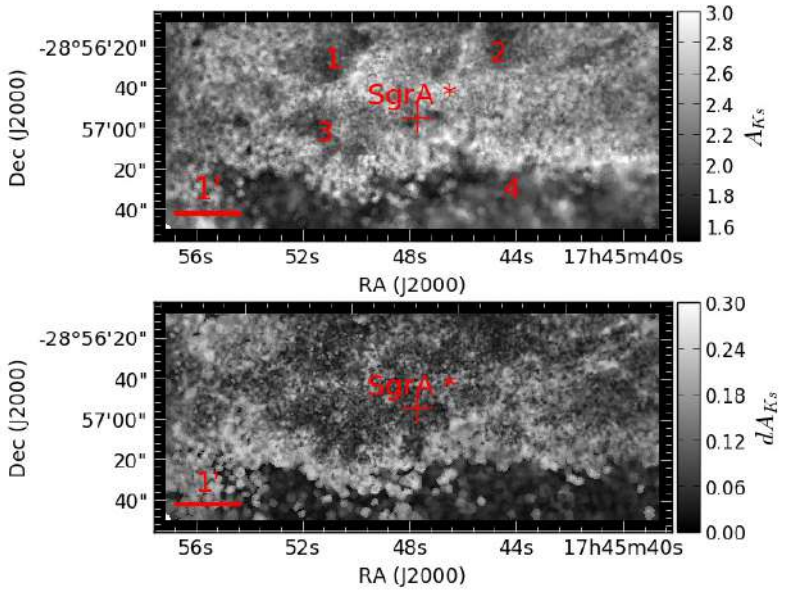

Fig. 7.21 Upper panel: Extinction map A_{K_s} obtained using stars with $12 < K_s < 17$ and $1.4 < H - K_s < 3.0$. Lower panel: Corresponding uncertainty map. The numbers in red indicate regions to be compared between the different extinction maps (see main text).

7.5 Stellar populations

7.5.1 CMDs

To obtain a rough idea of the stellar populations in Field 1 of our survey, we attempted to deredden the CMD. We transformed the A_{K_s} extinction maps into A_H using the RC effective wavelength and the extinction index of $\alpha_{JHK_s} = 2.30$, as determined by us. We used the two extinction maps computed previously according to the different $H - K_s$ colours. This enabled us to improve the dereddening process as we considered two different maps that correspond to two different layers in the line of sight. We used either one or the other, depending on the $H - K_s$ colour of a given star. The divisions were $1.4 < H - K_s < 1.7$ and $1.7 < H - K_s < 3.0$, which is similar to the $J - K_s$ cut in Fig. 7.3. Figure 7.24 shows the CMDs for K_s versus $H - K_s$ before and after de-reddening. Analogously, we repeated the process for J band but, in this case, we produced the extinction maps taking into account only stars identified

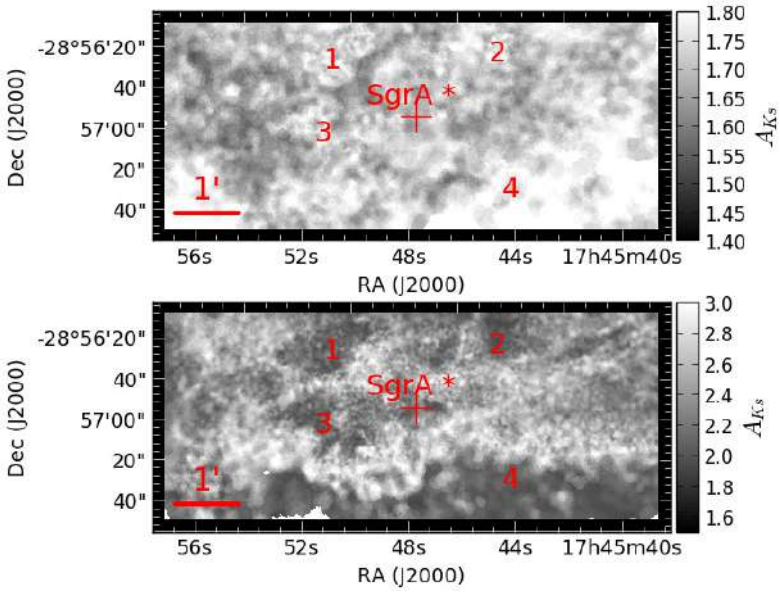

Fig. 7.22 Upper panel: Extinction map for stars with observed colours in the interval $1.4 < H - K_s < 1.7$. Lower panel: Extinction map for stars with observed colours in the interval $1.7 < H - K_s < 3$. The numbers in red indicate regions to be compared between the different extinction maps (see main text).

in all three bands, J, H, and K_s. By doing so, we obtain a consistent extinction map and avoid producing extinction maps biased towards too high extinction, as the completeness is higher in H and K_s than in J. Figure 7.25 depicts the CMD K_s versus $J - K_s$ before and after de-reddening. It can be seen that the extinction correction clearly reduces the scatter in the CMDs. On the other hand, we overplotted different Kurucz stellar models. The giant sequence follows clearly the main density ridge in both dereddened CMDs. In both cases, K_s versus $H - K_s$ and K_s versus $J - K_s$, the standard deviation of the dereddened colours around the giant branch is of the order of $\sigma = 0.2$.

7.5.2 CMD modelling

We overplotted three 5 Gyr isochrones (Marigo et al., 2017) with different metallicities (0.1,1 and 2.5 solar metallicity) to the CMD K_s versus $J - K_s$. In this way

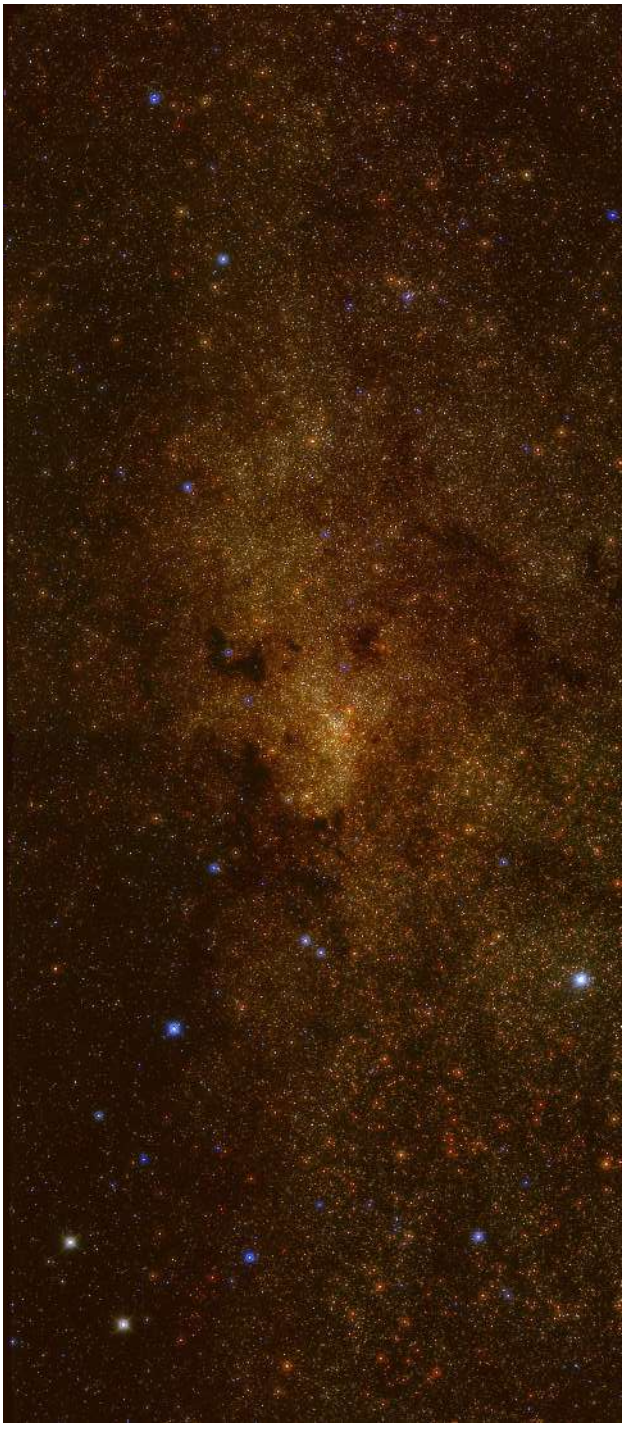

Fig. 7.23 RGB image of Field 1 (red for K_s, green for H, blue for J.)

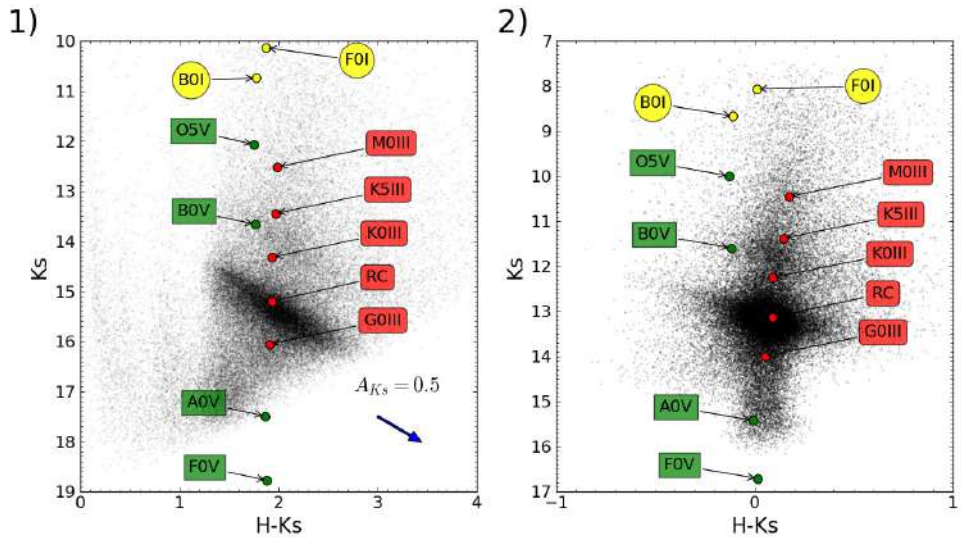

Fig. 7.24 Panel 1 shows the CMD K_s versus $H - K_s$. We have overplotted several Kurucz stellar models (assuming a mean extinction $A_{1.61} = 3.97$, see Sect. 7.3.1) to identify the expected position of those stars. Panel 2 depicts the dereddened map once we have applied the extinction maps. Both panels have different scales on the X-axis.

we are able to compare them with the stellar population. We can clearly see how a super-solar metallicity population fits better the data on the right hand side of the CMD. This is in particular indicated by the centring of the AGB bump. The RC bump appears to be centred at lower metallicities, but that is an effect of extinction and completeness, because the RC clump is cut off at the red end of the JK_s CMD. Therefore, a range of solar metallicities around the solar metallicity can explain the observed data. This is in agreement with the low number of low metallicity stars found in the central 4 pc^2 in Feldmeier-Krause et al. (2017). On the other hand, the scatter of the stars in the upper part of the diagram gives us an idea of the goodness of the extinction correction ~ 0.2, explaining the difference in comparison with the isochrones. This is the first study that infers the GC metallicity by using only photometric data.

The right panel of Fig. 7.26 shows a synthetic model population in comparison with the real data. The model assumes 2.5 solar metallicity and two different age

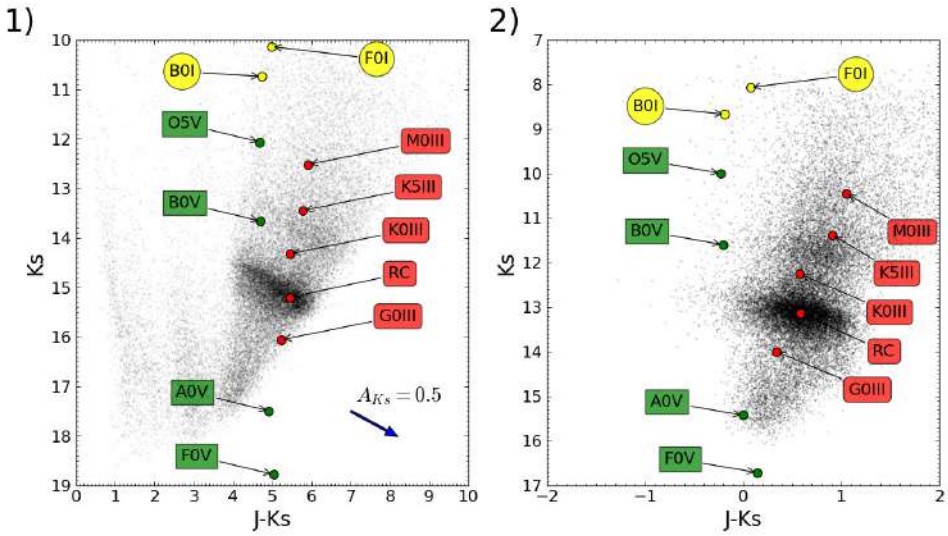

Fig. 7.25 Panel 1 shows the CMD K_s versus $J - K_s$. We have overplotted several Kurucz stellar models (assuming a mean extinction $A_{1.61} = 3.97$, see Sect. 7.3.1) to identify the expected position of those stars. Panel 2 depicts the dereddened map once we have applied the extinction maps. Both panels have different scales on the X-axis.

intervals, from 1 Gyr < t < 5 Gyr and from 5 Gyr < t < 12 Gyr. In both cases the star formation rate is constant over the time. The synthetic population was created analogously as described in Pfuhl et al. (2011), using the code of Aparicio & Gallart (2004) that used the stellar evolution library from Bertelli et al. (1994) and the bolometric correction library from Lejeune et al. (1997). It can be seen that taking into account the uncertainty that produces the scatter of around 0.2 mag, we are able to reproduce several features observed in the data like the RC bump or the AGB branch. Therefore, within the limits of the current study, we suggest that a solar or super-solar metallicity explains well the observed stellar distribution.

7.6 Results and discussion

Using the GALACTICNUCLEUS data of F1, we have used CMD to characterise the stellar population. We identify three stellar populations in the foreground, at

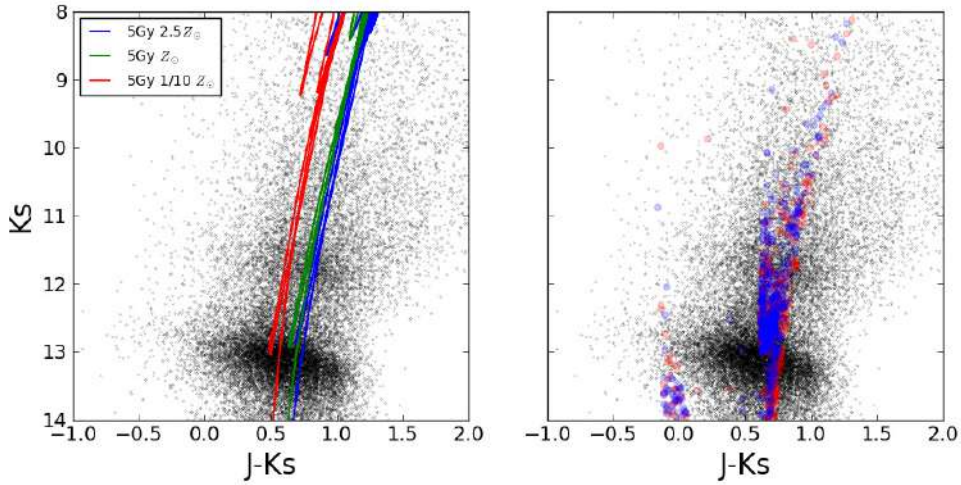

Fig. 7.26 Left panel depicts 5 Gyr stellar isochrones with different metallicities overlaid on the CMD K_s versus $J-K_s$. Right panel shows the comparison of the real data in the CMD K_s versus $J-K_s$ with a synthetic stellar model produced using the code of Aparicio & Gallart (2004), a metallicity of 2.5 solar metallicity, and a constant stellar formation between 1 Gyr < t < 5 Gyr (blue circles) and 5 Gyr < t < 12 Gyr (red diamonds).

low extinction, with mean observed $H-K_s \approx 0.2, 0.5, 0.8$, which we interpret to belong to spiral arms along the line of sight. At the distance of the GC, we identify a high-extinction population, with a mean $H-K_s \approx 2.0$, and a population at somewhat lower extinction at $H-K_s \approx 1.5$. Both populations appear clearly distinct in an HST/WFC3 $F105W-F153M$ versus $F153M$ CMD and can be separated relatively cleanly using a colour threshold of $J-K_s = 5.2$. Since the RC of the low-extinction population lies along the reddening line of the more extinguished RC, we believe that the low-extinction population lies approximately at the distance of the GC. As a tentative explanation, we hypothesise that we are seeing stars in front of the dust and molecular gas of the central molecular zone (CMZ). This is in agreement with the findings of Launhardt et al. (2002) that about 80% of the molecular gas in the CMZ appears to be concentrated in a torus with radii between 120 to 220 pc. The clumpiness of the interstellar medium (ISM) in the CMZ (see also Launhardt et al., 2002) will, of course, complicate this simple picture.

Our deep and sensitive data allow us to study the NIR extinction curve during the GC in unprecedented detail. We found some evidence for a possible difference in the extinction index between $J-H$ and $H-K_s$. However, it is small and the extinction index can be assumed to be roughly constant within the limits of our study. Moreover, the value found here, $\alpha_{JHK_s} = 2.30 \pm 0.08$, is in excellent agreement with the latest literature values on the NIR extinction curve towards the GC. Nishiyama et al. (2006a) found $\alpha_{JHK_s} = 2.23 \pm 0.23$ (value taken from Table 5 in Fritz et al., 2011), Schödel et al. (2010) found $\alpha_{JHK_s} = 2.21 \pm 0.24$, and Fritz et al. (2011) found $\alpha_{JHK_s} = 2.11 \pm 0.06$. The study carried out by Stead & Hoare (2009) found $\alpha_{JHK_s} = 2.14 \pm 0.05$ not towards the GC but towards eight regions of the Galaxy between $1 \sim 27^\circ$ and $\sim 100^\circ$. Zasowski et al. (2009) also found a compatible $\alpha_{JHK_s} = 2.26 \pm 0.17$ (value taken from Table 5 in Fritz et al., 2011) towards different regions of the Milky Way (over nearly 150° of contiguous Milky Way midplane longitude). This may indicate a universal value for α_{JHK_s} that is steeper than assumed in older work (e.g., Cardelli et al., 1989; Draine, 1989; Rieke & Lebofsky, 1985). Besides, Stead & Hoare (2009) also point out that great care must be taken in the choice of the filter wavelength when using broadband filters. This has been done in the current work by computing carefully the effective wavelengths accordingly, as shown in Appendix A.

We studied possible variations of α_{JHK_s} with position in the field and with the absolute value of extinction, but cannot find any evidence for any such dependence, as suggested, for example, by Gosling et al. (2009), who found a broad range for α_{JHK_s} in the GC with a strong dependency on the line of sight. We believe that the latter work suffered from crowding and low angular resolution, which limited the authors to make assumptions on the median properties of their observed stellar populations. They could not select specifically RC stars and had to rely on median colours of stars in their fields. Hence, we claim that the NIR extinction curve toward the GC can be approximated by a power law with constant index α_{JHK_s}. On the other hand, we have created several extinction maps and have identified a first layer of low varying extinction and a second one closer to the GC where the extinction varies in arc-second scales. Therefore, it appears that a significant part of the extinction toward the GC is originated from a highly clumpy medium near the GC. The clumpiness is in agreement with previous studies of the ISM in the CMZ (e.g., Launhardt

et al., 2002). This division enables us to improve the de-reddening process to obtain more accurate de-reddened CMDs. Using them, we have employed isochrones with different metallicities (Marigo et al., 2017) and a synthetic stellar model (Aparicio & Gallart, 2004) to infer the metallicity of the stellar population in the studied region. We found that a solar to super-solar metallicity fits the data well. This study supposes the first time that metallicity has been guess using only photometry in the near infrared for the GC.

"Lisa, haz el favor. En esta casa obedecemos las leyes de la ¡termodinámica!"

"La gente se inventa estadísticas con tal de demostrar algo, y esto lo sabe el 14% de la gente."

Homer Simpson

"Cállate, cerebro. Ahora tengo amigos, ya no te necesito."

Lisa Simpson

8

The near-infrared extinction curve toward the Galactic centre

In the study presented in this chapter, we used the J, H and K_s photometry of 14 different fields of the survey that cover a rectangular region of 90 pc $\times$ 20 pc centred on SgrA* and corresponding to the central part of the NB (Nogueras-Lara et al., submitted), as shown in Fig. 8.1.

8.1 Introduction

As it was shown in the previous chapter, it is generally accepted that the extinction curve in the NIR can be approximated by a power law (e.g. Fritz et al., 2011; Nishiyama et al., 2008) of the form $A_\lambda \propto \lambda^{-\alpha}$, where λ and α are the wavelength and the extinction index, respectively. However, the value of the extinction index

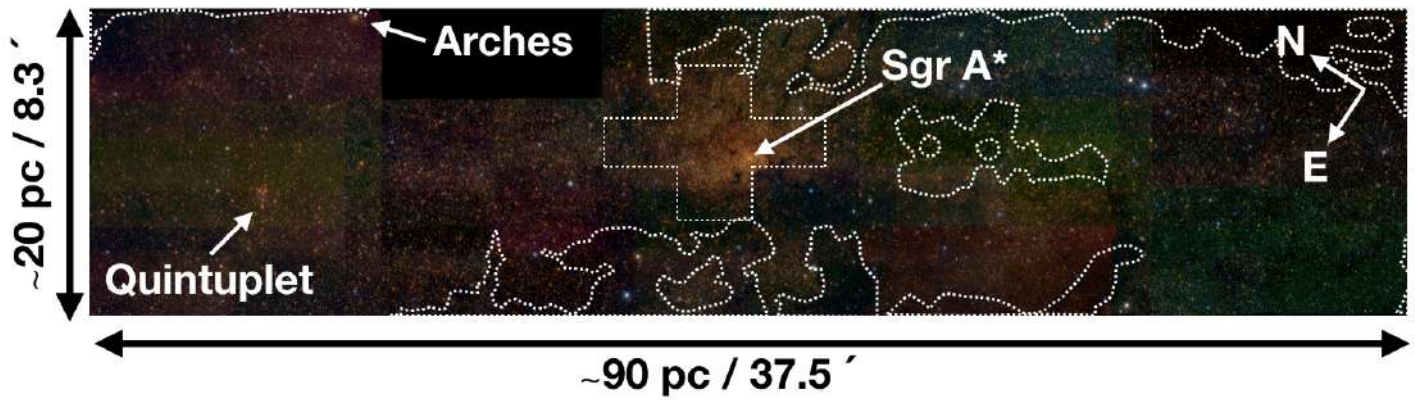

Fig. 8.1 RGB image of the studied region produced combining K_s, H and J bands as red, green and blue colours. Sagittarius A* and the Arches and Quintuplet clusters are marked by arrows. The black rectangle near the Arches cluster corresponds to a field with incomplete data. White dashed contours indicate regions dominated by dark clouds. The cross-shaped region corresponds to a low completeness region due to crowding (NSC).

has changed significantly in the last decades from values ~ 1.5 (e.g. Draine, 1989; Rieke & Lebofsky, 1985) to $\alpha > 2.0$ or even ~ 2.5 (e.g., Alonso-García et al., 2017; Fritz et al., 2011; Gosling et al., 2009; Nishiyama et al., 2006a; Nogueras-Lara et al., 2018a; Schödel et al., 2010; Stead & Hoare, 2009). In addition to this discrepancy, some evidence of a possible variation of the extinction index between the NIR bands JH and HK_s has been reported recently (see chapter 11, Hosek et al., 2018; Nogueras-Lara et al., 2018a). These different values can lead to generate a wrong picture of the inner structure of the galaxy. Namely, a small change of α ($\sim 10-15\%$) can result in a change of absolute extinction by ~ 0.3 mag, which corresponds to a bias in the estimation of distances based on the distance modulus by ~ 1 kpc (Matsunaga et al., 2016) at the GC distance (~ 8 kpc). The situation is even more complicated when inferring the stellar type of a star using NIR photometry, where a small variation correcting the extinction changes completely the type of a star (e.g., Figs. 33 and 34 Nogueras-Lara et al., 2018a).

In this chapter we characterise the extinction curve in the NIR bands JHK_s towards the nuclear bulge (NB) using the GALACTICNUCLEUS survey (Nogueras-Lara et al., 2018a) and two independent methods based on red clump (RC) stars (e.g., Girardi, 2016).

8.2 Colour-magnitude diagrams

Figure 8.2 depicts the colour-magnitude diagrams (CMD) H versus $J-H$ and K_s versus $H-K_s$. The highly populated region located at $J-H > 2.5$ and $H-K_s > 1.3$ corresponds to the GC stellar population, whereas stars at $J-H < 2.5$ and $H-K_s < 1.3$ trace foreground stars probably belonging to three spiral arms (Nogueras-Lara et al., 2018a). The high density regions within the blue dashed trapezoids show the GC RC feature following the reddening vector due to differential extinction. We clearly distinguish a bright and a faint RC, that trace an old stellar population $\gtrsim 8$ Gyr and stars formed in a younger star formation burst ~ 1 Gyr (Nogueras-Lara et al., submitted), respectively.

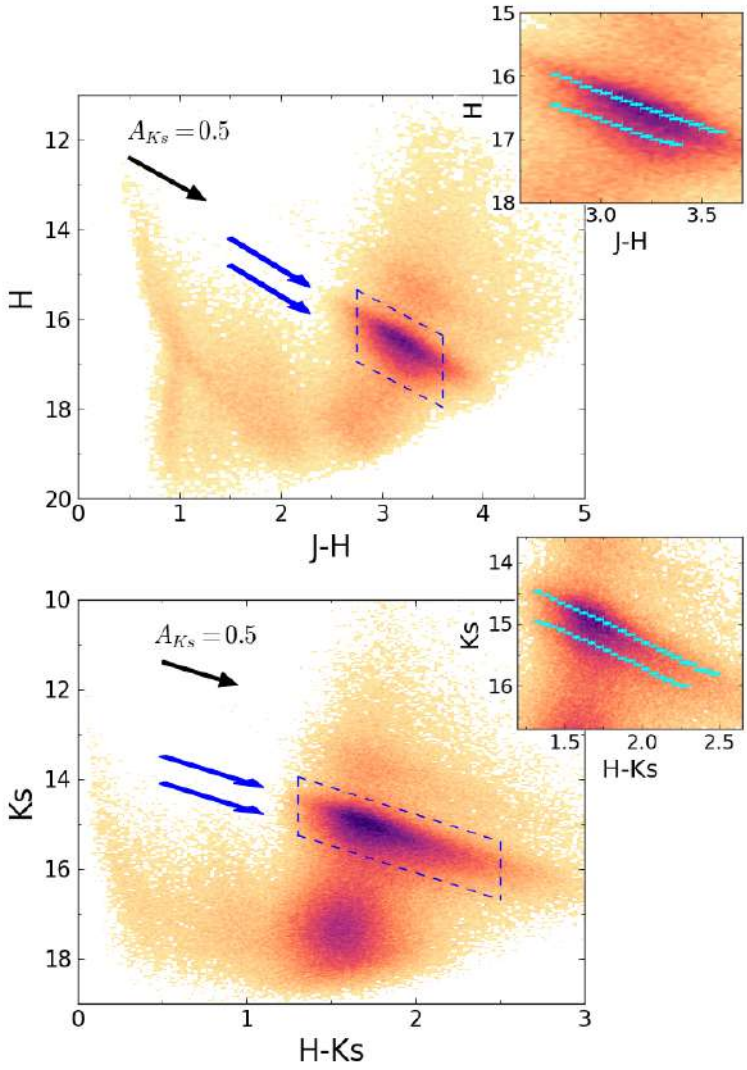

Fig. 8.2 Colour-magnitude diagrams H versus $J-H$ (upper panel) and K_s versus $H-K_s$ (lower panel). The RC is marked by the blue dashed parallelograms. The two blue arrows show a double feature in the RC. Black arrows depicts the reddening vector with an extinction $A_{K_s} = 0.5$ mag (computed using $\alpha = 2.30 \pm 0.08$, Nogueras-Lara et al., 2018a). The insets show the RC region with the two features obtained applying GMM and their uncertainties in cyan (see main text).

8.3 Extinction index analysis

We analysed the line-of-sight variability and the variation as a function of the wavelength of the extinction index.

8.3.1 Spatial variability of the extinction index

We employed the "grid method" described in Sec. 7.3.1 (and in Sec. 6.1. of Nogueras-Lara et al. (2018a)), increasing the area of the region analysed by a factor of ~ 10. This method uses RC stars -giant stars in their helium core burning stage (e.g., Girardi, 2016)- to compute simultaneously the extinction index and the extinction at a fixed wavelength ($\lambda = 1.61\ \mu m$). We used atmosphere models (Kurucz, 1993) to compute synthetic magnitudes of the RC stars for the filters used in our observations and minimised the corresponding χ^2. We reddened the synthetic stellar models using a grid of extinctions and α (with a step of 0.016 for both of them). To model RC stars we used an effective temperature of 4,750 K, $\log g = +2.5$ (Bovy et al., 2014), a radius of $10.0 \pm 0.5\ R_{\odot}$ (e.g., Chaplin & Miglio, 2013; Girardi, 2016) and twice solar metallicity according to recent work (e.g. Do et al., 2018, 2015; Feldmeier-Krause et al., 2017; Nandakumar et al., 2018; Schultheis et al., 2019), which allows us to decrease the uncertainty of the results. We also assumed a distance to the GC of 8.0 ± 0.1 kpc with lower uncertainty, averaging the last results obtained by Gravity Collaboration et al. (2018) and Do et al. (2019a). We selected the RC stars shown in the blue dashed parallelograms in Fig. 8.2. Some contamination of the red giant branch bump (RGBB) (see, e.g. Nataf et al., 2011a; Wegg & Gerhard, 2013) is expected, but since the intrinsic colour is similar to the RC (Nogueras-Lara et al., 2018b) it does not have a significant influence in our results. We computed the extinction index and $A_{1.61}$ for all the RC stars detected in all three bands (JHK_s) with an uncertainty < 0.05 mag in all three bands ($\sim 62,000$ stars in total). To study the variability of the extinction index with the line of sight, we computed extinction index maps using the results obtained for α_{JH}, α_{HK_s} and α_{JK_s}. We defined a pixel size of 1 arcmin and computed the extinction index using a 3-sigma clipping algorithm for all the RC stars within a pixel. We computed the maps for α_{JH}, α_{HK_s} and α_{JK_s} to study the variation with the wavelength. We only calculated the extinction index

value for a given pixel if the number of stars detected were larger than 80. Figure 8.3 shows the obtained results for α_{JH}, α_{HK_s} and α_{JK_s}. We estimated the statistical uncertainties via the standard deviation of the distribution of the obtained values for each pixel. We found that the uncertainties are below 0.016 for all the maps. The systematic uncertainties are not considered since they change all the pixels for each map in the same way, and we are analysing the relative difference between the pixels of the same map.

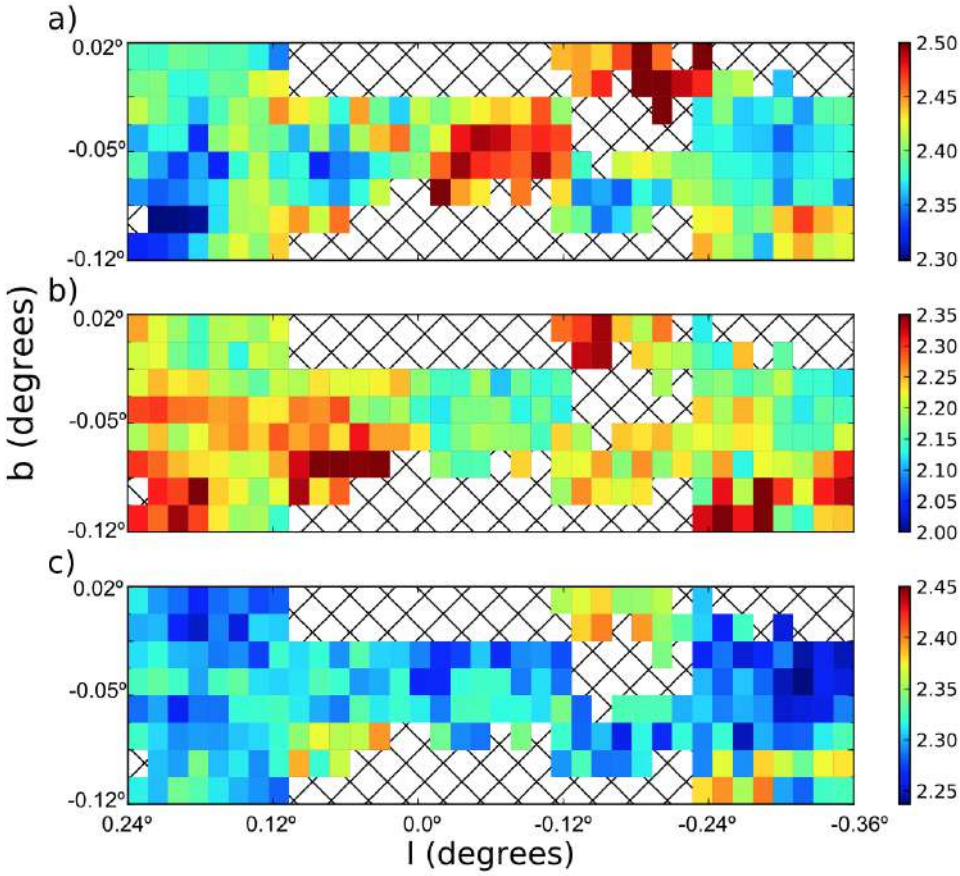

Fig. 8.3 Extinction-index maps. a) JH-map. b) HK_s-map. c) JK_s-map. Cross-shaped pixels indicate that there are not enough stars for a reliable estimate.

We observed some variation between different pixels, as it can be seen in Fig. 8.3. Nevertheless, we found that the systematic uncertainty of the ZP of the pointings

used to produced the catalogue (~ 0.036 mag in all three bands) can explain this variation. For this, we recomputed the extinction indices (α_{JH}, $alpha_{HK_s}$ and α_{JK_s}) considering that, for each band independently, the magnitude of the RC stars used is affected by the systematic uncertainty of the ZP. We combined quadratically the obtained extinction index uncertainty for each band and found that the expected variation of the extinction index is $\Delta\alpha_{JH} = 0.05$, $\Delta\alpha_{HK_s} = 0.08$ and $\Delta\alpha_{JK_s} = 0.03$. We also created histograms of the extinction-index values per pixel. Figure 8.4 shows the results. The standard deviation of the distributions are below the ZP systematic uncertainties. We conclude that there is no significant variation of the extinction index with the line of sight within the uncertainties of our data. This agrees with the no-variation of the extinction index measured between a region in the GC (Nogueras-Lara et al., 2018a) and two regions in the inner bulge located at a distance of $\sim 0.4°$ and $\sim 0.6°$ (Galactic north) from SgrA* (Nogueras-Lara et al., 2018b).

We also produced the corresponding maps for the extinction $A_{1.61}$ and checked that for all the bands' combinations (JH, HK_s and JK_s), we obtained equivalent maps, as it was expected since we are using common stars between all three bands.

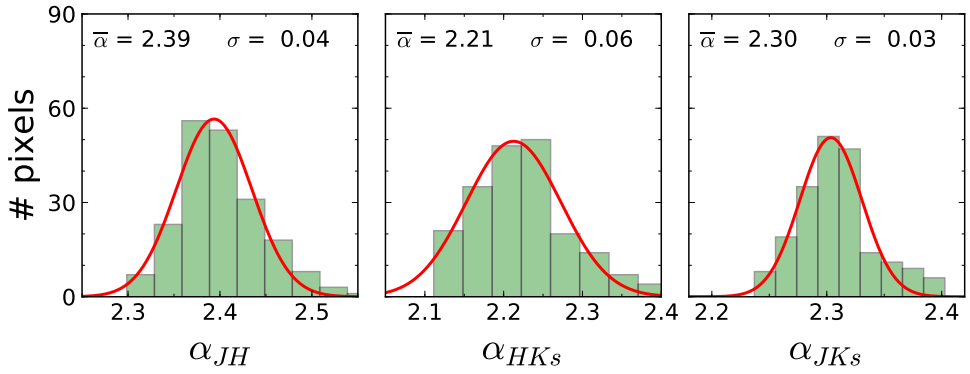

Fig. 8.4 Histograms of the extinction-index values per pixel. a) JH-map. b) HK_s-map. c) JK_s-map. The red line indicates a Gaussian fit. The mean and the standard deviation are specified in the figure.

8.3.2 A unique extinction index in the NIR?

To analyse the variation of the extinction index with the wavelength, we built histograms for values obtained for α_{JH}, α_{HK_s}, α_{JK_s}, α_{JHK_s} and the corresponding extinctions $A_{1.61}$, for all the stars used in the analysis. The obtained distributions are well fitted by a Gaussian model (Fig. 8.5). Table 8.1 summarises the results. The uncertainties refer to systematics and were computed varying independently all the parameters involved in the calculation in their uncertainty ranges as described in Nogueras-Lara et al. (2018a). We only used a different range to estimate the uncertainties in the case of the distance to the GC and the metallicity of the GC stellar population, where the updated values allowed us to reduce the systematics in comparison to our previous work. The statistical uncertainties were estimated using the error of the mean of the distributions and are negligible given the number of stars used for the calculation.

Table 8.1 Extinction index calculation following the method described in 8.3.1.

	Bands	α	$A_{1.61}$
Common stars	JH	2.41 ± 0.09	3.39 ± 0.15
	HK_s	2.19 ± 0.14	3.40 ± 0.14
	JK_s	2.29 ± 0.09	3.47 ± 0.18
	JHK_s	2.33 ± 0.09	3.43 ± 0.16

Notes. Only stars belonging to the RC detected in all three bands have been used.

Our results suggest that the extinction index depends on wavelength in the NIR. We obtained $\Delta\alpha = \alpha_{JH} - \alpha_{HK_s} = 0.22 \pm 0.13$, which supposes $\sim 2\ \sigma$ detection of a different extinction index between JH and HK_s. We estimated the uncertainty computing the difference between the extinction indices when varying all the parameters specified in Sec. 8.3.1. The uncertainty is lower than the one obtained simply using the quadratic propagation, because the variation of some parameters produces a change in both, α_{JH} and α_{HK_s} in the same direction.

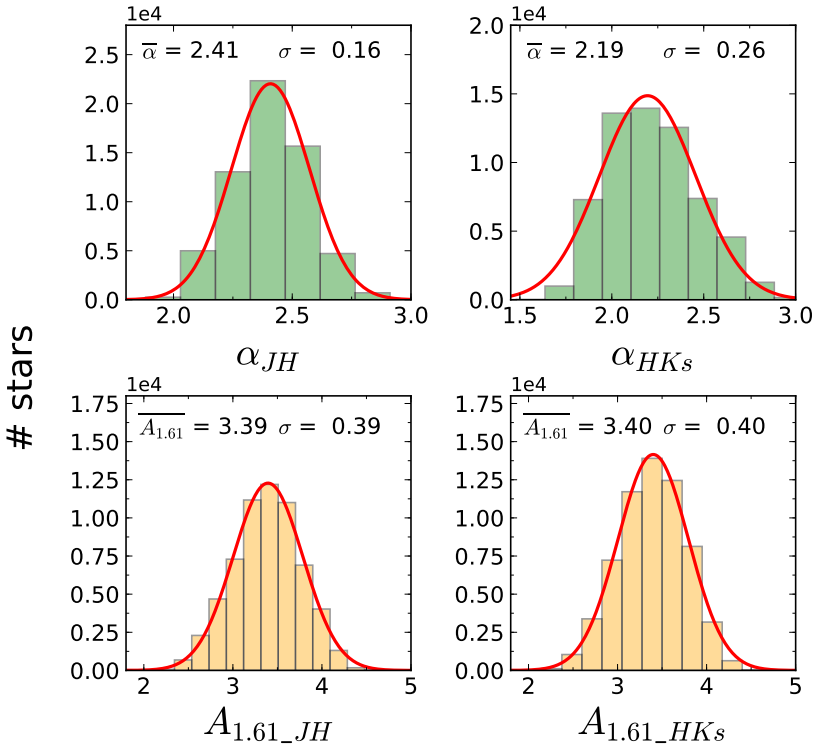

Fig. 8.5 Upper panels: histograms obtained for α_{JH} (left panel) and α_{HK_s} (right panel) using the method presented in Sec. 8.3.1. Lower panels: histograms obtained for $A_{1.61}$, associated to the calculations using JH and HK_s. Red lines show Gaussian fits to the data. The mean and the standard deviation of each histogram are specified in each panel.

8.3.3 Variation of the extinction index with the extinction

The spread of the RC along the reddening vector shown in Fig. 8.2 is mainly due to differential extinction. In this way, we analysed the variation of α_λ with the extinction ($A_{1.61}$), dividing the RC stars in the CMD into small bins of $J-K_s = 0.25$. We only used stars detected in all three bands with uncertainties < 0.05 mag. The results are shown in Table 8.2. The uncertainties are computed as explained in the Sec. 8.3.1. We found some dependence of α_{HK_s} on the extinction, whereas α_{JH} appears to be constant. Nevertheless, we conclude that both extinction indices can be considered constant within the estimated uncertainties. On the other hand, we

confirmed the previously computed value of $\alpha_{JH} - \alpha_{HK_s} \sim 0.2$ that is also observed for different $A_{1.61}$.

Table 8.2 Extinction index calculation for different extinctions 8.3.1.

$J - K_s$	α_{JH}	α_{HK_s}	A_{JH}	A_{HK_s}
4-4.25	2.41 ± 0.10	2.14 ± 0.16	2.83 ± 0.15	2.83 ± 0.15
4.25-4.5	2.40 ± 0.09	2.16 ± 0.15	3.04 ± 0.14	3.03 ± 0.14
4.5-4.75	2.39 ± 0.09	2.19 ± 0.15	3.22 ± 0.15	3.22 ± 0.15
4.75-5	2.39 ± 0.08	2.20 ± 0.14	3.44 ± 0.14	3.43 ± 0.14
5-5.25	2.40 ± 0.08	2.22 ± 0.13	3.61 ± 0.16	3.61 ± 0.15
5.25-5.5	2.40 ± 0.08	2.24 ± 0.13	3.78 ± 0.14	3.78 ± 0.15

Notes. Only stars belonging to the RC detected in all three bands have been used.

8.3.4 Slope of the RC features

To check the $\Delta\alpha = \alpha_{JH} - \alpha_{HK_s}$ obtained with the grid method, we studied the slopes of the RC features. We used all the RC stars shown in the blue dashed parallelograms in Fig. 8.2. Firstly, we divided the RC region in the CMD into small vertical bins to apply the SCIKIT-LEARN python function GaussianMixture (GMM, Pedregosa et al., 2011) to compare a 1-Gaussian model with a 2-Gaussians one to fit the K_s stellar distribution for each bin (Nogueras-Lara et al., 2018b). Using the Bayesian information criterion (Schwarz, 1978) and the Akaike information criterion (Akaike, 1974), we found that a double Gaussian model fits the data better as expected (Rui et al. (2019), Nogueras-Lara et al., submitted). We computed the slope of both RC features using a jackknife resampling method and calculating the systematic uncertainties varying the the bin width, the RC selection and the width and the number of bins used, as described in Nogueras-Lara et al. (2018b). We repeated the same analysis for the CMDs K_s versus $J - K_s$ and H versus $J - H$. The secondary

RC feature is more sensitive to extinction and completeness problems given that it is fainter than the main one. For this reason, we removed the last bins in the calculation of the slope of the secondary feature. Moreover, we excluded regions affected by dark clouds (using as reference the *J* band, as it is more prone to extinction) that can influence the slopes of the features as they could change the relative number of stars in each feature for faint magnitudes. We also masked the central region belonging to the nuclear star cluster (NSC) because it could have a different star formation history and a lower completeness (Nogueras-Lara et al., submitted). Using the slope of the features, we computed the extinction index by means of equation 1 in Nogueras-Lara et al. (2018b):

$$\alpha = -\frac{\log(1+\frac{1}{m})}{\log(\frac{\lambda_{\mathrm{eff}_1}}{\lambda_{\mathrm{eff}_2}})}, \tag{8.1}$$

where m is the slope of the features in the CMD λ_{eff_2} versus $\lambda_{\mathrm{eff}_1} - \lambda_{\mathrm{eff}_2}$, and λ_{eff_i} is the effective wavelength. Table 8.3 summarises the results obtained for each colour.

Table 8.3 Extinction index calculation using the slope of the RC.

Bands		Extinction index
JH	α_1	$2.45 \pm 0.03 \pm 0.04$
	α_2	$2.59 \pm 0.04 \pm 0.06$
HK_s	α_1	$2.26 \pm 0.01 \pm 0.01$
	α_2	$2.32 \pm 0.02 \pm 0.01$

Notes. α_1 is the extinction index found for the bright RC. α_2 is the extinction index found for the faint RC. The uncertainties correspond to statistics and systematics, respectively.

Combining the values for both clumps, we computed $\alpha_{HK_s} = 2.29 \pm 0.02$ and $\alpha_{JH} = 2.52 \pm 0.09$, where the uncertainties have been quadratically propagated. We obtained $\Delta\alpha = 0.23 \pm 0.09$. The uncertainty is even smaller if we just consider the

bright RC, $\Delta\alpha = 0.19 \pm 0.05$, which supposes that the difference in the inter-band extinction index is detected with $\sim 4\ \sigma$ significance. The results fully agree within the uncertainties with the previous values estimated using a completely independent method.

The extinction indices computed using this method are somewhat higher than the ones obtained in sec. 8.3.1. This could be as a consequence of a small shift, within the uncertainties, of the ZP calculation that affects the first method (and it is considered in the estimation of the uncertainties) but does not affect the second one. Nevertheless, all the values agree within the uncertainties. Moreover, the ZP uncertainty does not affect the estimation of $\Delta\alpha$ in the second method. Therefore, we considered the value $\Delta\alpha = 0.19 \pm 0.05$ as the best estimation.

8.4 Results and discussion

We have analysed the spatial variability of the extinction index and its dependence on the extinction, $A_{1.61}$. We find that there is no variation within the uncertainties. Therefore, it is possible to assume a constant α for the studied region of the NSD in the NIR. We have detected a difference in the extinction index between JH and HK_s of $\Delta\alpha = 0.19 \pm 0.05$, combining the values obtained using two independent methods ($\Delta\alpha = 0.22 \pm 0.13$ and $\Delta\alpha = 0.19 \pm 0.05$). We used a weighted average for the calculation and the uncertainty estimation. We also obtain the mean values of the extinction indices $\alpha_{JH} = 2.43 \pm 0.03$ and $\alpha_{HK_s} = 2.23 \pm 0.03$, computed combining the results from Tables 8.1 and 8.3 (bright feature), and calculating the uncertainties via the difference between values (also coincident with the standard deviation). We did not use a weighted mean given the much lower uncertainties of the values obtained with the slope of the RC, which might lead to a biased result. Comparing our findings with previous work, we suggest that some discrepancies towards different extinction-index values could be explained due to the direct assumption of having just one single α for JHK_s (e.g., Alonso-García et al., 2017; Fritz et al., 2011; Gosling et al., 2009; Nishiyama et al., 2006a; Stead & Hoare, 2009). This depends on the methodology used. In particular applying the method described in sec. 8.3.1, we obtained a value $\alpha_{JHK_s} = 2.32 \pm 0.09$ which is in between the two values computed for α_{JH} and α_{HK_s}. On the other hand, using the slope of the RC to derive the extinction curve implies

that it is necessary to know whether one or more RC features are present in the RC in the CMDs. Moreover, this method is quite dependent on the completeness of the photometry. The slope of the RC feature/s might change at the faint end if the completeness is not sufficient.

To the best of our knowledge this is the first time that the extinction curve in the GC has been shown to not depend on the line of sight or extinction and to depend on wavelength. Previous studies always used a uniform extinction curve with different values. The great accuracy of this work has only been possible thanks to the high angular resolution GALACTICNUCLEUS survey.

"Por mí, día y noche, the saludan bocas de deseos, ventura, felicidad y amabilidad. Ella es la Suprema Cúpula y nosotras sus hijas, aunque el favor y la gloria en mi clase me distinguen, al ser, sin duda, el corazón y ellas los miembros, pues en el corazón la potencia del espíritu y el alma reside. Si mis hermanas son constelaciones en su cielo en mí, y no en ellas recae el honor de tener el sol."

Salón de Comares. Ibn al-Ŷayyāb o Ibn al-Jatīb

9

The star formation history of the nuclear disc of the Milky Way

The nuclear disc is a dense stellar structure at the centre of the Milky Way, with a radius of $\sim$ 150 pc (Launhardt et al., 2002). It has been a place of intense star formation in the past several tens of millions of years (Bland-Hawthorn & Gerhard, 2016; Launhardt et al., 2002; Matsunaga et al., 2011) but its overall formation history has remained unknown up to now (Bland-Hawthorn & Gerhard, 2016). In this chapter, we analyse its star formation history fitting theoretical models to a de-reddened K_s luminosity function using the GALACTICNUCLEUS survey.

9.1 Introduction

The GALACTICNUCLEUS survey (Nogueras-Lara et al., 2018a) has been specifically designed to study the structure and formation history of this region of the GC. In this chapter, we analyse a rectangular region of $\sim 37.5' \times 8.3'$ (about 1,600 pc^2 at the distance of the GC) centred on Sagittarius A* (Sgr A*, $17h\ 45m\ 40.05s$, $-29^\circ\ 00'\ 27.9''$, Fig. 9.1, upper panel). A region close to Sgr A* was excluded from the analysis because of the extreme stellar crowding, so were regions dominated by dark foreground clouds. The final catalogue for this region includes accurate photometry for more than 700,000 stars, superseding other surveys of the GC by orders of magnitude (Nogueras-Lara et al., 2018a,b).

9.2 Data analysis

9.2.1 Removing dark clouds

We excluded regions with dark clouds because they are largely opaque and limit the observation of stars belonging to the nuclear stellar disc (NSD). Given that the extinction is larger for shorter wavelengths, we used a J-band density map to identify dark clouds (Nogueras-Lara et al., 2018a). We defined a pixel size of $\sim 6''$ and compute the J-band density for each pixel. We masked regions with less than 5% of the maximum density detected (Fig. 9.1, lower panel). Varying this percentage between 3% and 7% did not result in any significant change to our results.

9.2.2 Colour magnitude diagram

Figure 9.2 depicts the HK_s colour magnitude diagram of the used data. It shows a prominent vertical feature at $H - K_s > 1.3$, which corresponds to giant stars located at the GC. Stars with bluer colours lie in spiral arms in the foreground (as it was described in the Sec. 7.2). The diagonal high-density feature that extends from roughly ($K_s = 14.5, H - K_s = 1.3$) to ($K_s = 16.5, H - K_s = 3$) is caused by differential extinction and reddening of the so-called red clump (RC), which marks the location of helium core burning giants in metal-rich, old populations. Stars in the RC can be used as standard candles because of their highly similar luminosities and temperatures

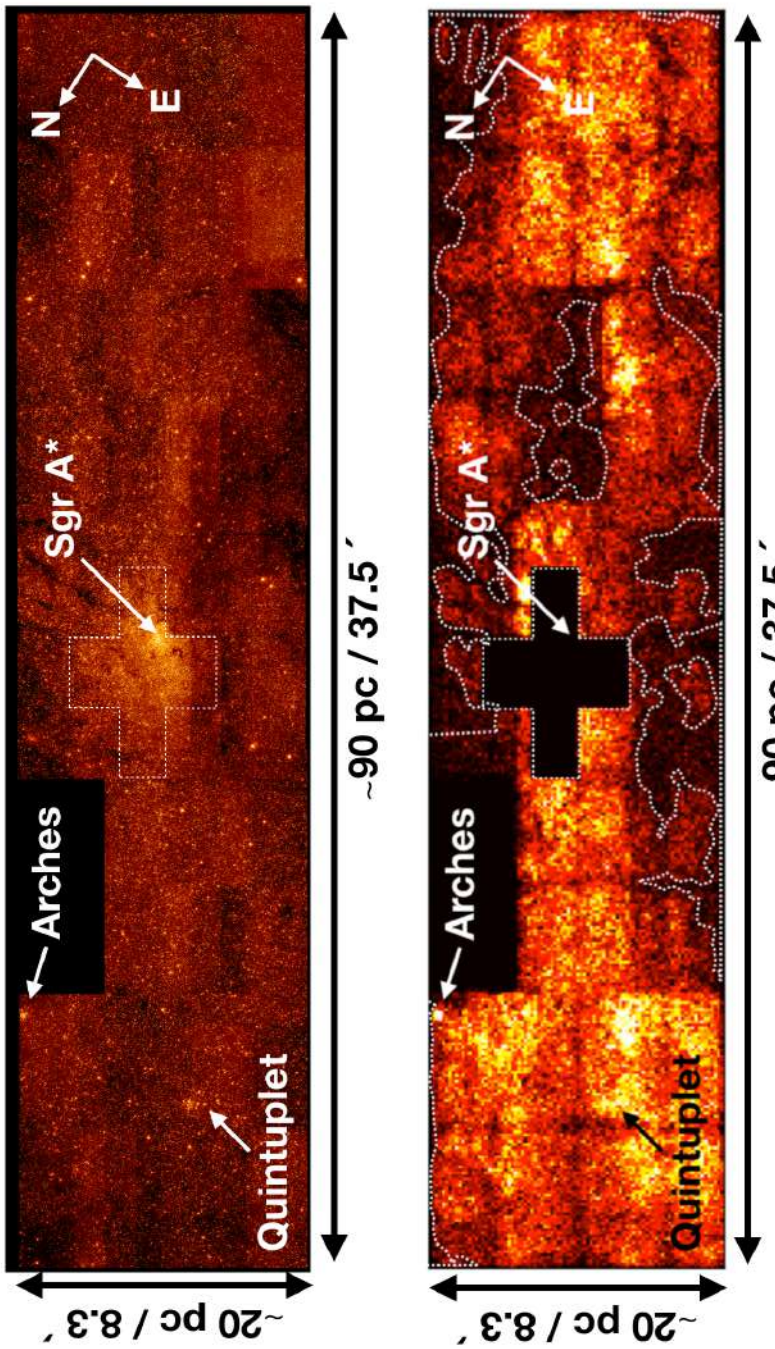

Fig. 9.1 Upper panel:K_s-band image of the GALACTICNUCLEUS survey region examined for this study. Lower panel: *J*-band density map. The dark patches are clouds of molecular gas and dust. They impede the view into the GC and were therefore excluded from this study (white dashed line contours.The positions of Sgr A*, the Arches and the Quintuplet clusters are indicated. The cross-shaped region outlined by a white dashed line was excluded because of too high source crowding. The dark rectangle right next to the Arches cluster is a field with incomplete data.

across a broad range of ages, metallicities, and masses (Girardi, 2016). We used these stars to correct our data for the effects of interstellar extinction and reddening as it is explained in the Sec. 9.2.3. The two arrows in Fig. 9.2 indicates the visual detection of two features in the RC region. This "double red clump" is also clearly detected in the region around the Quintuplet cluster by recently published HST observations (Rui et al., 2019).

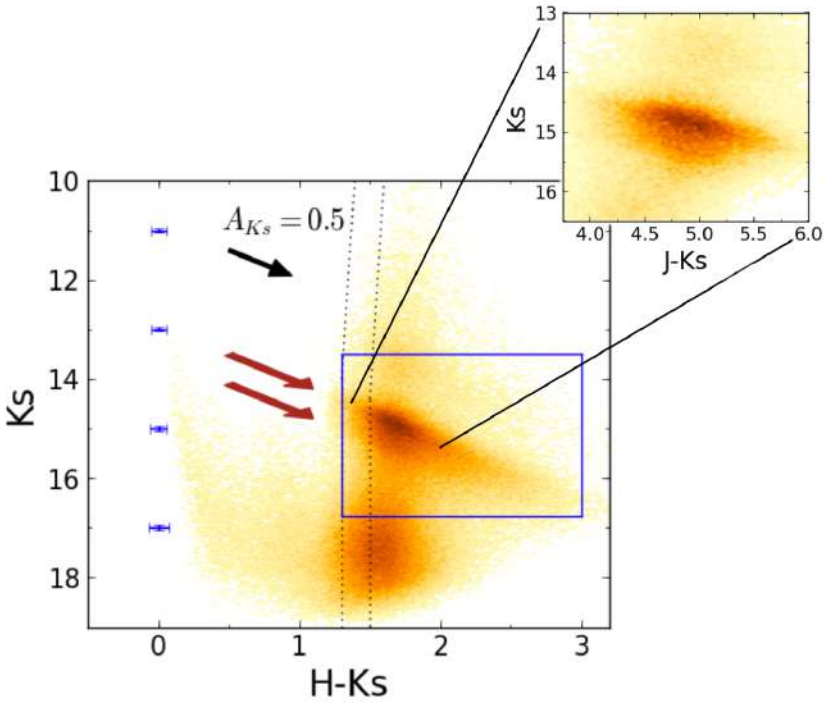

Fig. 9.2 Observed $H - K_s$ CMD. The vertical dashed lines show the two colour cuts used to exclude foreground stars (see Sec. 9.2.4). The two arrows indicate the direction of reddening and point toward the two parallel features that we detected in the RC, corresponding to old (brighter) and younger (fainter) stars (Sec. 8.3.4). The inset shows the double RC in the $J - K_s$ CMD. The blue rectangle indicates the stars used to create the extinction map. The error bars, in blue, show the uncertainties for different magnitude bins.

9.2.3 Extinction correction

As described in chapter 11, we used RC stars to compute an extinction map to de-redden the photometry and to correct for differential extinction (Nogueras-Lara et al., 2018a,b). We selected a pixel scale of $2.5''\text{pixel}^{-1}$ and computed the colour excess $H-K_s$ using only stars within $5''$ from a given pixel. Since the differential extinction and the extinction in the line of sight can vary significantly on arc second scales, we considered only stars whose $H-K_s$ value lies within 0.25 mag of the value corresponding to the star closest to any given pixel. We imposed a minimum of five stars fulfilling these conditions per pixel on the extinction map. We weighted the distances to the centre of the pixel with an inverse-distance weight (IDW) method (Nogueras-Lara et al., 2018a,b). We used the RC stars shown in the rectangle in Fig. 9.2 and assumed an extinction index of 2.30 ± 0.08 (Nogueras-Lara et al., 2018a). This value agrees well with the dependence of the extinction index on the wavelength shown in chapter 8. The selected region is mainly populated by RC stars or RGBB stars whose intrinsic colours are similar (Nogueras-Lara et al., 2018b). We computed the intrinsic colour $(H-K_s)_0 = 0.07 \pm 0.03$ taking into account different metallicities and stellar ages of RC and RGBB stars, BaSTI models (Pietrinferni et al., 2014) and the corresponding filters of HAWK-I. Fig. 9.3 shows the obtained extinction map. The statistical uncertainties of the pixels are $\sim 3\%$ and were calculated taking into account the dispersion of the stars used to compute the extinction value of each pixel and the standard deviation of the intrinsic colour computed previously. The systematics are $\sim 6\%$ and consider the systematic uncertainty of the zero point for H and K_s, and the uncertainties of the extinction index and the effective wavelength. These uncertainties do not influence the differential extinction in any significant way.

After applying the extinction map to the CMD, we obtained the de-reddened CMD shown in Fig. 9.4.

9.2.4 Foreground stars

About 50% of the interstellar extinction toward the GC is caused by dust in the Galactic disc. The bar/bulge is relatively dust free and roughly the other 50% of extinction is caused by dust in the Central Molecular Zone, which forms already part of the GC (Launhardt et al., 2002). The HK_s CMD (Fig. 1) shows how stars

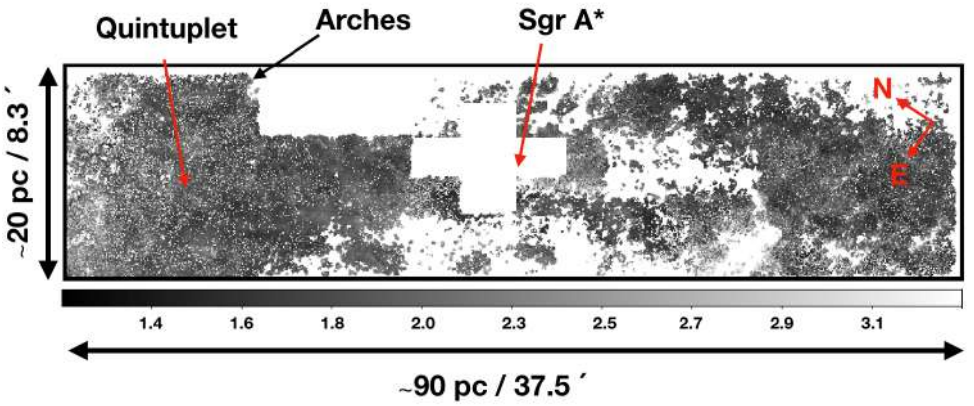

Fig. 9.3 Extinction map A_{K_s}. White patches and pixels indicate regions where the number of stars was not enough to compute an extinction value. Those regions mainly correspond to dark clouds and were previously excluded from our analysis.

in spiral arms in the foreground Galactic disk appear only in significant numbers at $H - K_s \lesssim 1$.

We have chosen a colour cut of $H - K_s = 1.3$ to exclude foreground stars. The most extreme intrinsic colours in $H - K_s$, about 0.2-0.3 mag, are reached by M-type dwarfs or giants. In order to contaminate our sample, those stars would have to suffer a reddening of $H - K_s > 1$ mag and thus lie in the innermost parts of the Disk or outer layers of the bar. However, M-type main sequence stars would be many magnitudes fainter (~ 5 mag) than our detection limit and can thus be ruled out as contaminants. M-type giants are very bright and rare. We would expect to see them in the top of the $H - K_s$ CMD. However, there are only stars with $H - K_s > 1.5$ in this part of the CMD. With our chosen colour cut we can therefore safely exclude contamination by foreground stars in the Galactic disk.

What about contamination by stars in the foreground bar/bulge? We have shown in previous work that the extinction toward the innermost parts of the bar (at ~90 pc vertical separation from Sgr A*) is $A_{K_s} \sim 1.2$, almost half the mean extinction as measured for the GC field studied here (Nogueras-Lara et al., 2018b). This corresponds to $H - K_s = 1.0$ using the reddening curve inferred for this work. With the scatter from measured uncertainties, stars from the innermost bulge/bar may

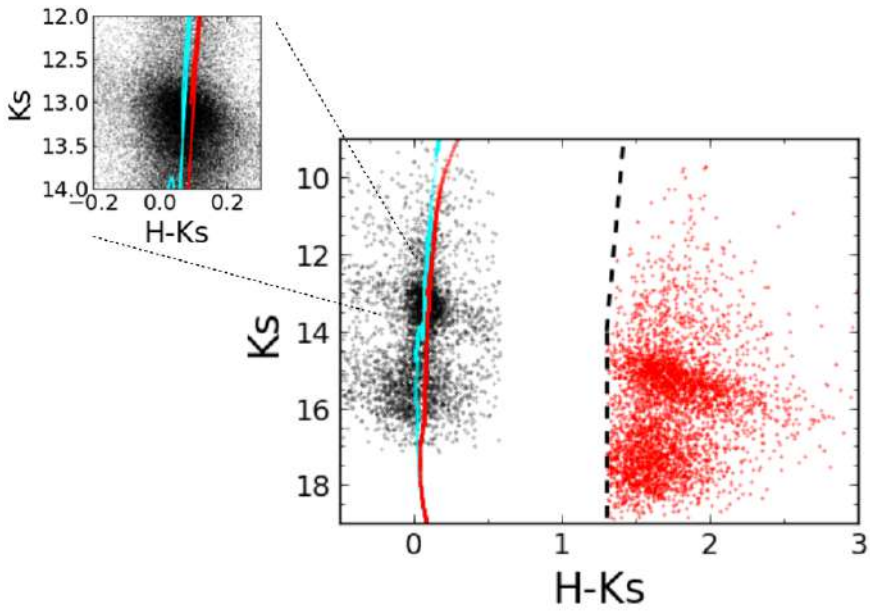

Fig. 9.4 CMD K_s versus $H-K_s$ showing original data (red dots) and the result after applying the extinction correction (in black). The black dashed line shows the cut in $H-K_s$ to exclude the foreground population. The red and cyan lines correspond to BaSTI isochrones of an old and a young population ∼10 Gyr and ∼1 Gyr, respectively according to our results. Only a random fraction of the total amount of stars is shown for clarity.

therefore contaminate our sample to a certain degree. We consider that this potential contamination does not pose any serious effect on our analysis because those contaminating stars would belong to a ∼ 12 Gyr old single age, metal-rich stellar population (Nogueras-Lara et al., 2018b) and would thus only affect the oldest age bin in the SFH. If we could cleanly subtract the contaminant stars, we would at most expect a decrease of the number of or a tendency toward somewhat young ages stars in the oldest age bin. We tested this effect by choosing a stricter colour cut of $H-K_s = 1.5$ and repeating our analysis of the SFH. Indeed, the age of the oldest stars tend to be somewhat younger (moving from ∼13 Gyr to 11 Gyr), but the rest of the SFH is unaffected.

In addition, to obtain a rough estimate of the potential contamination by foreground stars, we varied the colour cut by $\Delta(H-K_s) = 0.2$ mag. This corresponds to

the standard deviation, $\Delta A_{K_s} = 0.25$ mag, of the mean extinction determined for our survey region (see above). The number of stars that get included into or excluded from the final sample varies then by about 2%. We generated and analysed the KLFs (K_s luminosity functions) for both cases and applied the KLF fitting with MC estimation of uncertainties as described above. We did not find any significant difference with respect to our results.

For creating the KLF, we use all stars detected at K_s and do not require that they are detected at H, too. Since reddening rises steeply toward shorter wavelengths, highly reddened stars may not have any H-band counterparts. We can safely assume that stars without any H-band counterpart are not in the foreground.

Finally, it is important to point out that we are dealing with a complex situation here: The bar/bulge and the NSD cannot be spatially separate features and stars from the bar are expected to be present throughout the NSD. As described above this will not change any of our conclusions in a significant way because the contaminating population is old, single age, and metal rich.

9.2.5 Saturation

We corrected for saturation in the K_s-band by using the SIRIUS/IRSF survey (Nishiyama et al., 2006a) to replace the HAWK-I photometry for bright stars ($K_s < 11.5$ mag).

9.2.6 Completeness

Given the large size of the images, the great number of stars, the variability of stellar density with position, and the variation of the data quality for each field and filter, we considered the standard method of determining completeness through inserting and recovering of artificial stars as unviable because of its complexity and the enormous amount of computation time necessary for such a test (we estimate several weeks on our multi core server). We therefore used a previously developed alternative approach, which is based on determining the critical distance at which a star of any given magnitude can be detected around a brighter star (as it was explained in Sec. 6.1.3, Eisenhauer et al., 1998; Harayama et al., 2008). This critical distance can then be translated into completeness maps for each magnitude bin analysed. This method assumes that the probability of detecting a source with a given magnitude is

uniform across the analysed field. Since the stellar density is non-uniform across our survey area and the quality of the data depends on the specific observing conditions and filter for each of the 14 fields that make up the final mosaic, we divided the entire field into 108 smaller sub-regions of $2' \times 1.4'$, as it is shown in Fig. 9.5. We considered these sub-regions to be sufficiently small to assure the validity of the basic assumption of constant stellar density and homogeneous stellar population. To estimate the overall completeness of our star counts and its related uncertainty, we then averaged over the completeness solutions obtained for each of the sub-regions and used the corresponding standard deviation as uncertainty (Fig. 9.6).

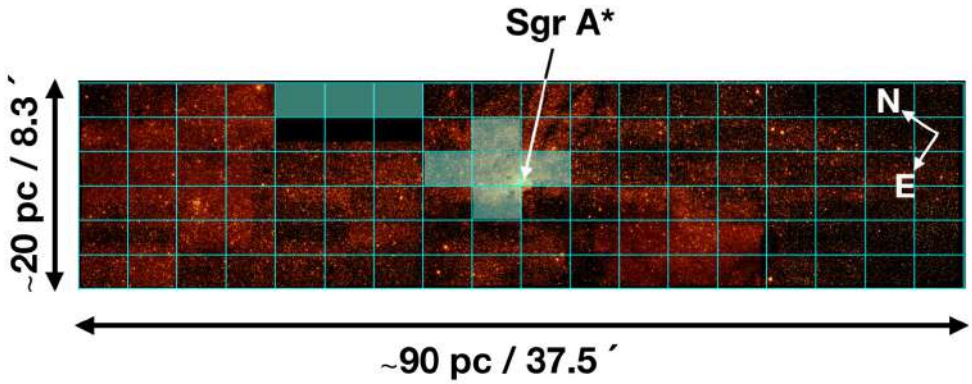

Fig. 9.5 Grid of 108 regions used to compute the completeness. Regions masked due to low completeness in solid cyan.

To test the reliability of our approach, we performed two independent tests in the central field of the mosaic, where crowding is most significant, using the K_s band: (1) We estimated completeness through a standard artificial star test and found that the completeness is $\sim$80% at $K_s \sim 16$ mag, in agreement with the completeness estimation based on the above-described method. (2) We computed and compared a KLF (Sec. 9.3) with a KLF obtained from diffraction limited NACO/VLT images ($\sim 0.06''$ angular resolution) of the NSC (Gallego-Cano et al., submitted to A&A) at a projected distance of about 2 pc from Sgr A*. Again, we found a completeness of $\sim 80\%$ at $K_s \sim 16$ mag, in agreement with our completeness estimation.

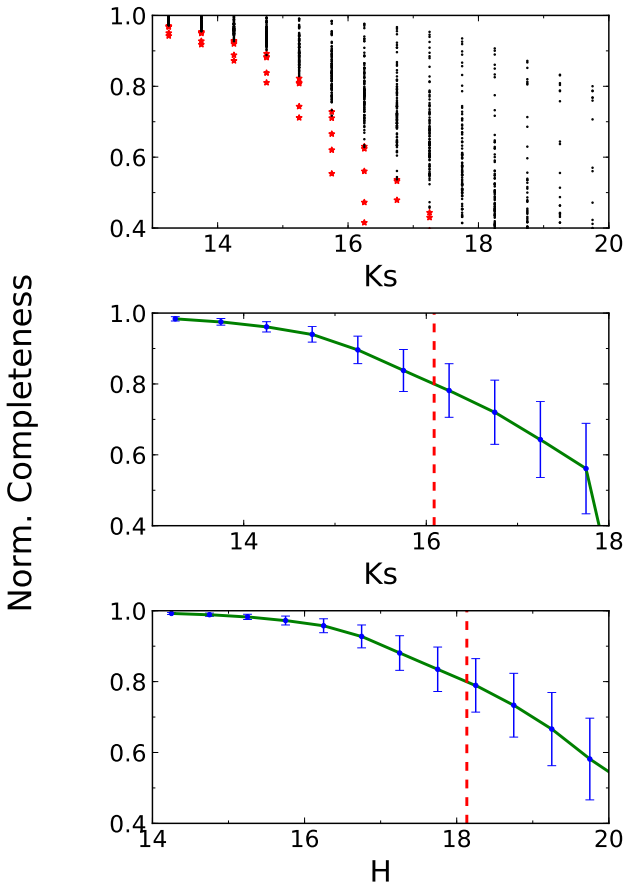

Fig. 9.6 Top panel: completeness for each region and magnitude bin. Red stars correspond to deleted regions due to contamination of the NSC or low completeness. Middle and lower panel: K_s and H completeness function. The red dashed line indicates 80% of completeness.

9.3 K_S Luminosity function

We created a K_s-band luminosity function (Fig. 9.7) using all the stars detected in each band, once we removed the foreground population and excluded the dark cloud regions, as explained previously. Finally, we applied the extinction correction

and limited the magnitude range where the completeness is $> 2/3$ ($K_s \sim 15.3$ mag extinction corrected).

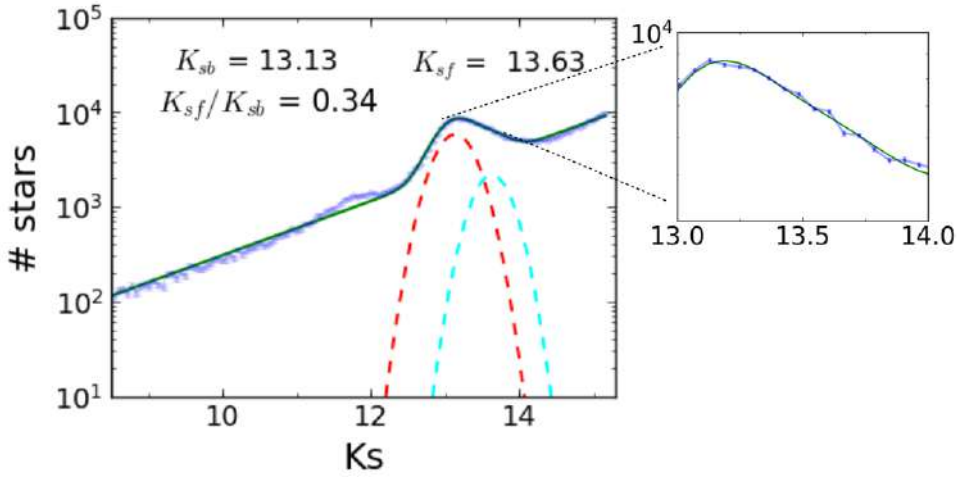

Fig. 9.7 KLF obtained with the K_s de-reddened data applying the completeness correction. In green a two Gaussian plus an exponential background fit. Red and cyan dashed lines show the position of the Gaussians. The inset shows the quality of the data in detail, including the error bars and model fit.

We fitted a simple model of two Gaussians plus an exponential background (Nogueras-Lara et al., 2018b) to the de-reddened KLF (Fig. 9.7). The two Gaussians correspond to the double RC feature that appears in the CMD.

9.4 Star formation history

The luminosity function of a stellar population changes depending on its age. Therefore, the observed KLF can be interpreted as the superposition of the LFs from star formation events at different times. It thus contains the imprint of the formation history of the nuclear disc. We fitted linear combinations of theoretical single age LFs to our measurements. Tracers that constrain the SFH significantly are the relative changes in magnitude and number of stars between three different remarkable features in the LFs (Nogueras-Lara et al., 2018b): the asymptotic giant branch bump, the red clump bump and the red giant branch bump (RGBB).

We assumed a Salpeter initial mass function for the models. Initially, we explored the age-metallicity space by using between two and five single age populations and three different metallicities (Z = 0.02, 0.03 and 0.04). We used the same metallicity for all populations in each fit. The best fit was determined by Chi squared minimisation. The bulk of best fits required a metallicity of Z = 0.04, consistent with the metallicity of the innermost bulge, adjacent to the GC region (Nogueras-Lara et al., 2018b). Although we found that a combination of five ages can already provide us with a satisfactory fit to the measured luminosity function (characterised by a reduced Chi squared value close to 1), a priori, a more complex SFH cannot be excluded. To analyse the SFH more in detail, we resorted to Monte Carlo (MC) simulations to explore the parameter space spanned by the ages and masses of the different star formation events. Additional fitting parameters were a constant interstellar extinction toward the GC (with differential offsets in extinction having already been accounted for through our use of extinction maps), and a parameter for Gaussian smoothing across bins to absorb magnitude variations due to variable distances and measurement uncertainties. From the measured KLF and assuming Gaussian uncertainties, we created 1,000 random KLFs and fitted them with linear combinations of theoretical single age KLFs of ages 13.5, 11, 8, 5, 3, 1, 0.8, 0.6, 0.4, 0.2, 0.1, 0.08, 0.05, 0.03 Gyr (BaSTI models). The oldest isochrone was assumed to be enhanced in alpha elements (Nogueras-Lara et al., 2018b). We selected the fit with the least Chi squared value for each of the 1000 simulated measurements and thus obtained probability distributions for the ages and masses. Because of degeneracies between the contributions of model populations with similar ages (and thus similar LFs), which can be significant for ages > 8 Gyr, we summed the contributions of the different populations into larger bins to avoid larger uncertainties due to degeneracies. To obtain the optimum bin widths, we simulated different SFH with uncertainties equivalent to the ones in real data and apply our technique. Thus, we selected the bin width according to the minimum uncertainties for a given bin (Sec. 9.4.5). We also used MIST isochrones (http://waps.cfa.harvard.edu/MIST/) (Choi et al., 2016; Dotter, 2016; Paxton et al., 2011, 2013, 2015) as an alternative to the BaSTI models, we explored the influence of the assumed stellar evolution models on our results (see Appendix D). While there are some shifts in the best-fit ages, the overall result is unchanged (Fig. 9.8).

The derived SFH is summarised in Fig. 9.8. Over 80% of the stars formed between 8-13.5 Gyr ago. This initial formation was followed by a quiescent period of more than 6 Gyr duration, which was ended by a remarkable event 600 Myr or 1 Gyr ago (depending on the models used), during which $\sim$ 5% of the stellar mass formed (in the following we refer to this as the "1 Gyr event"). Star formation continued in the recent past, but on a lower level. The past 30 Myr have been relatively active with a star formation rate 0.2-0.8 $M_{\odot}$/yr (using BaSTI and MIST models to estimate the uncertainties). Figure 9.9 shows the best fit of the KLF obtained for MIST models.

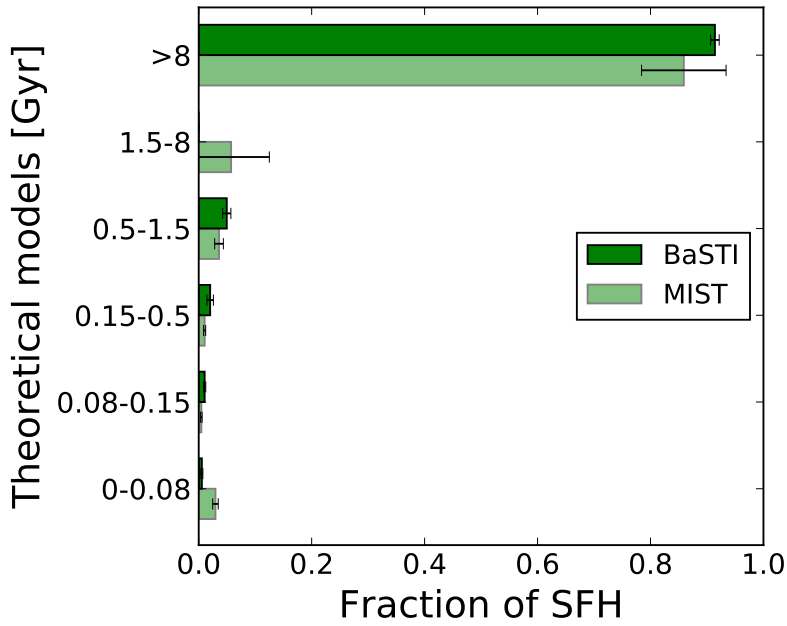

Fig. 9.8 Star formation history of the nuclear stellar disc as derived from the model fits to the KLF with BaSTI and MIST isochrones. There was no contribution for any of the BaSTI models in the range 1.5-8 Gyr.

9.4.1 Analysis of systematic uncertainties

We addressed potential sources of systematic effects and check that the derived SFH does not change significantly:

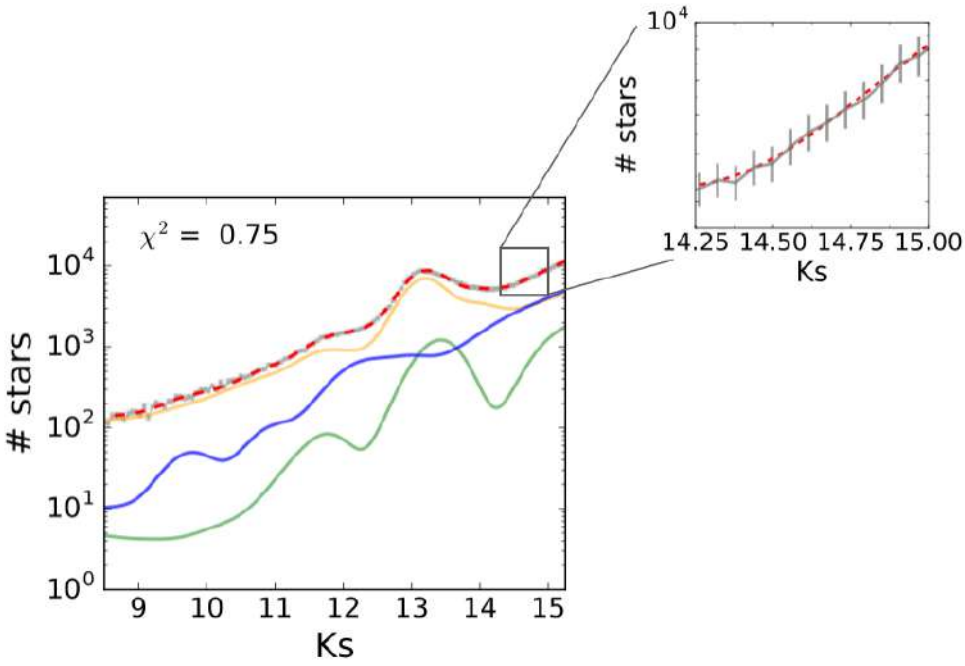

Fig. 9.9 Upper right: KLF (grey), obtained after extinction correction of the observed stars, and best-fit model of the star formation history (red dashed line). For simplicity we combined the theoretical LFs used into old, intermediate and young ages (orange, green and blue, respectively). The zoom shows the quality of the data in detail, including error bars and model fit.

1. **Potential contamination by foreground stars**.

   As discussed previously, contamination by stars from the Galactic disk is negligible and contamination from the innermost bar/bulge may be on the order of a few percent. We repeated our analysis by varying the colour-cut used for the exclusion of foreground stars between $H - K_s = 1.1$ and $H - K_s = 1.5$ and did not find any significant effects. As discussed above, there will be stars from the innermost bar present throughout the NSD, but this population is ~ 12 Gyr old, metal rich, and single age (Nogueras-Lara et al., 2018b) and thus will not affect our conclusions in any significant way.

2. **Contamination from the Galactic bulge**.

Depending on the precise value of the $(H-K_s)$ colour that is used to de-select foreground stars, more or fewer stars from the Galactic bulge may contaminate our nuclear bulge sample. With a stricter criterion ($H-K_s > 1.5$, Fig. 9.2) we can minimise the contribution from inner bulge stars. For this LF, we produced a new extinction map using only RC stars with $H-K_s > 1.5$. The SFH resulting from model fitting to the data with this criterion is very similar, but results in a shift of the oldest nuclear bulge stars toward somewhat (by ~ 2 Gyr) younger ages. This is not surprising given that the innermost bulge (the main contaminant of the nuclear bulge sample) has recently been found to have an age of about 13 Gyr (Nogueras-Lara et al., 2018b).

3. **Using MIST models**.

   We did not find any significant change in the obtained SFH. We note, however that the age of the intermediate age stars shifts from 600 Myr to 1 Gyr when using MIST isochrones (see Sec. 9.4.2).

4. **Bin width of the luminosity functions**.

   We also selected different bin widths for the KLFs, 0.03, 0.06 and 0.1 mag, and confirmed that the results do not change in any significant way.

5. **Dark cloud exclusion**.

   We checked that changing the limit to exclude dark cloud regions does not affect the results.

6. **Extinction maps**.

   We produced different extinction maps for each of the tests involving different selections of stars. In this way, we created extinction maps considering different criteria for the colour cut $H-K_s$ (2), different constrains for excluding the dark clouds regions (5) and a different radius for close stars of $10''$ instead of $5''$. We did not find any significant change in the results.

7. **Different initial mass function**.

   The majority of stars covered by our sample belong to the red giant branch. This means that their stellar evolution is so fast that assuming different IMFs does

not change the results (Fuel consumption theorem Renzini & Fusi Pecci, 1988). To check it, we repeated the analysis using BaSTI models but considering an IMF with alpha = 1.9. We did not find any significant difference.

9.4.2 Theoretical models

We used models from two independent groups to check the possible systematics introduced by the use of any specific theoretical model. We sampled the age parameter according to the differences that appear between the main features present in the LF (AGBB, RC and RGBB) and the relative fraction of stars between them. The LFs change slowly for ages > 5 Gyr, but very rapidly for ages < 2 Gyr which is why we sample young ages more densely. We realised that there are significant differences between the BaSTI and the MIST LFs of certain ages, which will result in age shifts in the inferred SFH. Therefore, we compared the models and selected a slightly different sample of ages for each of them to equally cover the age-space parameter. Fig. 9.10 depicts a comparison between BaSTI and MIST models for different ages with the same metallicity. As can be seen, at ages < 2 Gyr, the MIST LFs that resemble BaSTI LFs correspond to stellar populations around twice as old.

9.4.3 Metallicity of the stellar population

We assumed twice solar metallicity for all theoretical LFs used to derive the SFH. This has to be interpreted as a mean metallicity and does not exclude that the underlying population can show a relatively broad range of metallicities. Spectroscopic studies support that the metallicity of stars of both very old and young ages at the GC have a mean (super-) solar metallicity (e.g., Alves-Brito et al., 2010; Do et al., 2015; Najarro et al., 2009; Nandakumar et al., 2018; Rich et al., 2017; Schultheis et al., 2019). Twice solar metallicity was also found in a photometric study of the innermost bulge, 60-90 pc to Galactic north of Sgr A* (Nogueras-Lara et al., 2018b). Our methodology cannot distinguish between different metallicities at levels more than twice solar. This is due to the fact that the relative distance between the main features in the KLF for young ages (AGBB, RC and RGBB) and their relative stellar fraction do not change much for high metallicities (Fig. 9.11).

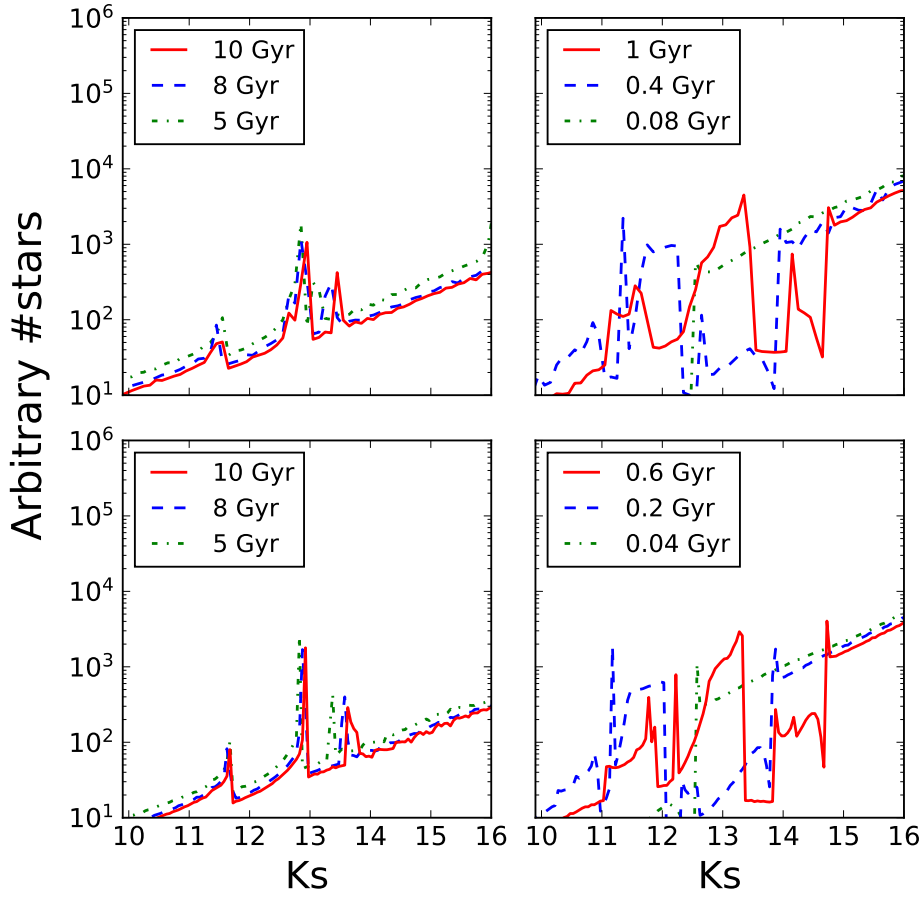

Fig. 9.10 Comparison between MIST models (upper panels) and BaSTI models (lower panels) of different ages and twice solar metallicity.

9.4.4 Alpha-element enhancement of the stellar population

We have assumed the oldest LF in our BaSTI model to be alpha element enhanced ($[\alpha/Fe] = +0.4$) to account for the inner bulge population (Alves-Brito et al., 2010; Nogueras-Lara et al., 2018b). On the other hand, we have used non-alpha element enhanced isochrones to fit the stellar population at the NSD. In this way, we have restricted the parameter space and have decreased the computing time to make it

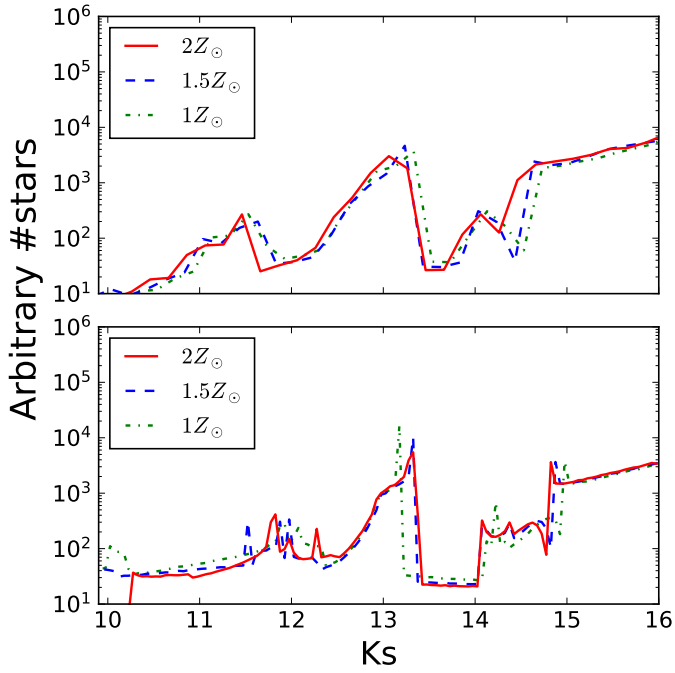

Fig. 9.11 Theoretical ∼1 Gyr KLFs with different metallicities. Upper panel: MIST models. Lower panel: BaSTI models.

affordable. Nevertheless, we have also carried out several tests to check the effect of an alpha element enhanced stellar population at the NSD. In this way, we performed a fit using 5 models varying their ages to cover the age-space parameter, with twice the solar metallicity and with the possibility of being alpha element enhanced or not. We found that the best solution obtained agrees with the scenario that we found using our 14 models fitting. Namely, we found that the minimum chi-square is obtained for a bulk of old stars (alpha element enhanced in this case), followed by a quiescence period, ended by a intermediate-age star formation burst (non-alpha enhanced) and some young star formation (alpha-enhanced). Moreover, we also tested a simple scenario using all the models with an alpha element enhanced population ($[\alpha/Fe] = +0.4$). We obtained that the chi-square increases its value in more than 200 % with respect to the best fit obtained using a non-alpha enriched population for the NSD.

9.4.5 Test with artificial SFHs

To assess the correct performance of our method, we tested it trying to recover artificially created SFHs. We generated three SFHs simulating different scenarios: (1) A non-continuous SFH, similar to the one derived in this work, (2) a continuous constant SFH, and (3) a continuous exponentially decreasing SFH, using BaSTI models. Then, we produced mock KLFs introducing noise according to the real one. Applying our method, we are able to recover the different SFHs within the uncertainties and to distinguish between the different scenarios, in particular between the quasi-continuous and the non-continuous SFHs (Fig. 9.12). This shows that the small uncertainties of our data allow us to overcome possible degeneracies between similar models.

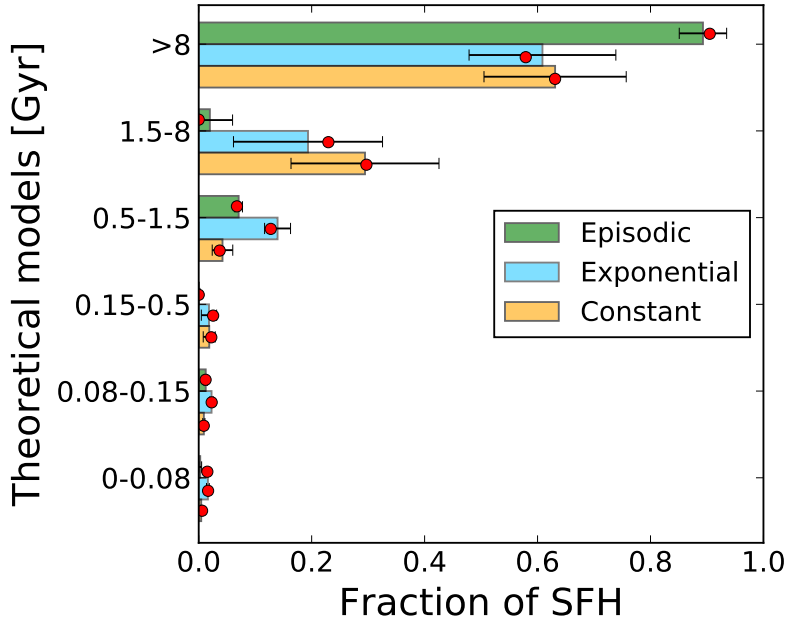

Fig. 9.12 Recovery of simulated star formation histories. Red dots: Assumed SFH. Green, blue and orange bars: Recovered star formation.

9.4.6 Properties of the 1 Gyr event

To estimate the uncertainty in age of the star formation event at 600 Myr/1 Gyr, we used the probability distributions computed for the MC simulations carried out with BaSTI models (Fig. 9.13). The bin that includes the star formation event is composed of three models (1 Gyr, 800 Myr and 600 Myr). We found that for the vast majority of MC samples the only component that contributes to the SFH is the 600 Myr one. Since the RC peak is very sensitive to small age changes for young stellar models (Sec. 9.4.2) and we have considered for the full fitting procedure models of 800 and 400 Myr besides the most probable of 600 Myr, we estimate that the uncertainty in age cannot be larger than 100 Myr for the detected star formation event.

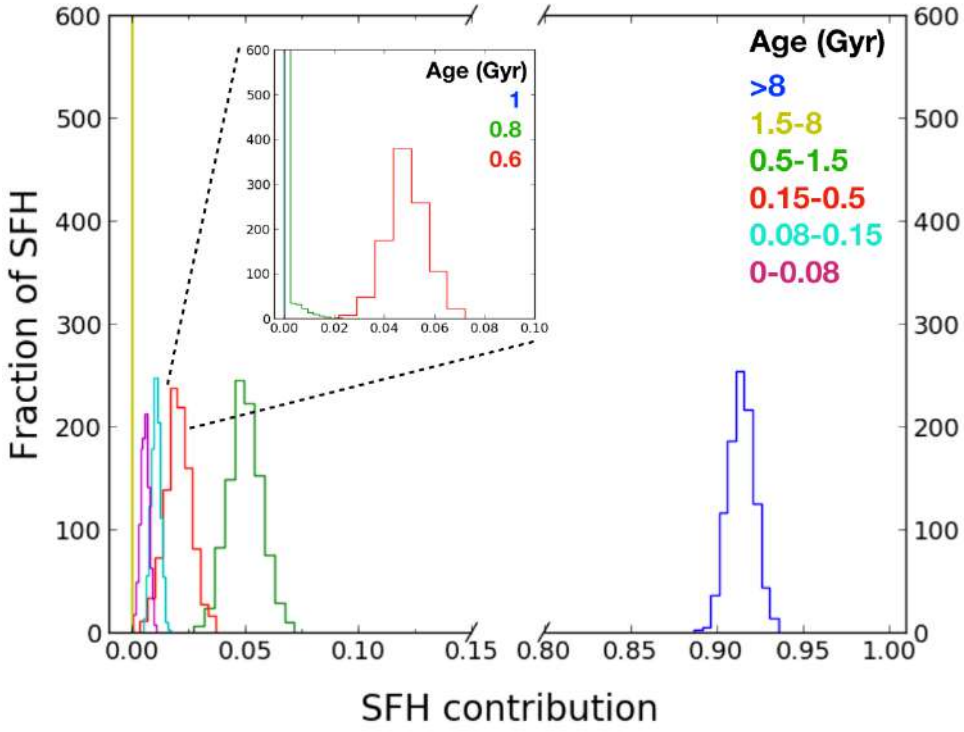

Fig. 9.13 Probability distribution for the MC simulations carried out using BaSTI models. The legend indicates the contribution of each age bin. The inset shows all the models contributing to the bin where we detect the star formation event at ∼1Gyr.

Analysis of the secondary clump in the CMD

A direct confirmation of the detected intermediate age star formation event is the presence of a secondary feature in the RC in the CMD that is indicated by the red arrows in Fig. 9.2. To check that the secondary feature is real, we defined a region that includes both features containing stars with $H-K_s \in [1.3, 2.5]$ and divided it into $H-K_s$ bins of 0.05 mag. For each of them, we fitted the Ks distribution with a single and a double Gaussian model applying the expectation maximisation algorithm implemented in the SCIKIT-LEARN python object GaussianMixture (GMM, Pedregosa et al., 2011). Using the Bayesian Information Criterion (Schwarz, 1978) and the Akaike Information Criterion (Akaike, 1974), we confirmed that a combination of two Gaussians provides a better fit for the data. Both features run parallel to the reddening vector with slopes of $1.19 \pm 0.02 \pm 0.01$ and $1.15 \pm 0.02 \pm 0.01$ for the first and the second feature, respectively, as shown in Fig. 9.14. The uncertainties refer to the statistics and the systematic and were computed using a Jackknife resampling method, with different bin widths and lower cuts for the RC region employed. The distance between features is $\Delta K_s = 0.44 \pm 0.01$. We also estimated the extinction to each feature assuming an extinction index of 2.30 ± 0.08 and a grid of reddened intrinsic colour $(H-K_s)_0$ in steps of 0.01 mag. We minimised the difference between data and the model and obtained very similar extinction values of 1.92 ± 0.14 mag and 1.94 ± 0.16 mag, for the bright and the faint feature, respectively. These similar values allowed us to exclude the alternative scenario of a stellar population beyond the GC to explain the secondary clump. Finally, we also tried to fit a single theoretical LF to the data to exclude the RGBB (Nogueras-Lara et al., 2018b) as the explanation of the secondary feature. We did not get any satisfactory fit. Thus, although RGBB stars must necessarily be present (and are taken into account in the theoretical models used here), it is necessary to consider a secondary RC to fully explain the detected feature.

9.4.7 CMD analysis

The lower completeness in H band due to the lower sensitivity impedes to perform an analysis of its luminosity function as we have shown for the K_s band. Instead, to assess the obtained SFH, we also simulated a CMD K_s versus $H-K_s$ using BaSTI

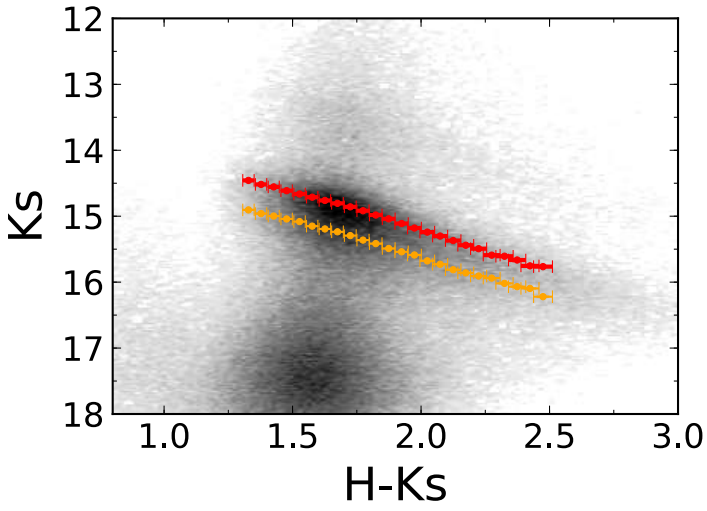

Fig. 9.14 CMD K_s versus $H-K_s$. Red and orange points and uncertainty bars depict the peaks of the best double-Gaussian fit found for each bin of $H-K_s$.

models. We added random noise to the models in H and K_s bands according to the uncertainty of the data, and took into account the reddening using the computed extinction of the RC stars in our sample. We based our analysis exclusively on the relative distance between the RC features to avoid problems related to completeness. From our LF fit we found that the main contributions to the double RC feature arise from the oldest stars ($\gtrsim 80\%$ of the mass is $\gtrsim 8$ Gyr) and from the star formation event at $\sim$1 Gyr. Therefore, we simulated several synthetic CMDs to check this scenario:

1. We simulated just an old population of 8 Gyr to study the contamination by the RGBB. We analysed the RC features using the SCIKIT-LEARN python object GaussianMixture as explained in the previous section. We detected a secondary clump that corresponds to the RGBB at $\Delta K_s = 0.62 \pm 0.02$ mag. This scenario is not compatible with the real data since the relative distance between RC and RGBB is 0.18 ± 0.02 mag larger than in the data, where the uncertainties from real data and the simulation have been propagated quadratically. We concluded

that there is some contamination from the RGBB but it is not enough to explain the double RC detected with our analysis.

2. We generated a SFH similar to the one obtained using stellar models of 8 Gyr, 600 Myr and 40 Myr. We obtained that there is a secondary RC as the one observed in the real data. We computed the distance between features and obtained $\Delta K_s = 0.46 \pm 0.03$ in good agreement with the result obtained for real data ($\Delta K_s = 0.44 \pm 0.01$).

3. We simulated a continuous SFH with a constant star formation rate. We used 5 different models from 0.1 to 10.1 Gyr equally spaced in age and combined them. We repeated the previous analysis and found a two feature structure with $\Delta K_s = 0.61 \pm 0.03$ mag, where the secondary clump is due to the RGBB as in model (1) and incompatible with the data.

4. Finally, we created an exponential star formation history using BaSTI models of 10 Gyr, 8 Gyr, 5 Gyr, 3 Gyr, 1 Gyr, 600 Myr, 200 Myr and 30 Myr. We found a secondary clump due mainly to the 600 Myr models. We found $\Delta K_s = 0.36 \pm 0.04$, which is smaller than what we measure in the actual data. Moreover, the AGBB is much more prominent in this simulation given the fraction of young stars (Fig. 9.15d).

Fig. 9.15 shows the original data and the simulations obtained for (2), (3) and (4). We conclude that only the SFH simulated using the parameters obtained with the KLF analysis is able to reproduce the observed data.

9.5 Mass Estimation

We calculated the total mass of the NSD using the results obtained when fitting the 1000 MC samples with MIST models. For our region, we obtain $(6.5 \pm 0.4) \times 10^7$ $M_\odot$. The NSD was previously estimated to contain $(8 \pm 2) \times 10^8$ $M_\odot$ within R = 120 pc of Sgr A*, based on its near-infrared emission (Launhardt et al., 2002). To cross check this number, we use an extinction and PAH-emission corrected Spitzer 4.5 μm image of the GC42 and integrate the light inside an ellipse centred on Sgr A*

with 120 pc radius along the Galactic plane and a minor-to-major axis ratio of 0.36 (Schödel et al., 2014), after previous subtraction of a model for the bulge emission (Gallego-Cano et al., submitted to A&A). We then scale with a mass-to-luminosity ratio of 0.6 ± 0.2 (Meidt et al., 2014) to obtain a total stellar mass of $(8 \pm 4) \times 10^8$ $M_\odot$, consistent with the one derived from the near-infrared measurements. After scaling the mass derived from the KLF fits of the region studied here to the nuclear bulge inside of 120 pc, we obtain a consistent value of $(9.8 \pm 0.6) \times 10^8$ $M_\odot$, which indicates that our basic method and assumptions, in particular about the initial mass function, appear to be adequate. We computed the total mass of supernovae assuming a standard Salpeter IMF and propagating the uncertainties obtained when considering the total stellar mass formed $\sim$1 Gyr ago (obtained by means of MIST model fitting).

9.6 Results and discussion

In this chapter we present the first detailed star formation history of this region. The bulk of its stars formed at least eight billion years ago. This initial activity was followed by a long period of quiescence that was ended by an outstanding event about 1 Gyr ago, during which roughly 5% of its mass formed in a time window $\sim$100 Myr, in what may arguably have been one of the most energetic events in the history of the Milky Way. Star formation continued subsequently on a lower level, creating a few percent of the stellar mass in the past $\sim$500 Myr, with an increased rate up to $\sim$30 Myr ago. Our findings contradict the previously accepted paradigm of quasi-continuous star formation at the centre of the Milky Way (Figer et al., 2004). The long quiescent phase agrees with the overall quiescent history of the Milky Way (Bland-Hawthorn & Gerhard, 2016; Wyse, 2001) and suggests that our Galaxy's bar may not have existed until recently, or that gas transport through the bar was extremely inefficient during a long stretch of the Milky Way's life, and that the central black hole may have acquired most of its mass already in the early days of the Milky Way.

The obtained SFH is in good agreement with constraints from classical Cepheids (Matsunaga et al., 2011), and requires that a few 10^6 $M_\odot$ stars formed in the recent past in the GC. This implies that, in addition to the known young, massive clusters (the Arches, Quintuplet, and Central clusters), there must be a large number of

clusters that have eluded detection so far because of their partial dissolution in a heavily crowded field (Portegies Zwart et al., 2002). The 1 Gyr event has left a visible imprint in the CMD (Fig. 9.14). The RC sequence is double (see Sec. 9.4.6), with a weaker one, corresponding to stars created in the 1 Gyr event, running parallel to the primary one, about 0.5 magnitudes fainter, that corresponds to the oldest stars. The NSD region within 120 pc of Sgr A* contains $(8 \pm 2) \times 10^8$ $M_\odot$ based on near-infrared flux densities (Launhardt et al., 2002), which we confirm here using independent, mid-infrared measurements. If we scale the $\sim$1,600 pc^2 studied here (Fig. 9.1) to the $\sim$17,000 pc^2 corresponding to the 120 pc radius, then our analysis of the KLF results in a fully consistent mass of $(9.8 \pm 0.6) \times 10^8$ $M_\odot$. If the 1 Gyr event comprised the same area, then it created stars with a total mass of $(4.2 \pm 0.7) \times 10^7$ $M_\odot$. Our modeling shows that the duration of this event was probably shorter than 100 Myr. The star formation rate was thus 0.4-0.5 $M_\odot$/yr, not much lower than the $\sim$1-2 $M_\odot$/yr assumed for the entire Galaxy at present time (Bland-Hawthorn & Gerhard, 2016), but limited to less than 1% of its volume. Hence, scaled to the size of the Milky Way, the conditions in the GC during the 1 Gyr event must have resembled those in starburst galaxies, that form stars at rates $\gtrsim$ 100 $M_\odot$/yr. As a consequence, the 1 Gyr event must have resulted in $\gtrsim 2 \times 10^5$ core collapse supernovae and thus have driven a powerful outflow from the GC region.

The SFH that we found disagrees with the so far accepted paradigm of a quasi-continuous star formation with a roughly constant rate at the GC (Figer et al., 2004). To cross check our results and methodology we applied our method to the previously used NICMOS data set (Figer et al., 2004). We created extinction maps for each field using the same approach described previously. We combined the $\sim$6,000 stars detected in all the NICMOS fields and generated an extinction corrected F205W LF, applying a completeness correction and removing foreground stars as explained before. We found that the SFH is compatible with both a constant SFH and the one that we obtain with our data (Fig. 9.16). This is due to the large uncertainty associated with each LF bin given the low number of stars present in the small regions used. Our GALACTICNUCLEUS data set includes $\sim$100 times more stars and allowed us to constrain the uncertainties pointing towards a non-constant SFH.

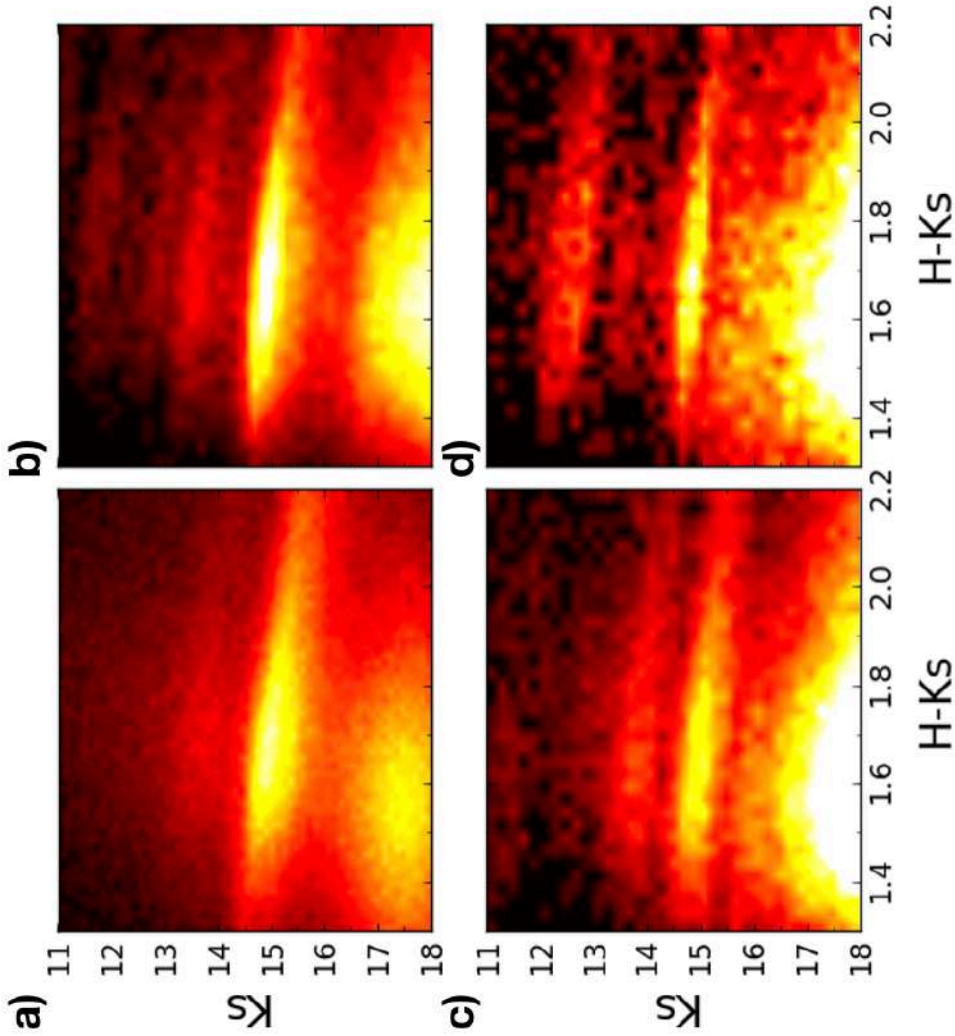

Fig. 9.15 Comparison between CMDs produced using real data (a) and several simulations using BaSTI models: (b) Best-fit solution obtained from the KLF. (c) Continuous SFH. (d) Exponential SFH.

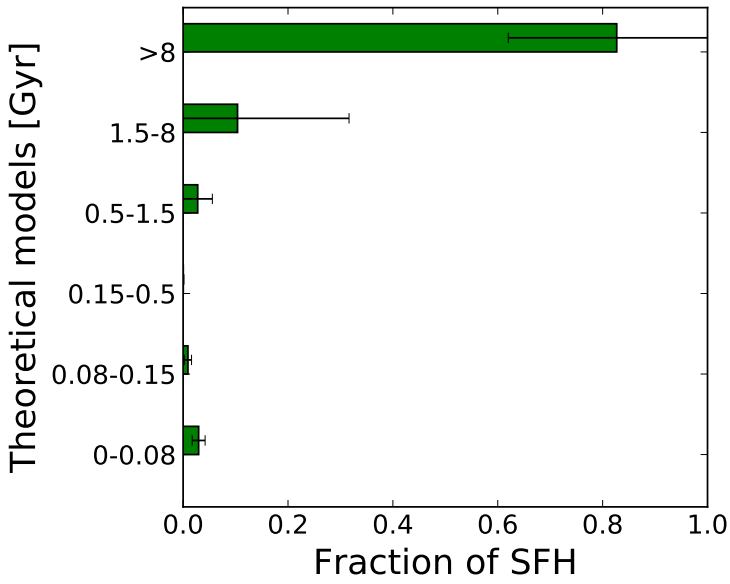

Fig. 9.16 SFH obtained for NICMOS data using BaSTI models.

"Cultiva el alma
y el corazón cautiva
la poesía"

Aurelia Nogueras Lara

10

Star formation history and metallicity in the Galactic inner bulge

In this chapter we computed the SFH for the inner bulge regions covered by GALACTICNUCLEUS to compare it with the SFH derived for the NSD.

10.1 Introduction

Intensive work in the past decade has led to the following approximate picture: About 90% of the population of the Milky Way bulge belong to a bar structure. The stellar population is old (>10 Gyr), with metallicities ranging from [Fe/H] $\lesssim$ -1.0 to supersolar (e.g. Babusiaux et al., 2010; Bensby et al., 2011, 2017; Hill et al., 2011; Johnson et al., 2013; Ness et al., 2013). Enrichment in α elements points towards a rapid formation (Fulbright et al., 2006, 2007). The relative weight of

these populations changes depending on the height above the Galactic plane, and the metal-rich population becomes the dominant population close to the Galactic plane (see review by Barbuy et al., 2018, and references therein). However, the study of its central most regions is very complex because of the extremely high interstellar extinction and source crowding.

Some of the most recent and best data on the structure of the Galactic bulge are provided by the VISTA Variables in the Via Lactea (VVV) survey (Minniti et al., 2010). However, in the innermost degree of the Galaxy, the VVV data suffer from seeing-limited angular resolution and strong saturation of point sources, which mean that the completeness limit is close to or, for the innermost fields, even brighter than the RC.

The high angular resolution GALACTICNUCLEUS survey is key to a better understanding of the structure of the innermost parts of our Galaxy and, in particular, the inner regions of the galactic bulge. In this chapter, we analyse and compare three fields of the survey: One of them is centred on the massive black hole, Sagittarius A* (F1), and the other two lie in the Galactic bar and/or bulge, at about 0.6° and 0.4° to Galactic north, respectively (B1 and B2). We clearly identify a double bump in the luminosity functions of the inner bulge that can be explained as the combination of the RC and the red giant branch bump (RGBB) (see, e.g. Nataf et al., 2011a; Wegg & Gerhard, 2013).

This feature has not been identified before because of the lack of data with sufficiently high angular resolution and/or wavelength coverage. On the other hand, the point spread function (PSF) photometry that is being carried out on the VVV survey (Alonso-García et al., 2017) will improve the situation. It is possible to see the detected feature in Fig. 2 of Alonso-García et al. (2017). This supports the reality of the detection and shows that it is not located only in the fields analysed in this work. The high dependence of the separation between these two features on metallicity allows us to estimate the metallicity and its gradient in the inner bulge fields under study.

10.2 Data

For this study we used three pointings of the GALACTICNUCLEUS survey: F1 corresponds to a GC comparison field, centred on SgrA* ($17^h\ 45^m\ 40.1^s$, -29° 00′ 28″) and two fields in the bulge (B1 and B2), located ∼0.6° and ∼0.4° to Galactic North, outside of the Nuclear Bulge (NB) of the Galaxy (Launhardt et al., 2002; Nishiyama et al., 2013), with centre coordinates $17^h\ 43^m\ 11.6^s$, -28° 41′ 54″ and $17^h\ 43^m\ 53.8^s$, -28° 48′ 07″. The approximate size of the fields is 7.95′ × 3.43′. Figure 10.1 shows the location of the fields (see Fig. 3.5 for further details).

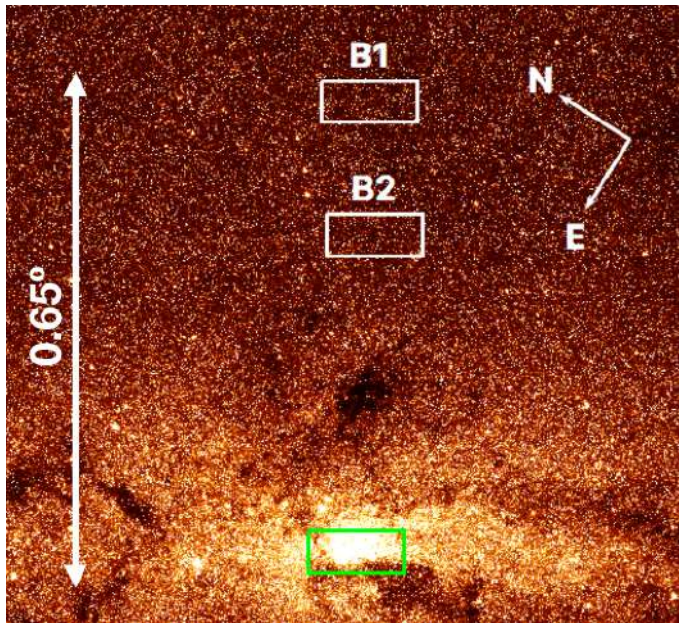

Fig. 10.1 Scheme of the observed fields over-plotted on a Spitzer/IRAC image at 3.6 μm. B1 and B2 correspond to fields in the bulge, and the field at the bottom (in green) is centred on Sagittarius A*.

10.3 CMD and identification of a double red clump

Figure 10.2 shows the $J - K_s$ colour-magnitude diagram (CMD) of the two fields in the bulge with respect to the GC comparison field (in red). Stars with colours

$J-K_s \lesssim 3$ lie in the foreground, with three over-densities indicating spiral arms (Nogueras-Lara et al., 2018a). The vertical feature at $J-K_s$ between $\approx 3-3.5$ in the upper panel corresponds to the bulge stars in B1, while the extended and highly populated feature at $4 \lesssim J-K_s \lesssim 6$ traces the stars in F1. Analogously, the black vertical feature at $J-K_s \approx 4$ in the lower panel corresponds to the bulge stars in B2. This field has a higher interstellar extinction than F1. The dense regions at $K_s \approx 14$ and $K_s \approx 15$ indicate the location of RC stars in B1-B2 and F1, respectively. The stars in F1 lie deeply embedded in the central molecular zone, and their extinction is about 1 mag higher in K_s than in B1. The RC populations of all three fields are aligned following the same reddening vector.

A secondary clump is visible at fainter magnitudes below the RC in B1 and B2. To better characterise the visually detected features, we defined a region in the CMD that includes both features ($J-K_s \in [3.1, 3.75]$ for B1 and $J-K_s \in [3.6, 4.3]$ for B2) and divided it into small bins of 0.05 mag in colour. We analysed the distribution of stars in each bin using the SCIKIT-LEARN python function GaussianMixture (GMM, Pedregosa et al., 2011). In this way, we applied the expectation maximisation algorithm to fit and compared a single- and double-Gaussian model. For this, we used the Bayesian information criterion (BIC) (Schwarz, 1978) and the Akaike information criterion (AIC) (Akaike, 1974). We confirmed the visual detection and obtained that a double-Gaussian model fits the data better. Figure 10.3 shows a linear fit to the means of the two Gaussians in each bin. For B1 we obtained a slope of $0.45 \pm 0.05 \pm 0.04$ for the bright and $0.45 \pm 0.05 \pm 0.02$ for the faint clump. Analogously, we obtained $0.42 \pm 0.03 \pm 0.03$ and $0.43 \pm 0.05 \pm 0.04$ for B2. The first uncertainty corresponds to the statistical uncertainty and was calculated using a jackknife resampling method. The second uncertainty refers to the systematics and was computed considering different bin widths and lower limits of the $J-K_s$ cut-off. Both slopes agree perfectly within their uncertainties.

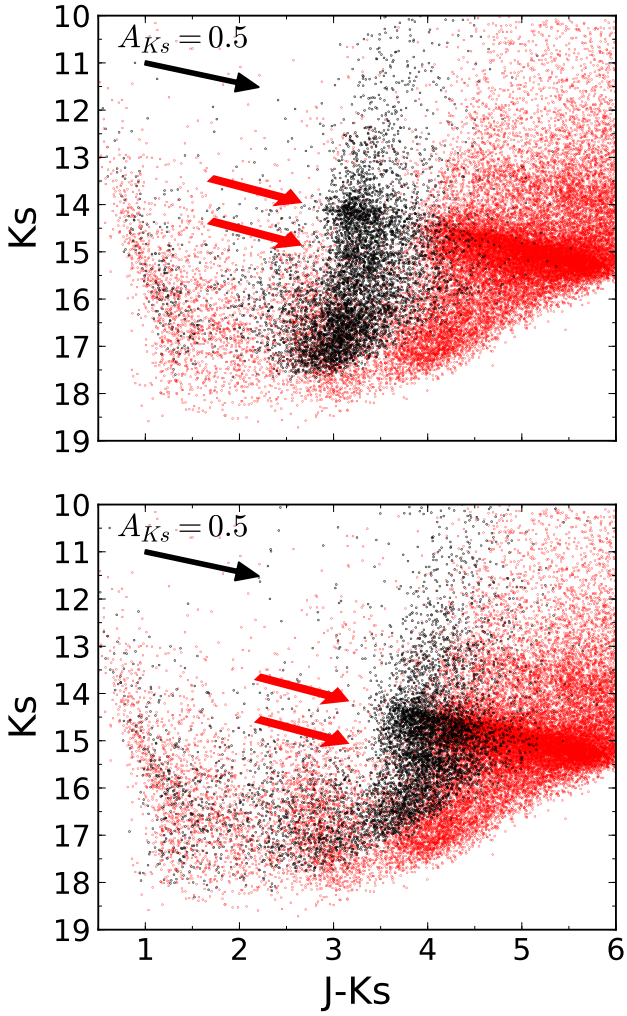

Fig. 10.2 CMD for bulge fields (black) and F1 (red). The upper and lower panel show B1 and B2, respectively, and the GC comparison field, F1. The red arrows indicate the RC in each CMD as well as the fainter density features running parallel to the RC below the red clump. Only a randomly selected fraction of the stars is shown for clarity. The black arrows correspond to an extinction of $A_{Ks} = 0.5$ mag.

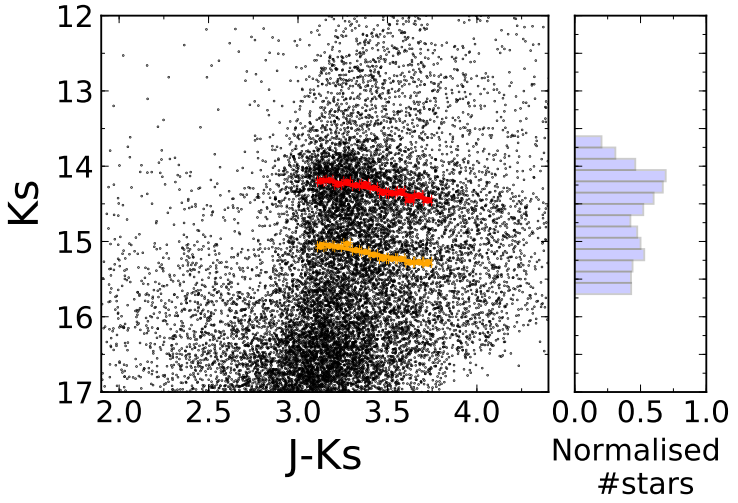

Fig. 10.3 Derivation of the slopes for B1. Main panel: CMD for B1. Red and orange lines indicate the mean values obtained using the GMM and linear fits in several bins 0.05 mag wide in colour. Right panel: Normalised histogram of all the stars in $J-K_s \in [3.1, 3.75]$ and $K_s \in [13.6, 15.7]$.

10.4 Characterisation of the features

10.4.1 Interstellar extinction

In this section we compute the extinction of the two different groups (RC and faint bump) in the two fields and compare it. First of all, for the two fields in the bulge, we computed the stars belonging to each group by obtaining the line that indicates a 50% probability of membership using the GMM. In addition, to avoid the bias introduced by the initial RC selection, we accepted a star in one of the two groups only if it was within 2σ of the corresponding Gaussian distribution. We built histograms for each feature and obtained a Gaussian-like distribution with mean values of $K_{s\_bright} = 14.28 \pm 0.01 \pm 0.05$ mag and $K_{s\_faint} = 15.15 \pm 0.01 \pm 0.04$ mag for B1 and $K_{s\_bright} = 14.60 \pm 0.01 \pm 0.06$ mag and $K_{s\_faint} = 15.37 \pm 0.01 \pm 0.06$ mag for B2. The errors refer to statistical and systematic uncertainties, respectively. The systematics take into account different cuts of the lower limit of $J-K_s$ and different

selections of the bin width. The difference in mean K_s between the two features is thus 0.87 ± 0.08 mag and 0.77 ± 0.08 mag for B1 and B2, respectively, where the uncertainties were propagated quadratically. If this magnitude difference were only due to extinction, then the fainter clump should have a significantly redder colour. Assuming the extinction curve of Nogueras-Lara et al. (2018a), the corresponding difference in colour would be $\Delta(J-K_s) \approx 1.9 \pm 0.2$ for both fields. However, the observed colours are similar in both cases.

An alternative way to assess whether interstellar extinction may contribute to the magnitude separation between the features is the following: If both features have approximately the same extinction, then their magnitude separation computed from the difference of the means of the two Gaussians should be equal to the one obtained by averaging over the Gaussian means obtained for each 0.05 mag bin that were computed above to compare the slopes of the two features (see Fig. 10.3). The latter value is 0.86 ± 0.03 mag and 0.75 ± 0.03 mag for B1 and B2, respectively. The uncertainty refers to the standard deviation of the distribution of the distances. Comparing these two values, we can assume that extinctions between features are very similar in both cases.

Finally, we computed the extinction to each clump from the measured magnitudes of each star. We assumed the extinction index 2.30 ± 0.08 derived in Nogueras-Lara et al. (2018a). We computed the theoretical intrinsic colours $J-H$ and $H-K_s$ expected for the stars in the clumps. All these stars lie along a (reddened) red giant branch and will therefore have similar intrinsic colours if their luminosities are not extremely different. Thus, we chose an RC theoretical model to calculate the intrinsic colours following the method described in Sec. 6.1. of Nogueras-Lara et al. (2018a). We created a grid of extinctions in steps of 0.01 mag and computed the corresponding reddened colours. Then, we defined the χ^2 of the differences between the grid of colours and the real data for each RC feature. We computed the average extinctions and obtained almost equal values for stars belonging to each feature. The mean values are $A_{K_{s\_bright}} = 1.19 \pm 0.08$ and $A_{K_{s\_faint}} = 1.20 \pm 0.08$ for B1 and $A_{K_{s\_bright}} = 1.47 \pm 0.10$ and $A_{K_{s\_faint}} = 1.48 \pm 0.10$, for B2. The uncertainty corresponds to systematics and the statistical uncertainty is negligible. The systematics were computed analogously to those in Sec. 6.1. of Nogueras-Lara et al. (2018a).

We conclude that there is no significant difference in absolute interstellar extinction between the two groups of stars. With the obtained absolute extinction values and the slopes of the features, we computed the extinction index using the following expression:

$$\alpha = -\frac{\log(1+\frac{1}{m})}{\log(\frac{\lambda_{\mathrm{eff}_1}}{\lambda_{\mathrm{eff}_2}})}, \tag{10.1}$$

where m is the slope in the CMD λ_{eff_2} versus $\lambda_{\mathrm{eff}_1} - \lambda_{\mathrm{eff}_2}$, with $\lambda_{\mathrm{eff}_1} = J$ and $\lambda_{\mathrm{eff}_2} = K_s$ and $\lambda_{\mathrm{eff_i}}$ is the effective wavelength (for details, see Nogueras-Lara et al., 2018a). For B1, we obtained $\alpha_{bright} = 2.22 \pm 0.15 \pm 0.13$ and $\alpha_{faint} = 2.21 \pm 0.13 \pm 0.07$, whereas for B2 $\alpha_{bright} = 2.31 \pm 0.09 \pm 0.08$ and $\alpha_{faint} = 2.28 \pm 0.15 \pm 0.13$. These values agree perfectly with the extinction index of 2.30 ± 0.08 obtained in Nogueras-Lara et al. (2018a). Therefore we can conclude that the extinction curve in the near-infrared between J and K_s does not vary spatially between these fields within the uncertainties. The higher uncertainties found for B1 can be explained by the lower extinction of this field. The higher the extinction, the wider the spread of the stars along the reddening vector, which facilitates calculating the slope of the distribution.

10.4.2 Extinction map

To better characterise the detected features, we need to produce extinction maps that allow us to correct the extinction (and the differential extinction) in the studied fields. We calculated extinction maps using the method described in Sec. 7.4 (and in Nogueras-Lara et al., 2018a).

We defined a pixel scale of $0.5''$/pixel and used the following equation to compute the extinction:

$$ext = \frac{m_1 - m_2 - (m_1 - m_2)_0}{\left(\frac{\lambda_{m_1}}{\lambda_{m_2}}\right)^{-\alpha} - 1}, \tag{10.2}$$

where m_1 and m_2 are the magnitudes for two bands, the subindex 0 indicates the intrinsic colour, and λ_i are the effective wavelengths. We used the colour $J - K_s$ since the difference in wavelength is larger than between $H - K_s$ or $J - H$. In this way, we reduced by a factor of three the systematic uncertainty of the map associated to

the uncertainty of the ZP in comparison with using $H - K_s$. Moreover, the relative uncertainty of the intrinsic colour is much lower in the case of $J - K_s$ because the uncertainties of the intrinsic magnitudes are of the same order, but the colour term $(J - K_s)$ is ∼6 times larger than for $(H - K_s)$.

To build the extinction map, we used only the stars in the two features. They are most probably RC stars or RGBB stars and have similar intrinsic colours (see Table 10.1). We computed the extinction for each pixel taking into account only the ten closest stars (within a maximum radius of 15″) and weighting the distances with an inverse-distance weight (IDW) method (see Nogueras-Lara et al. 2018a for details). We did not assign any value to the pixels without the minimum number of required close stars. For the subsequent analysis, we excluded stars located in regions where the extinction maps have no value (∼ 20% of the image for both fields). We obtained fairly homogenous extinction maps for B1 and B2 with mean extinctions of $A_{K_s} = 1.14$ mag and $A_{K_s} = 1.39$ mag and a standard deviation of 0.06 mag and 0.06 mag, respectively. The statistical and systematic uncertainties for the extinction maps are ∼ 3% and ∼ 7% for B1 and ∼ 3% and ∼ 6% for B2. The statistical uncertainty considers the dispersion of the values of the ten closest stars and the possible variation of the intrinsic colour, whereas the systematics take into account the uncertainties of the extinction index, the ZP and the effective wavelengths.

Figure 10.4 shows the extinction-corrected CMDs K_s versus $J - K_s$ for both fields. To exclude the foreground population and highly extinguished or intrinsically reddened stars, we selected only stars between the red dashed lines in the uncorrected CMDs, as indicated in the figure. As can be seen, the application of the extinction map considerably reduces the scatter of the points since it lets us correct the differential extinction. The standard deviation of the distribution of the de-reddened colours around the detected features is $\sigma = 0.07$ in both cases.

10.4.3 Luminosity function

To obtain the luminosity function (LF) of the de-reddened K_s data, we used the extinction map computed in the previous section and applied it to the K_s-band data. To deselect foreground stars, we used the $H - K_s$ colour because the $H-$ and K_s- band data are far more complete than the J-band data due to the steep NIR extinction

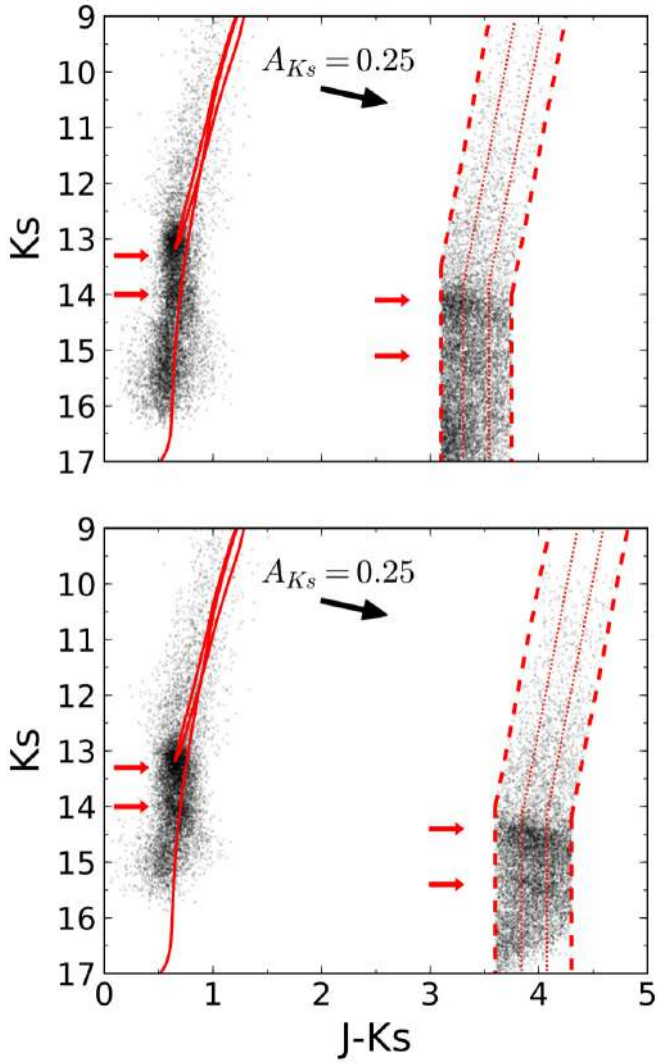

Fig. 10.4 CMD K_s vs. $J - K_s$ with and without extinction correction. Red arrows show the position of the detected features. The black arrow indicates the reddening vector. The red continuous line corresponds to an isochrone of 13.5 Gyr and Z = 0.04 plotted over the de-reddened stars. Upper and lower panels show B1 and B2, respectively. Red dotted lines show different divisions of the data used to produce LFs. Accounting for atomic diffusion would reduce the age of the depicted isochrone $\sim 0.7 - 1$ Gyr (see main text).

law. We converted the colour cuts shown in Fig. 10.4 into the corresponding colours in $H-K_s$ with the extinction curve given by Nogueras-Lara et al. (2018a). Figure 10.5 shows the obtained LFs, which are complete down to 2 mag fainter than the faint feature clump.

To determine the reddening-free magnitude of the detected features and the associated distance between them, we fitted a two Gaussian model plus an exponential background to the LFs (as done in Wegg & Gerhard, 2013). We selected a bin width of 0.035 mag to produce the LFs and found that this simple model fits the data well (reduced χ^2 = 1.39 and 1.61 for B1 and B2 respectively). We obtained $K_{s\ bright} = 13.12 \pm 0.01 \pm 0.08$ mag and $K_{s\ faint} = 13.92 \pm 0.03 \pm 0.08$ mag for B1 and $K_{s\ bright} = 13.24 \pm 0.01 \pm 0.07$ mag and $K_{s\ faint} = 14.03 \pm 0.02 \pm 0.07$ mag for B2. The uncertainties correspond to the statistical uncertainty and the systematics, respectively. The systematics were computed considering the systematic error of the extinction map, the values of the fit using different bin widths to create the LF and the ZP uncertainty. The distance between the two features is $\Delta K_s = 0.80 \pm 0.03$ mag for B1 and $\Delta K_s = 0.79 \pm 0.02$ for B2. The uncertainty corresponds to the quadratic propagation of the statistical errors, because the systematics affect both peaks equally.

Moreover, we computed the relative fraction of stars between both features, $f_{f/b}$ (number of stars in the faint feature / number of stars in the bright feature) integrating over the Gaussians corresponding to each individual peak. We obtained $f_{f/b} = 0.32 \pm 0.04$ and $f_{f/b} = 0.33 \pm 0.04$ for B1 and B2, respectively. The uncertainty was calculated through Monte Carlo simulations considering the uncertainties of the parameters of the best fit of the LFs.

10.5 Discussion

We discuss the following possible explanations for the two peaks observed in the K_s-band LF: 1) RC stars at different distances. 2) A combination of different ages and/or metallicities of the RC stars. 3) The fainter feature could be explained by the red giant branch bump (RGBB).

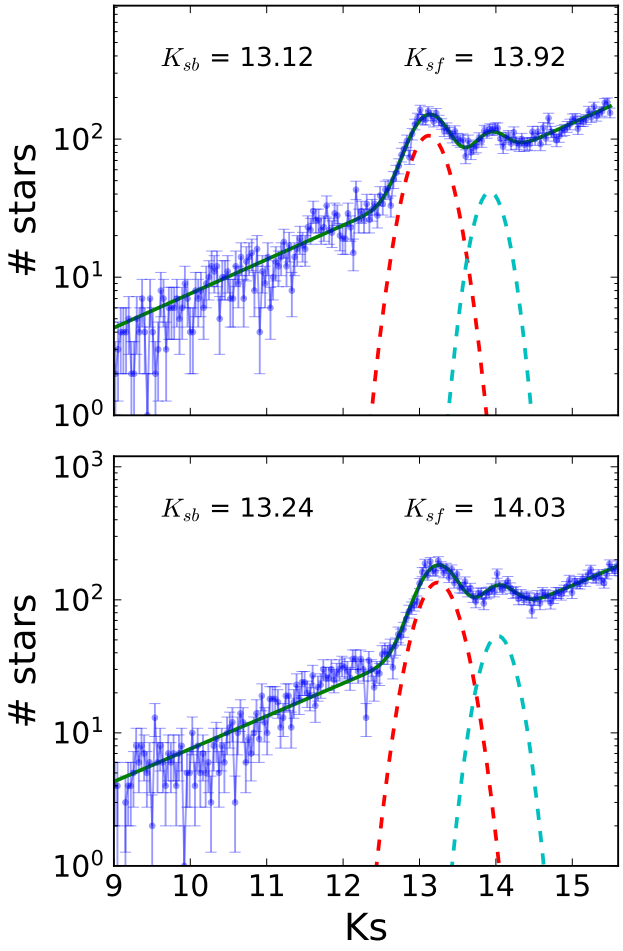

Fig. 10.5 K_s-band de-reddened LF. The green line depicts the best fit using an exponential plus two Gaussians model. Red and cyan dashed lines show the position of the two Gaussians of the model. K_{sb} and K_{sf} correspond to the Gaussian peaks of the bright and faint feature, respectively. Upper and lower panel show B1 and B2, respectively.

10.5.1 Possible scenarios

1) Different distances between the two observed RCs could explain the detected features. Since we have computed the extinction-corrected magnitudes and distance between the two features, we can use the distance modulus to calculate the distances to each one assuming that both correspond to RC stars. For this, we took the values obtained for B1. We assumed an absolute RC magnitude of $M_K = -1.54 \pm 0.04$ as in Groenewegen (2008) and considered that the difference between the K and the K_s magnitudes is ≈ 0.01 (Nishiyama et al., 2006b). In addition, we used a population correction factor, $\Delta M_{K_s} = -0.07 \pm 0.07$ (Nishiyama et al., 2006b). The extinction-corrected magnitude for the bright peak is $K_{s\_bright} = 13.12 \pm 0.08$ (adding quadratically the systematics and statistical uncertainties), and the difference with respect to the faint peak is 0.80 ± 0.03 mag. The obtained distance for the bright clump is 8.3 ± 0.4 kpc, fully consistent with the well-determined distance of the GC ($8.32 \pm 0.07|_{stat} \pm 0.14|_{sys}$ kpc, Gillessen et al., 2017). Accordingly, the faint RC feature would be located at a distance of 3.7 ± 0.4 kpc beyond the bright clump, clearly beyond the GC. However, this scenario is very unlikely, because we previously determined the extinction to each feature and obtained a very similar value for both features. It is highly improbable that there is no extinction between the GC and more than three kpc beyond it. The situation for B2 is analogous. Moreover, similar detections of a second bump in the LF located at $\sim 0.70 - 0.74$ mag fainter than the RC have been made previously at larger latitudes ($b > 2°$) (e.g., Nataf et al., 2013, 2011b; Wegg & Gerhard, 2013). In those cases, the distance from the Galactic plane means that a spiral arm beyond the GC is highly improbable. For all of this, we can safely exclude this possibility.

2) The luminosity of RC stars depends on their ages and metallicities. However, this variation can account for at most 0.5 mag in K_s (see Figure 6 in Girardi, 2016) if one of the two stellar populations happens to be very young. Even then, this is still ~ 0.2 mag smaller than the observed difference between the detected features. If we assume that all RC stars in our CMD are older than about 2 billion years, then we obtain an even stronger constraint because then the separation between any two populations cannot be larger than $\Delta K_s \approx 0.2$. Therefore, we cannot explain the observed feature as a consequence of RC stars with different ages or metallicities.

3) The RGBB is a feature in the CMD of old stellar populations corresponding to the evolutionary stage during which the H-burning shell approaches the composition discontinuity left by the deepest penetration of the convective envelope during the I^{th} dredge-up (Cassisi & Salaris, 1997; Nataf et al., 2014; Salaris et al., 2002, and references therein). Since the RGBB brightness depends on the maximum depth attained by the convective envelope and on the chemical profile above the advancing H-burning shell, its brightness depends on the stellar metallicity and age (see Cassisi & Salaris (2013) for a detailed discussion of this issue). To study the magnitude difference between the RGBB and the RC, we used the BaSTI[1] isochrones (Pietrinferni et al., 2004, 2006) extended along the asymptotic giant branch (some of the isochrones have been computed specifically for this work, using the same BaSTI code as for the freely available ones[1]). To simulate the stellar population of the bulge, we considered that it can be modelled by a mostly old, α-enhanced system (Alves-Brito et al., 2010; Johnson et al., 2014; Lecureur et al., 2007; McWilliam & Rich, 1994; McWilliam & Zoccali, 2010; Meléndez et al., 2008; Zoccali et al., 2003). We constructed the LFs corresponding to a range of metallicities and ages (between 5 Gyr and 13 Gyr) using the BaSTI web tools[1]. We fitted the LFs with a three-Gaussian model plus an exponential background, which takes into account theasymptotic giant branch bump (AGBB)[2] , the RC, and the RGBB. The results are shown in Table 10.1. For the calculations, we assumed a distance modulus of $\mu = 14.60 \pm 0.05$ (Gillessen et al., 2017). To take into account the uncertainties caused by the different distances of the stars along the line of sight as well as by the extinction correction, we smoothed the theoretical LF data points with Gaussians, the FWHM of which was a free parameter during the fits. For the uncertainties we also considered the (minor) differences between the K and K_s bands. Table 10.1 summarises the resulting RC and RGBB brightnesses and their relative fractions according to the isochrones of different ages and metallicities. Given that the RGBB is expected to be present in LFs of old population and given the good fit by the isochrone models, we can conclude that the detection of the RGBB is the most plausible explanation for the observed greater faintness of the secondary clump compared to the RC.

[1] http://basti.oa-teramo.inaf.it

[2] This feature has not been taken into account for the data analysis as it might be too faint to be observed within the uncertainties.

Table 10.1 Properties of the AGBB, RC and RGBB obtained using the alpha-enhanced BaSTI isochrones.

Age (Gyr)	Z	Y	[Fe/H]	[M/H]	K_{AGBB} (mag)	K_{RC} (mag)	K_{RGBB} (mag)	$(J-K)_{RC}$ (mag)	$(J-K)_{RGBB}$ (mag)	f^{RC}_{RGBB}	$\Delta_{RGBB-RC}$ (mag)
	0.0198	0.2734	-0.29	0.06	11.62	12.92	13.28	0.65	0.69	0.16 ± 0.02	0.36±0.02
	0.03	0.288	-0.09	0.26	11.52	12.91	13.33	0.66	0.69	0.16 ± 0.01	0.42±0.02
5	0.035	0.295	-0.02	0.329	11.54	12.87	13.33	0.69	0.70	0.15 ± 0.01	0.46±0.01
	0.04	0.303	0.05	0.4	11.52	12.86	13.42	0.66	0.70	0.16 ± 0.01	0.56±0.02
	0.045	0.310	0.105	0.454	11.5	12.82	13.43	0.70	0.70	0.16 ± 0.01	0.61±0.01
	0.05	0.316	0.16	0.51	11.47	12.77	13.43	0.74	0.70	0.15 ± 0.01	0.66±0.01
	0.0198	0.2734	-0.29	0.06	11.63	13.02	13.43	0.64	0.69	0.22 ± 0.01	0.41±0.02
	0.03	0.288	-0.09	0.26	11.58	12.97	13.59	0.65	0.73	0.24 ± 0.01	0.62±0.01
8	0.035	0.295	-0.02	0.329	11.55	12.94	13.52	0.68	0.75	0.21 ± 0.01	0.58±0.01
	0.04	0.303	0.05	0.4	11.53	12.92	13.63	0.70	0.69	0.23 ± 0.01	0.71±0.01
	0.045	0.310	0.105	0.454	11.49	12.89	13.67	0.68	0.70	0.23 ± 0.01	0.78±0.01
	0.05	0.316	0.16	0.51	11.5	12.87	13.67	0.71	0.70	0.22 ± 0.01	0.80±0.01
	0.0198	0.2734	-0.29	0.06	11.64	13.02	13.52	0.65	0.65	0.24 ± 0.01	0.50±0.01
	0.03	0.288	-0.09	0.26	11.59	12.97	13.63	0.70	0.69	0.25 ± 0.01	0.66±0.01
9	0.035	0.295	-0.02	0.329	11.58	12.97	13.62	0.69	0.70	0.24 ± 0.0	0.65±0.01
	0.04	0.303	0.05	0.4	11.55	12.92	13.68	0.70	0.69	0.24 ± 0.01	0.76±0.01
	0.045	0.310	0.105	0.454	11.52	12.87	13.72	0.75	0.70	0.25 ± 0.01	0.85±0.01
	0.05	0.316	0.16	0.51	11.5	12.87	13.72	0.70	0.70	0.24 ± 0.01	0.85±0.01

Table 10.1 Properties of the AGBB, RC and RGBB obtained using the alpha-enhanced BaSTI isochrones.

Age (Gyr)	Z	Y	[Fe/H]	[M/H]	K_{AGBB} (mag)	K_{RC} (mag)	K_{RGBB} (mag)	$(J-K)_{RC}$ (mag)	$(J-K)_{RGBB}$ (mag)	f^{RC}_{RGBB}	$\Delta_{RGBB-RC}$ (mag)
	0.0198	0.2734	-0.29	0.06	11.66	13.07	13.57	0.65	0.65	0.25 ± 0.01	0.50±0.01
	0.03	0.288	-0.09	0.26	11.6	13.02	13.68	0.65	0.66	0.26 ± 0.01	0.66±0.01
10	0.035	0.295	-0.02	0.329	11.57	12.97	13.67	0.70	0.75	0.26 ± 0.01	0.70±0.01
	0.04	0.303	0.05	0.4	11.54	12.92	13.72	0.75	0.70	0.26 ± 0.01	0.80±0.01
	0.045	0.310	0.105	0.454	11.52	12.91	13.72	0.71	0.75	0.25 ± 0.01	0.81±0.01
	0.05	0.316	0.16	0.51	11.5	12.87	13.77	0.75	0.70	0.24 ± 0.01	0.90±0.01
	0.0198	0.2734	-0.29	0.06	11.67	13.07	13.56	0.66	0.71	0.26 ± 0.01	0.49±0.01
	0.03	0.288	-0.09	0.26	11.6	13.02	13.67	0.70	0.70	0.26 ± 0.01	0.65±0.01
11	0.035	0.295	-0.02	0.329	11.58	12.97	13.73	0.70	0.69	0.27 ± 0.01	0.76±0.01
	0.04	0.303	0.05	0.4	11.56	12.97	13.77	0.70	0.70	0.26 ± 0.01	0.80±0.01
	0.045	0.310	0.105	0.454	11.54	12.97	13.82	0.70	0.65	0.27 ± 0.01	0.85±0.01
	0.05	0.316	0.16	0.51	11.5	12.92	13.77	0.70	0.75	0.25 ± 0.01	0.85±0.01
	0.0198	0.2734	-0.29	0.06	11.7	13.13	13.56	0.64	0.76	0.25 ± 0.02	0.43±0.02
	0.03	0.288	-0.09	0.26	11.61	13.07	13.68	0.65	0.74	0.27 ± 0.01	0.61±0.01
12	0.035	0.295	-0.02	0.329	11.59	13.04	13.75	0.68	0.72	0.27 ± 0.01	0.71±0.01
	0.04	0.303	0.05	0.4	11.56	12.97	13.77	0.70	0.75	0.27 ± 0.01	0.80±0.01
	0.045	0.310	0.105	0.454	11.54	12.97	13.82	0.70	0.70	0.27 ± 0.01	0.85±0.01
	0.05	0.316	0.16	0.51	11.5	12.92	13.82	0.75	0.70	0.26 ± 0.01	0.90±0.01

Table 10.1 Properties of the AGBB, RC and RGBB obtained using the alpha-enhanced BaSTI isochrones.

Age (Gyr)	Z	Y	[Fe/H]	[M/H]	K_{AGBB} (mag)	K_{RC} (mag)	K_{RGBB} (mag)	$(J-K)_{RC}$ (mag)	$(J-K)_{RGBB}$ (mag)	f^{RC}_{RGBB}	$\Delta_{RGBB-RC}$ (mag)
	0.0198	0.2734	-0.29	0.06	11.73	13.24	13.66	0.58	0.71	0.26 ± 0.02	0.42 ± 0.02
	0.03	0.288	-0.09	0.26	11.64	13.12	13.72	0.65	0.70	0.27 ± 0.01	0.60 ± 0.01
13	0.035	0.295	-0.02	0.329	11.6	13.07	13.77	0.65	0.70	0.28 ± 0.01	0.70 ± 0.01
	0.04	0.303	0.05	0.4	11.58	13.02	13.82	0.71	0.70	0.28 ± 0.01	0.80 ± 0.01
	0.045	0.310	0.105	0.454	11.55	13.02	13.79	0.70	0.78	0.27 ± 0.01	0.77 ± 0.02
	0.05	0.316	0.16	0.51	11.53	12.97	13.82	0.70	0.75	0.26 ± 0.01	0.85 ± 0.01

Notes. K_{AGBB}, K_{RC} , and K_{RGBB} are the K-band peaks obtained for the Gaussian fits of the LF. f^{RC}_{RGBB} is the relative fraction of RGBB stars of that in RC stars. $\Delta_{RGBB-RC}$ is the distance between the peaks $K_{RGBB} - K_{RC}$. The uncertainties that are not specified in the table are $\Delta K_{AGBB} = \pm 0.05$, $\Delta K_{RC} = \pm 0.05$, $\Delta K_{RGBB} = \pm 0.05$, $\Delta(J-K)_{RC} = 0.01$, and $\Delta(J-K)_{RGBB} = 0.01$. Accounting for atomic diffusion would reduce the age of the models $\sim 0.7 - 1$ Gyr (see main text).

$\Delta_{RGBB-RC}$ is strongly dependent on the metallicity (Nataf et al., 2014), and f^{RC}_{RGBB} is a good indicator of age, as can be seen from the Table 10.1. We can thus use the values measured by us, $f^{RC}_{RGBB} = 0.33 \pm 0.04$ and $\Delta_{RGBB-RC} = 0.80 \pm 0.02$, to constrain the age and metallicity of the inner bulge. We can exclude with more than 4σ significance all scenarios with metallicities below $Z = 0.035$. Similarly, ages younger than about 9 Gyr can be excluded at a $\gtrsim 3\ \sigma$ level. The best fits are obtained for ages $\gtrsim 10$ Gyr and metallicity $Z = 0.04$, which corresponds to twice solar metallicity.

We also fitted the K_s LFs directly with the theoretical LFs obtained from BaSTI minimising $\chi^2 = \sum(data - model)/\sigma^2$. The width of the Gaussian to smoothen the theoretical LFs and the distance modulus were set as free parameters. The distance modulus was constrained to lie within 5σ of the expected value $\mu = 14.60 \pm 0.05$ to avoid false minima in the model fits caused by unphysical values of μ. Figure 10.6 shows the distribution of reduced χ^2 obtained by comparing models with different ages and metallicities with the observed data. A clear minimum appears for B1 and B2 at Z = 0.04 and ages $\sim 13 - 14$ Gyr. To estimate the uncertainties, we used a Monte Carlo (MC) simulation generating 1,000 synthetic LFs from the real data and errors. We fitted the LFs in the same way as the real data using a range of ages from 12 to 15 Gyr (in steps of 1 Gyr) and metallicities Z = 0.03, 0.04 and 0.05. The models we employed do not account for atomic diffusion (Pietrinferni et al., 2004, 2006). This effect is important for isochrones with ages greater than a few Gyr (Pietrinferni et al., 2004). Including atomic diffusion reduces the age of the models $\sim 0.7 - 1$ Gyr (see sec. 3.9.6, Cassisi & Salaris, 2013), and applying this correction makes our analysis compatible with the age of the Universe as derived from modelling of the cosmic microwave background (e.g., Bennett et al., 2013). Although Figure 10.7 for instance illustrates an unphysically old age for the models, the correction should be considered to be implied in that figure, and in the associated analysis. Figure 10.7 shows the results of the MC analysis for B2; the result for B1 is similar. Moreover, we estimated the systematic uncertainty introduced by the bin width selection by repeating the fit using a range of different bin widths. Finally, we obtained 13.64 ± 0.35 Gyr and Z = 0.040 ± 0.003 and 13.50 ± 0.74 Gyr and Z = 0.040 ± 0.003 for B1 and B2, respectively. Taking into account the atomic diffusion, we estimate a final age of 12.8 ± 0.4 and 12.7 ± 0.8 for B1 and B2, respectively

(one-sigma uncertainty). The final uncertainty was obtained considering that the atomic diffusion contributes reducing the ages by 0.85 ± 0.15, and propagating the uncertainties quadratically. Figure 10.8 shows the best fits. We conclude that the observed LFs can be satisfactorily modelled by an old single-age population with Z = 0.0400 ± 0.003 (or $[Fe/H] = 0.05 \pm 0.04$ dex). The statistical and systematic uncertainties have been propagated quadratically. It is important to note that the theoretical LFs used probably also contain systematic uncertainties whose magnitude is difficult to estimate. To check the obtained results, we used the CMD 3.0 tool (http://stev.oapd.inaf.it/cgi-bin/cmd) (Bressan et al., 2012a; Chen & Amaro-Seoane, 2014; Girardi et al., 2010; Marigo et al., 2008; Tang et al., 2014) to fit PARSEC evolutionary tracks (version 1.2S) to our data. The best fit was found for an old stellar population model (12 Gyr, which was the oldest population used) with twice solar metallicity. This is in perfect agreement with the result obtained using the BaSTI models.

Accordingly, the density of the nuclear bulge stellar population in B1 and B2 amounts to approximately 15% and 30%, respectively, of the central density of the NB. As a result of factors such as a significantly different foreground extinction towards the NB and bulge fields and a more complex stellar population in the NB, correcting for any potential bias would be a complex procedure prone to systematic uncertainties. Nevertheless, while this caveat should be kept in mind, we believe that it does not significantly affect our results because the potential contamination is fairly low for field B1 and because the result of our analysis of field B2 is fully consistent with the one for B1.

The fields we studied here have hardly been investigated before. Figer et al. (2004) studied several fields in the nuclear stellar disc with NICMOS/HST observations. They found that the LFs of most fields provide evidence for continuous star formation in the Galactic centre. Only one of their fields, denominated zc, lies at 0.3 degree to the Galactic north of the nuclear stellar disc. This field alone can be compared to the fields studied here. Figer et al. (2004) found fewer bright stars in this field than in those closer to the GC, in agreement with an older population. The main sequence turn-off in field zc also broadly agrees with a stellar population older than in their other fields. We note that this is only evident if the significantly different extinction towards the different fields is taken into account. Pfuhl et al. (2011) analysed

spectroscopic observations of a few hundred giants within 1 pc of Sagittarius A*. They adopted metallicity measurements from other authors and found that at least 80% of the stellar mass formed more than 5 Gyr ago. However, an important caveat when comparing the results of Pfuhl et al. (2011) to ours is that the stars analysed in the former are all located within the nuclear star cluster of the Milky Way. This has a complex star formation history and even shows evidence of very recent star formation. Stellar populations in nuclear clusters should probably not be compared with those in the surrounding bulges (see, e.g. Böker, 2010; Neumayer, 2017).

10.5.2 Fraction of young stars

Previous studies in the bulge have found a significant fraction of stars with ages < 5 Gyr (e.g. Bensby et al., 2017, 2013). Although a single stellar population gives a satisfactory fit to our data, we also repeated the analysis assuming two stellar populations of twice solar metallicity: a young (0.5, 1, 2, 3, 4 and 5 Gyr) and an old population (from 7 to 14 Gyr in steps of 1 Gyr). We found that the young component does not contribute significantly. The χ^2 values do not improve significantly over those obtained with single-population fits. This is in agreement with Clarkson et al. (2011), who reported that the young stellar population (studied at $b = 1.25°$) can be at most $\sim 3\%$ and it is also compatible with zero. The more recent work by Renzini et al. (2018) also constrained the contribution of young, high-metallicity stars to $\lesssim 3\%$.

10.5.3 Spatial variability

We also analysed the age and metallicity variability with the position in the two studied fields. For each field, we randomly selected 30 regions of $\sim 1.8'$ of radius, where we found enough stars to produce a complete LF. Then, we analysed the obtained LFs following the procedure described in the previous section. The ages of all the random regions follow a quasi-Gaussian distribution with a mean of 13.94 and 13.65 Gyr, and a standard deviation of 0.15 and 0.35 Gyr for B1 and B2 respectively. We did not observe any variation in metallicity and obtained a constant value of twice solar metallicity, in agreement with the results obtained in the previous section.

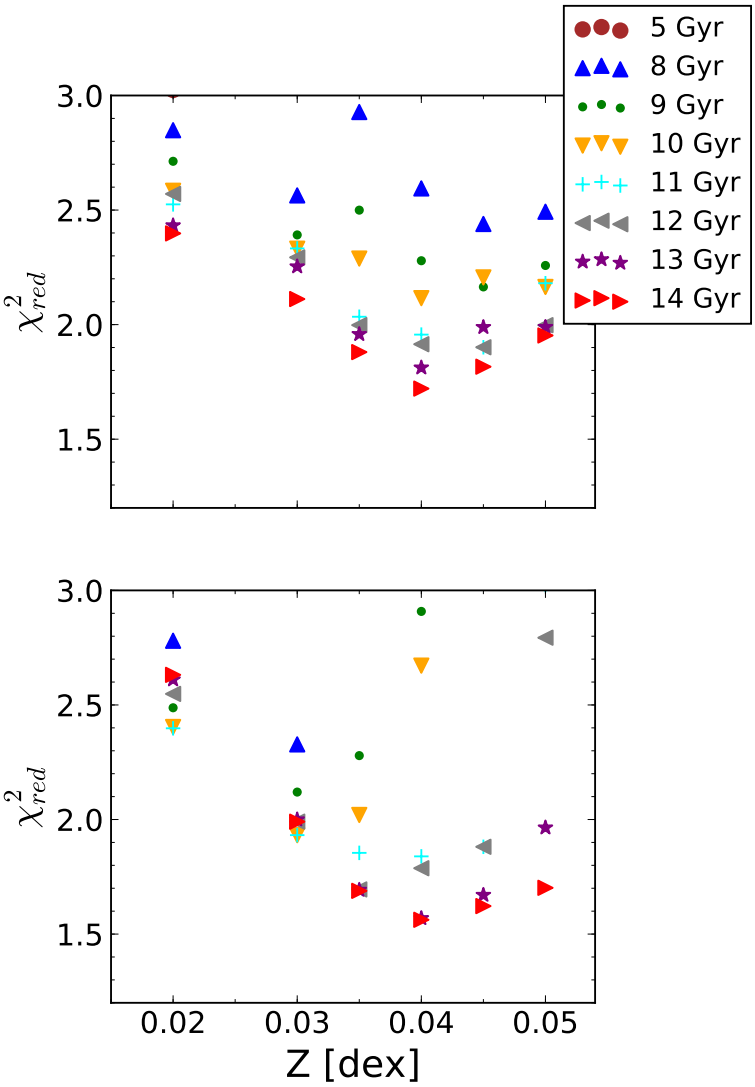

Fig. 10.6 Distribution of the reduced χ^2 for B1 and B2 (upper and lower panel, respectively). No points are associated with 5 Gyr since they have a large reduced χ^2 and the scale is optimised for lower values of the reduced χ^2. Accounting for atomic diffusion would reduce the age of the models $\sim 0.7 - 1$ Gyr (see main text).

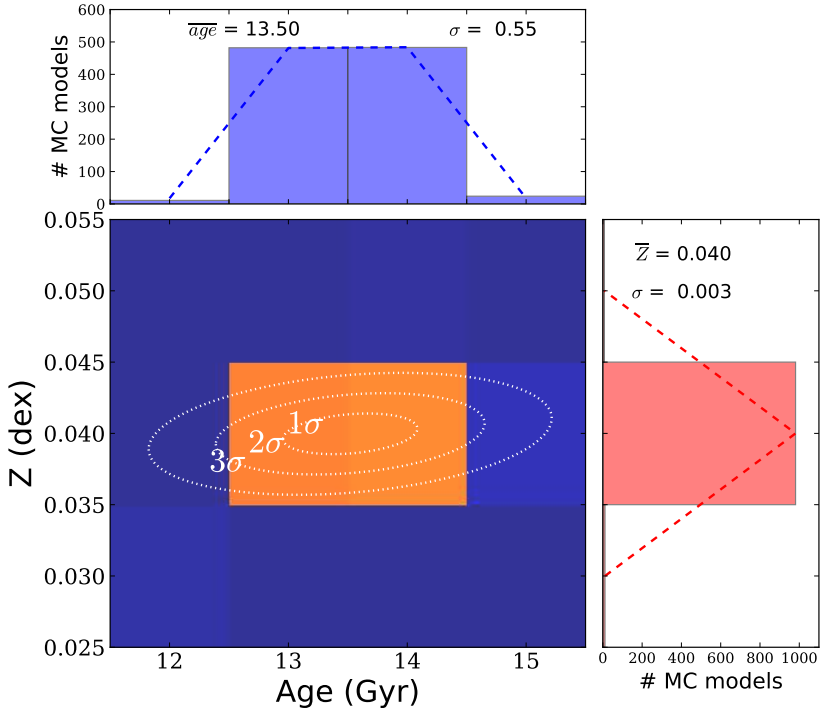

Fig. 10.7 Distribution of ages and metallicities for B2 obtained by fitting 1,000 MC samples with the theoretical BaSTI LFs. Upper panel: Age distribution. Right panel: Metallicity distribution. Central panel: Density map of ages and metallicities. Sigma contours are over-plotted in white. Dashed lines show Gaussian fits for ages and metallicities with the values specified in the panels. Accounting for atomic diffusion would reduce the age of the models $\sim 0.7 - 1$ Gyr (see main text).

10.5.4 Variation with extinction

To study the possible influence of the extinction and different distances to the stars analysed (depth of the bulge), we divided the stars in the CMDs of the two fields into three different sub-sets as shown by the red dashed lines in Fig. 10.4. We de-reddened each sub-set using the derived extinction map and built LFs. We again fitted all the LFs with the theoretical models and found that there is no significant variation within the uncertainties for ages and metallicities in either field. For B1,

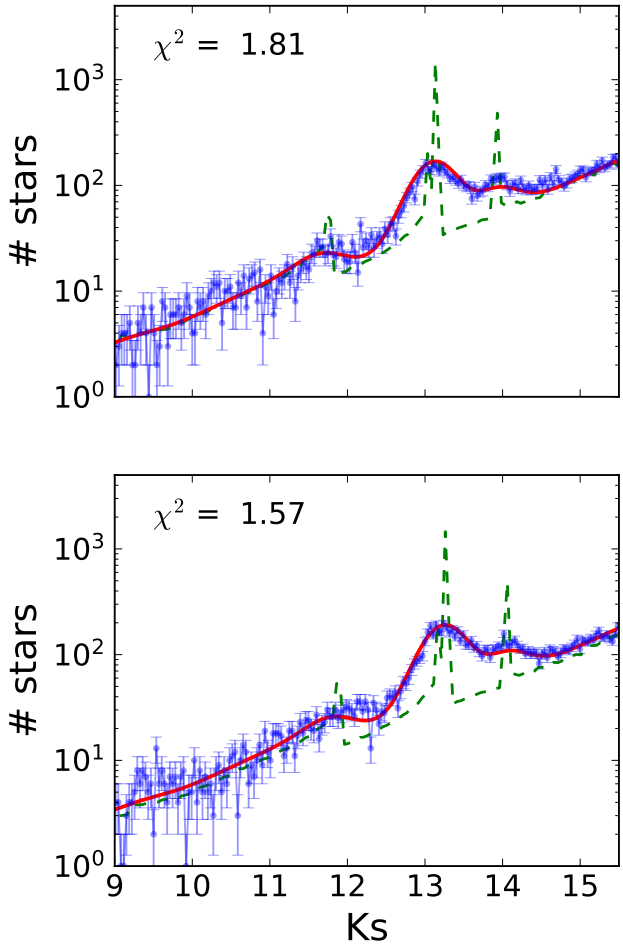

Fig. 10.8 K_s-band de-reddened luminosity function. The upper and lower panel show B1 and B2, respectively. The red line depicts the best fit. It is a smoothed 13.5 Gyr, Z = 0.04 LF. Considering the atomic diffusion in the model would reduce the age $\sim 0.7 - 1$ Gyr (see main text). The green dashed line corresponds to the LF from BaSTI models, without applying any smoothing.

the best fit was a star population of 14 Gyr and Z = 0.04 in all three cases, whereas for B2, we found two cases with 14 Gyr and one with 13 Gyr; the metallicity was always Z = 0.04.

10.5.5 Metallicity gradient

An RGBB feature $\sim 0.70 - 0.74$ mag fainter than the RC was identified in fields located at vertical distances of $b > 2^{\circ}$ from the GC (e.g. Nataf et al., 2013, 2011b; Wegg & Gerhard, 2013). According to Table 10.1, this separation implies a metallicity of $[Fe/H] \sim 0$ dex, which is in agreement with the metallicity maps shown for these latitudes by Gonzalez et al. (2013). Based on these maps, we assumed a metallicity of $[Fe/H] \sim 0$ dex at a vertical distance of 2.5° from the GC. This means a distance of ~ 300 pc with respect to B2. Then, we computed the expected metallicity for B2 assuming measured values of the vertical metallicity gradient. We used 0.28, 0.45, and 0.6 dex/kpc (Gonzalez et al., 2013; Ness et al., 2013; Zoccali et al., 2008). We obtained an expected metallicity of $[Fe/H] \sim 0.08$, ~ 0.14 and ~ 0.18 dex, respectively. Thus, our result favours a lower metallicity gradient for the regions in the inner bulge. This is in agreement with the flattening of the metallicity gradient in the inner regions inferred by Rich et al. (2007). This is also compatible with the more prominent fraction of metal-rich stars found close to the plane in comparison with the metal-poor ones and a significantly larger scale height of the latter population, so that its contribution does not vary significantly at small Galactic latitudes (Barbuy et al., 2018; Ness et al., 2013; Rojas-Arriagada et al., 2014).

Figure 10.9 shows the median values of the metallicities obtained by several authors at different latitudes. We assumed symmetry with respect to the Galactic plane, in agreement with Fig. 7 of Gonzalez et al. (2013). For each position, the inferred metallicity value results from the median of the metallicities determined by the respective authors for several hundred stars. We estimated an uncertainty of ~ 0.05 dex on the data points. This uncertainty should also account for any differences that may exist between the fields above and below the Galactic disc. The literature values at lowest latitudes, obtained by Zoccali et al. (2008), have a metallicity that is compatible within the uncertainties with the values obtained here. This supports a flat metallicity gradient in the inner parts of the bulge. Assuming

that the Galactic bulge has probably formed from evolutionary processes of the metal-poor thick disc and the metal-rich thin disc, its metallicity gradient may result from the changing relative weights of these two components (see Babusiaux et al., 2010; García Pérez et al., 2018). The different scales heights of $z^t_{thin\ disk} = 300 \pm 50$ pc and $z^t_{thick\ disk} = 900 \pm 180$ pc near the location of the Sun (Bland-Hawthorn & Gerhard, 2016) and the higher metallicity in the thin disc would produce the measured metallicity gradient. Our fields are at low latitudes where the contribution from the thick disc will be practically constant, in agreement with a flat gradient in the inner few hundred parsecs.

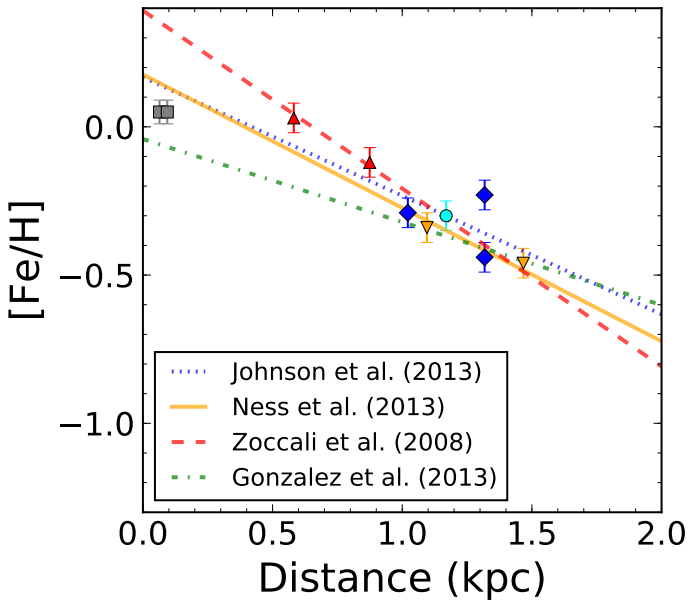

Fig. 10.9 Metallicity measurements at different latitudes reported by previous studies: red triangles correspond to (l, b) = (+1, -4) and (0, -6) fields from Zoccali et al. (2008), blue diamonds are from Johnson et al. (2013) and correspond to (l, b) = (8.5, 9), (-5.5, -7) and (-4, -9), the inverted yellow triangles correspond to (l, b) = (0, -7.5) and (0, -10) from Ness et al. (2013), the cyan circle corresponds to (0, -8) from Johnson et al. (2011), and the grey squares are from this work. The lines show several metallicity gradients obtained by the authors in the legend. The lines and points share the same colour if they are part of the same work.

10.6 Results and discussion

We present deep, $0.2''$ angular resolution JHK_s photometry of two fields in the inner bulge, of size $7.95' \times 3.43'$ at vertical separations of only 0.4° and 0.6° (~ 60 and ~ 90 pc) from the Galactic centre. Based on data from the GALACTICNUCLEUS survey, we could thus overcome the high extinction and crowding in the inner bulge of the Milky Way and present deep studies of the CMDs and LFs of stars in the innermost bulge, where no comparable data from previous studies exist. We identified the RGBB in the innermost bulge regions of the Milky Way. Thanks to its dependence on metallicity and age, we were able to constrain the properties of the stellar population using BaSTI isochrones. For the two fields, we obtained best fits for a single, old ($\sim 12.8 \pm 0.6$ Gyr) stellar population with a metallicity Z = 0.040 ± 0.003 dex. Given that the age of the stellar population was only measured indirectly in this work through a fit of model isochrones, there may be a significant bias. In particular, it is not easily conceivable how a large stellar population almost as old as the Universe could achieve super-solar metallicities. Nevertheless, given the results of our analysis, we can conservatively state that the population in the inner bulge, close to the nuclear stellar disc, is at least as old as or older than the age of the bulge population measured by other authors at larger latitudes (e.g., Clarkson et al., 2008; Freeman, 2008; Zoccali et al., 2003). In this context, we would like to point out that our findings show that observations of the inner bulge of the Milky Way could be used to test and improve stellar evolutionary models for high metallicities.

We did not need to assume the contribution of any young stellar population ($\sim$ 5 Gyr) to obtain a satisfactory fit of the data, as in previous studies (Clarkson et al., 2011; Renzini et al., 2018). On the other hand, comparing the obtained metallicity in the studied fields with previous measurements at $b \approx 2^\circ$, we obtained that our result favours a low-metallicity gradient that is compatible with a flattening of it in the inner regions.

As a secondary result, we found that the extinction index for the two bulge fields is consistent with the one derived in chapters 11 and 8 (see also Nogueras-Lara et al. (2018a) and Nogueras-Lara et al. 2019 submitted), $\alpha = 2.30 \pm 0.08$, which indicates within the measurement uncertainties that the extinction curve across the Galactic centre region does not vary significantly.

Finally, the stellar population of the regions in the inner bulge appears to be different from the population found at lower latitudes (in the NB), which is compatible with a continuous star formation history with recent stellar bursts (e.g. Figer et al., 2004; Pfuhl et al., 2011). Future investigations of a larger field at same spatial resolution will be helpful to map the metallicity and age distribution of the bulge population at low latitudes.

"Ay, mi familia Oiga mi gente Canten a coro nuestra canción Amor verdadero, nos une por siempre En el latido de mi corazón"

Miguel Rivera (Coco)

11 Conclusions

I have presented the work carried out during my PhD thesis on the centre of the Milky Way. The main results that we obtain are:

11.1 GALACTICNUCLEUS

We explain in detail the necessity of a high angular resolution NIR survey of the GC to study the extinction curve and the stellar population and structure of the NB of the MW. To address this problem, we present the GALACTICNUCLEUS survey, a high angular resolution NIR survey that improves the state of the art superseding in wavelength coverage, dynamical magnitude range and angular resolution all existing surveys for the GC. We obtain accurate JHK_s photometry of $\sim 3.3 \times 10^6$ stars in the GC detecting around 20 % in J, 65 % in H and 90 % in K_s. The survey covers a total area of ~ 0.3 square degrees, which corresponds to $\sim 6,000$ pc^2. The

GALACTICNUCLEUS survey reaches 5 σ detections for $J \sim 22$ mag, $H \sim 21$ mag and $K_s \sim 21$ mag. The uncertainties are below 0.05 mag at $J \sim 21$ mag, $H \sim 19$ mag and $K_s \sim 18$ mag. The zero point systematic uncertainty is $\lesssim 0.04$ mag in all three bands.

We describe in detail the process from the design of the observation to the publication of the final catalogue (Nogueras-Lara et al., 2019). We also carry out a number of tests to assess the data quality and the performance of the obtained photometry and astrometry.

The immediate results of the GALACTICNUCLEUS survey are the most complete CMDs of the GC so far that include regions in the NSD, inner bulge and the transition region between them. The CMDs between the studied regions show clear differences caused by differential extinction and distinct stellar evolutionary stages. We identified distinct stellar population: the foreground population, the AGBB, the post main sequence, the ascending giant branch and cover the RC and the RGBB.

11.2 Extinction curve towards the GC in the NIR

We show that the determination of the extinction curve in the NIR regime is fundamental to characterise the stellar structure and population of the GC. We firstly use our central field (F1) data to analyse the near-infrared extinction curve and find some evidence for a wavelength-dependence of the extinction curve. However, we conclude that within the uncertainties a single power law is sufficient to describe the extinction curve from J to K_s. We obtained a extinction index of $\alpha_{JHK_s} = 2.30 \pm 0.08$. We do not find any evidence of a line-of-sight dependence of the extinction curve.

Subsequently, we increase the analysed region using 14 fields in the NSD and study the spatial variation of the extinction index. We also apply two independent methods based on red clump stars to compute the extinction index between different bands and its variation with the wavelength. We do not detect any significant line-of-sight or extinction dependence of α within the studied region in the NSD. The extinction index between JH and HK_s differs by 0.19 ± 0.05. We obtained mean values for the extinction indices $\alpha_{JH} = 2.43 \pm 0.03$ and $\alpha_{HK_s} = 2.23 \pm 0.03$. The dependence of the extinction index on the wavelength could explain the differences obtained for α_λ in the literature since it was assumed constant for the NIR regime.

We also compute the extinction index towards two regions in the inner bulge and find that the extinction curve is compatible with the one derived for the NSD.

11.3 Star formation history in the NSD

We study in detail the SFH of the NSD using the GALACTICNUCLEUS catalogue. We report the first detailed star formation history of this region. The bulk of its stars formed at least eight billion years ago. This initial activity was followed by a long period of quiescence that was ended by an outstanding event about 1 Gyr ago, during which roughly 5 % of its mass formed in a time window ∼100 Myr, in what may arguably have been one of the most energetic events in the history of the Milky Way. Star formation continued subsequently on a lower level, creating a few percent of the stellar mass in the past few 100 Myr, with an increased rate up to ∼30 Myr ago. Our findings contradict the previously accepted paradigm of quasi-continuous star formation at the centre of the Milky Way. The long quiescent phase agrees with the overall quiescent history of the Milky Way and suggests that our Galaxy's bar may not have existed until recently, or that gas transport through the bar was extremely inefficient during a long stretch of the Milky Way's life, and that the central black hole may have acquired most of its mass already in the early days of the Milky Way.

11.4 Star formation history of the Inner region of the Milky Way bulge

We study the stellar population within two $8.0' \times 3.4'$ fields, about 0.6° and 0.4° to the Galactic north of the Milky Way centre (in the inner bulge) and compare it with the one in the immediate surroundings of Sagittarius A*.

We present K_s luminosity functions that are complete down to at least two magnitudes below the red clump (RC). We detect a feature in the luminosity functions that is fainter than the RC by 0.80 ± 0.03 and 0.79 ± 0.02 mag, respectively, in the K_s band. It runs parallel to the reddening vector. We identify the feature as the red giant branch bump. Fitting α-enhanced BaSTI luminosity functions to our data, we find that a single old stellar population of $\sim 12.8 \pm 0.6$ Gyr and $Z = 0.040 \pm 0.003$

provides the best fit. Our findings thus show that the stellar population in the innermost bulge is old, similar to the one at larger distances from the Galactic plane, and that its metallicity is about twice solar at distances as short as about 60 pc from the centre of the Milky Way, similar to what is observed at about 500 pc from the Galactic Centre.

Comparing the obtained metallicity with previous known values at larger latitudes ($|b| > 2^\circ$), our results favour a flattening of the gradient at $|b| < 2^\circ$. As a secondary result we obtain that the extinction index in the studied regions agrees within the uncertainties with our previous value of $\alpha = 2.30 \pm 0.08$ that was derived for the very Galactic centre.

12 Future work

Thanks to the GALACTICNUCLEUS survey, this thesis is just the first step of follow up work that can be developed to improve our knowledge about the stellar population of the GC based on the new catalogue that is now available to the community.

12.1 Improvement of the data set

We aim at improving the limitations that the GALACTICNUCLEUS presents in its first data release. In this sense, as it was outlined in Sec. 6.3, the way of obtaining the final catalogue was very conservative. We accept a star as a real detection only if it is detected in three independent images obtained dividing the whole number of images to produce three intermediate sub-images to estimate the uncertainties. In this way, we removed a number of faint stars that are present in the long exposure image (the one produced combining all the frames), but are not clearly identified in

the sub-images. Therefore, the main goals are: (a) Improving source detection. (b) Developing a new method to estimate uncertainties that does not need the sub-images. In this way, we are working on a bootstrapping algorithm to estimate the uncertainties based on images produced combining a high fraction of frames to be able to increase the number of stars. We estimate that it is possible to increase $\sim 30-40\,\%$ the number of sources detected.

The saturation of the bright stars ($K_s \lesssim 11.5$ mag) is also a problem in the current data release. To address this problem, we designed a program to observe the GC in H and K_s (the bands suffering more from saturation) using the same configuration that we used for GALACTICNUCLEUS, but under bad seeing conditions $\sim 1''$ (0103.B-0841, PI F. Nogueras-Lara). In this way, the bright sources are not saturated. Up to date, the program has been observed up to 95 % in K_s band. We expect to be able to replace the photometry of saturated stars in the near future. We have already analysed the preliminary results for the first field of the bad seeing program and have achieved a significant improvement of the photometry for saturated sources, as is shown in Fig. 12.1.

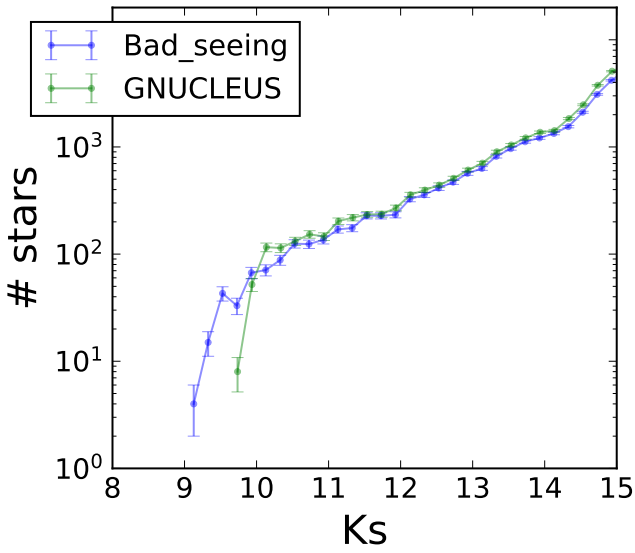

Fig. 12.1 Comparison of the K_s luminosity functions obtained using data from GALACTICNUCLEUS and the bad seeing program.

12.2 Analysis of the extinction curve in the whole region of the survey

The exciting results on the extinction curve obtained in this thesis have been focused on two regions in the inner bulge and part of the central area covered by the GALACTICNUCLEUS survey (14 pointings located at the central region). The next step to fully understand the extinction behaviour towards the GC would imply to extend the analysis to the whole region observed by GALACTICNUCLEUS. In this way, it is necessary to create new extinction maps that take into account the wavelength dependence of the extinction index. This will allow us to correct properly for extinction.

On the other hand, we aim at connecting the NIR to the optical extinction curve via extending NIR photometry to even shorter wavelengths. Also, diffraction limited imaging may improve the photometry toward selected fields and using sets of more and narrower filters could help to constrain the shape of the extinction curve.

12.3 Analysis of the stellar population

The analysis carried out on the central region of the survey covering the central area of the NB is suitable to be repeated for the transition regions as well as the interesting regions in the vicinity of Sgr B (D12, D13 pointings). In this way, we would obtain a detailed picture of the stellar population in the NB and might detect some regions with potential current star forming activity.

12.4 Proper motion analysis

The high precision astrometry obtained with GALACTICNUCLEUS survey is very appropriate for a proper motion analysis. We are using NICMOS/HST data available for the central region of our survey (Dong et al., 2011) to compute the proper motion in some small regions (Shahzamanian et al. in prep.). The results are very promising and will be key to detect co-moving group of stars that might trace young dissolved clusters.

12.5 Follow-up studies

I am highly interested in continuing with follow-up studies of the GALACTICNUCLEUS survey. In particular, I am working on identifying early-type stellar candidates by means of their intrinsically different colours in the blue part of the NIR spectrum. These stars can help to identify new young clusters. In this sense, the new obtained extinction curve in the NIR following a power law with an extinction index varying depending on the wavelength, will be of great usefulness.

On the other hand, I have applied for time with HAWK-I + GRAAL (ground layer adaptive optics module) to observe several fields in the GC in Y and J bands. Correcting for extinction and comparing with data from GALACTICNUCLEUS survey will allow us to compare the colours with theoretical models breaking the degeneracy between extinction and stellar type and identifying early-type stellar candidates. Moreover, obtaining HAWK-I + GRAAL J-band observations will make it possible to improve the completeness of the LF in J band around 1-1.5 mag, complementing the K_s LF obtained using GALACTICNUCLEUS. In this way, it will be possible to better constrain the SFH by fitting theoretical models simultaneously to both bands, breaking the degeneracy that can appear between different ages and metallicities.

References

Akaike, H. 1974, Automatic Control, IEEE Transactions on, 19, 716

Alonso-García, J., Minniti, D., Catelan, M., et al. 2017, ApJ, 849, L13

Alonso-García, J., Saito, R. K., Hempel, M., et al. 2018, A&A, 619, A4

Alves-Brito, A., Meléndez, J., Asplund, M., Ramírez, I., & Yong, D. 2010, A&A, 513, A35

Aparicio, A. & Gallart, C. 2004, AJ, 128, 1465

Arsenault, R., Paufique, J., Kolb, J., et al. 2014, The Messenger, 156, 2

Babusiaux, C., Gómez, A., Hill, V., et al. 2010, A&A, 519, A77

Balcells, M., Graham, A. W., & Peletier, R. F. 2007, ApJ, 665, 1084

Barbuy, B., Chiappini, C., & Gerhard, O. 2018, ArXiv e-prints [[arXiv]1805.01142]

Bennett, C. L., Larson, D., Weiland, J. L., et al. 2013, ApJS, 208, 20

Bensby, T., Adén, D., Meléndez, J., et al. 2011, A&A, 533, A134

Bensby, T., Feltzing, S., Gould, A., et al. 2017, ArXiv e-prints [[arXiv]1707.05960]

Bensby, T., Yee, J. C., Feltzing, S., et al. 2013, A&A, 549, A147

Bertelli, G., Bressan, A., Chiosi, C., Fagotto, F., & Nasi, E. 1994, A&AS, 106

Bland-Hawthorn, J. & Gerhard, O. 2016, ARA&A, 54, 529

Boehle, A., Ghez, A. M., Schödel, R., et al. 2016, ApJ, 830, 17

Böker, T. 2010, in IAU Symposium, Vol. 266, IAU Symposium, ed. R. de Grijs & J. R. D. Lépine, 58–63

Bovy, J., Nidever, D. L., Rix, H.-W., et al. 2014, ApJ, 790, 127

Bressan, A., Marigo, P., Girardi, L., et al. 2012a, MNRAS, 427, 127

Bressan, A., Marigo, P., Girardi, L., et al. 2012b, MNRAS, 427, 127

Cardelli, J. A., Clayton, G. C., & Mathis, J. S. 1989, ApJ, 345, 245

Cassisi, S. & Salaris, M. 1997, MNRAS, 285, 593

Cassisi, S. & Salaris, M. 2013, Old Stellar Populations: How to Study the Fossil Record of Galaxy Formation (Wiley-VCH)

Chaplin, W. J. & Miglio, A. 2013, ARA&A, 51, 353

Chen, X. & Amaro-Seoane, P. 2014, ApJ, 786, L14

Choi, J., Dotter, A., Conroy, C., et al. 2016, ApJ, 823, 102

Clarkson, W., Sahu, K., Anderson, J., et al. 2008, ApJ, 684, 1110

Clarkson, W. I., Sahu, K. C., Anderson, J., et al. 2011, ApJ, 735, 37

Contopoulos, G. & Grosbol, P. 1989, A&A Rev., 1, 261

Crocker, R. M. 2012, MNRAS, 423, 3512

Dalton, G. B., Caldwell, M., Ward, A. K., et al. 2006, in Proc. SPIE, Vol. 6269, Society of Photo-Optical Instrumentation Engineers (SPIE) Conference Series, 62690X

Diolaiti, E., Bendinelli, O., Bonaccini, D., et al. 2000, A&AS, 147, 335

Do, T., Ghez, A. M., Morris, M. R., et al. 2009, ApJ, 703, 1323

Do, T., Hees, A., Ghez, A., et al. 2019a, arXiv e-prints, arXiv:1907.10731

Do, T., Kerzendorf, W., Konopacky, Q., et al. 2018, ApJ, 855, L5

Do, T., Kerzendorf, W., Winsor, N., et al. 2015, ApJ, 809, 143

Do, T., Witzel, G., Gautam, A. K., et al. 2019b, arXiv e-prints, arXiv:1908.01777

Doane, D. P. 1976, The American Statistician, 30, 181

Doeleman, S. S., Fish, V. L., Broderick, A. E., Loeb, A., & Rogers, A. E. E. 2009, ApJ, 695, 59

Dong, H., Lacy, J. H., Schödel, R., et al. 2017a, MNRAS, 470, 561

Dong, H., Schödel, R., Williams, B. F., et al. 2017b, MNRAS, 471, 3617

Dong, H., Wang, Q. D., Cotera, A., et al. 2011, MNRAS, 417, 114

Dotter, A. 2016, ApJS, 222, 8

Draine, B. T. 1989, in ESA Special Publication, Vol. 290, Infrared Spectroscopy in Astronomy, ed. E. Böhm-Vitense, 93–98

Eisenhauer, F., Quirrenbach, A., Zinnecker, H., & Genzel, R. 1998, ApJ, 498, 278

Emerson, J., McPherson, A., & Sutherland, W. 2006, The Messenger, 126, 41

Falcke, H., Melia, F., & Agol, E. 2000, ApJ, 528, L13

Feldmeier-Krause, A., Kerzendorf, W., Neumayer, N., et al. 2017, MNRAS, 464, 194

Feldmeier-Krause, A., Neumayer, N., Schödel, R., et al. 2015, A&A, 584, A2

Figer, D. F., Rich, R. M., Kim, S. S., Morris, M., & Serabyn, E. 2004, ApJ, 601, 319

Freedman, D. & Diaconis, P. 1981, Probability Theory and Related Fields, 57, 453

Freeman, K. C. 2008, in IAU Symposium, Vol. 245, Formation and Evolution of Galaxy Bulges, ed. M. Bureau, E. Athanassoula, & B. Barbuy, 3–10

Fritz, T. K., Chatzopoulos, S., Gerhard, O., et al. 2014, ArXiv e-prints [[arXiv]1406.7568]

Fritz, T. K., Chatzopoulos, S., Gerhard, O., et al. 2016, ApJ, 821, 44

Fritz, T. K., Gillessen, S., Dodds-Eden, K., et al. 2011, ApJ, 737, 73

Fulbright, J. P., McWilliam, A., & Rich, R. M. 2006, ApJ, 636, 821

Fulbright, J. P., McWilliam, A., & Rich, R. M. 2007, ApJ, 661, 1152

Gallego-Cano, E., Schödel, R., Dong, H., et al. 2018, A&A, 609, A26

García Pérez, A. E., Ness, M., Robin, A. C., et al. 2018, ApJ, 852, 91

Genzel, R., Eisenhauer, F., & Gillessen, S. 2010, Reviews of Modern Physics, 82, 3121

Gillessen, S., Plewa, P. M., Eisenhauer, F., et al. 2017, ApJ, 837, 30

Girardi, L. 2016, ARA&A, 54, 95

Girardi, L., Williams, B. F., Gilbert, K. M., et al. 2010, ApJ, 724, 1030

Gonzalez, O. A., Rejkuba, M., Zoccali, M., et al. 2013, A&A, 552, A110

Gosling, A. J., Bandyopadhyay, R. M., & Blundell, K. M. 2009, MNRAS, 394, 2247

Graham, A. W. & Spitler, L. R. 2009, MNRAS, 397, 1003

Gravity Collaboration, Abuter, R., Amorim, A., et al. 2018, A&A, 615, L15

Groenewegen, M. A. T. 2008, A&A, 488, 935

Harayama, Y., Eisenhauer, F., & Martins, F. 2008, ApJ, 675, 1319

Hill, V., Lecureur, A., Gómez, A., et al. 2011, A&A, 534, A80

Hosek, Matthew W., J., Lu, J. R., Anderson, J., et al. 2018, ApJ, 855, 13

Johnson, C. I., Rich, R. M., Fulbright, J. P., & Reitzel, D. B. 2011, in Bulletin of the American Astronomical Society, Vol. 43, American Astronomical Society Meeting Abstracts #217, 153.12

Johnson, C. I., Rich, R. M., Kobayashi, C., Kunder, A., & Koch, A. 2014, AJ, 148, 67

Johnson, C. I., Rich, R. M., Kobayashi, C., et al. 2013, ApJ, 765, 157

Kissler-Patig, M., Pirard, J.-F., Casali, M., et al. 2008, A&A, 491, 941

Kruijssen, J. M. D., Longmore, S. N., Elmegreen, B. G., et al. 2014, MNRAS, 440, 3370

Kurucz, R. L. 1993, VizieR Online Data Catalog, 6039, 0

Landsman, W. B. 1993, in Astronomical Society of the Pacific Conference Series, Vol. 52, Astronomical Data Analysis Software and Systems II, ed. R. J. Hanisch, R. J. V. Brissenden, & J. Barnes, 246

Launhardt, R., Zylka, R., & Mezger, P. G. 2002, A&A, 384, 112

Lecureur, A., Hill, V., Zoccali, M., et al. 2007, A&A, 465, 799

Ledo, H. R., Sarzi, M., Dotti, M., Khochfar, S., & Morelli, L. 2010, MNRAS, 407, 969

Lejeune, T., Cuisinier, F., & Buser, R. 1997, A&AS, 125 [astro-ph/9701019]

Lenzen, R., Hartung, M., Brandner, W., et al. 2003, in Society of Photo-Optical Instrumentation Engineers (SPIE) Conference Series, Vol. 4841, Society of Photo-Optical Instrumentation Engineers (SPIE) Conference Series, ed. M. Iye & A. F. M. Moorwood, 944–952

Longmore, S. N., Kruijssen, J. M. D., Bally, J., et al. 2013, MNRAS, 433, L15

Malkin, Z. 2013, in IAU Symposium, Vol. 289, IAU Symposium, ed. R. de Grijs, 406–409

Marigo, P., Girardi, L., Bressan, A., et al. 2008, A&A, 482, 883

Marigo, P., Girardi, L., Bressan, A., et al. 2017, ApJ, 835, 77

Massari, D., Fiorentino, G., McConnachie, A., et al. 2016, A&A, 595, L2

Matsunaga, N., Feast, M. W., Bono, G., et al. 2016, MNRAS, 462, 414

Matsunaga, N., Kawadu, T., Nishiyama, S., et al. 2011, Nature, 477, 188

Mauerhan, J. C., Cotera, A., Dong, H., et al. 2010a, ApJ, 725, 188

Mauerhan, J. C., Muno, M. P., Morris, M. R., Stolovy, S. R., & Cotera, A. 2010b, ApJ, 710, 706

McWilliam, A. & Rich, R. M. 1994, ApJS, 91, 749

McWilliam, A. & Zoccali, M. 2010, ApJ, 724, 1491

Meidt, S. E., Schinnerer, E., van de Ven, G., et al. 2014, ArXiv e-prints [[arXiv]1402.5210]

Meléndez, J., Asplund, M., Alves-Brito, A., et al. 2008, A&A, 484, L21

Minniti, D., Lucas, P. W., Emerson, J. P., et al. 2010, New A, 15, 433

Morris, M. & Serabyn, E. 1996, ARA&A, 34, 645

Nagayama, T., Nagashima, C., Nakajima, Y., et al. 2003, in Proc. SPIE, Vol. 4841, Instrument Design and Performance for Optical/Infrared Ground-based Telescopes, ed. M. Iye & A. F. M. Moorwood, 459–464

Najarro, F., Figer, D. F., Hillier, D. J., Geballe, T. R., & Kudritzki, R. P. 2009, ApJ, 691, 1816

Nandakumar, G., Ryde, N., Schultheis, M., et al. 2018, MNRAS, 478, 4374

Nataf, D. M., Cassisi, S., & Athanassoula, E. 2014, MNRAS, 442, 2075

Nataf, D. M., Gould, A., Fouqué, P., et al. 2013, ApJ, 769, 88

Nataf, D. M., Udalski, A., Gould, A., & Pinsonneault, M. H. 2011a, ApJ, 730, 118

Nataf, D. M., Udalski, A., Gould, A., & Pinsonneault, M. H. 2011b, ApJ, 730, 118

Ness, M., Freeman, K., Athanassoula, E., et al. 2013, MNRAS, 430, 836

Neumayer, N. 2017, in IAU Symposium, Vol. 316, Formation, Evolution, and Survival of Massive Star Clusters, ed. C. Charbonnel & A. Nota, 84–90

Neumayer, N. & Walcher, C. J. 2012, Advances in Astronomy, 2012 [[arXiv]1201.4950]

Nishiyama, S., Nagata, T., Kusakabe, N., et al. 2006a, ApJ, 638, 839

Nishiyama, S., Nagata, T., Sato, S., et al. 2006b, ApJ, 647, 1093

Nishiyama, S., Nagata, T., Tamura, M., et al. 2008, ApJ, 680, 1174

Nishiyama, S., Yasui, K., Nagata, T., et al. 2013, ApJ, 769, L28

Nogueras-Lara, F., Gallego-Calvente, A. T., Dong, H., et al. 2018a, A&A, 610, A83

Nogueras-Lara, F., Schödel, R., Dong, H., et al. 2018b, A&A, 620, A83

Nogueras-Lara, F., Schödel, R., Gallego-Calvente, A. T., et al. 2019, arXiv e-prints, arXiv:1908.10366

Paufique, J., Bruton, A., Glindemann, A., et al. 2010, in Proc. SPIE, Vol. 7736, Adaptive Optics Systems II, 77361P

Paumard, T., Genzel, R., Martins, F., et al. 2006, ApJ, 643, 1011

Paxton, B., Bildsten, L., Dotter, A., et al. 2011, ApJS, 192, 3

Paxton, B., Cantiello, M., Arras, P., et al. 2013, ApJS, 208, 4

Paxton, B., Marchant, P., Schwab, J., et al. 2015, ApJS, 220, 15

Pedregosa, F., Varoquaux, G., Gramfort, A., et al. 2011, Journal of Machine Learning Research, 12, 2825

Petr, M. G., Coude Du Foresto, V., Beckwith, S. V. W., Richichi, A., & McCaughrean, M. J. 1998, ApJ, 500, 825

Pfuhl, O., Fritz, T. K., Zilka, M., et al. 2011, ApJ, 741, 108

Pietrinferni, A., Cassisi, S., Salaris, M., & Castelli, F. 2004, ApJ, 612, 168

Pietrinferni, A., Cassisi, S., Salaris, M., & Castelli, F. 2006, ApJ, 642, 797

Pietrinferni, A., Molinaro, M., Cassisi, S., et al. 2014, Astronomy and Computing, 7, 95

Pizzella, A., Corsini, E. M., Morelli, L., et al. 2002, ApJ, 573, 131

Plewa, P. M., Gillessen, S., Eisenhauer, F., et al. 2015, MNRAS, 453, 3234

Portegies Zwart, S., McMillan, S., & Gieles, M. 2010, ArXiv e-prints [[arXiv]1002.1961]

Portegies Zwart, S. F., Makino, J., McMillan, S. L. W., & Hut, P. 2002, ApJ, 565, 265

Primot, J., Rousset, G., & Fontanella, J. C. 1990, Journal of the Optical Society of America A, 7, 1598

Reid, M. J. & Brunthaler, A. 2004, ApJ, 616, 872

Renzini, A. & Fusi Pecci, F. 1988, ARA&A, 26, 199

Renzini, A., Gennaro, M., Zoccali, M., et al. 2018, ArXiv e-prints [[arXiv]1806.11556]

Rich, R. M., Origlia, L., & Valenti, E. 2007, ApJ, 665, L119

Rich, R. M., Ryde, N., Thorsbro, B., et al. 2017, AJ, 154, 239

Rieke, G. H. & Lebofsky, M. J. 1985, ApJ, 288, 618

Rojas-Arriagada, A., Recio-Blanco, A., Hill, V., et al. 2014, A&A, 569, A103

Rossa, J., van der Marel, R. P., Böker, T., et al. 2006, AJ, 132, 1074

Rousset, G., Lacombe, F., Puget, P., et al. 2003, in Society of Photo-Optical Instrumentation Engineers (SPIE) Conference Series, Vol. 4839, Society of Photo-Optical Instrumentation Engineers (SPIE) Conference Series, ed. P. L. Wizinowich & D. Bonaccini, 140–149

Rui, N. Z., Hosek, Matthew W., J., Lu, J. R., et al. 2019, arXiv e-prints, arXiv:1904.02395

Saito, R. K., Minniti, D., Dias, B., et al. 2012, A&A, 544, A147

Salaris, M., Cassisi, S., & Weiss, A. 2002, PASP, 114, 375

Schödel, R. 2011, in Astronomical Society of the Pacific Conference Series, Vol. 439, Astronomical Society of the Pacific Conference Series, ed. M. R. Morris, Q. D. Wang, & F. Yuan, 222–+

Schödel, R., Eckart, A., Alexander, T., et al. 2007, A&A, 469, 125

Schödel, R., Feldmeier, A., Kunneriath, D., et al. 2014, A&A, 566, A47

Schödel, R., Gallego-Cano, E., Dong, H., et al. 2018, A&A, 609, A27

Schödel, R., Merritt, D., & Eckart, A. 2009, A&A, 502, 91

Schödel, R., Najarro, F., Muzic, K., & Eckart, A. 2010, A&A, 511, A18+

Schödel, R., Yelda, S., Ghez, A., et al. 2013, MNRAS, 429, 1367

Schultheis, M., Rich, R. M., Origlia, L., et al. 2019, A&A, 627, A152

Schwarz, G. 1978, The Annals of Statistics, 6, 461

Scott, D. W. 1979, Biometrika, 66, 605

Scoville, N. Z., Stolovy, S. R., Rieke, M., Christopher, M., & Yusef-Zadeh, F. 2003, ApJ, 594, 294

Seth, A. C., Blum, R. D., Bastian, N., et al. 2008, ApJ, 687, 997

Seth, A. C., Dalcanton, J. J., Hodge, P. W., & Debattista, V. P. 2006, AJ, 132, 2539

Seth, A. C., Neumayer, N., & Boeker, T. 2019, arXiv e-prints, arXiv:1908.00022

Sharples, R., Bender, R., Agudo Berbel, A., et al. 2013, The Messenger, 151, 21

Stead, J. J. & Hoare, M. G. 2009, MNRAS, 400, 731

Sturges, H. A. 1926, Journal of the American Statistical Association, 21, 65

Tang, J., Bressan, A., Rosenfield, P., et al. 2014, MNRAS, 445, 4287

Tokunaga, A. T. & Vacca, W. D. 2005, PASP, 117, 421

Trippe, S., Gillessen, S., Gerhard, O. E., et al. 2008, A&A, 492, 419

Walcher, C. J., Böker, T., Charlot, S., et al. 2006, ApJ, 649, 692

Wegg, C. & Gerhard, O. 2013, MNRAS, 435, 1874

Wyse, R. F. G. 2001, in Astronomical Society of the Pacific Conference Series, Vol. 230, Galaxy Disks and Disk Galaxies, ed. J. G. Funes & E. M. Corsini, 71–80

Yusef-Zadeh, F., Hewitt, J. W., Arendt, R. G., et al. 2009, ApJ, 702, 178

Zasowski, G., Majewski, S. R., Indebetouw, R., et al. 2009, ApJ, 707, 510

Zhao, J.-H. & Wright, M. C. H. 2011, ApJ, 742, 50

Zoccali, M., Hill, V., Lecureur, A., et al. 2008, A&A, 486, 177

Zoccali, M., Renzini, A., Ortolani, S., et al. 2003, A&A, 399, 931

A

Effective wavelength

To compute the effective wavelength, $\lambda_{\rm eff}$, we used Eq. (A3) of Tokunaga & Vacca (2005). We used the transmission curves for the HAWK-I J, H, and K_s filters from the instrument website and the atmospheric transmission from the Gemini telescope web site. Because the $\lambda_{\rm eff}$ was computed for several stellar types (RC stars, late-type stars with known metallicity and temperature, and young stars), we used the more adequate Kurucz model for every case. We took the extinction index and $A_{1.61}$ obtained with the grid method described in Sect. 7.3.1, being the value specified in every section accordingly.

To calculate α we used an iterative approach in some of the methods. In those cases, we recomputed $\lambda_{\rm eff}$ using the α that was obtained in the first step and repeated the process updating the value until reaching convergence. The uncertainties for every $\lambda_{\rm eff}$ were estimated varying the parameters that affect them in their uncertainty

ranges. In that way, we computed λ_{eff} varying the same parameter and keeping the rest constant. We considered:

- The temperature of the model. For the RC stars, we used 4,500, 4,750, and 5,000 K. For the known young stars we used 20,000, 30,000, and 40,000 K.
- The metallicity of the model. We varied for all the cases from -1 dex to +1 dex in steps of 0.5.
- We took three different values for the $\log g$ that we used in the Kurucz model: for RC, 2.0, 2.5 and 3.0, and for the young known stars 3.5, 4.0, and 4.5.
- The amount of precipitable water vapour. We used 1.0, 1.6, and 3.0 mm.
- The extinction index and $A_{1.61}$. We varied them according to the value and uncertainties obtained in Sect. 7.3.1.

The final uncertainty was computed adding quadratically all the uncertainties. The final value was computed using the central parameters that were described for the uncertainties. Then, 4,750 K and 30,000 K, solar metallicity, and 1.6 mm of precipitable water vapour were used for the final values of the λ_{eff} for RC stars and young stars, respectively. Tables A.1 and A.2 summarise the effective wavelength and the uncertainties for the high extinguished RC stars and young stars. The largest error came from α and $A_{1.61}$. In the case of late-type stars with known metallicity, we applied an individual model for each of them.

Table A.1 Effective wavelength and uncertainties for RC stars.

		J	H	K_s
λ_{eff}		1.2685	1.6506	2.1629
	T	0.0004	0.0003	0.0001
	met	0.0011	0.0002	0.0003
	$\log g$	0.00007	0.00002	0.00003
$\Delta\lambda_{eff}$	hum	0.0003	0.0001	0.0003
	α	0.0007	0.0013	0.0002
	$A_{1.61}$	0.0013	0.0014	0.0008
	Total	0.0015	0.0020	0.0009

Notes. Table shows the computed effective wavelength, the uncertainties associated to every parameter (from top to bottom: temperature of the model, metallicity, water vapour column density, extinction index, and extinction at 1.61 μm) and the final uncertainty for high extinguished RC stars.

Table A.2 Effective wavelength and uncertainties for known young stars.

		J	H	K_s
λ_{eff}		1.2687	1.6498	2.1637
	T	0.0012	0.0007	0.00014
	met	0.00005	0.00005	0.00004
	$\log g$	0.00002	0.00003	0.000003
$\Delta\lambda_{eff}$	hum	0.0003	0.00011	0.0003
	α	0.0009	0.0014	0.0002
	$A_{1.61}$	0.0016	0.0016	0.0009
	Total	0.0022	0.0022	0.0009

Notes. The uncertainties are shown independently depending on every parameter, from top to bottom: temperature of the model, metallicity, water vapour column density, extinction index, and extinction at 1.61 μm.

B

Intrinsic colour calculation

The intrinsic colours $(J-H)_0$ and $(H-K_s)_0$ were computed using the appropriate Kurucz models for each type of star. We took into account the transmission curves for the HAWK-I J, H, and K_s filters from the instrument web site and the atmospheric transmission from the Gemini telescope web site. We computed the total magnitude for every band and then normalised it using a Vega reference model (Kurucz model). As in the calculation of $\lambda_{\rm eff}$, and taking the same values, we estimate the uncertainty varying the parameters that affect the intrinsic colour calculation (temperature of the model, metallicity, $\log g$, and precipitable water vapour). The values for RC stars and young known stars are presented in tables B.1 and B.2. For RC stars we used a model with solar metallicity, 4750 K, and 1.6 mm of precipitable water vapour. For the young known stars, we only changed the temperature of the model to 30,000 K. As in Appendix A, the final uncertainty was computed adding quadratically all the individual uncertainties. In this way, we obtained an upper limit for the uncertainty.

Table B.1 Intrinsic colour for RC stars.

		$(J-H)_0$	$(H-K_s)_0$
Value		0.495	0.089
Uncertainty	T	0.074	0.012
	met	0.025	0.004
	$\log g$	0.002	0.001
	hum	0.0006	0.0003
	Total	0.078	0.013

Notes. The uncertainties are shown independently depending on every parameter. From top to bottom: temperature of the model, metallicity, and water vapour column density.

It can be seen that the most important factor is the temperature of the model. In the case of known late-type stars, we computed for each of them the corresponding value, depending on the metallicity and temperature.

Table B.2 Intrinsic colour for known young stars.

		$(J-H)_0$	$(H-K_s)_0$
Value		-0.090	-0.117
	T	0.018	0.02
	met	0.003	0.003
Uncertainty	$\log g$	0.002	0.001
	hum	0.0002	0.00003
	Total	0.019	0.02

Notes. The uncertainties are shown independently depending on every parameter. From top to bottom: temperature of the model, metallicity, and water vapour column density.

C

GALACTICNUCLEUS images

This appendix contains RGB images from all the pointings covered by the GALACTICNUCLEUS survey (F7 and B6 are not included due to bad observing conditions in one of the bands). It allows to visually check the high angular resolution of the catalogue and some characteristics of the observed pointings as the high crowding and the patchy extinction patterns due to differential extinction.

C.1 Inner Bulge South catalogue

C.2 Transition West catalogue

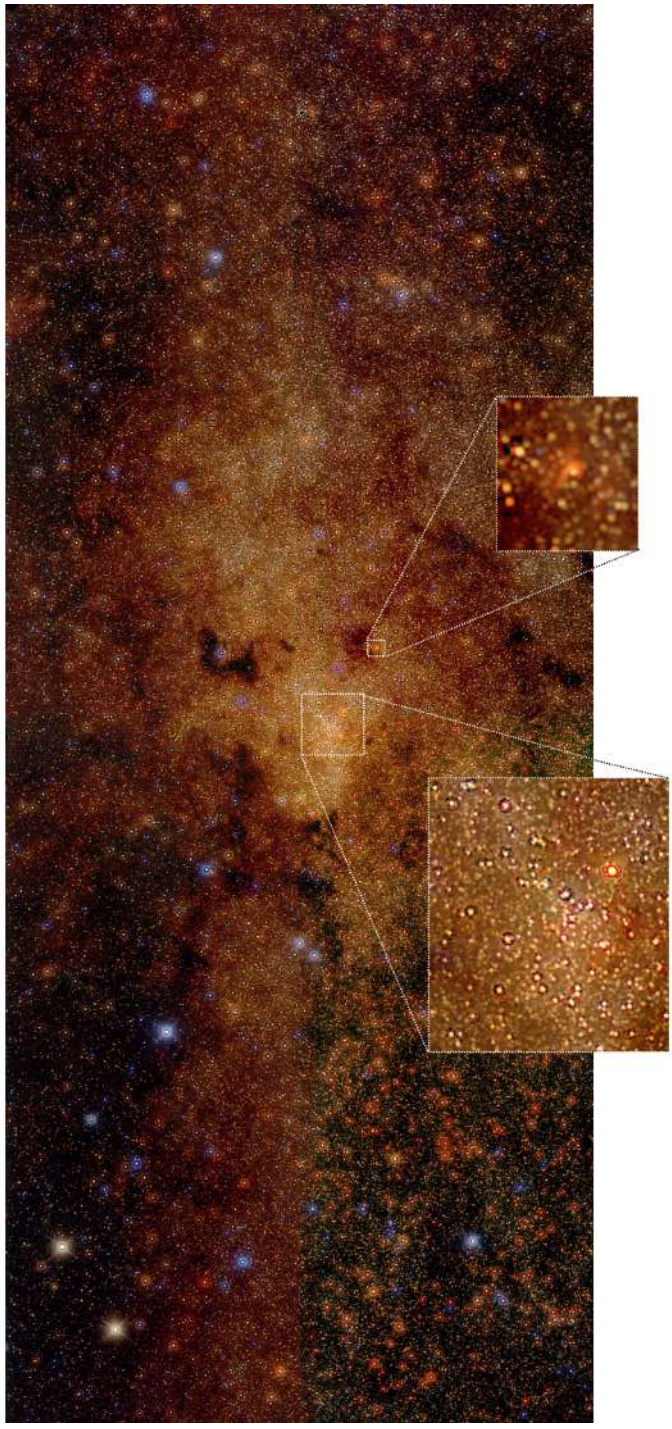

Fig. C.1 RGB image of F1 (red = K_s band, green = H band and blue = J band).

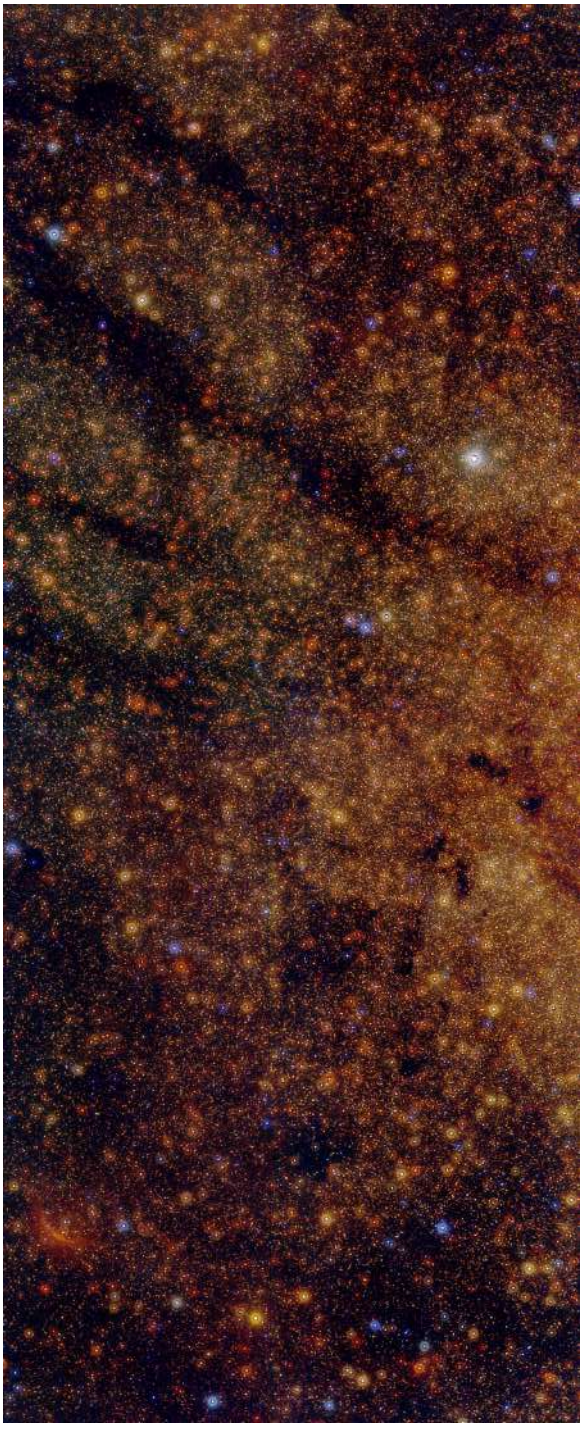

Fig. C.2 RGB image of F2 (red = K_s band, green = H band and blue = J band).

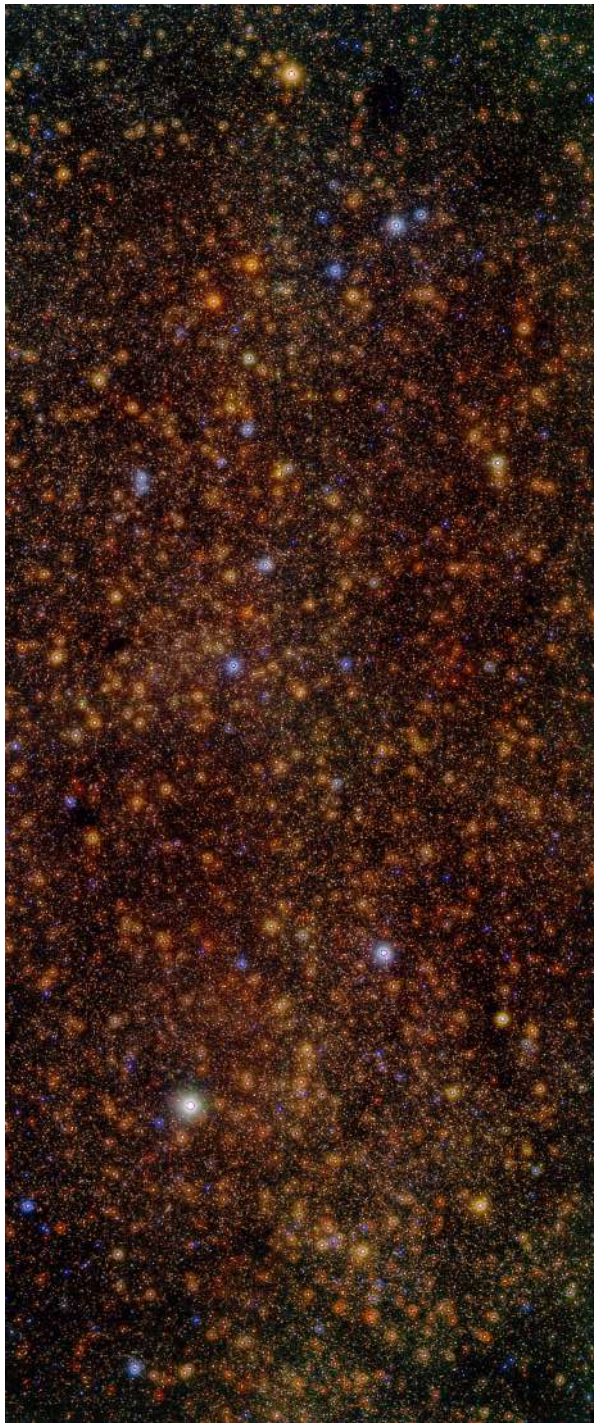

Fig. C.3 RGB image of F3 (red = K_s band, green = H band and blue = J band).

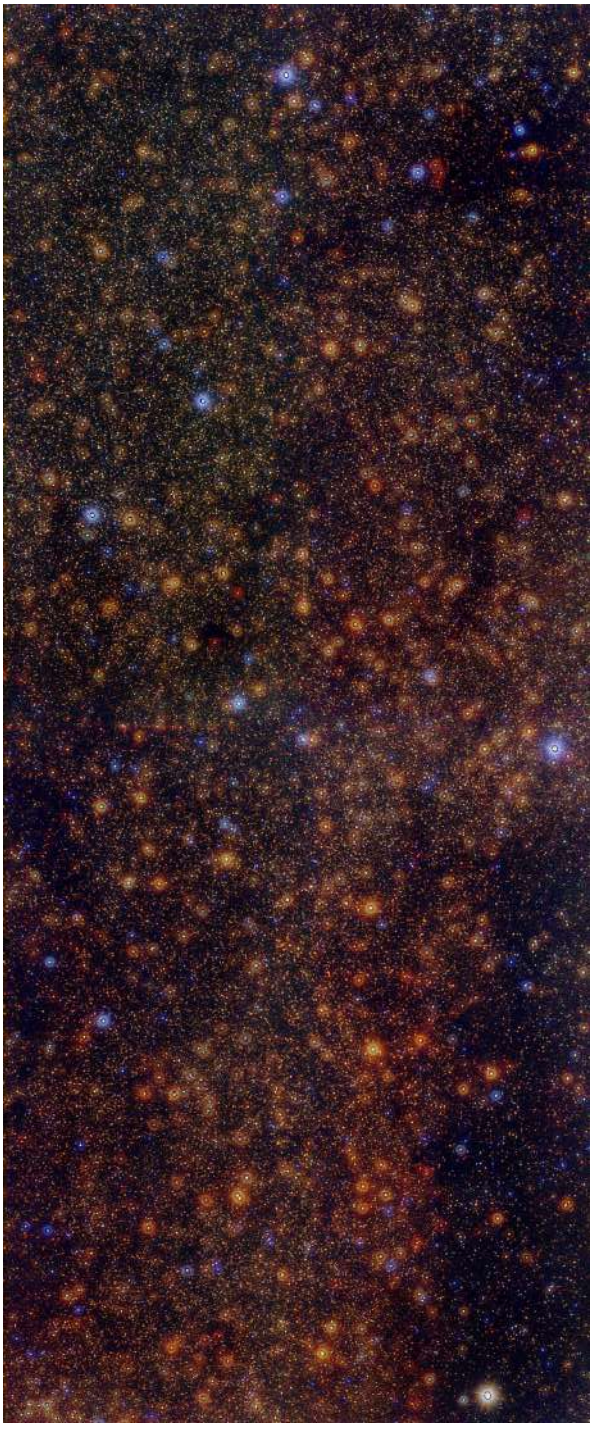

Fig. C.4 RGB image of F4 (red = K_s band, green = H band and blue = J band).

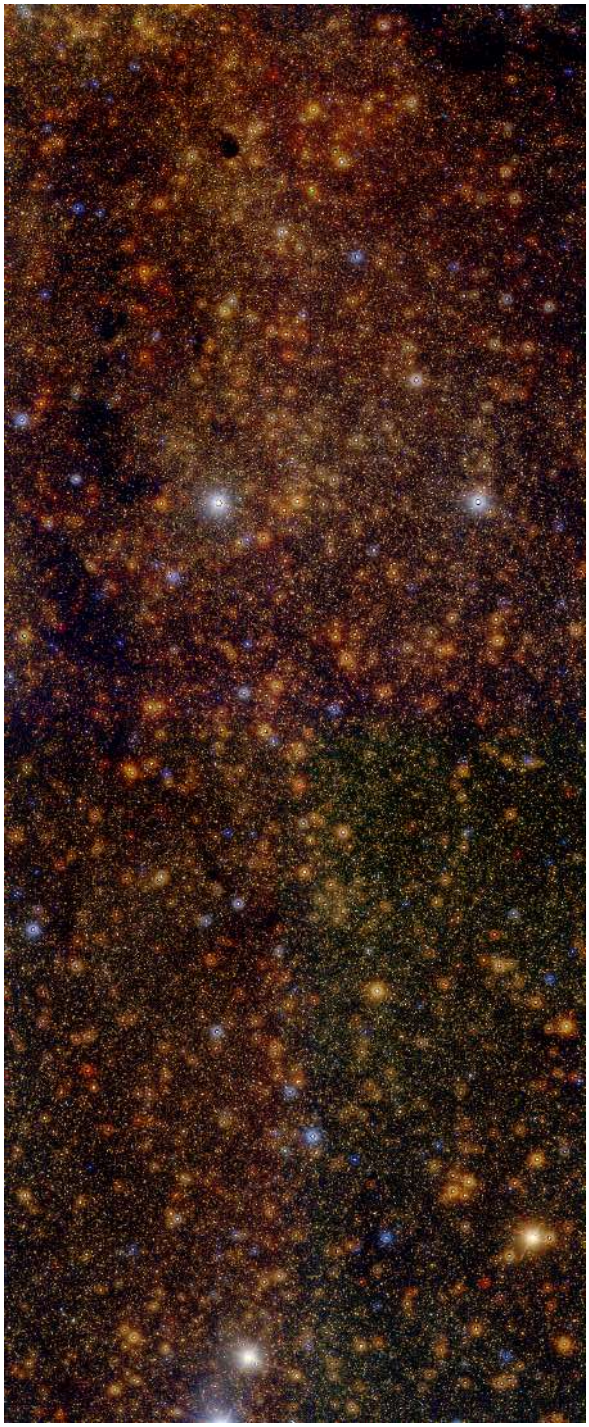

Fig. C.5 RGB image of F5 (red = K_s band, green = H band and blue = J band).

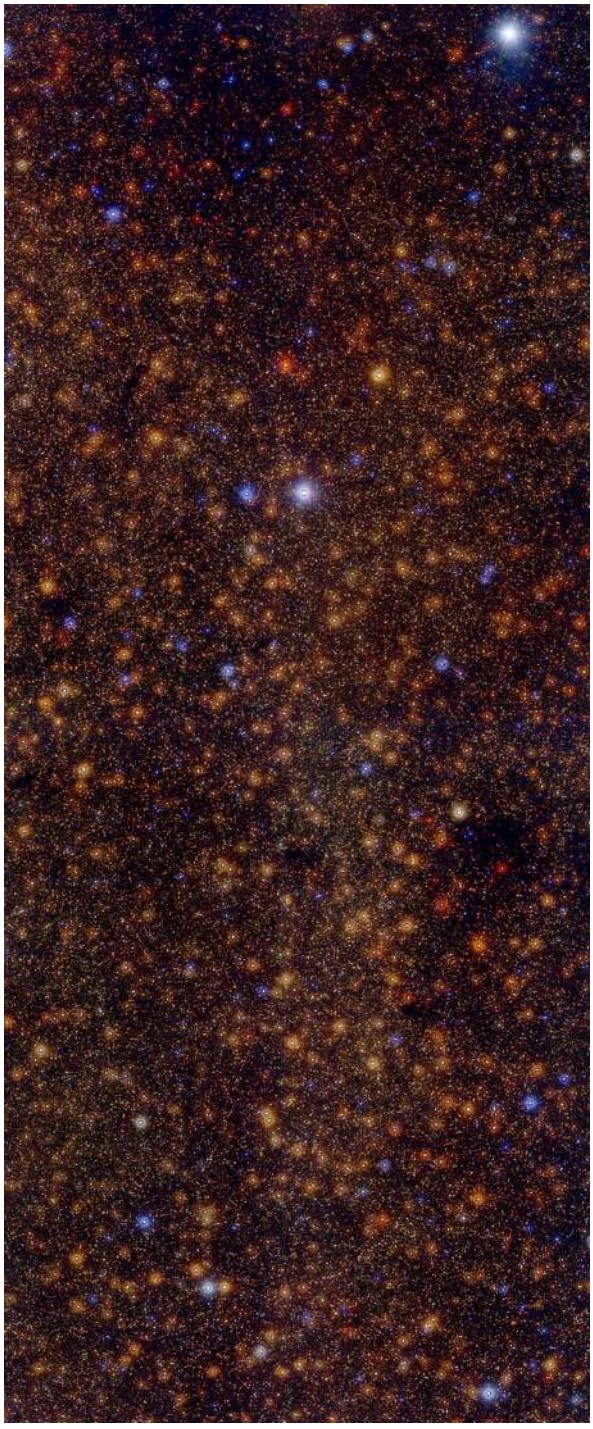

Fig. C.6 RGB image of F6 (red = K_s band, green = H band and blue = J band).

Fig. C.7 RGB image of F8 (red = K_s band, green = H band and blue = J band).

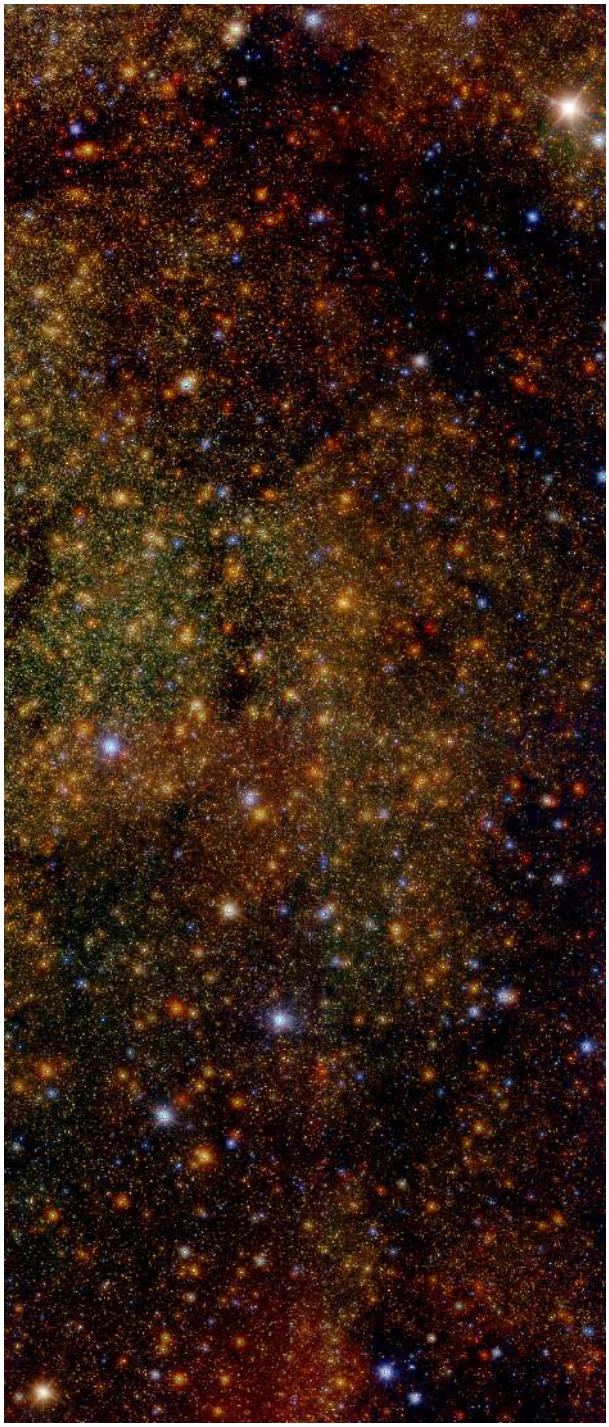

Fig. C.8 RGB image of F9 (red = K_s band, green = H band and blue = J band).

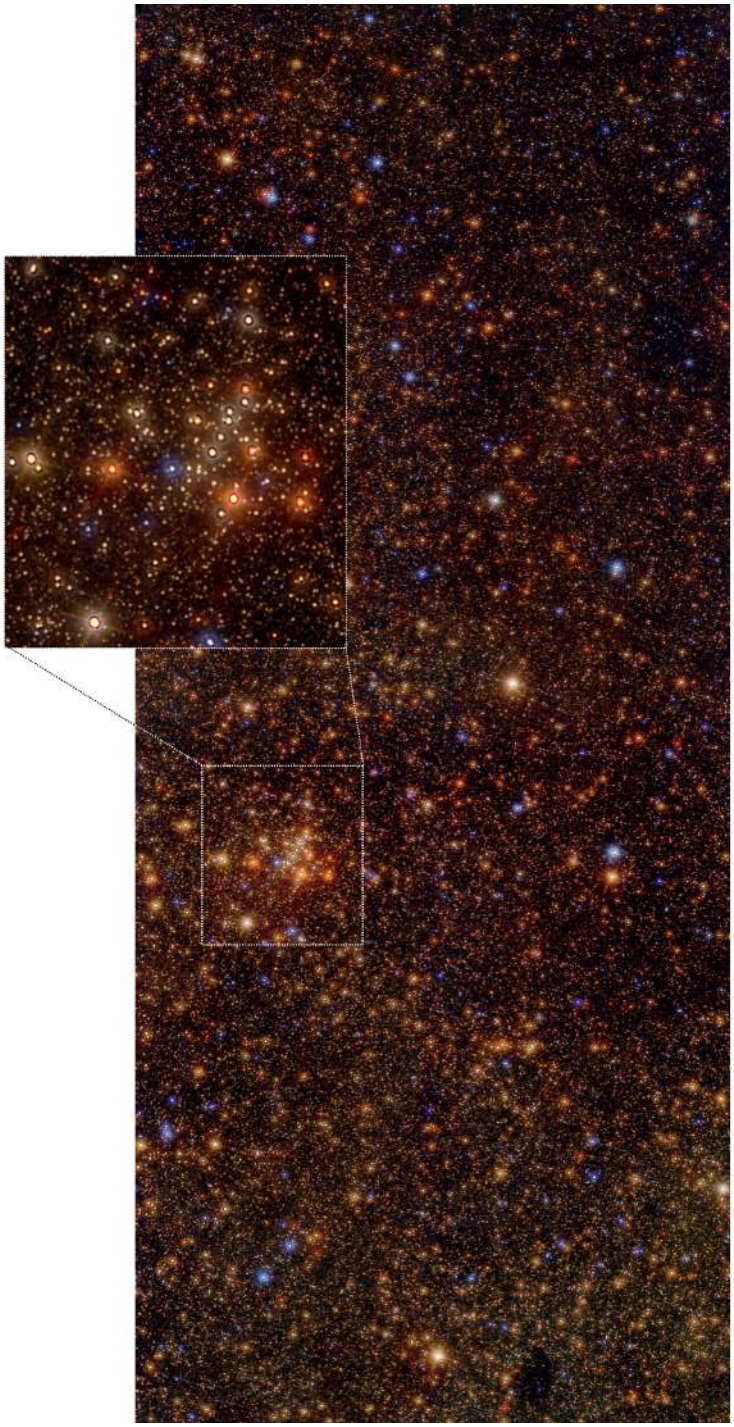

Fig. C.9 RGB image of F10 (red = K_s band, green = H band and blue = J band).

Fig. C.10 RGB image of F11 (red = K_s band, green = H band and blue = J band).

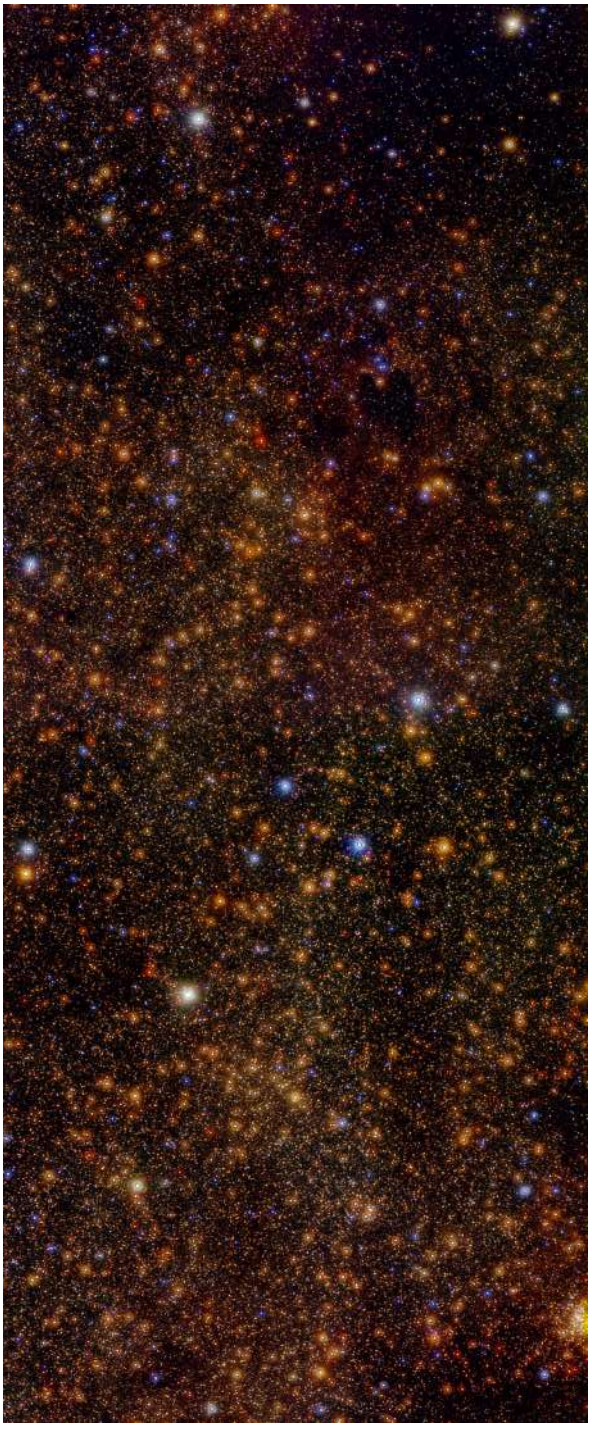

Fig. C.11 RGB image of F12 (red = K_s band, green = H band and blue = J band).

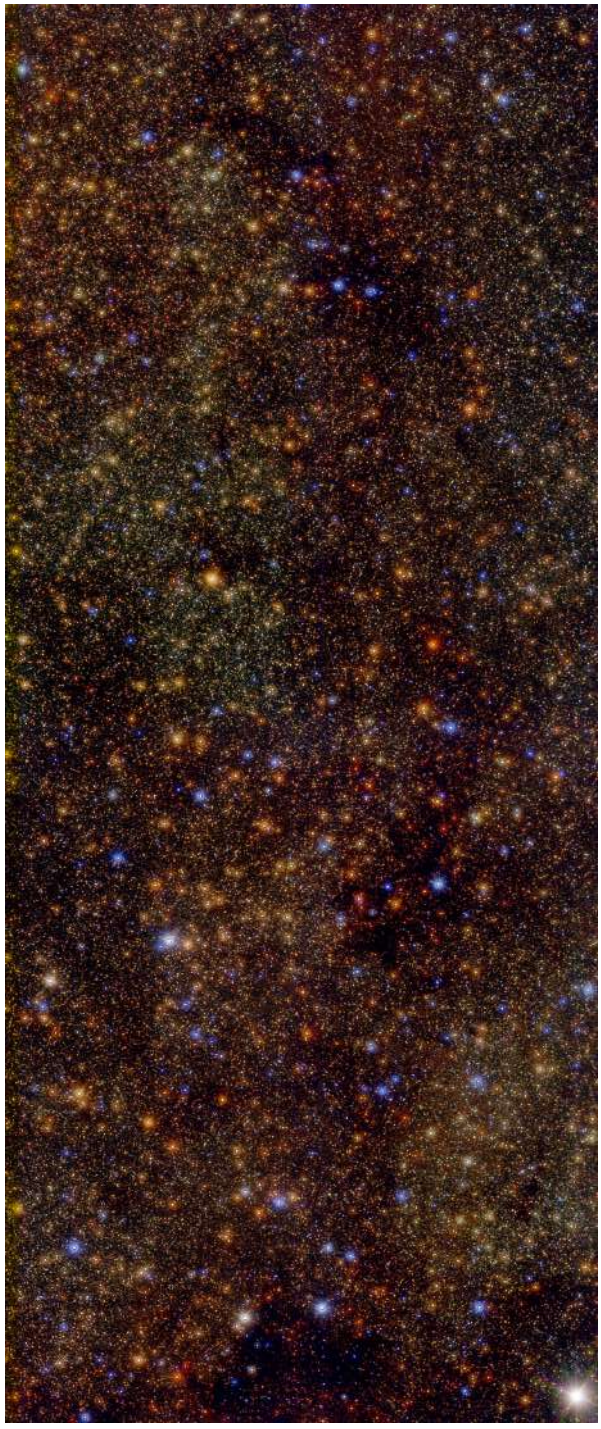

Fig. C.12 RGB image of F13 (red = K_s band, green = H band and blue = J band).

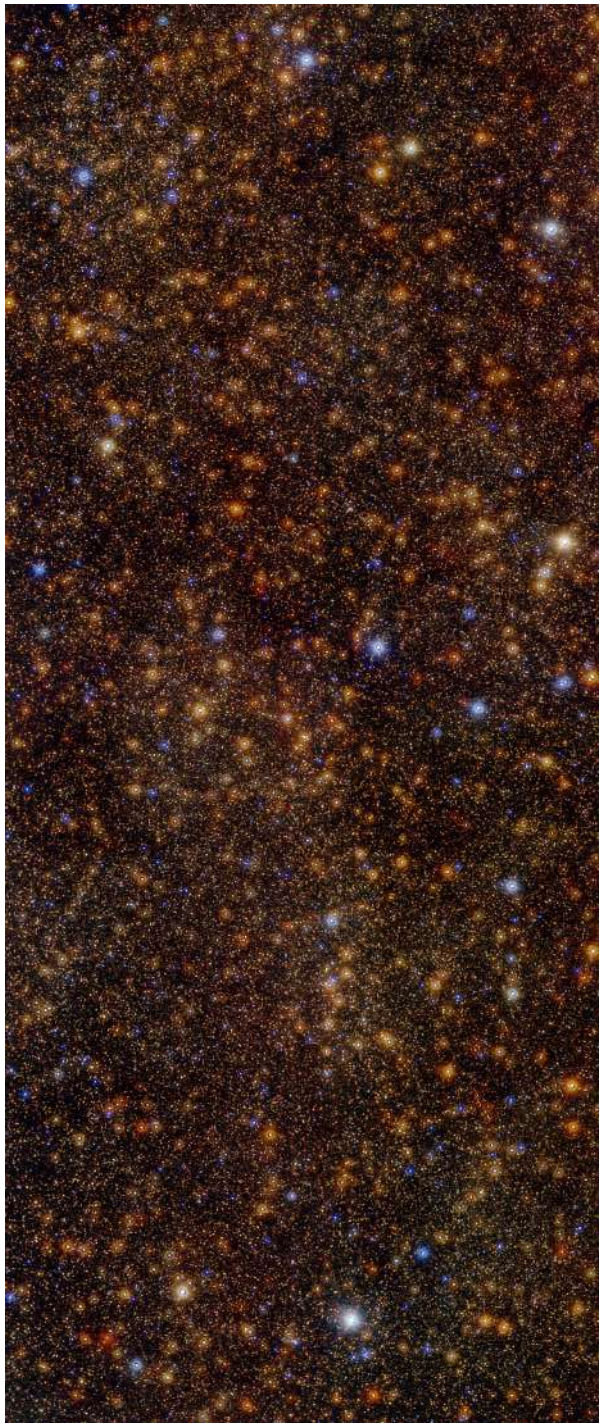

Fig. C.13 RGB image of F14 (red = K_s band, green = H band and blue = J band).

Fig. C.14 RGB image of F15 (red = K_s band, green = H band and blue = J band).

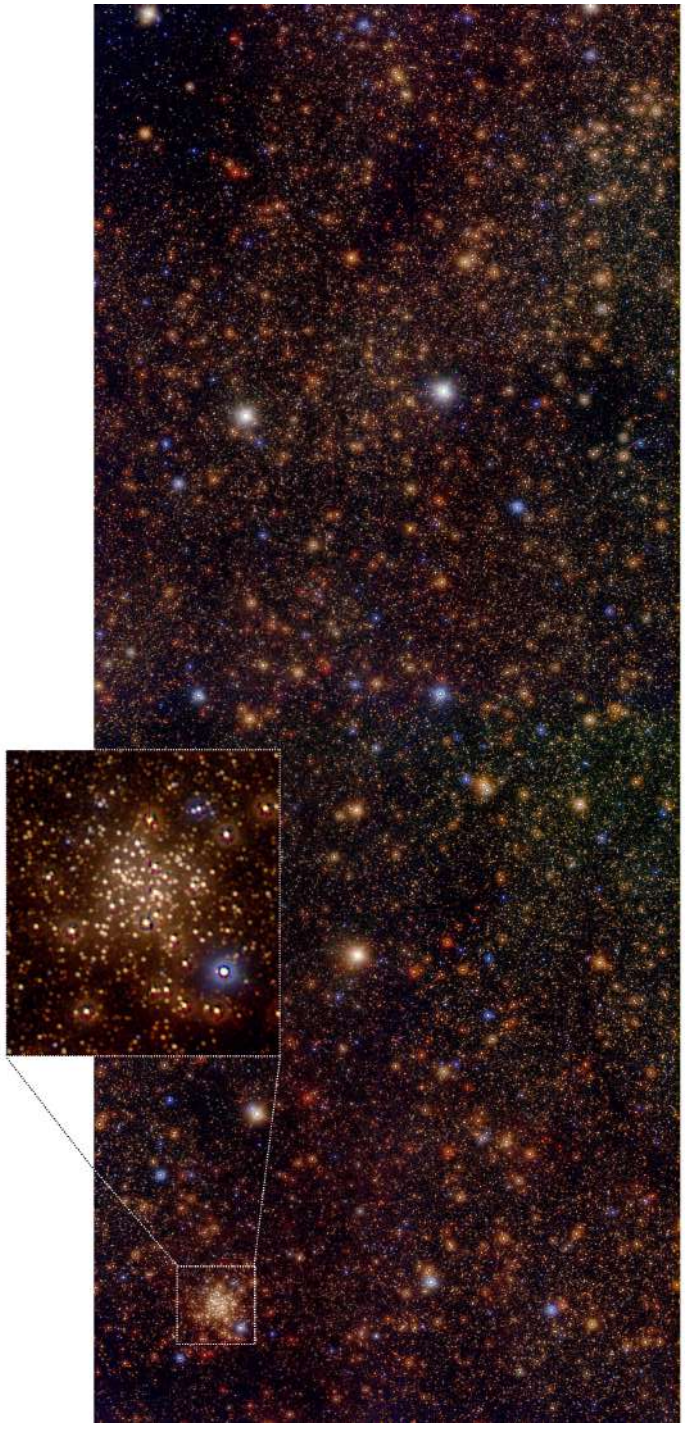

Fig. C.15 RGB image of F16 (red = K_s band, green = H band and blue = J band).

Fig. C.16 RGB image of F17 (red = K_s band, green = H band and blue = J band).

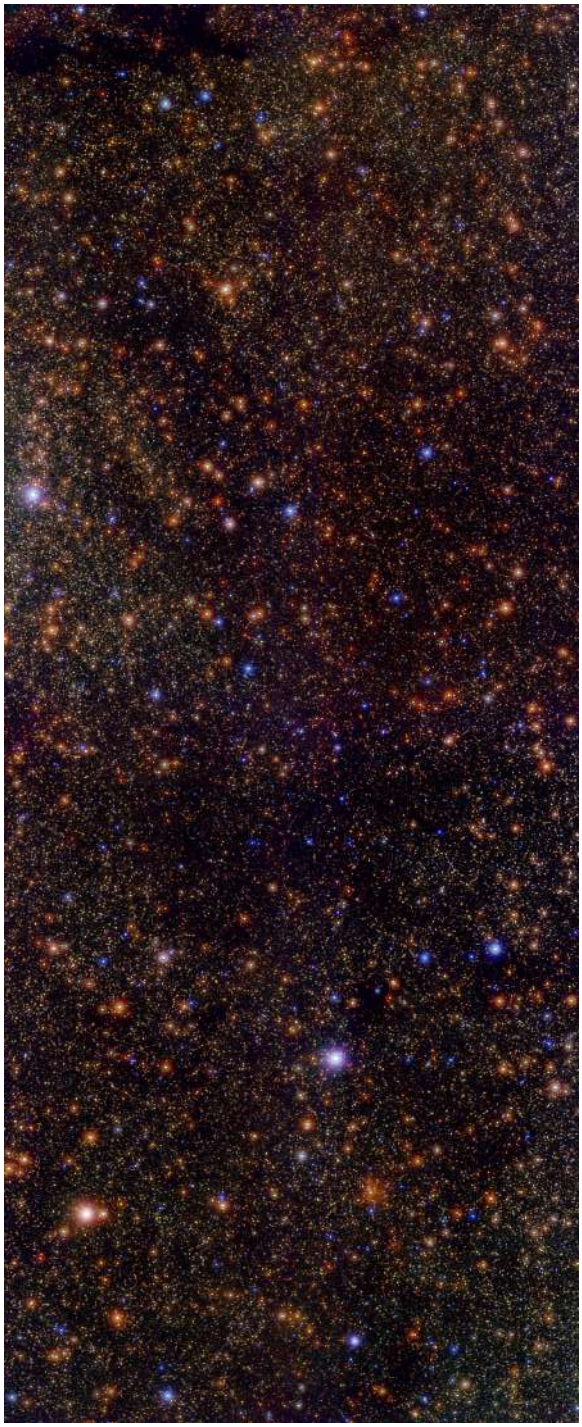

Fig. C.17 RGB image of F18 (red = K_s band, green = H band and blue = J band).

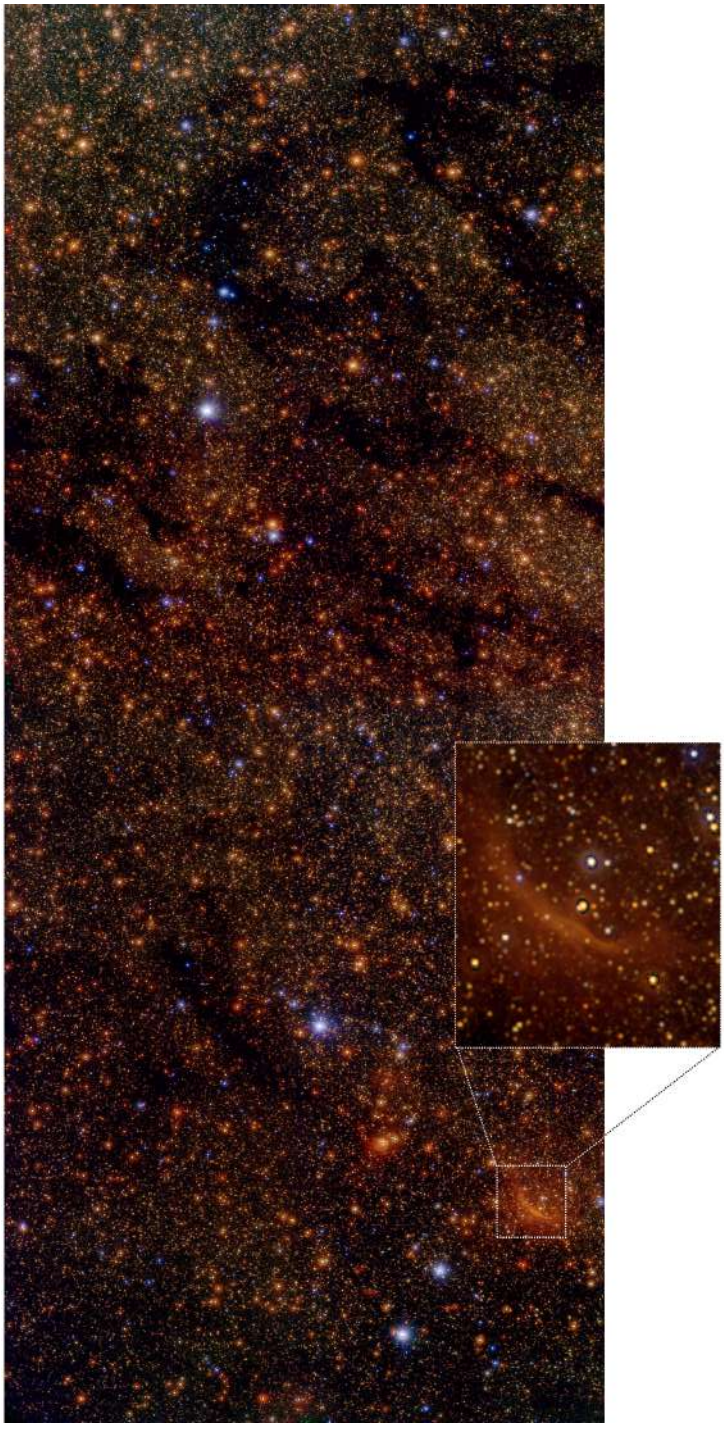

Fig. C.18 RGB image of F19 (red = K_s band, green = H band and blue = J band).

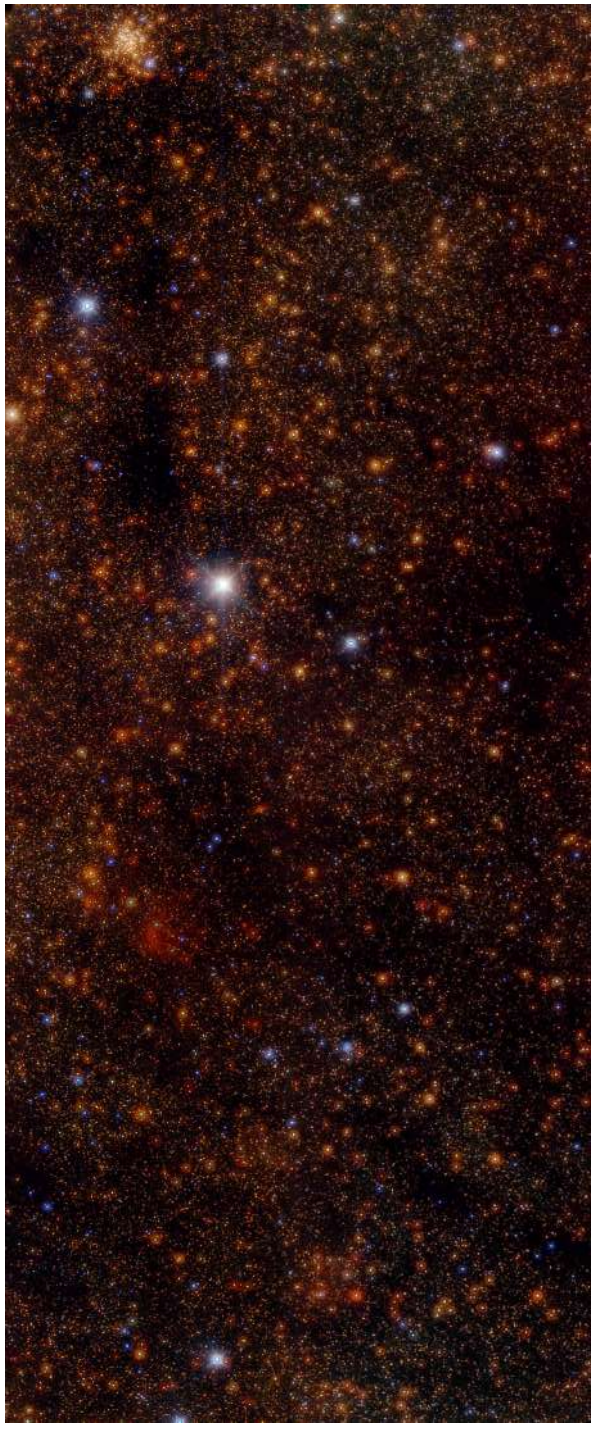

Fig. C.19 RGB image of F20 (red = K_s band, green = H band and blue = J band).

Fig. C.20 RGB image of F21 (red = K_s band, green = H band and blue = J band).

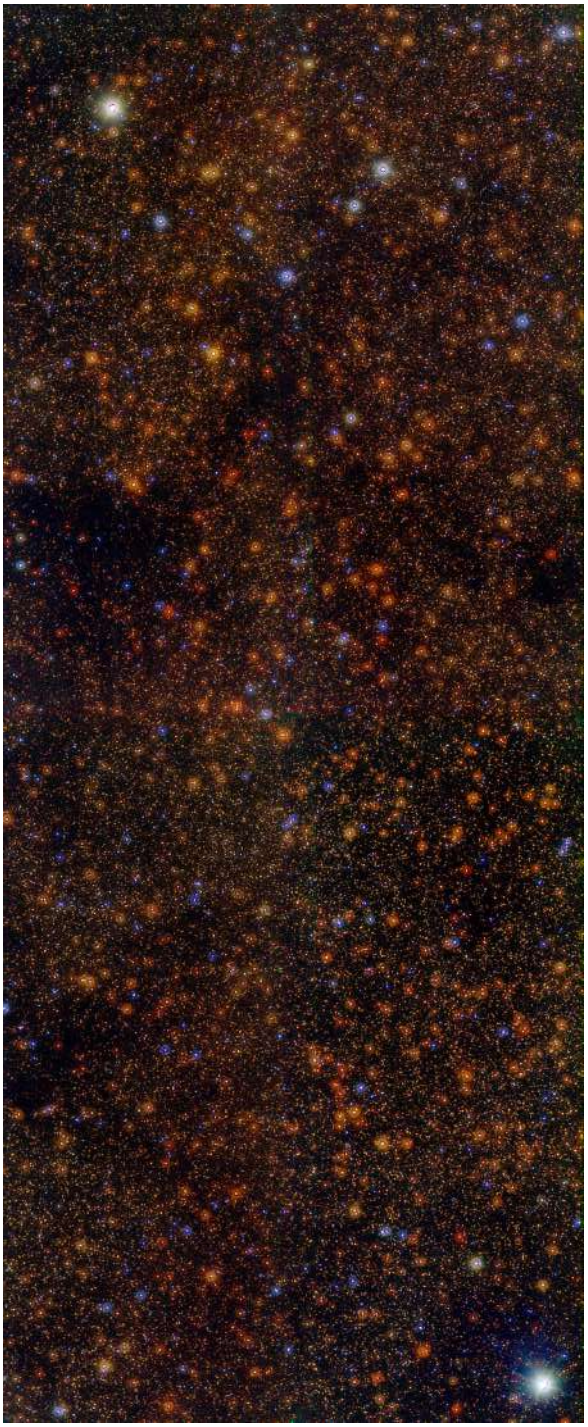

Fig. C.21 RGB image of F22 (red = K_s band, green = H band and blue = J band).

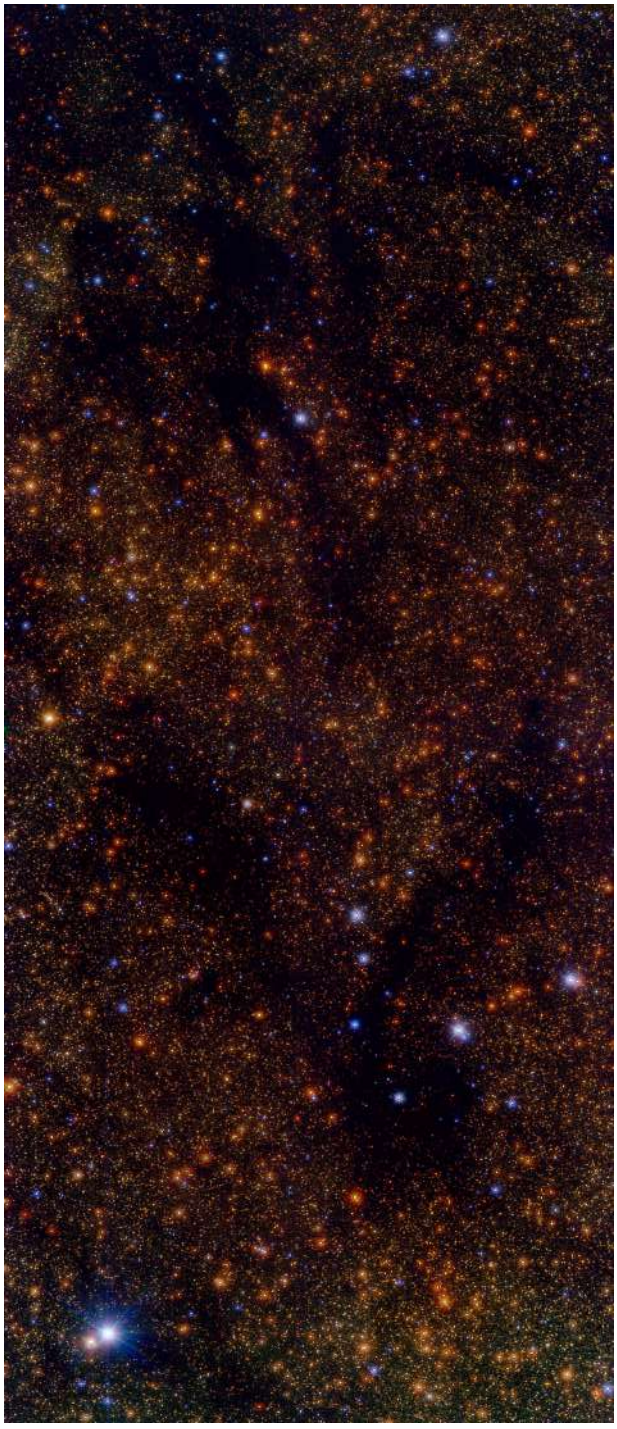

Fig. C.22 RGB image of F23 (red = K_s band, green = H band and blue = J band).

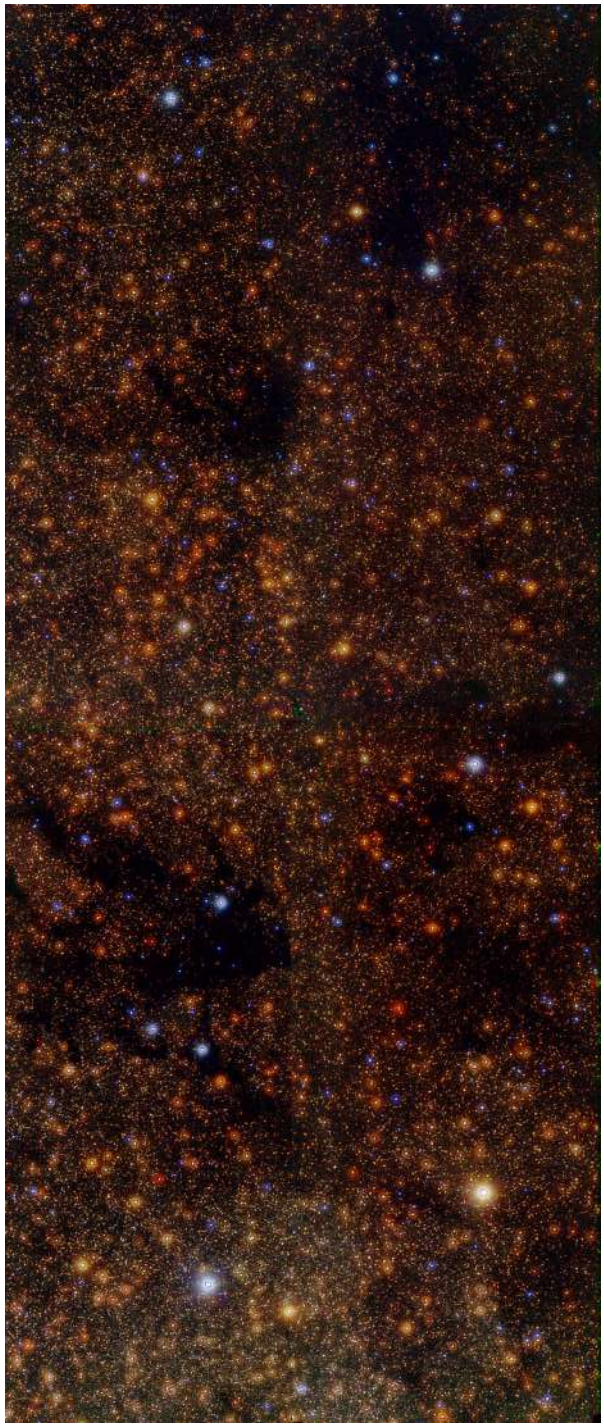

Fig. C.23 RGB image of F24 (red = K_s band, green = H band and blue = J band).

Fig. C.24 RGB image of F25 (red = K_s band, green = H band and blue = J band).

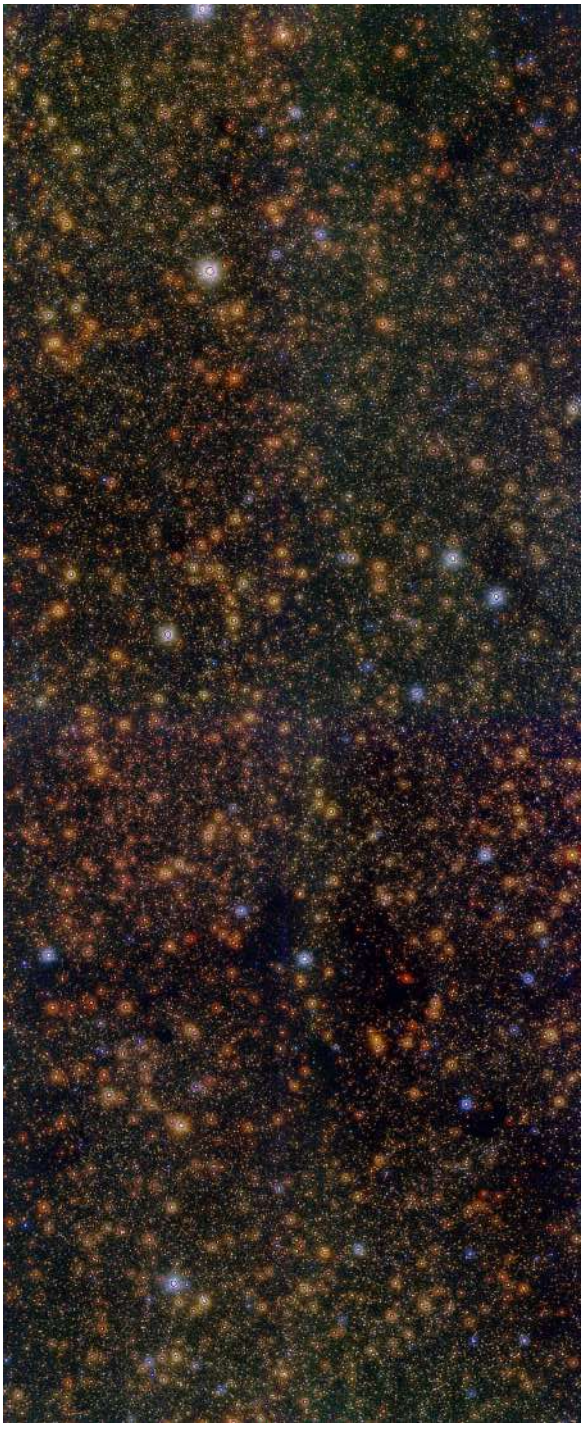

Fig. C.25 RGB image of F26 (red = K_s band, green = H band and blue = J band).

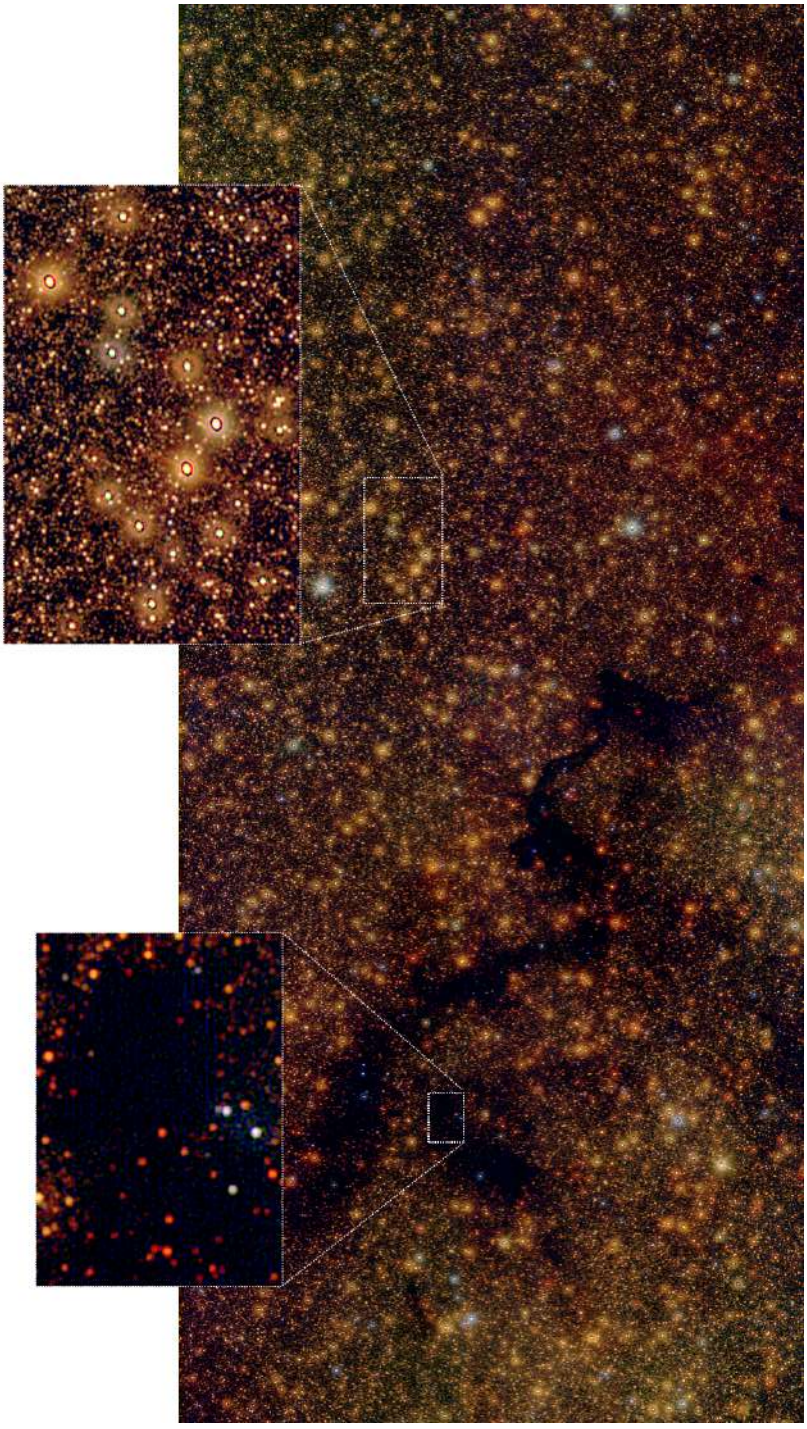

Fig. C.26 RGB image of F27 (red = K_s band, green = H band and blue = J band).

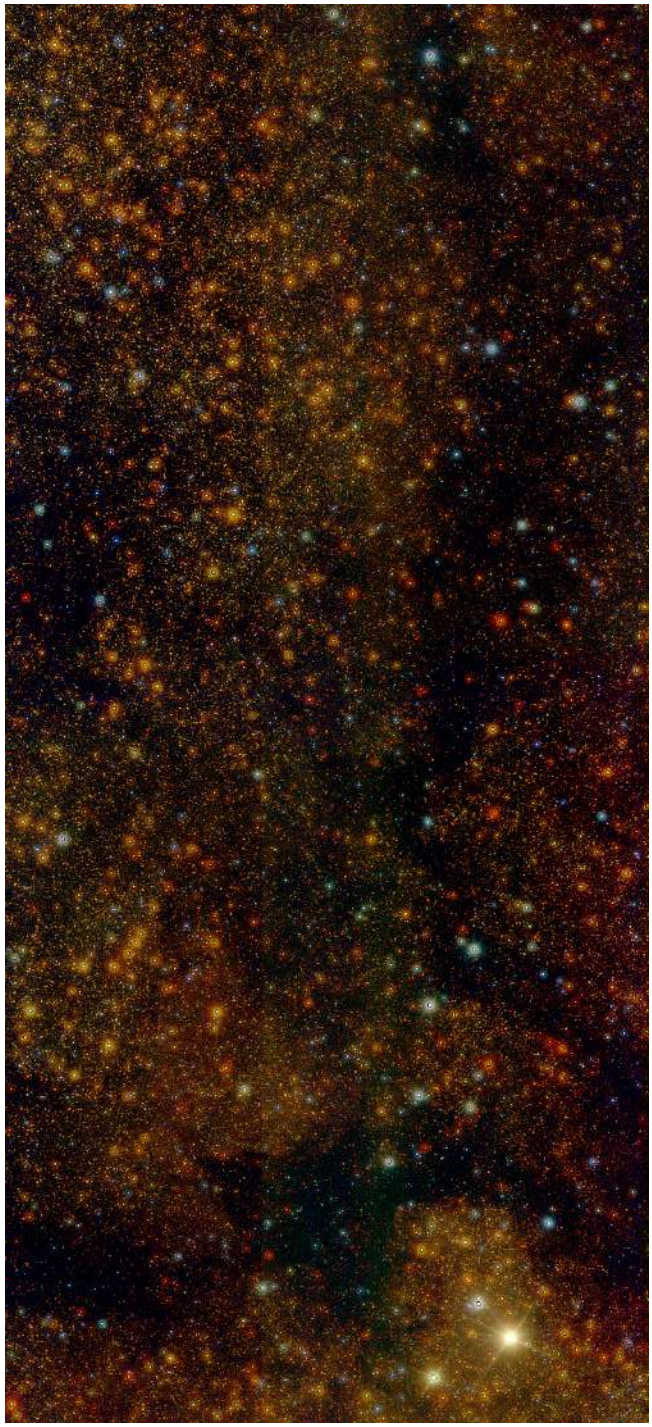

Fig. C.27 RGB image of F28 (red = K_s band, green = H band and blue = J band).

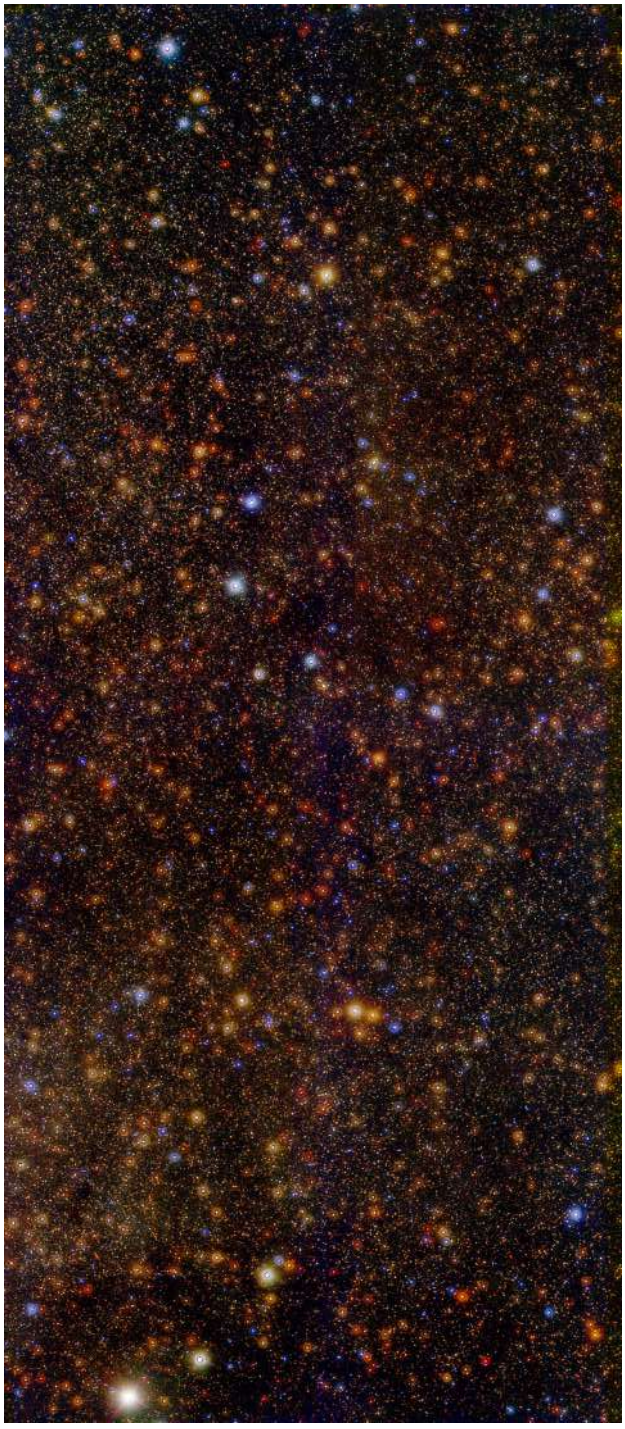

Fig. C.28 RGB image of F29 (red = K_s band, green = H band and blue = J band).

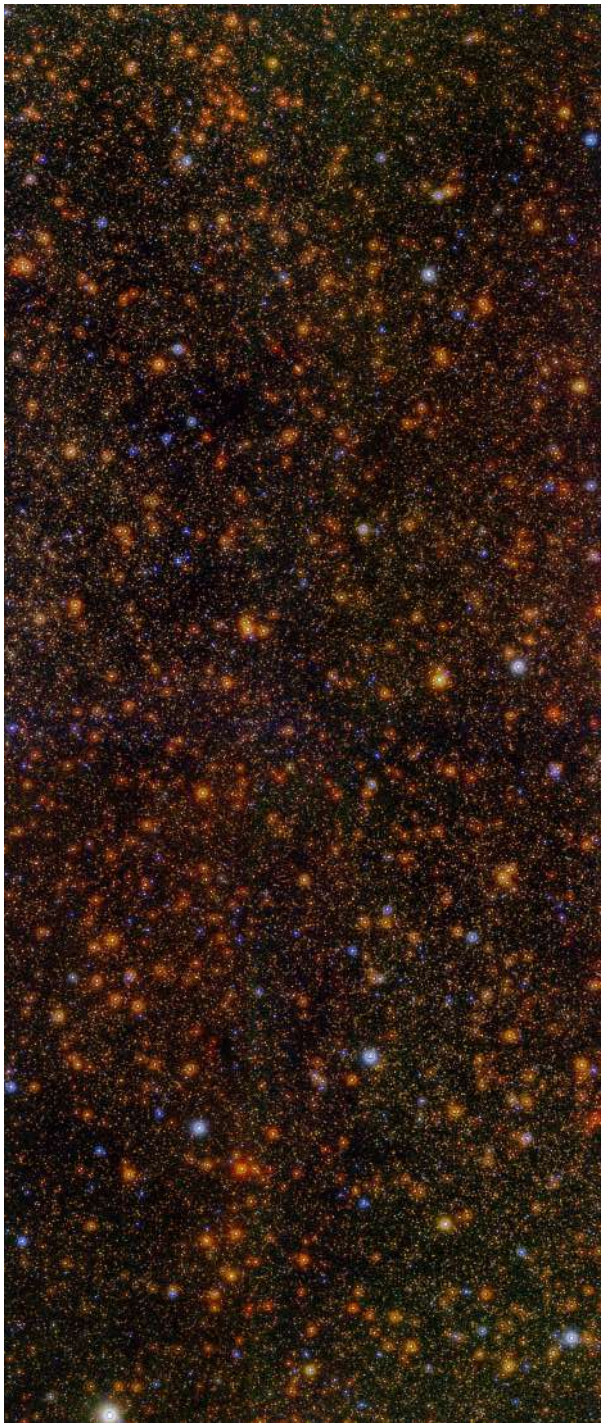

Fig. C.29 RGB image of F30 (red = K_s band, green = H band and blue = J band).

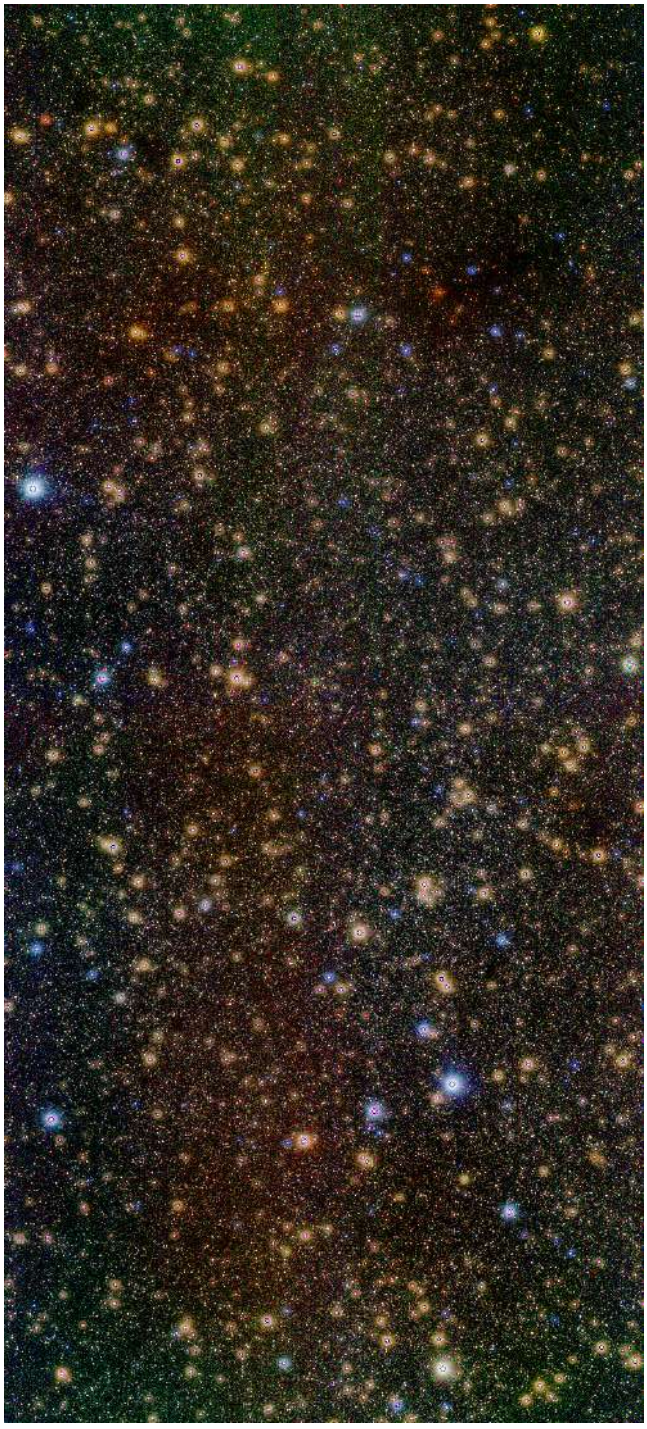

Fig. C.30 RGB image of B1 (red = K_s band, green = H band and blue = J band).

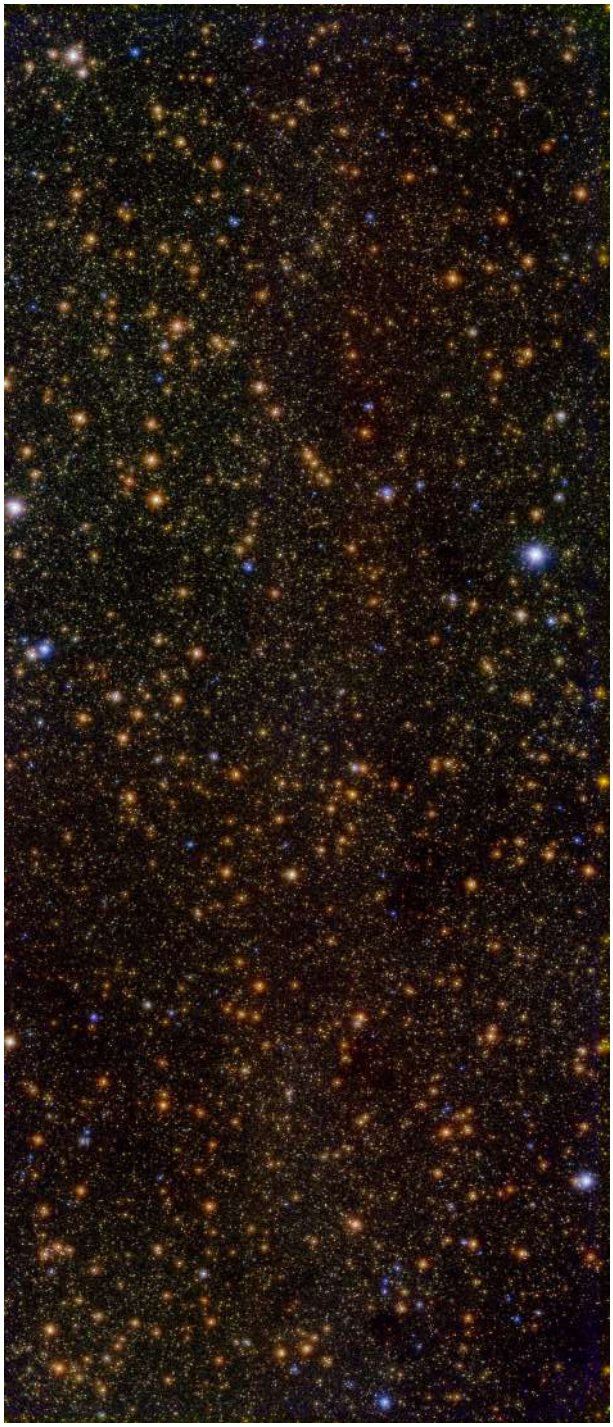

Fig. C.31 RGB image of B2 (red = K_s band, green = H band and blue = J band).

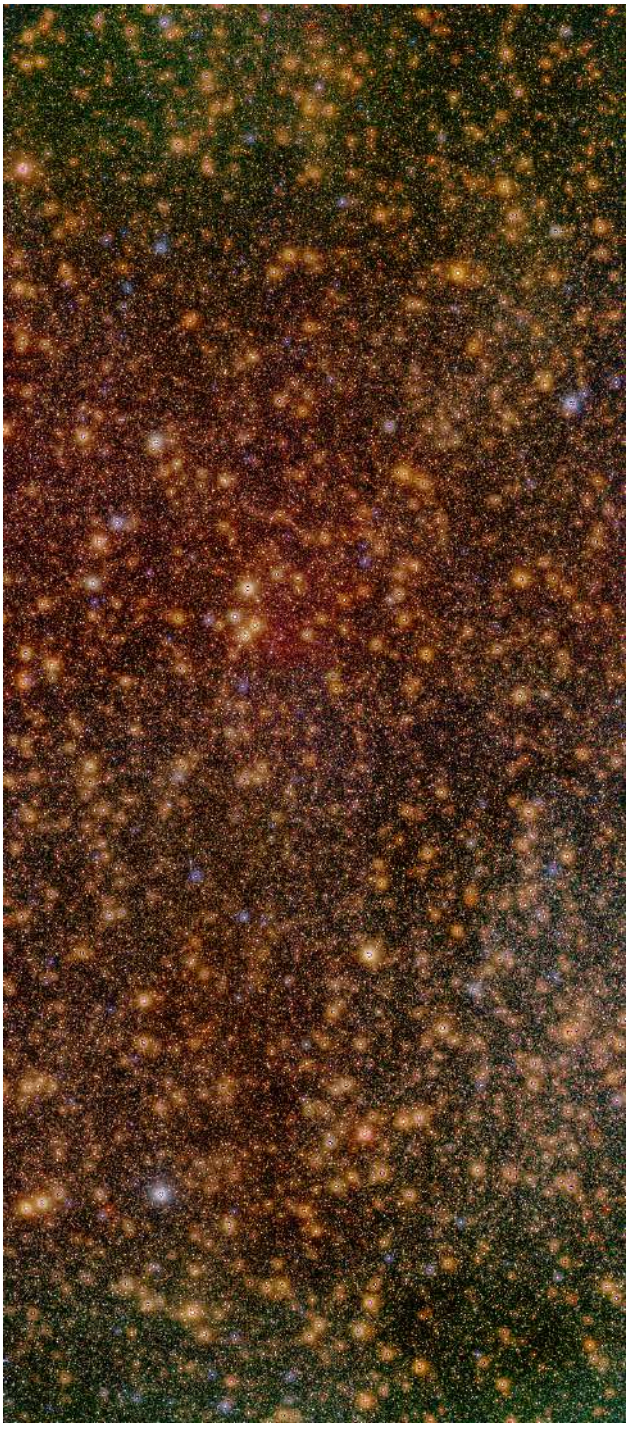

Fig. C.32 RGB image of T3 (red = K_s band, green = H band and blue = J band).

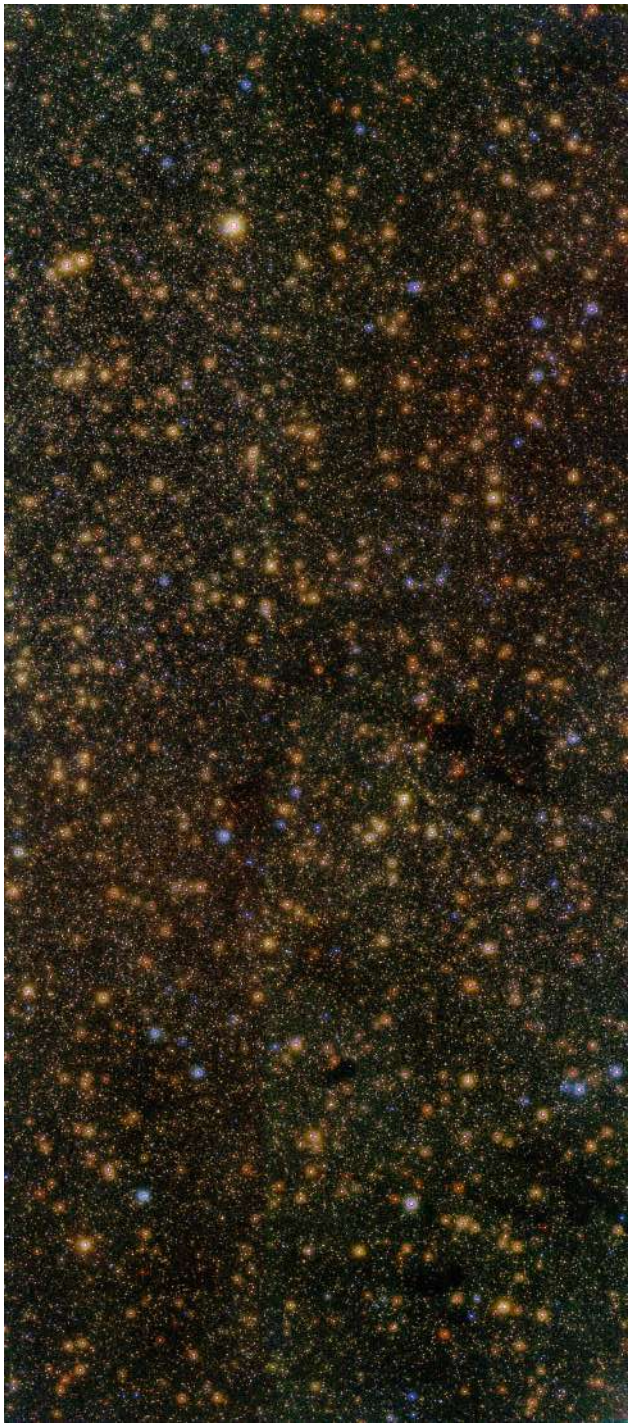

Fig. C.33 RGB image of T4 (red = K_s band, green = H band and blue = J band).

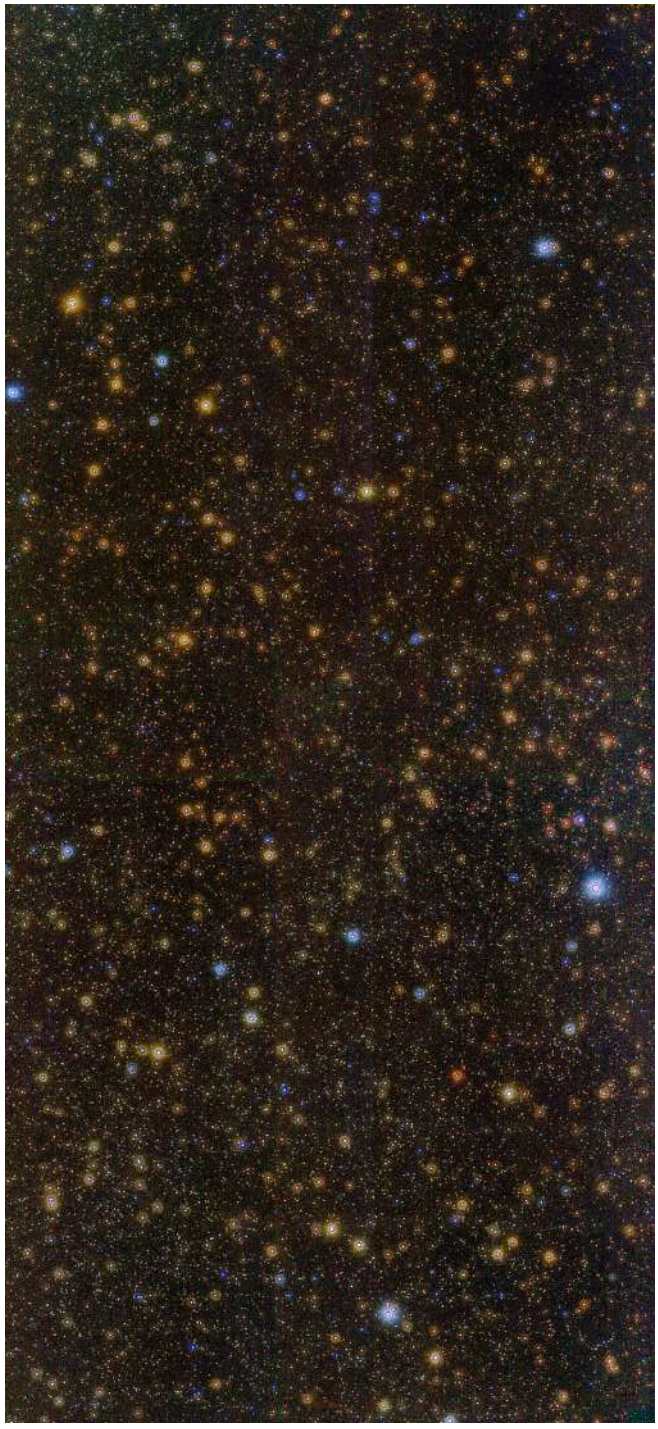

Fig. C.34 RGB image of B5 (red = K_s band, green = H band and blue = J band).

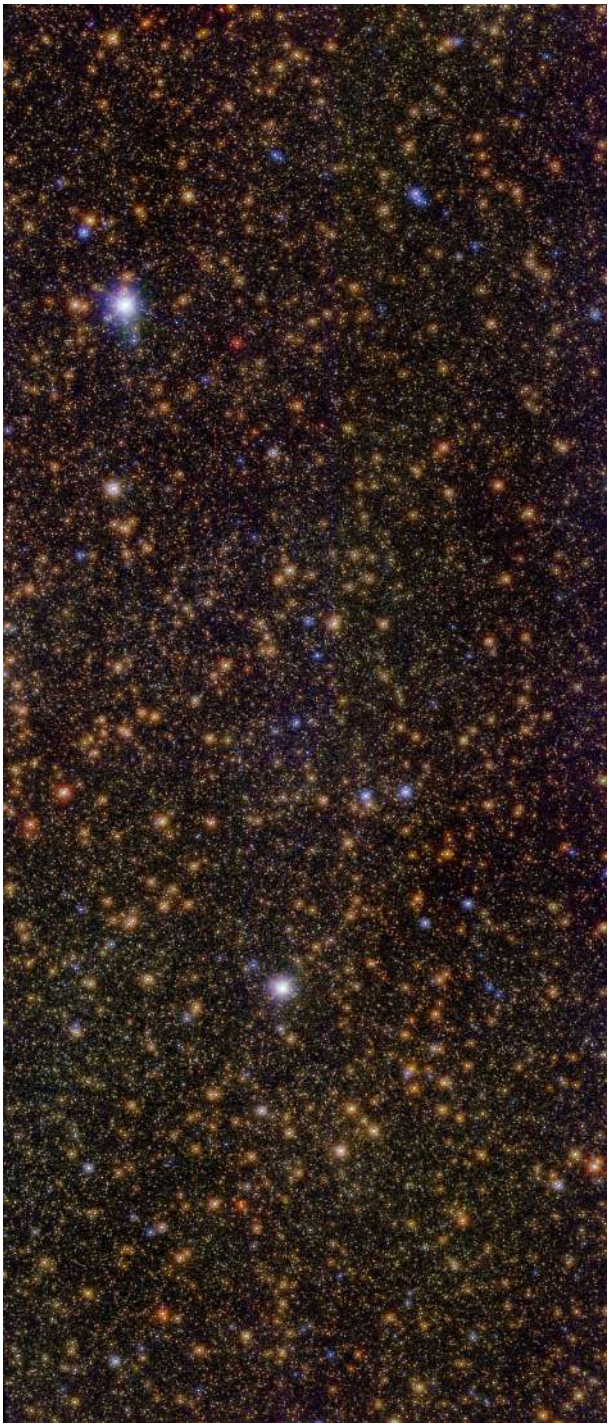

Fig. C.35 RGB image of T7 (red = K_s band, green = H band and blue = J band).

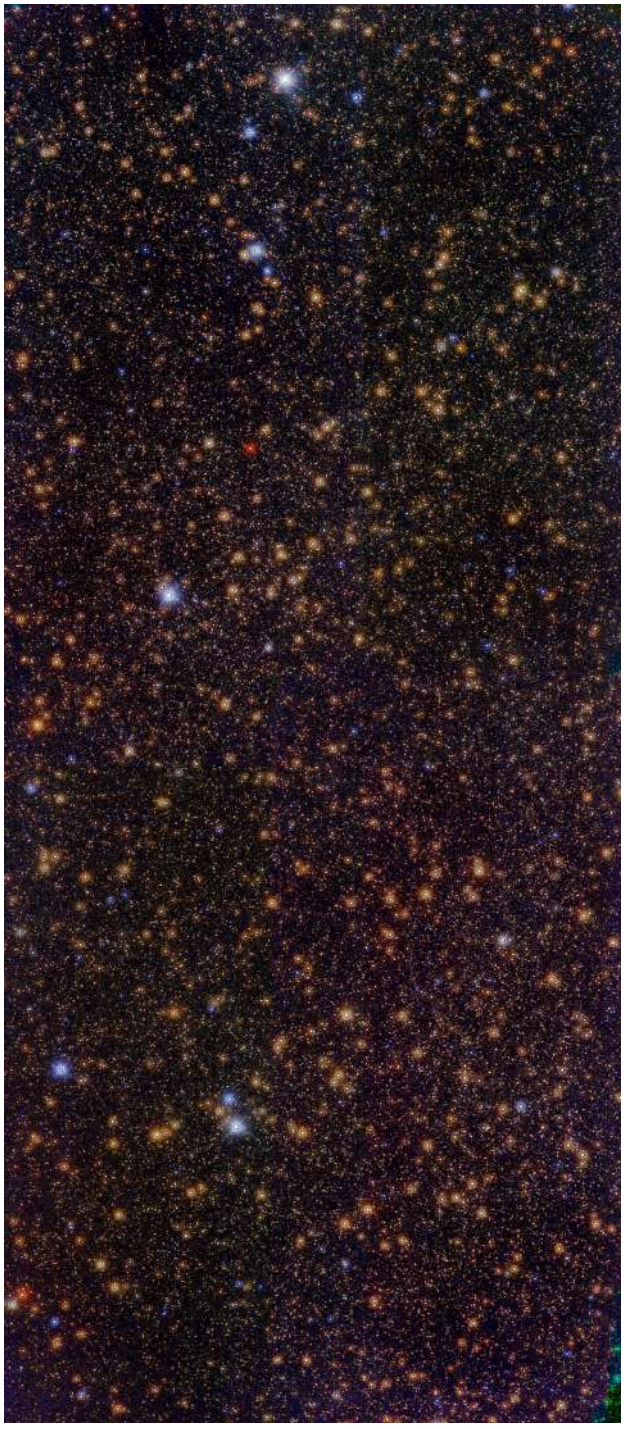

Fig. C.36 RGB image of T8 (red = K_s band, green = H band and blue = J band).

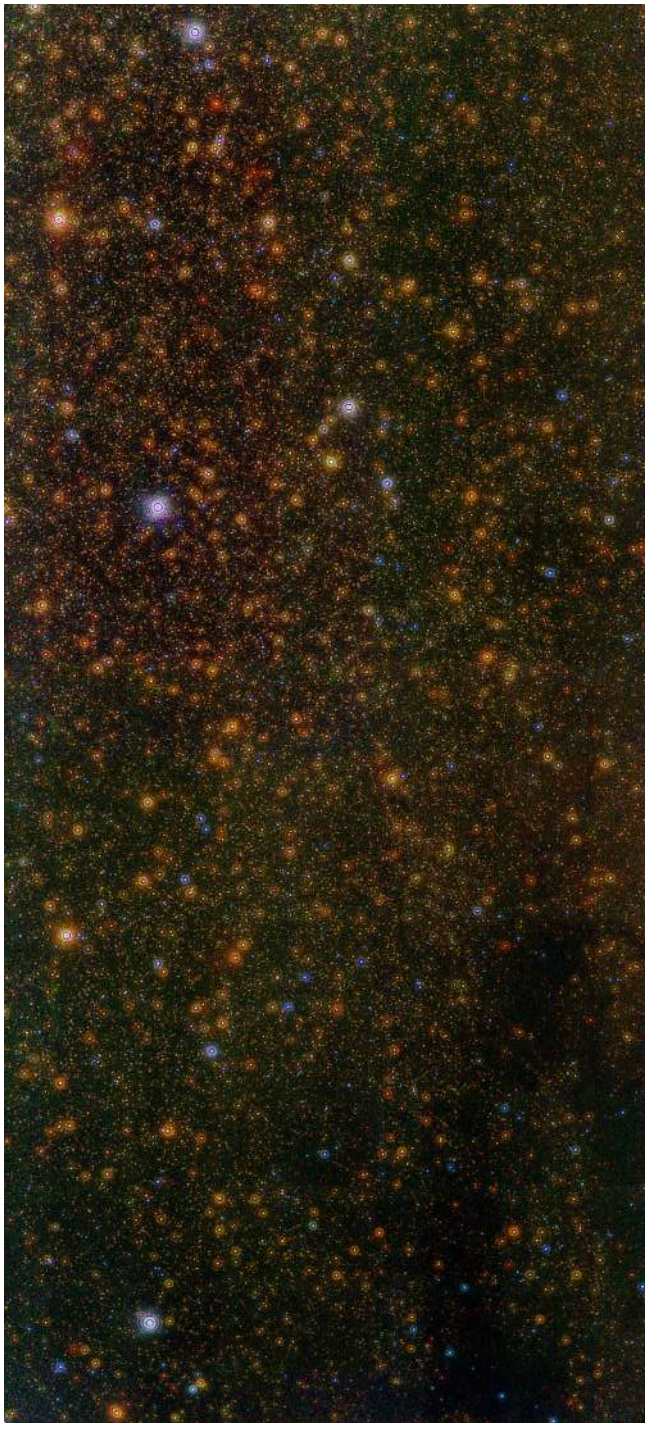

Fig. C.37 RGB image of D9 (red = K_s band, green = H band and blue = J band).

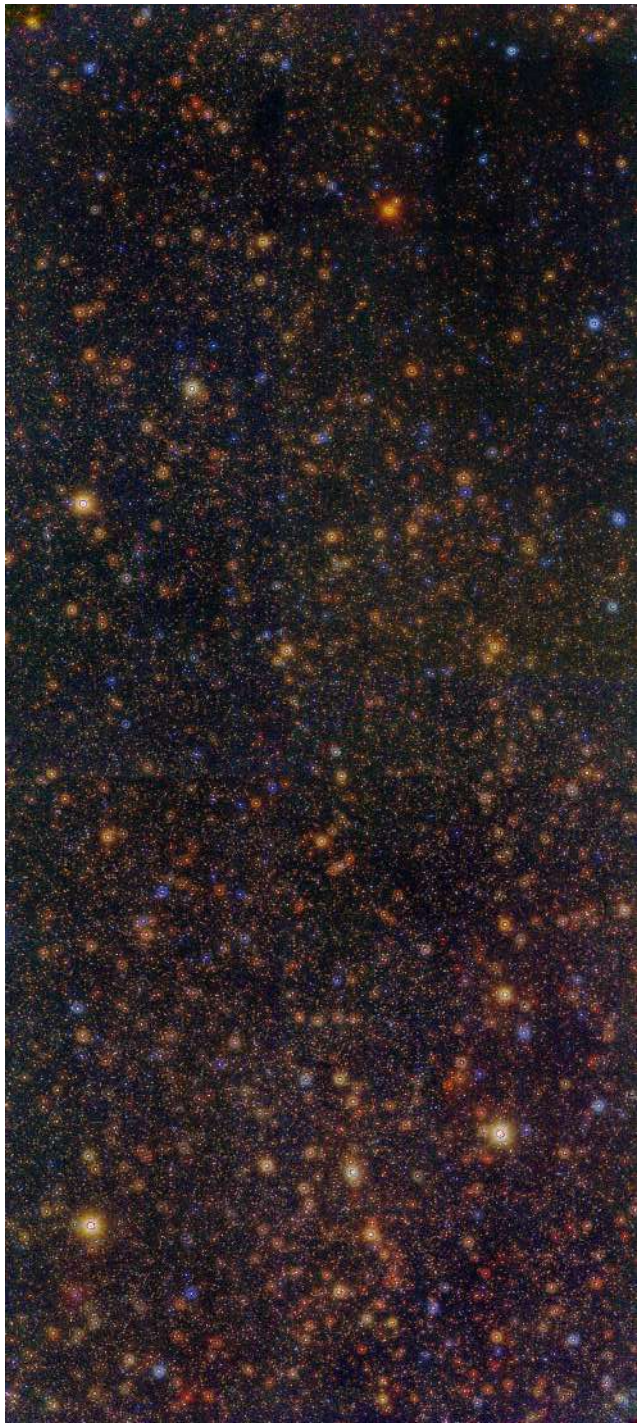

Fig. C.38 RGB image of D10 (red = K_s band, green = H band and blue = J band).

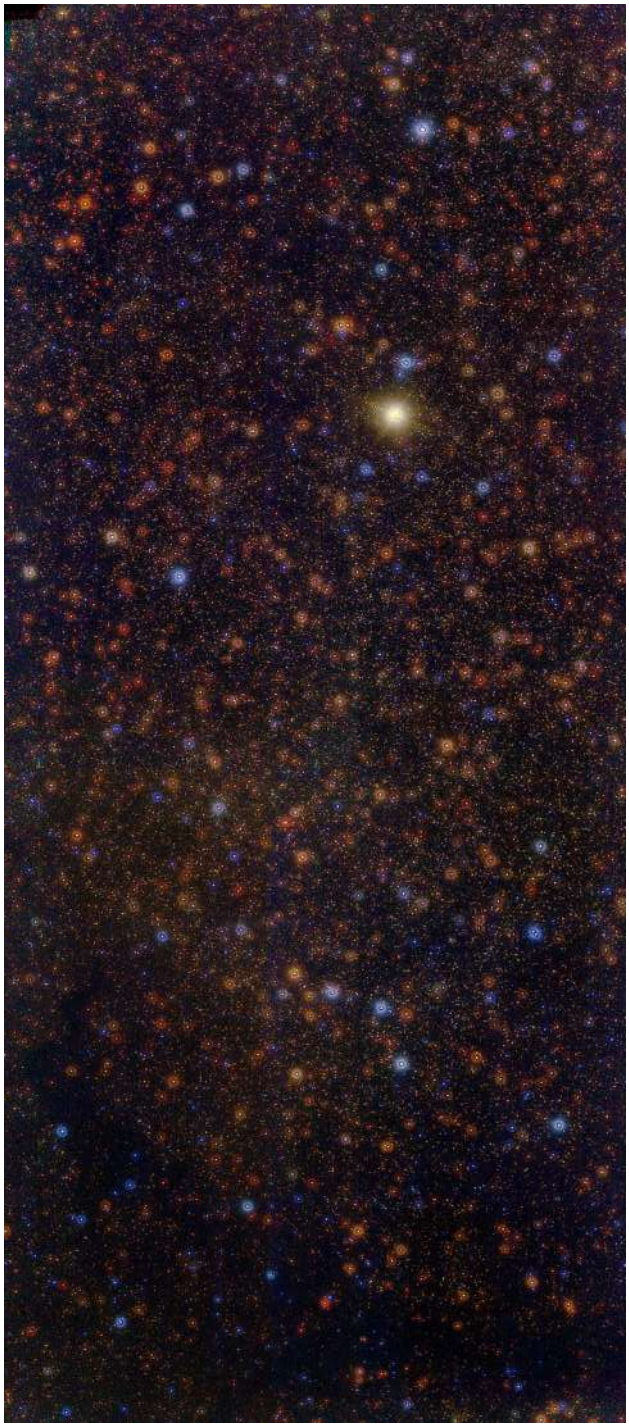

Fig. C.39 RGB image of D11 (red = K_s band, green = H band and blue = J band).

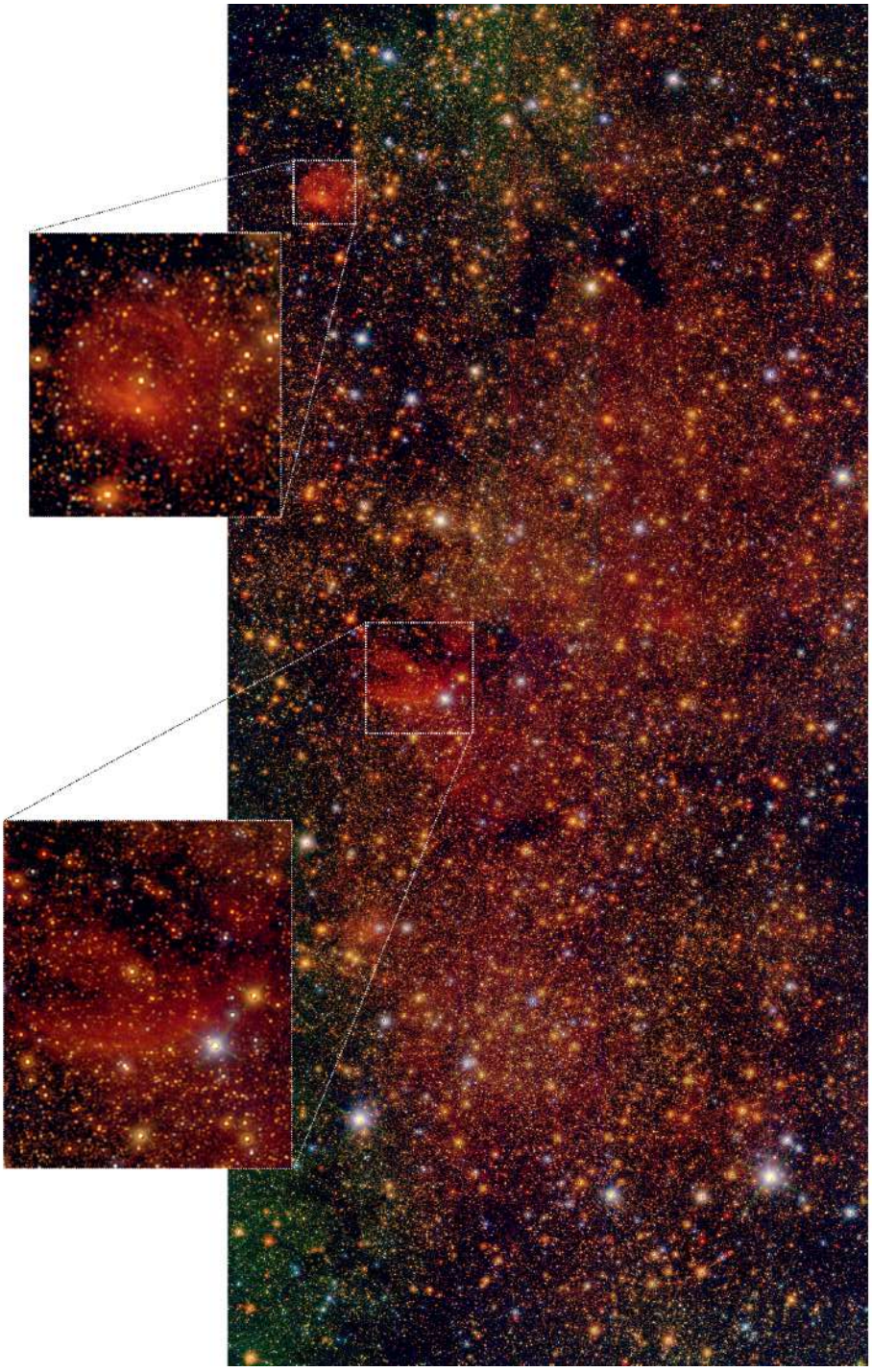

Fig. C.40 RGB image of D12 (red = K_s band, green = H band and blue = J band).

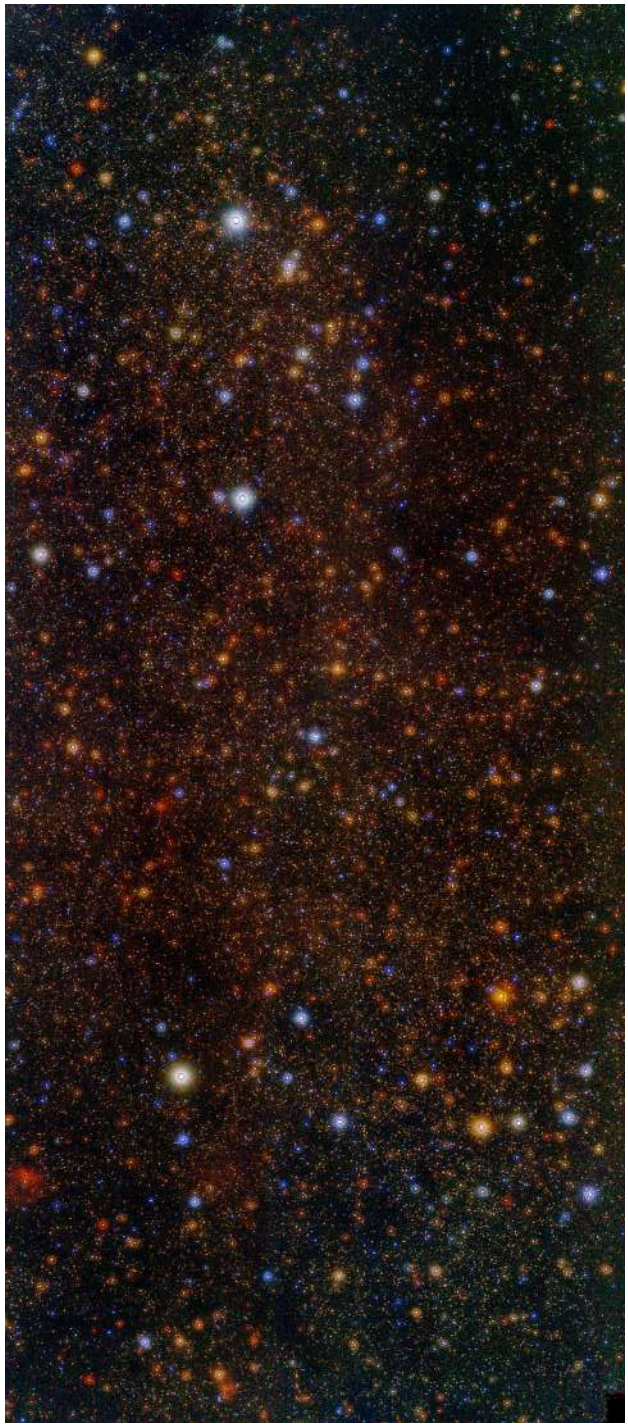

Fig. C.41 RGB image of D13 (red = K_s band, green = H band and blue = J band).

Fig. C.42 RGB image of D14 (red = K_s band, green = H band and blue = J band).

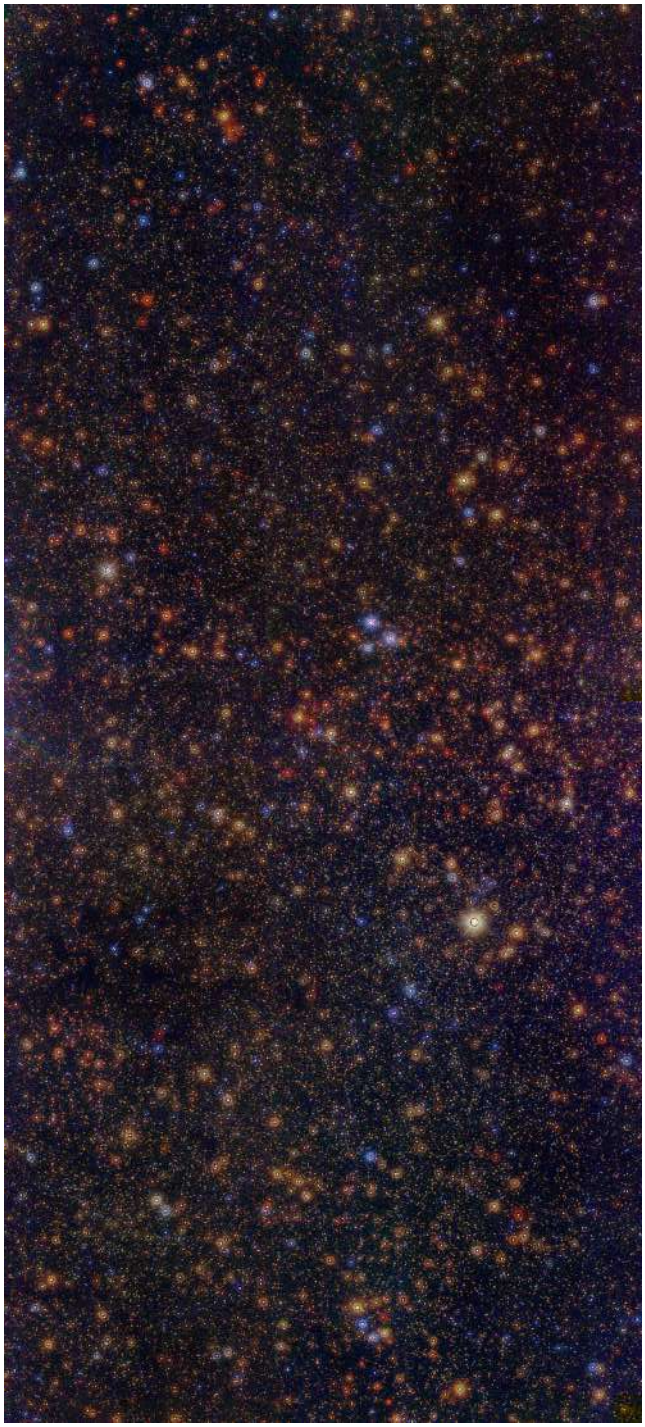

Fig. C.43 RGB image of D15 (red = K_s band, green = H band and blue = J band).

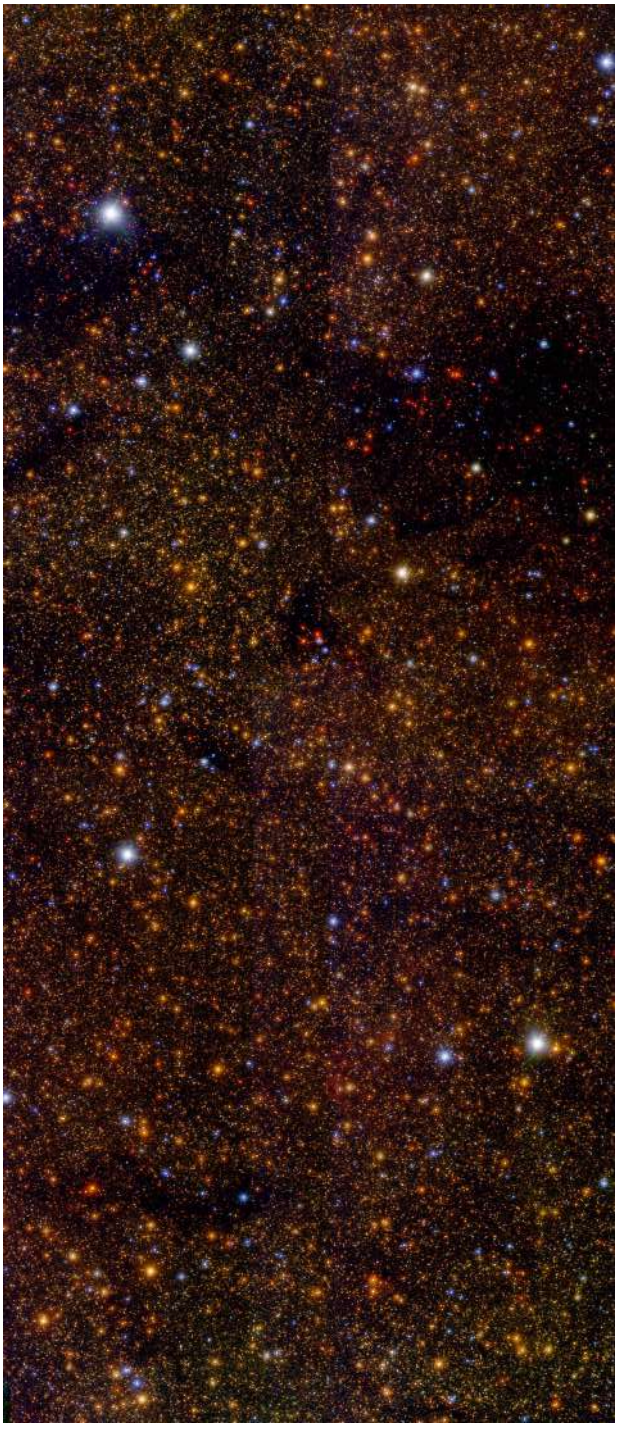

Fig. C.44 RGB image of D17 (red = K_s band, green = H band and blue = J band).

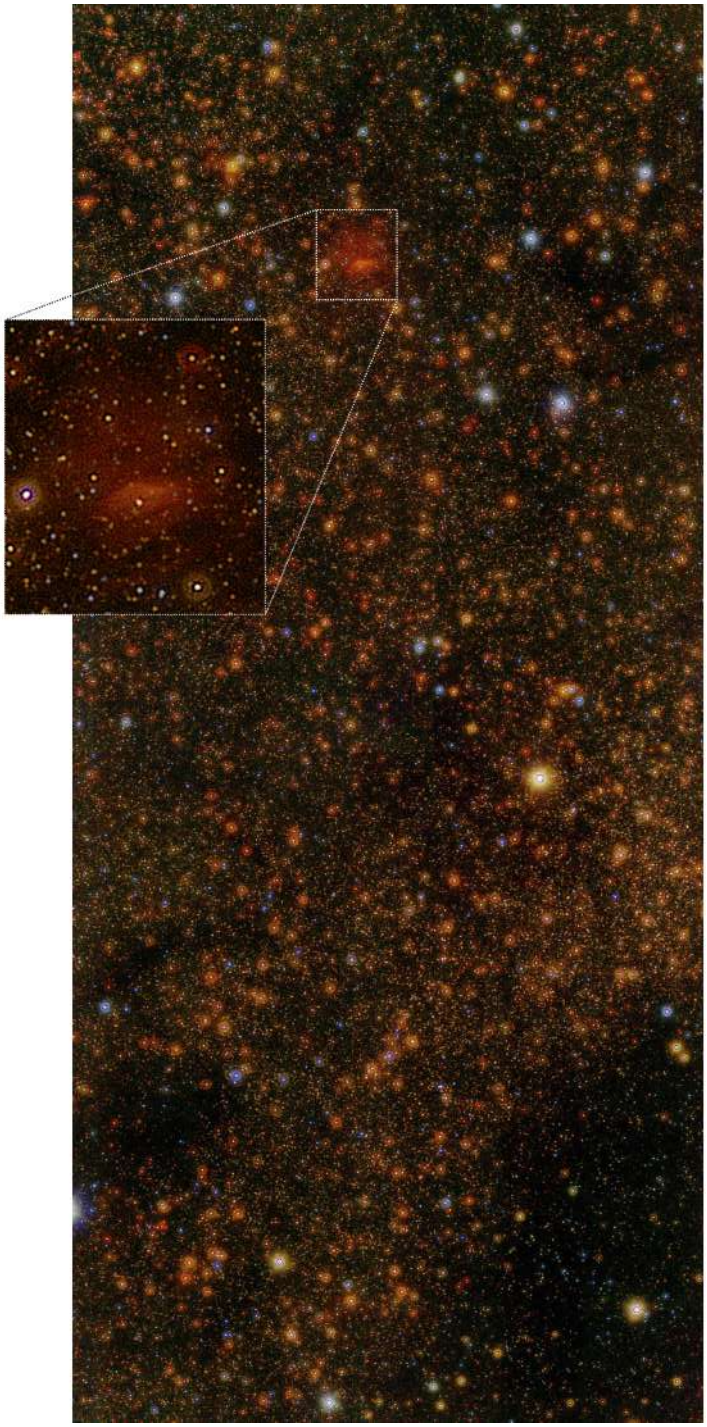

Fig. C.45 RGB image of D18 (red = K_s band, green = H band and blue = J band).

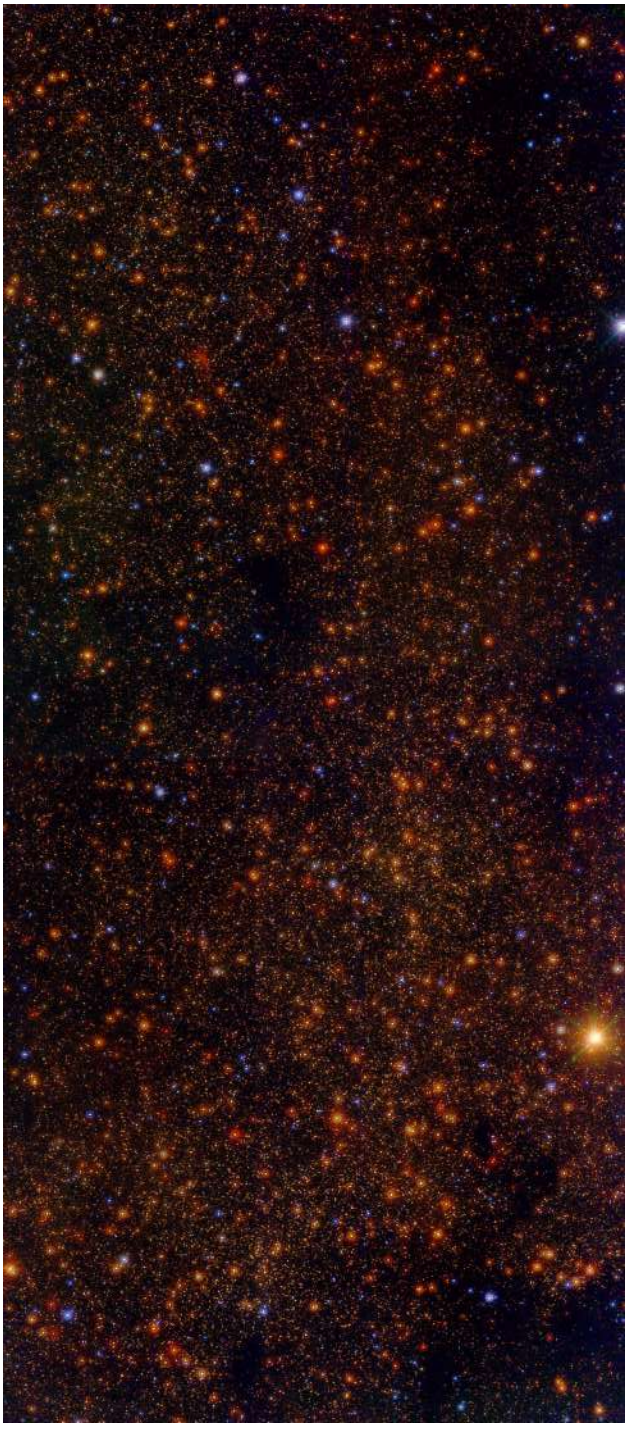

Fig. C.46 RGB image of D19 (red = K_s band, green = H band and blue = J band).

Fig. C.47 RGB image of D21 (red = K_s band, green = H band and blue = J band).

D

Theoretical models for K_s luminosity functions

We compared different theoretical models to analyse the behaviour of their K_s luminosity functions for metal rich populations (as it is needed for the metallicity of the NSD, see chapter 9). We used models from three different groups and compared their performances. We used MIST (Choi et al., 2016; Dotter, 2016; Paxton et al., 2011, 2013, 2015), BaSTI (Pietrinferni et al., 2014) and PARSEC+Colibri (Bressan et al., 2012b; Marigo et al., 2017) models. In particular, we were interested in the distance between the RC and the RGBB and the relative fraction of stars belonging to each of those features. Figure D.1 shows the comparison for the different models assuming a range of ages and twice the solar metallicity. We noticed that PARSEC models might not be appropriate to deal with old metal rich populations. The relative distance, ΔK_s, between the RC and the RGBB changes homogeneously as a function of age

in BaSTI/MIST, while the RGBB appears to behave more erratically in the Parsec models (becoming first brighter and then fainter again). We found this behaviour in BaSTI and MIST models, whereas PARSEC models show an anomalous behaviour for models around 5 Gyr. Therefore, we used BaSTI and MIST models for our analysis in chapter 9.

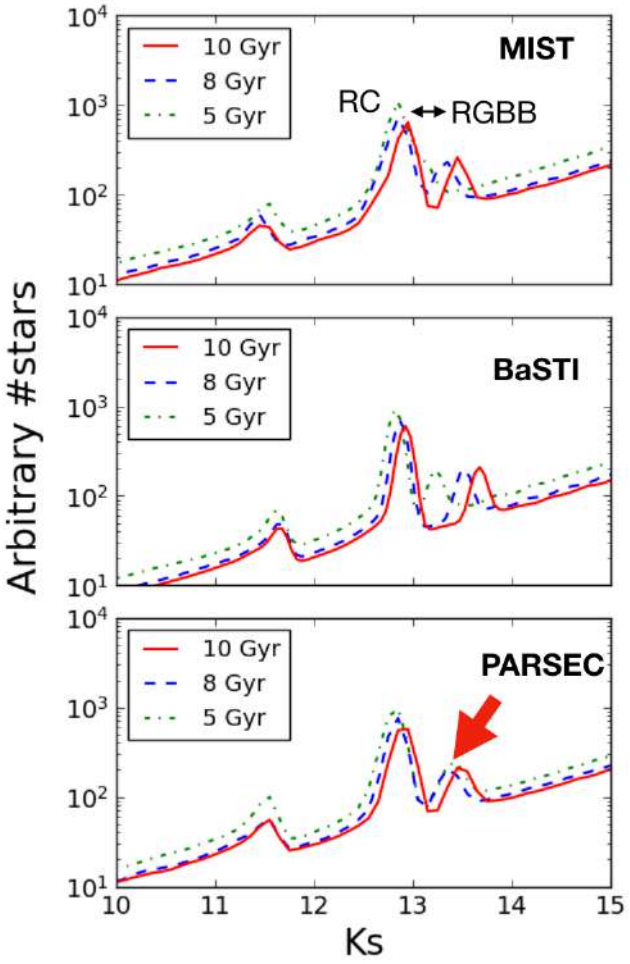

Fig. D.1 K_s luminosity function for different theoretical models. The red arrow indicates the anomalous behaviour observed for PARSEC+Colibri models.